NEUTRINO FLUX PREDICTIONS FOR THE T2K LONG BASELINE NEUTRINO OSCILLATION EXPERIMENT

VYACHESLAV GALYMOV

A DISSERTATION SUBMITTED TO
THE FACULTY OF GRADUATE STUDIES
IN PARTIAL FULFILMENT OF THE REQUIREMENTS
FOR THE DEGREE OF

DOCTOR OF PHILOSOPHY

GRADUATE PROGRAM IN DEPARTMENT OF PHYSICS AND ASTRONOMY
YORK UNIVERSITY
TORONTO, ONTARIO

MARCH 2012

Abstract

T2K is a long baseline neutrino oscillation experiment. It utilizes a 30 GeV proton beam at Japan Proton Accelerator Research Complex to produce an intense muon neutrino beam which is aimed in the direction of the Super-Kamiokande detector located 295 km away. As neutrinos travel towards the Super-Kamiokande site, they convert or oscillate to neutrinos of another flavour. One of the main goals of T2K is to observe ν_μ to ν_e oscillations and measure the last unknown mixing angle θ_{13} that governs these transitions. In addition, the experiment also plans to make precise measurements of the Δm^2_{32} and θ_{23} neutrino mixing parameters. This work presents the analysis of the neutrino flux predictions in T2K, one of the key inputs necessary to determine the oscillation parameters. The effects of the associated systematic uncertainties on the measurement of the oscillation parameters are also considered.

Acknowledgements

Firstly, I would like to thank my adviser, Sampa Bhadra, for giving me a chance to explore the fascinating world of neutrinos and for the support throughout this journey. In addition, I also want to express my gratitude to all of the members of the OTR group: Mircea Cadabeschi, Akira Konaka, John Martin, Dave Morris, Alysia Marino, Mark Hartz, and Patrick de Perio. In many different ways each one of them was instrumental not only to the successful completion of this dissertation, but also to my growth as a scientist.

I would like to acknowledge the contribution of Brian Kirby whose work laid the foundation for the OTR system. Thanks are also in order to Kentaro Mizouchi for his help with the FPGA programming and the interface box development.

Throughout the years, it has been a privilege working within the T2K beam group. I would especially like to thank A. Ichikawa, H. Kakuno, H. Kubo, A. Marchionni, T. Nakadaira, K. Matsuoka, K. Sakashita, T. Sekiguchi, M. Tada, Y. Yamada, and E. Zimmerman.

It takes a lot of dedicated people to make an experiment in the particle physics a success. Therefore I would like to thank all of the members of the T2K collaboration. Special thanks also go to the J-PARC accelerator group and the support staff both here at York and at J-PARC and KEK. The contribution of the NA61 collaboration that provided the data crucial for this analysis should also be acknowledged.

This work has been supported by: the Natural Science and Engineering Research Council of Canada; TRIUMF; the National Research Council, Canada; the Ontario Graduate Scholarships in Science and Technology; the JSPS Fellowship program.

A special credit is due to my partner Stephanie Conway for her support throughout the years. Finally I want to express gratitude to my mother without whom I would not be writing this.

Vyacheslav Galymov

Toronto, Canada

March, 2012

Contributions to the T2K experiment

I joined the T2K experiment in 2005 working, with a small group from York University, University of Toronto, and TRIUMF laboratory, on a design for a proton monitor to operate near the T2K target. The T2K experiment is a long-baseline neutrino oscillation experiment. One of its main goals is the discovery of the ν_μ to ν_e oscillations governed by the last unknown mixing angle θ_{13}. Additionally T2K aims to make precision measurements of the Δm^2_{32} and θ_{23} oscillation parameters. The experiment utilizes a new high power proton accelerator J-PARC (Japan Proton Accelerator Research Complex) meant to deliver 750 kW proton beam to make an intense neutrino beam. The experiment uses the "off-axis" method to produce a narrow band neutrino beam. The position of the proton beam on the target has to be precisely controlled as shifts on the order of a millimeter would result in significant changes in the energy of the neutrinos thereby making it hard to meet the physics requirements of the experiment. Due to the high radiation environment near the target, electronic equipment and conventional proton monitors, however,

could not be used.

This led us to propose using Optical Transition Radiation (OTR) to monitor the beam protons near the T2K target. OTR is a phenomenon where a charged particle can produce visible light when crossing a boundary between two materials with different dielectric constants. A thin metallic foil placed in the path of the protons would produce the OTR light when the beam travels through it and a system of mirrors would collect this light and guide it out of the radiation area to form a 2D image of the beam at a camera. Since both the foil and the mirrors would be made out of metal, such a system would not be very susceptible to radiation damage.

This was the idea at the time I joined. There was, however, no concrete design for a mirror system capable of transporting the light efficiently from the target area. My first contribution was to work on an optical system simulation the York group had started to develop. In addition to developing the simulation package, my main priority was conducting the studies of the alignment tolerances for the position and orientation of the mirrors. The focus of this work was to come up with a design capable of measuring the proton beam with a required precision, given the large distances of the optical path and a reasonable set of assumptions on capabilities of the mechanical support structure for the mirrors. Based on our studies, we built a 1/15 scaled prototype. Using this system we were able to observe OTR light from

an electron beam at the National Research Council in Ottawa. This prompted us to proceed with the construction of a full scale detector.

My simulations had shown that the parabolic mirrors used in the optical system were introducing a certain amount of distortion. Such distortion could lead to a significant bias in the beam position measurements and therefore had to be corrected. I developed a method and wrote the necessary software which enabled correction of the distortion effects introduced by the system using an image of a known precisely machined calibration pattern. In addition to the distortion effects, my studies of the system performance indicated that the light collection efficiency from the different regions of the OTR foil was not uniform and that such an effect could also lead to significant biases in the measurements of the proton beam profile. It is possible to calibrate the light collection efficiency by imaging a highly uniform diffuse light source. A standard tool in photometry for this type of calibration is an integrating sphere. Unfortunately the large dimensions of the sphere required by our application made the commercially available models prohibitively expensive. I demonstrated, however, that it was feasible to build such a device from inexpensive components and obtain a light source sufficiently uniform for the calibration of the monitor.

In addition to working on the OTR monitor calibration and image analysis, I was one of the principal developers of the OTR monitor data acquisition system. I

designed and tested the software for the readout of the camera images. I also worked on the development of the trigger logic for the monitor image acquisition circuitry. This involved a substantial amount of programming of Field-Programmable Gate Arrays.

The OTR monitor was successfully commissioned with the rest of the T2K beam-line in the spring of 2009. My extended stay in J-PARC at that time was supported by the Japan Society for the Promotion of Science fellowship. During the commissioning the monitor was especially useful as an aid to tune the proton beam orbit. Since then, it has been reliably taking data and proved a valuable tool in understanding proton beam properties.

I became involved with the evaluation of the neutrino flux predictions and associated systematic uncertainties which were essential inputs for the analysis of the T2K neutrino data. This meant working extensively with the Monte Carlo simulations designed for predicting the neutrino flux. When I started the Monte Carlo simulation used at T2K for the flux predictions was based on GEANT 3. This was a problem, since the simulation of the hadron production, crucial for the prediction of the neutrino flux, was done using obsolete models. Extensive comparisons with the particle production data from recent experiments have indicated that FLUKA was a better model to use. Unfortunately its GEANT interface was no longer supported. Nonetheless I was able to integrate it into the T2K neutrino

flux simulation. Subsequently I was put in charge of the neutrino flux Monte Carlo simulation production for the analysis of the T2K data.

I was part of the group involved in the analysis of the first T2K data. My responsibility was to provide the predicted neutrino flux, which is one of the inputs required to measure the oscillation parameters. I also worked on evaluating the systematic uncertainties in the neutrino flux predictions related to the proton beam parameter uncertainties and the component alignment in the T2K beamline.

In T2K neutrinos originate predominantly from the decays of pions and kaons produced in the interactions of the beam protons with a carbon target. While the majority of the produced neutrinos are of muon flavor, other types of neutrinos are also present. The contamination of electron neutrinos in the muon neutrino beam is particularly important for the ν_μ to ν_e oscillation searches and measurement of θ_{13}. Since a sizable fraction of these neutrinos come from the kaon parents, understanding the uncertainties associated with the kaon production is a crucial input to an oscillation analysis. After the first analysis of the T2K data was completed, I have been working on incorporating the measurements of the kaon production cross-sections from NA61 and other hadron production experiments into the T2K analysis. This led to a significant reduction in the uncertainties associated with ν_e contamination in the beam and improvement in the sensitivity for the electron appearance signal.

Table of Contents

List of Tables

List of Figures

Abbreviations

CC	Charged Current neutrino interactions
CCQE	Charged Current Quasi-Elastic neutrino interactions
CT	Current Transform monitor
DAQ	Data AcQuisition
ECAL	Electromagnetic CALorimenter
ESM	ElectroStatic Monitor
FGD	Fine Grained Detector
FLUKA	Package for calculation of particle transport and interactions
GCALOR	Package for simulating particle interactions in GEANT3
GEANT3	Collection of software libraries for simulating particle interactions with detectors
GFLUKA	Package for simulating particle interactions in GEANT3
INGRID	Interactive Neutrino GRID detector: part of the near detector complex at T2K
K2K	KEK to Kamioka experiment
KamLAND	Kamioka Liquid Scintillator Anti-neutrino Detector
MC	Monte Carlo
MINOS	Main Injector Neutrino Oscillation Search

MUMON	MUon MONitor
ND280	One of the near detectors at T2K
OTR	Optical Transition Radiation
PØD	Pi-Zero detector
PDF	Probability Density Function
POT	Protons on Target
SK	Super-Kamiokande detector
SSEM	Segmented Secondary Emission Monitor
SSM	Standard Solar Model
T2K	Tokai to Kamioka experiment
TPC	Time Projection Chamber

1 Introduction

Our present knowledge of the subatomic world is encapsulated in the Standard Model (SM) of particle physics. The model describes all of the known particles and the three fundamental forces[1]—strong, electromagnetic, and weak—that act upon them. It has successfully explained a large variety of experimental results and its predictions have been proved to be remarkably accurate. The building blocks of the model, shown in Fig. 1.1, are six quarks, six leptons, and four particles (force carriers) called gauge bosons that act as the mediators of interactions. The model also postulates the existence of Higgs particle(s) (not shown in the figure) currently being sought at the Large Hadron Collider (LHC) at CERN. The numbers in the top left corner of each block are the electric charge (first from the top) of a given particle and its intrinsic angular momentum called spin. Particles with fractional spin are called fermions while those with integer spin are called bosons. Quarks and leptons belong to the former group, while the force carriers are part of the latter.

[1]The fourth fundamental force, the force of gravity, is not part of the Standard Model and attempts of including it into a single framework with the three other forces are ongoing.

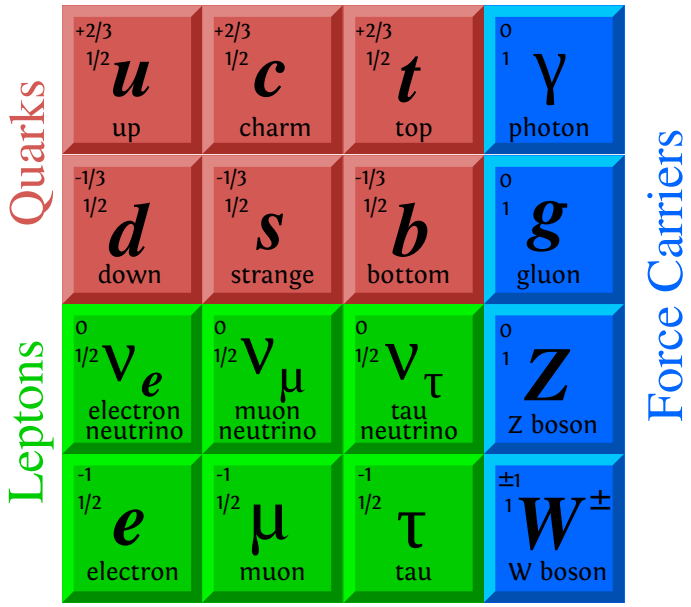

Figure 1.1: Standard Model of particles physics. The natural units are used ($\hbar = c = 1$) and the electric charge is expressed in units of e.

Charged particles in the SM also have partners that possess the same mass, but carry an opposite charge. These are called antiparticles and are often marked by a bar over the particle symbol (*e.g.*, $\bar{u}$ is an anti-u quark). The antiparticle of the electron, for example, is the positively charged positron. Collectively we refer to the substance composed of particles (antiparticles) as matter (antimatter). The situation is more complicated in the case of neutrinos. Since neutrino is not charged, it is not known whether its "anti" partner is a distinct particle or whether the two are actually the same particle.

The interactions between particles occur by exchanging one of the gauge bosons (which for this reason are called force carriers). This is illustrated in Fig. 1.2

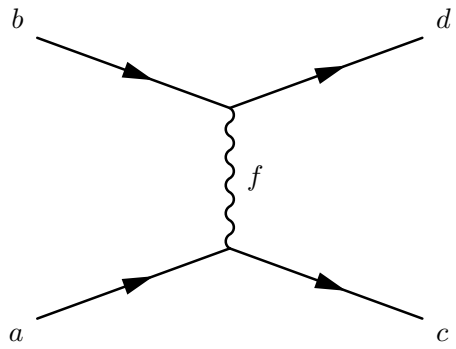

Figure 1.2: Two particle interaction with exchange of a generic vector boson f. The arrows indicate the direction of time.

where two particles a and b are shown colliding leaving them in some altered state (elastic or quasi-elastic collisions) or even creating new particles c and d (inelastic collisions). The gauge boson, generically labeled as f in the figure, is the force carrier that mediates the interaction. The type of this boson determines which force is involved in a process.

The strong force, mediated by gluons, is responsible for binding quarks inside particles called hadrons of which protons and neutrons are examples. The more familiar electromagnetic force acts on any particle that carries an electric charge. Both quarks and charged leptons (e, μ, and τ) can therefore participate in the electromagnetic interactions. At a distance scale on the order of 10^{-15} meters, it is approximately 100 times weaker than the strong force. Finally, the weak force affects all fermions. It is the weakest of the three forces with the strength $\sim 10^{-4}$ smaller than the electromagnetic force. The three neutrinos are only sensitive to

this force.

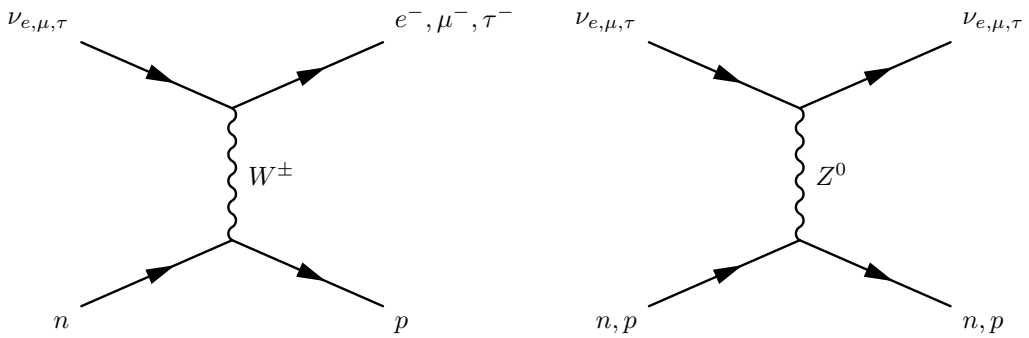

(a) Charged current interaction mediated by $W^\pm$ boson

(b) Neutral current interaction mediated by Z boson

Figure 1.3: Neutrino interactions with protons and neutrons.

The simplest possible neutrino interactions with neutrons and protons (nucleons) are illustrated in Fig. 1.3. Fig. 1.3a shows a neutrino exchanging a $W^\pm$ boson with one of the quark constituents (not shown in the figure) of a neutron n which leads to the production of a charged lepton and a proton p. The type, or flavour, of the produced lepton defines the flavour of the interacting neutrino. Since $W^\pm$ bosons carry an electric charge, such processes are referred to as charged current (CC) interactions.

Neutrino interactions with nucleons involving the exchange of the neutral Z^0 boson are also possible. These types of processes, shown in Fig. 1.3b, are referred to as neutral current (NC) interactions.

Neutrinos are abundant in nature. One of the largest producers is the sun, which

radiates a large number of electron neutrinos—over 10^{11} of these solar neutrinos cross every square centimeter of the Earth's surface each second. Neutrinos are also produced in the upper layers of the Earth's atmosphere by cosmic rays (mostly protons) colliding with the air nuclei. About two thirds of these atmospheric neutrinos are muon neutrinos with the rest being electron neutrinos.

The standard approach of detecting neutrinos is by observing charged leptons produced in the CC interactions. However, the cross-section, the quantity that determines the probability of interaction, for these reactions is minute. For example, for 1 GeV neutrinos it is on the order of 10^{-38} cm^2, which is about 10^{-13} times smaller than the cross-section for proton-nucleus interactions. Since the number of neutrinos a given detector can expect to collect is proportional to the product of the cross-section, detector mass, and neutrino flux (the number of neutrinos crossing a unit area per unit time), both large detectors and high neutrino flux are needed to observe these particles.

In addition to the difficulty of their detection, neutrinos have another distinct property. They are the only fermions in the Standard Model that were believed to have no mass. The situation changed at the end of the 20^{th} century.

In 1998, a rather dramatic discovery was made by a collaboration of scientists at the Super-Kamiokande neutrino observatory in Kamioka, Japan [1]. The group observed that the number of the atmospheric downward-going muon neutrinos was

about two times larger than the number of the upward-going neutrinos. As neutrinos are weakly interacting, they can pass through the Earth with very little absorption. It was therefore expected that the two numbers should be close to each other. As no significant excess in the observed number of electron neutrinos was seen, the best hypothesis that could explain such discrepancy was that muon neutrinos have converted or "oscillated" to tau neutrinos during their travel through the Earth. Since the tau neutrinos could not be experimentally detected at Super-Kamiokande, the "disappearance" of the upward-going neutrinos was observed. As oscillations are only possible if neutrinos have mass, the Super-Kamiokande result was the first experimental indication that the Standard Model was incomplete.

The neutrino oscillation hypothesis was later tested by the K2K and MINOS experiments. The two experiments used particle accelerators to produce muon neutrinos in a controlled way. These neutrinos are made by colliding a beam of energetic protons with some amount of material (called a target). The interactions of the protons with target nuclei result in the generation of the unstable particles called pions which produce muon neutrinos when they decay. Similar to Super-Kamiokande, a significant disappearance of muon neutrinos due to their conversion to tau neutrinos was observed by K2K [2] and MINOS [3].

Since there are three neutrinos, it is also theoretically possible for ν_μ to convert to ν_e. This, however, has not been seen so far. Measuring such a conversion can

give clues for one of the most interesting questions fundamental to the existence of the Universe. At the time of the Big Bang, matter and antimatter were produced in equal amounts. As the Universe cooled, matter and antimatter annihilated with each other. A tiny fraction of matter, however, survived proceeding to form stars, planets, and galaxies: everything we see around us today. How it was possible for such an excess to develop is one of the great puzzles. Precise measurements of ν_μ to ν_e oscillations may help shed some light on this mystery.

One of the primary goals of the Tokai-to-Kamioka (T2K) experiment is to detect ν_μ to ν_e oscillations in an intense muon neutrino beam produced by 30 GeV protons. The experiment also aims to significantly improve our understanding of the parameters governing the disappearance of ν_μ. One of the key ingredients necessary to make these measurements is the knowledge of the expected neutrino flux. That is the subject of this dissertation.

The layout of the work is as follows. A brief overview of neutrino history is given at first in Chap. 2. The phenomenology of the neutrino mixing is discussed in Chap. 3. The description of the T2K experiment is given in Chap. 4 followed by the chapter on the Optical Transition Radiation proton beam monitor that has been developed for the T2K proton beamline. The rest of the work deals with the estimation of the neutrino flux for the analysis of the neutrino oscillations at T2K. A brief summary and concluding remarks are given in Chap. 10.

2 A Short History of Neutrinos

2.1 From hypothesis to detection

At the end of the 19^{th} century, Henri Becquerel accidentally discovered that some elements were natural emitters of strange particles, which he called rays [4]. Materials with such properties are now called radioactive. They are made of unstable elements that can sporadically disintegrate, or decay, emitting different types of particles (radiation). Ernest Rutherford classified the radiation into three types: α, β, and γ according the penetrating power of each particle. The α particles were later shown to be helium nuclei, while β and γ particles were identified as electrons (and positrons) and photons, respectively.

From the principle of the conservation of energy, the energy spectrum of the emitted rays was expected to be discrete. The observation of the broad energy distribution of β electrons by James Chadwick [5] in 1914 therefore came as a surprise and generated a considerable amount of debate (see, for example, [6] for historical overview).

The difficulty in explaining the energy spectrum of β rays led to a view, advocated at the time by Niels Bohr, that the energy conservation had to be violated. Wolfgang Pauli was not inclined to accept such a radical explanation. In 1930, he postulated the existence of a new particle emitted along with the electron which he called "neutron" (the English translation of the letter outlining his proposal can be found in [7]). The released energy could be shared between the electron and neutron resulting in an observation of the broad energy spectrum for the former. The new particle had to be neutral and have a great penetrating power to explain the lack of experimental detection.

A different type of neutron was discovered in 1932 by Chadwick [8] who measured its mass to be close to that of the proton. This neutron was too heavy to be the partner of the β electron.

Enrico Fermi followed Pauli's hypothesis and assumed an invisible partner to the β electron which he named "neutrino" to distinguish it from Chadwick's neutron. Fermi then proceeded to formulate a quantitative description of β decay [9]. In his theory, the transition of the neutron to a proton was associated with the creation of an electron and an anti-neutrino in case of the β^- decays:

$$n \rightarrow p + e^- + \bar{\nu}_e. \tag{2.1}$$

For β^+ decays, on the other hand, it was the proton that converted to a neutron accompanied by the production of the positron-neutrino pair:

$$p \rightarrow n + e^+ + \nu_e. \tag{2.2}$$

The Fermi Theory of β decay, as it is known now, successfully explained the broad energy spectrum of β rays. In addition, it also predicted processes of the type:

$$\bar{\nu}_e + p \rightarrow n + e^+, \tag{2.3}$$

where $\bar{\nu}_e$ are anti-particles of neutrinos or anti-neutrinos.

From the experimental point a view the reaction Eq. 2.3, sometimes called inverse β decay, was a possible way to detect a neutrino. In their 1934 paper, H. Bethe and R. Peierls [10] estimated the neutrino capture rate for this reaction. It turned out to be so minute that they were prompted to conclude: "there is no practically possible way of observing the neutrino".

In the 1950s Clyde Cowan and Frederick Reines [11], however, realized a way to detect (anti-)neutrinos using the reaction Eq. 2.3. They placed a detector next to a nuclear reactor hoping to measure anti-neutrinos coming from the β decays of fission fragments. The detection principle relied on observing both the positron and the neutron in Eq. 2.3. This provided them with a distinct signal that could

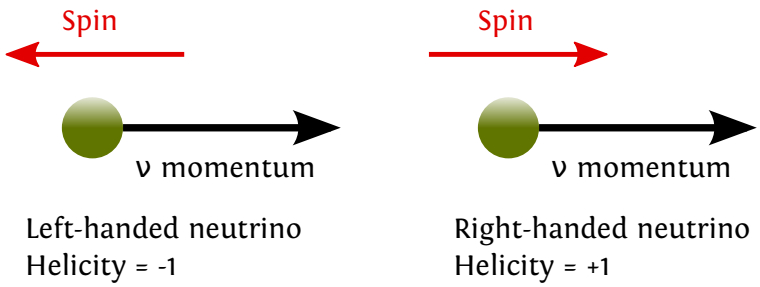

Figure 2.1: Illustration of neutrino helicity concept.

be easily distinguished from the backgrounds caused by natural radioactivity and cosmic rays. They saw on average 3 events per hour that were consistent with the expected neutrino signature. After more than 20 years Pauli's hypothesis had been proven to be correct.

2.2 Neutrino handedness and mass

Two years after the neutrino discovery, Maurice Goldhaber *et al.* [12] were able to measure the neutrino helicity or handedness. Helicity (handedness) is the term used to describe the projection of a particle's spin on its direction of motion. The spin can be either aligned with the motion or point in the opposite direction (see Fig. 2.1). In the former case the particle is said to be right-handed while in the latter case it is called left-handed.

Goldhaber *et al.* analyzed the polarization of the photons produced in

$$^{152}\mathrm{Eu} + e^- \rightarrow {}^{152}\mathrm{Sm}^* + \nu_e \rightarrow {}^{152}\mathrm{Sm} + \gamma + \nu_e. \tag{2.4}$$

From the conservation of total angular momentum, they were able to infer that the neutrinos were only left-handed. It was a significant result, as it implied that neutrinos were massless. This follows from the fact that if they did have mass, it would be possible to find a reference frame where they would move in the opposite direction and therefore appear right-handed. Since no right-handed neutrinos were detected, it was concluded that neutrinos had to have no mass. Later on the massless neutrino fit well within the framework of the Standard Model.

2.3 The solar neutrino problem

Neutrinos are copiously produced in the nuclear reactions inside the core of the sun. There are about 10^{11} of these solar ν_e neutrinos passing through every square centimeter of the Earth surface per second [13]. In 1964 Ray Davis [14], in close collaboration with John Bahcall [15], proposed an experiment for observing the solar neutrinos via the Cl-Ar mechanism, a detection principle suggested nearly two decades earlier by Bruno Pontecorvo [16]. In this method, neutrinos are captured by an isotope of chlorine, ^{37}Cl, in the reaction:

$$\nu_e + {}^{37}\mathrm{Cl} \rightarrow e^- + {}^{37}\mathrm{Ar}. \tag{2.5}$$

The atoms of ^{37}Ar are then extracted from a detector volume and counted to determine the number of the neutrino interactions.

In 1968, Davis and collaborators [17] reported the first measurement of the neutrino capture rates in chlorine, which was in disagreement with the expectation from the Standard Solar Model (SSM). This discrepancy became known as the "solar neutrino problem" and turned out to be of profound significance.

2.4 Accelerator neutrino beams and discovery of neutrino flavour

The reactor sources and the sun allowed the study of neutrino interactions at energies of only up to about 10 MeV. This was not high enough, however, if one wanted to observe a reaction of the type

$$\nu_\mu + n \rightarrow p + \mu^- \tag{2.6}$$

in addition to

$$\nu_e + n \rightarrow p + e^-. \tag{2.7}$$

The process in Eq. 2.6 is not kinematically permitted for neutrino energies $E_\nu < 106$ MeV (which is the mass of the muon).

Around 1960 Pontecorvo [18] and Melvin Schwartz [19] independently proposed to use proton accelerators to generate high energy neutrino beams. It was known that the charged π mesons decayed into a muon and a neutrino:

$$\pi^+ \rightarrow \mu^+ + \nu_\mu. \tag{2.8}$$

Since pions could be easily produced by colliding protons with a stationary target, it was feasible to make a pion beam of high enough energy and intensity to produce a neutrino beam.

The idea was put to a test a few years later by Schwartz and a group of scientists from Columbia University and Brookhaven National Laboratory (BNL) [20]. Under the hypothesis that ν from π^+ decays (emitted with muons) were the same particles as ν from β decays (emitted with electrons), the group expected to see as many electron as muon tracks in their detector. The tracks they observed, however, were only those whose signature was consistent with muons. It was therefore concluded that the neutrinos emitted in pion decays along with muons were of different type or "flavour" than the ones coming from the β decays.

A very important milestone for the future accelerator neutrino beams was the invention of the magnetic focusing horns by Simon van der Meer in 1961 [21]. In the BNL experiment, the pions created in the collisions of the protons with a target

formed a divergent beam. Van der Meer's proposal was to create a device that would act as a lens focusing pions into a nearly parallel beam. This would significantly increase the neutrino yields as most of neutrinos could be aimed towards a detector.

2.5 Three neutrino flavours

The discovery of the ν_μ suggested a picture where each charged lepton had an accompanying neutrino partner. The detection of the τ lepton by Martin Perl *et al.* [22] at Standford Linear Accelerator Center (SLAC) in the mid-seventies thus led to the belief that there existed a third neutrino species ν_τ.

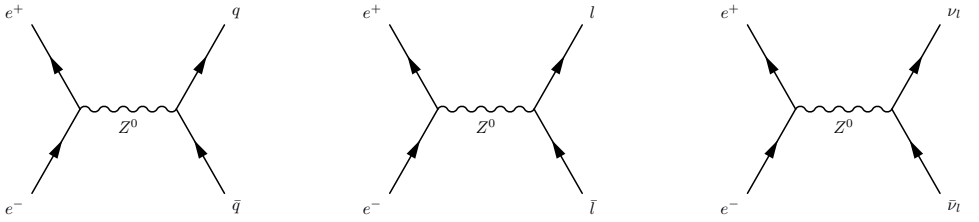

(a) Z^0 decay to quark-antiquark pair

(b) Z^0 decay to charged leptons ($l = e, \mu, \tau$).

(c) Z^0 decay to neutrinos ($l = e, \mu, \tau$).

Figure 2.2: Decay modes of Z^0 boson.

In the late eighties and early nineties experiments at the Large Electron Positron (LEP) accelerator at CERN were able to deduce the total number of (active) neutrino flavours by studying the decay rates of the Z^0 boson. The bosons were produced by colliding e^+ and e^- together. They decayed almost immediately (the lifetime of Z^0 is on the order of 10^{-25} sec) producing particle-antiparticle pairs.

The three simplest Z^0 decay scenarios are shown in Fig. 2.2.

It is possible to measure the Z^0 decay rates to a quark-antiquark (Γ_{had}) pair and the charged lepton pair (Γ_{l}) by detecting the decay products. Since neutrinos escape undetected, their contribution to the decay rate of Z^0 cannot be directly measured. One can, however, determine this "invisible" contribution, Γ_{inv}, by subtracting the sum of Γ_{had} and Γ_{l} from the total decay rate. The number of neutrinos, N_ν, can then be deduced from Γ_{inv}. It turned out to be [23]

$$N_\nu = 2.984 \pm 0.008, \tag{2.9}$$

confirming that there was one more neutrino waiting to be discovered.

The first direct detection of the third neutrino flavour ν_τ was made in 2000 by DONuT (Direct Observation of NU Tau) at Fermilab [24].

2.6 Disappearing solar neutrinos

The deficit in the number of electron neutrinos coming from the sun first observed by Davis *et al.* was later confirmed by GNO [25], GALLEX [26], SAGE [27], and Super-Kamiokande [28] experiments. The consistency of the experimental observations by diverse detectors with different neutrino detection techniques provided strong evidence that the solar neutrino problem was real. The solution appeared in the

works of B. Pontecorvo [29] and Z. Maki, M. Nakagawa, and S. Sakata [30] who, between 1960-1970, independently introduced the idea of neutrino mixing. This mixing could lead to an effect where neutrinos of different flavour can convert into each other. For example, neutrinos produced purely as ν_e can turn into ν_μ, while those in turn can convert back to ν_e, resulting in an oscillatory flavour change.

If neutrino flavours could mix, the deficit of the solar neutrinos could be interpreted to be caused by the fact that a fraction of electron neutrinos that reach the Earth have converted to muon or tau neutrinos. Since the experiments were not sensitive to the detection of these flavours, a deficit was observed. The hypothesis could be tested by detecting neutrinos via a process that is sensitive to all neutrino flavours [31]. This was done at the Sudbury Neutrino Observatory (SNO) [32]. The SNO collaboration was able to show that the predicted solar neutrino rates from the SSM were correct and the observed deficit was indeed due to the neutrino mixing.

2.7 Atmospheric neutrino oscillations

As mentioned earlier, in 1998 the Super-Kamiokande collaboration published the results of their observations of atmospheric neutrinos [1]. These neutrinos, composed of ν_μ, $\bar{\nu}_\mu$, ν_e, and $\bar{\nu}_e$ flavours, are produced in the decays of the unstable particles (mostly π mesons) created in the collisions of the energetic cosmic rays

with the nuclei in the atmosphere. Since the cosmic ray flux is isotropic, the resultant neutrino flux is also uniform. The Super-Kamiokande collaboration, however, reported a significant deficit in the number of muons produced by the up-going muon neutrinos. As no significant excess was observed in the expected number of electron neutrinos, such disappearance could then be explained by assuming that muon neutrinos oscillated into tau neutrinos while traveling through the Earth.

This observation was verified by two accelerator-based neutrino experiments K2K [2] and MINOS [3]. K2K used a 12 GeV proton beam from the KEK proton synchrotron accelerator to produce a predominantly ν_μ beam. A detector near the production point was employed to measure the initial neutrino flux prior to any oscillation effects. The oscillated flux was observed by Super-Kamiokande located 250 km from KEK (the production site). The neutrino beam energy was optimized to achieve a maximum conversion of ν_μ to ν_τ at the location of Super-Kamiokande.

The MINOS experiment, still in operation at Fermilab, followed the same two-detector approach as K2K. The muon neutrino beam is produced by 120 GeV protons from the Main Injector accelerator at Fermilab, while the baseline distance (distance from the production site to the far detector location) is 735 km.

2.8 Current status

The discovery of neutrino mixing was of profound significance for the Standard Model of particle physics. The measurements of Goldhaber *et al.* of the neutrino helicity implied that neutrinos were massless, in agreement with the SM expectations. The framework of neutrino mixing, however, required that at least two out of the three neutrinos had masses distinct from each other. Various extensions to the Standard Model have been proposed to accommodate the non-zero neutrino masses. These theories are yet to be tested. Nonetheless the study of neutrinos has provided the first experimentally compelling evidence of the existence of new physics beyond what is contained in the Standard Model.

The phenomenological model that best describes the neutrino oscillation data so far relies on the existence of three neutrinos ν_1, ν_2, and ν_3 with distinct masses m_1, m_2, and m_3. These neutrinos are related to ν_e, ν_μ, and ν_τ by a mixing matrix. The neutrino oscillations in this framework are described in terms of six parameters: two mass square differences, $\Delta m^2_{21} = m^2_2 - m^2_1$ and $\Delta m^2_{32} = m^2_3 - m^2_2$, and four parameters, θ_{12}, θ_{23}, θ_{13}, and δ, that determine the mixing matrix. The two mass square differences define the frequency while the three θs (mixing angles) control the amplitude of the neutrino oscillations. The parameter δ allows for the possibility that the neutrino oscillations behave differently from the anti-neutrino oscillations

(CP violation). Observing such a difference and measuring $\delta \neq 0$ would put us closer to finding an answer to the matter-antimatter asymmetry puzzle mentioned in the introduction.

The measurements of the θ_{12} and Δm^2_{21} parameters come from the observations of solar neutrinos. For this reason these are sometimes referred to as solar parameters.

The observation of the atmospheric neutrino flux at Super-Kamiokande was the first indication of oscillations governed by θ_{23} and Δm_{32}. Consequently these are called atmospheric parameters. It should be noted, however, that only the absolute value of $|\Delta m_{32}|$ is currently known. The ordering of masses according to $m_1 < m_2 < m_3$ where $\Delta m^2_{32} > 0$ is called the normal hierarchy. On the other hand, the ordering where $\Delta m^2_{32} < 0$ is called the inverted hierarchy.

In addition to the mass hierarchy, the value of the last mixing angle θ_{13} is unknown as is the magnitude of the CP violating parameter δ. The next generation of the neutrino oscillation experiments—one of which is the T2K experiment [33]—is aiming to shed some light on these mysteries.

3 Mixed Neutrinos

3.1 Neutrino mixing in vacuum

The neutrinos produced in weak interactions are of a specific flavour, which is defined by the type of the charged lepton $\alpha = e, \mu, \tau$ involved in a given CC reaction. In the language of quantum mechanics this means that a neutrino is produced in a flavour eigenstate $|\nu_\alpha\rangle$. Oscillations are possible because $|\nu_\alpha\rangle$ is not the same as the mass eigenstate $|\nu_i\rangle$ $(i = 1, 2, 3)$. Assuming there are only three neutrinos, $|\nu_\alpha\rangle$ can be expressed as a linear combination of $|\nu_i\rangle$ states:

$$|\nu_\alpha\rangle = \sum_{i=1}^{3} U^*_{\alpha i} |\nu_i\rangle \tag{3.1}$$

where $U^*_{\alpha i}$ (the star superscript indicates it is a complex conjugate of $U_{\alpha i}$) is a unitary mixing matrix. Mathematically, this means that

$$\mathbf{U}^\dagger \mathbf{U} = \mathbf{U}\mathbf{U}^\dagger = \mathbf{I}, \tag{3.2}$$

where **I** is the identity matrix.

The **U** matrix in Eq. 3.1 is also called the PMNS mixing matrix after Pontecorvo, Maki, Nakagawa, and Sakahata, the four scientists who introduced the idea of neutrino mixing [29], [30].

If a neutrino is produced in the state $|\nu_\alpha\rangle$ at time $t = 0$ and at a point $x = 0$, we want to calculate the amplitude for detecting a neutrino of flavour ν_β at a distance x from the source

$$\mathcal{A}(\nu_\alpha \to \nu_\beta) = \langle \nu_\beta | \Psi(x,t) \rangle \tag{3.3}$$

where $\Psi(x,t)$ is the evolved neutrino state wave function. The corresponding oscillation probability is the squared modulus of the amplitude in Eq. 3.3:

$$P_{\nu_\alpha \to \nu_\beta}(x,t) = |\mathcal{A}(\nu_\alpha \to \nu_\beta)|^2 \tag{3.4}$$

For neutrinos propagating in vacuum, the evolved state $\Psi(x,t)$ in natural units ($\hbar = c = 1$) is

$$\Psi(x,t) = \sum_{i=1}^{3} U^*_{\alpha i} e^{-i(E_i t - p_i x)} |\nu_i\rangle, \tag{3.5}$$

where E_i and p_i are the energy and momentum of a neutrino in the i^{th} mass eigenstate. Thus

$$\mathcal{A}(\nu_\alpha \to \nu_\beta) = \sum_i U^*_{\alpha i} U_{\beta i} e^{-i(E_i t - p_i x)} \tag{3.6}$$

where the orthogonality of the mass eigenstates $\langle \nu_i | \nu_j \rangle = \delta_{ij}$ was used. The probability of detecting the neutrino of flavour β in a detector at a distance L from the source is then

$$P_{\nu_\alpha \to \nu_\beta}(t) = \sum_{i,j} U^*_{\alpha i} U_{\beta i} U_{\alpha j} U^*_{\beta j} e^{-i(E_i t - p_i L)} e^{i(E_j t - p_j L)}. \tag{3.7}$$

Since the time is not measured in a neutrino oscillation experiment, it is necessary to average the probability in Eq. 3.7 over the time coordinate. As the time average of $\langle e^{-i(E_i - E_j)t} \rangle$ is zero unless $E_i = E_j$, only the mass eigenstates with a common energy can contribute coherently to produce the oscillation pattern.

Since the neutrino masses m_i are small compared to the neutrino energy ($m_i \ll E$), the relativistic expression for the neutrino momentum can be expanded as

$$p_i = \sqrt{E^2 - m_i^2} \approx E - \frac{m_i^2}{2E}. \tag{3.8}$$

The time averaged probability of Eq. 3.7 is then

$$\begin{aligned} P_{\nu_\alpha \to \nu_\beta} &= \sum_{i,j} U^*_{\alpha i} U_{\beta i} U_{\alpha j} U^*_{\beta j} \exp\left(-i \frac{\Delta m^2_{ji} L}{2E}\right) \\ &= \sum_i |U_{\alpha i}|^2 |U_{\beta i}|^2 + 2\mathrm{Re} \sum_{j>i} U^*_{\alpha j} U_{\beta j} U_{\alpha i} U^*_{\beta i} \exp\left(-i \frac{\Delta m^2_{ji} L}{2E}\right), \end{aligned} \tag{3.9}$$

where

$$\Delta m^2_{ji} = m^2_j - m^2_i \tag{3.10}$$

and

$$\sum_{j>i} \ldots = \sum_{i=1}^{2} \sum_{j=i+1}^{3} \ldots . \tag{3.11}$$

It is possible to simplify Eq. 3.9 by taking into account the unitarity conditions for the mixing matrix:

$$\sum_i U_{\alpha i} U^*_{\beta i} = \delta_{\alpha\beta} \tag{3.12a}$$

$$\sum_\alpha U^*_{\alpha i} U_{\alpha j} = \delta_{ij}. \tag{3.12b}$$

It follows from Eq. 3.12a that

$$\sum_i |U_{\alpha i}|^2 |U_{\beta i}|^2 = \delta_{\alpha\beta} - 2\mathrm{Re} \sum_{j>i} U^*_{\alpha j} U_{\beta j} U_{\alpha i} U^*_{\beta i}.$$

Using this result and the fact that $\mathrm{Re}(XY) = \mathrm{Re}(X)\mathrm{Re}(Y) - \mathrm{Im}(X)\mathrm{Im}(Y)$ Eq. 3.9 can be rewritten as

$$\begin{aligned} P_{\nu_\alpha \to \nu_\beta} = \delta_{\alpha\beta} &- 4 \sum_{j>i} \mathrm{Re}(U^*_{\alpha j} U_{\beta j} U_{\alpha i} U^*_{\beta i}) \sin^2 \left(\frac{\Delta m^2_{ji} L}{4E} \right) \\ &+ 2 \sum_{j>i} \mathrm{Im}(U^*_{\alpha j} U_{\beta j} U_{\alpha i} U^*_{\beta i}) \sin \left(\frac{\Delta m^2_{ji} L}{2E} \right). \end{aligned} \tag{3.13}$$

The oscillation probability for the anti-neutrinos can be derived in a similar way

and is given by

$$P_{\bar{\nu}_\alpha \to \bar{\nu}_\beta} = \delta_{\alpha\beta} - 4 \sum_{j>i} \mathrm{Re}(U^*_{\alpha j} U_{\beta j} U_{\alpha i} U^*_{\beta i}) \sin^2 \left(\frac{\Delta m^2_{ji} L}{4E} \right) - 2 \sum_{j>i} \mathrm{Im}(U^*_{\alpha j} U_{\beta j} U_{\alpha i} U^*_{\beta i}) \sin \left(\frac{\Delta m^2_{ji} L}{2E} \right). \tag{3.14}$$

A number of observations can be made about Eq. 3.13 and Eq. 3.14. Firstly, the neutrino flavour transition probabilities exhibit oscillatory behaviour as a function of L/E with the frequency determined by the mass squared difference Δm^2_{ji}. Secondly, the amplitude of these oscillations is determined by the elements of the mixing matrix. Finally, a complex valued $\mathbf{U}$ can lead to the violation of the CP (Charge Parity) symmetry where the oscillation probability for neutrinos is not the same as for anti-neutrinos

$$P_{\nu_\alpha \to \nu_\beta} \neq P_{\bar{\nu}_\alpha \to \bar{\nu}_\beta}. \tag{3.15}$$

This is evident from the fact that the imaginary parts in Eq. 3.13 and Eq. 3.14 have different signs.

3.1.1 Two neutrino mixing

We first consider an application of Eq. 3.14 to a two-neutrino mixing scenario:

$$\begin{pmatrix} \nu_e \\ \nu_\mu \end{pmatrix} = \begin{pmatrix} U_{e1} & U_{e2} \\ U_{\mu 1} & U_{\mu 2} \end{pmatrix} \begin{pmatrix} \nu_1 \\ \nu_2 \end{pmatrix}. \tag{3.16}$$

The unitary mixing matrix in this case takes the form:

$$\mathbf{U} = \begin{pmatrix} \cos\theta & \sin\theta \\ -\sin\theta & \cos\theta \end{pmatrix}. \tag{3.17}$$

If we start with a beam of pure ν_μ, the probability of detecting ν_e appearance at a distance L can be derived from the general expression in Eq. 3.13 and is shown to be

$$P_{\mu e} \equiv P_{\nu_\mu \to \nu_e} = \sin^2 2\theta \sin^2 \left(1.27 \frac{L(\text{km})}{E(\text{GeV})} \Delta m^2(\text{eV}^2) \right) \tag{3.18}$$

where $\hbar$ and c have been re-introduced:

$$\frac{\Delta m^2 L}{4E} = \frac{\Delta m^2 c^4 L}{4E\hbar c} = 1.27 \frac{L(\text{km})}{E(\text{GeV})} \Delta m^2(\text{eV}^2) = 1.27 \frac{L(\text{m})}{E(\text{MeV})} \Delta m^2(\text{eV}^2). \tag{3.19}$$

The probability of detecting ν_μ at a distance L (survival or disappearance probability) is

$$P_{\mu\mu} \equiv P_{\nu_\mu \to \nu_\mu} = 1 - \sin^2 2\theta \sin^2 \left(1.27 \frac{L(\text{km})}{E(\text{GeV})} \Delta m^2(\text{eV}^2) \right). \tag{3.20}$$

It is trivial to see from Eq. 3.18 and Eq. 3.20 that

$$P_{\mu\mu} + P_{\mu e} = 1,$$

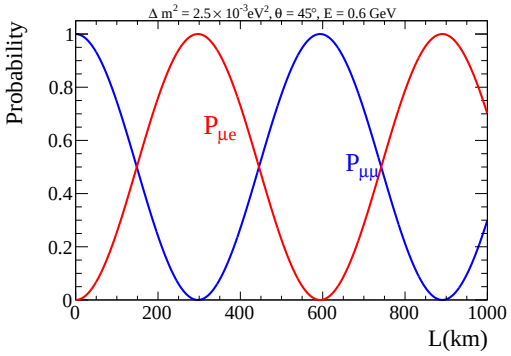

(a) Probabilities as a function of distance from a detector for a neutrino energy $E = 0.6$ GeV

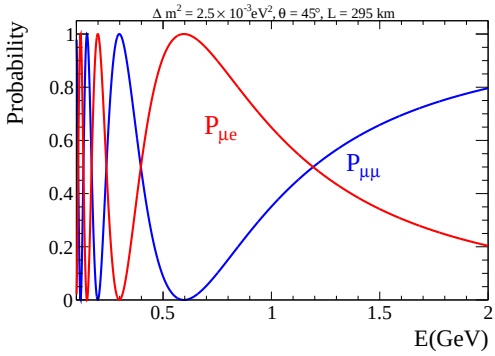

(b) Probabilities as a function of neutrino energy for a detector distance $L = 295$ km

Figure 3.1: Oscillation probabilities for two neutrino scenario with $\Delta m^2 = 2.5 \times 10^{-3}$ eV^2 and $\theta = 45^\circ$ parameter values.

which means that the total neutrino flux is conserved.

The oscillation probabilities in Eq. 3.18 and Eq. 3.20 are plotted in Fig. 3.1 for $\Delta m^2 = 2.5 \times 10^{-3}$ eV^2 and $\theta = 45^\circ$ oscillation parameters. Fig. 3.1a shows the appearance and disappearance probabilities as a function of a detector distance L for a neutrino energy $E = 0.6$ GeV while Fig. 3.1a displays them as a function of a neutrino energy for a baseline length of $L = 295$ km. The first oscillation maximum for $P_{\mu e}$ (minimum for $P_{\mu\mu}$) occurs when the ratio of L/E is such that

$$\frac{L}{E} \simeq \frac{1}{1.27\Delta m^2}\frac{\pi}{2}. \tag{3.21}$$

To maximize the sensitivity for measuring neutrino oscillations for a given baseline, the energy of a neutrino beam is optimized so that the condition in Eq. 3.21 is met.

Conversely if the energy cannot be controlled (*e.g.*, reactor neutrinos), the distance to the detector is set such that Eq. 3.21 is still satisfied.

3.1.2 Three neutrino mixing

In the case of the mixing between three neutrino flavours e, μ, and τ

$$\begin{pmatrix} \nu_e \\ \nu_\mu \\ \nu_\tau \end{pmatrix} = \begin{pmatrix} U_{e1} & U_{e2} & U_{e3} \\ U_{\mu 1} & U_{\mu 2} & U_{\mu 3} \\ U_{\tau 1} & U_{\tau 2} & U_{\tau 3} \end{pmatrix} \begin{pmatrix} \nu_1 \\ \nu_2 \\ \nu_3 \end{pmatrix}, \tag{3.22}$$

the mixing matrix is parametrized in terms of four parameters: three mixing angles θ_{12}, θ_{13}, and θ_{23} and a CP violating phase δ.

$$\begin{aligned} \mathbf{U} &= \begin{pmatrix} c_{12} & s_{12} & 0 \\ -s_{12} & c_{12} & 0 \\ 0 & 0 & 1 \end{pmatrix} \begin{pmatrix} c_{13} & 0 & s_{13}e^{-i\delta} \\ 0 & 1 & 0 \\ -s_{13}e^{i\delta} & 0 & c_{13} \end{pmatrix} \begin{pmatrix} 1 & 0 & 0 \\ 0 & c_{23} & s_{23} \\ 0 & -s_{23} & c_{23} \end{pmatrix} \\ &= \begin{pmatrix} c_{12}c_{13} & s_{12}c_{13} & s_{13}e^{-i\delta} \\ -s_{12}c_{23} - c_{12}s_{23}s_{13}e^{i\delta} & c_{12}c_{23} - s_{12}s_{23}s_{13}e^{i\delta} & s_{23}c_{13} \\ s_{12}s_{23} - c_{12}c_{23}s_{13}e^{i\delta} & -c_{12}s_{23} - s_{12}c_{23}s_{13}e^{i\delta} & c_{23}c_{13} \end{pmatrix} \end{aligned} \tag{3.23}$$

where $c_{ij} \equiv \cos\theta_{ij}$ and $s_{ij} \equiv \sin\theta_{ij}$.

Unlike the case of the two neutrinos, the oscillatory behaviour is more complicated for the three neutrino mixing, since there are now three mixing angles involved as well as two mass differences Δm^2_{21} and Δm^2_{32} that set distinct oscillation frequencies. Fortunately, the mass splittings differ by almost two orders of

magnitude:

$$\frac{\Delta m^2_{21}}{\Delta m^2_{32}} \simeq 0.03 \tag{3.24}$$

Under certain circumstances, this often makes it possible to considerably simplify the description of the three flavour neutrino oscillations.

3.1.3 Probability for electron neutrino disappearance

The simplest expression for $P_{\alpha\beta}$ in the three flavour formalism is for the $\nu_e \to \nu_e$ survival probability P_{ee}, which is given by (see Appendix A)

$$P_{ee} = 1 - c^4_{13} \sin^2 2\theta_{12} \sin^2 \Delta_{21} - \sin^2 2\theta_{13}(c^2_{12} \sin^2 \Delta_{31} + s^2_{12} \sin^2 \Delta_{32}), \tag{3.25}$$

where Δ_{ji} stands for

$$\Delta_{ji} = \frac{\Delta m^2_{ji} L}{4E} \tag{3.26}$$

The fact that P_{ee} is independent of the CP phase δ implies the disappearance probability for anti-electron neutrinos is expected to be the same as for electron neutrinos.

Fig. 3.2 shows the plot of Eq. 3.25 for a 5 MeV neutrino energy using the parameter values from the global three flavour fit reported in [34]. The two distinct oscillation frequencies can be clearly seen as the total oscillation probability (solid

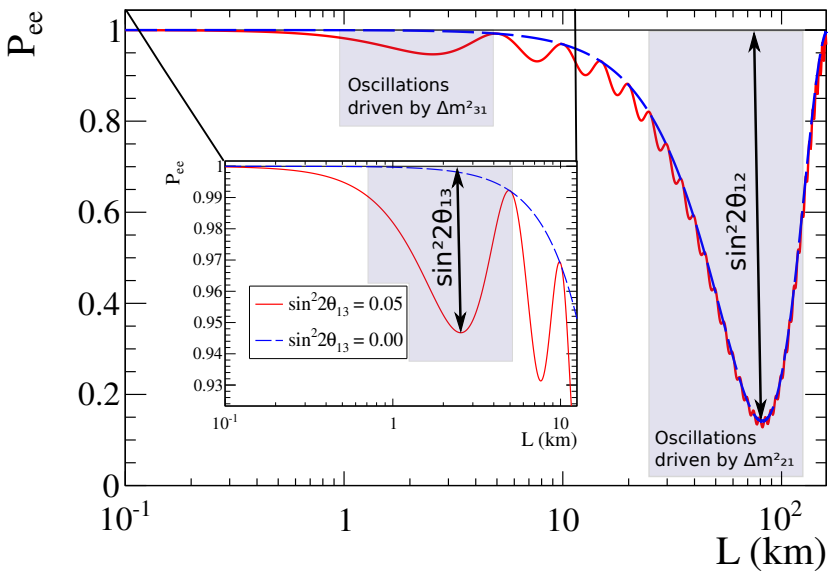

Figure 3.2: Electron neutrino disappearance probability in the three neutrino oscillation scenario for a 5 MeV neutrino beam energy. The values of the parameters (taken from [34]): $\Delta m^2_{21} = 7.59 \times 10^{-5}$ eV^2, $\Delta m^2_{31} = 2.50 \times 10^{-3}$ eV^2, $\sin^2 2\theta_{12} = 0.86$, and $\sin^2 2\theta_{13} = 0.05$ ($\sin^2 2\theta_{13} = 0.0$ for the dashed curve).

line) is the combination of the rapidly varying Δm^2_{31} term modulated by the slowly varying Δm^2_{21} contribution (dashed line).

The value of the yet undetermined θ_{13} parameter is currently measured to be small ($\sin^2 2\theta_{13} < 0.1$) and is the subject of intense searches by both accelerator and reactor based experiments. In case of the latter, θ_{13} can be measured (CHOOZ [35], Double CHOOZ [36], RENO [37], and Daya Bay [38] experiments) by looking for the disappearance of the reactor produced anti-electron neutrinos (whose energy is on order of a few MeV) over a short baseline, where the Δm^2_{31} term is still dominant (see the insert in Fig. 3.2). In this case, the contribution of the Δm^2_{21}

can be neglected and P_{ee} is approximately

$$P_{ee} \simeq 1 - \sin^2 2\theta_{13} \sin^2 \Delta_{31}, \tag{3.27}$$

where $\Delta m^2_{31} \simeq \Delta m^2_{32}$ was used.

For longer distances, P_{ee} is governed by the $\sin^2 \Delta_{21}$ term in Eq. 3.25:

$$P_{ee} \simeq 1 - \sin^2 2\theta_{12} \sin^2 \Delta_{21}. \tag{3.28}$$

Measurement of the disappearance of the reactor anti-electron neutrinos over the distance of $\sim$ 100km (KamLAND experiment [39]) gives access to the Δm^2_{21} and θ_{12} parameters.

Fig. 3.3 shows the ratio of observed to expected $\bar{\nu}_e$ flux for various reactor experiments. The clear deficit of $\bar{\nu}_e$ events at a distance of $\sim$ 100 km is due to the oscillations driven by Δm^2_{21} (Eq. 3.28).

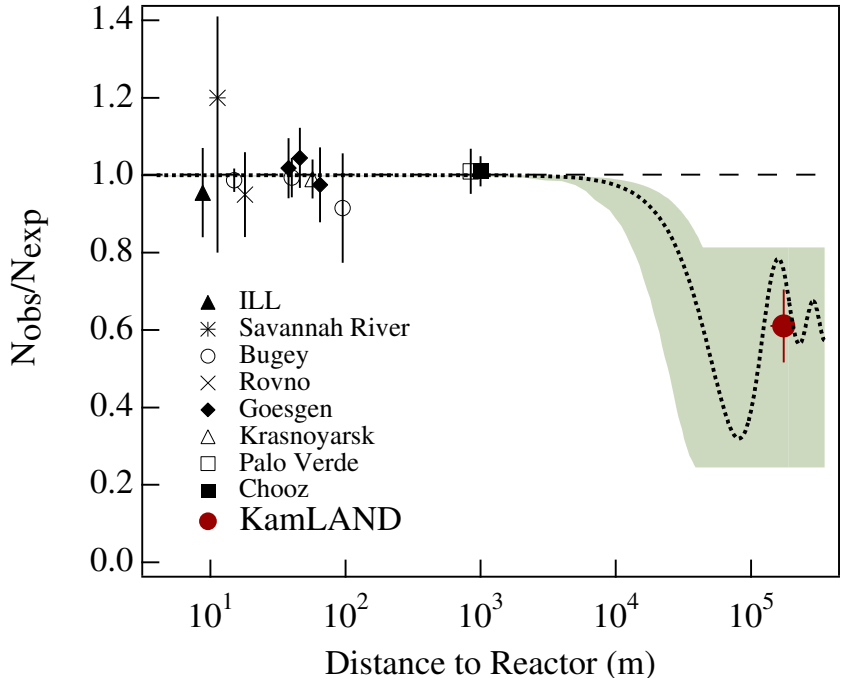

Figure 3.3: Ratio of observed to expected anti-neutrino flux as a function of distance from nuclear reactors taken from [40]. The dashed curve is expected for no oscillations while the dotted curve is obtained with $\Delta m_{21} = 5.5 \times 10^{-5}$ eV^2 and $\sin^2 2\theta_{12} = 0.833$.

3.1.4 Probability for muon neutrino disappearance

The survival probability for muon neutrinos $P_{\mu\mu}$ can be expressed (see Appendix A) as

$$P_{\mu\mu} = 1 - 4|U_{\mu 3}|^2(|U_{\mu 1}|^2 \sin^2 \Delta_{31} + |U_{\mu 2}|^2 \sin^2 \Delta_{32}) - P_{\rm sol}^{\mu\mu}, \tag{3.29}$$

where

$$P_{\rm sol}^{\mu\mu} = 4|U_{\mu 1}|^2|U_{\mu 2}|^2 \sin^2 \Delta_{21}. \tag{3.30}$$

Eq. 3.29 is invariant under CP transformation, *i.e.*, $P_{\mu\mu} = P_{\bar{\mu}\bar{\mu}}$.

Normally the ν_μ disappearance is measured at the first minimum of $P_{\mu\mu}$, where the deficit of muon neutrinos is maximal. At this distance the contribution of $P_{\rm sol}$ is negligibly small and can be ignored. In addition, the difference between Δm^2_{32} and Δm^2_{31} cannot be resolved and Eq. 3.29 can be further simplified to

$$\begin{aligned} P_{\mu\mu} &= 1 - 4|U_{\mu 3}|^2(1 - |U_{\mu 3}|^2) \sin^2 \Delta_{32} \\ &= 1 - c_{13}^4 \sin^2 2\theta_{23} \sin^2 \Delta_{32} - s_{23}^2 \sin^2 2\theta_{13} \sin^2 \Delta_{32}. \end{aligned} \tag{3.31}$$

Fig 3.4 shows the plot of muon neutrino survival probability as a function of the detector distance for neutrino energy $E = 0.6$ GeV. Both the full expression in Eq. 3.29 and the approximation in Eq. 3.31 are displayed. The fact that the two

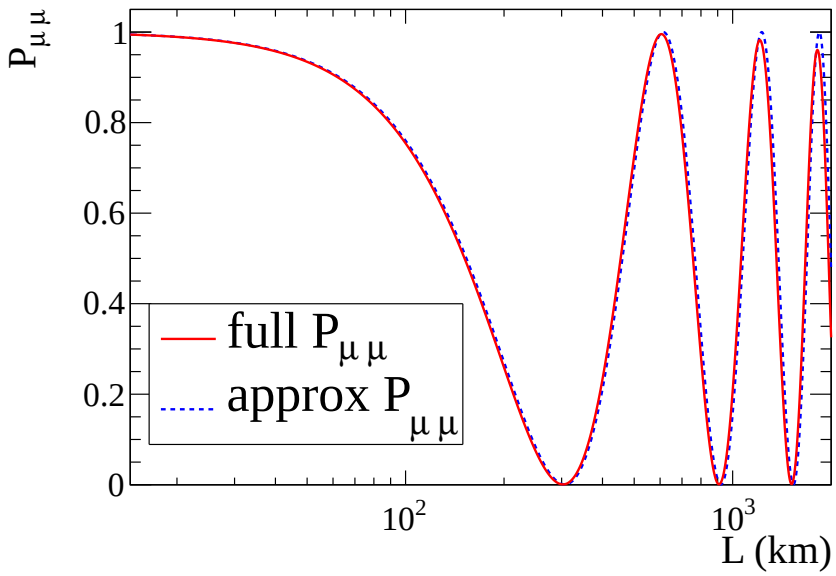

Figure 3.4: Muon neutrino survival probability in the three neutrino oscillation scenario. The values of the parameters (taken from [34]): $\Delta m^2_{21} = 7.59 \times 10^{-5}$ eV^2, $\Delta m^2_{31} = 2.50 \times 10^{-3}$ eV^2, $\sin^2\theta_{12} = 0.86$, $\sin^2 2\theta_{23} = 0.998$, and $\sin^2 2\theta_{13} = 0.05$.

probabilities virtually overlap for the first few minima justifies the approximation in Eq. 3.31.

3.1.5 Probability for electron neutrino appearance

The electron neutrino appearance probability can be expressed for neutrinos (see Appendix A) as

$$P_{\mu e} \simeq P^{\mu e}_{\text{atm}} + P^{\mu e}_{\text{sol}} + 2\sqrt{P^{\mu e}_{\text{sol}}}\sqrt{P^{\mu e}_{\text{atm}}}\cos\left(\Delta_{32} + \delta\right) \tag{3.32}$$

and for anti-neutrinos as

$$P_{\bar{\mu}\bar{e}} \simeq P^{\mu e}_{\text{atm}} + P^{\mu e}_{\text{sol}} + 2\sqrt{P^{\mu e}_{\text{sol}}}\sqrt{P^{\mu e}_{\text{atm}}}\cos\left(\Delta_{32} - \delta\right) \tag{3.33}$$

where, following [41], the $\sqrt{P^{\mu e}_{\text{sol}}}$ and $\sqrt{P^{\mu e}_{\text{atm}}}$ terms are defined as

$$\sqrt{P^{\mu e}_{\text{atm}}} = s_{23}\sin 2\theta_{13}\sin\Delta_{31}, \tag{3.34}$$

and

$$\sqrt{P^{\mu e}_{\text{sol}}} = c_{13}c_{23}\sin 2\theta_{12}\sin\Delta_{21}. \tag{3.35}$$

This gives a simple interpretation that $P_{\mu e}$ is composed of two oscillation probabilities P_{atm} and P_{sol} (driven by Δm^2_{31} and Δm^2_{21}) and an interference term. This is illustrated in Fig. 3.5a where the total probability in Eq. 3.32 as well as the contributions from P_{atm} and P_{sol} are plotted for $E = 0.6$ GeV. The appearance probability at the first oscillation maximum (at around 300 km for the 0.6 GeV neutrinos) is dominated by the contribution from P_{atm} and consequently determined by the value of θ_{13}.

The ν_e appearance probability also depends on the CP phase δ, which affects it through the interference term. As shown in Fig. 3.5b, even at the first oscillation maximum the value of δ can have a significant effect.

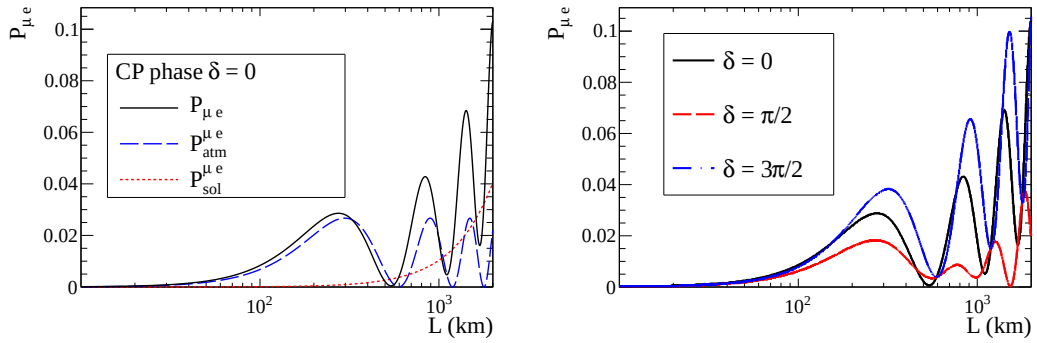

(a) $P_{\mu e}$ with contributions for $\delta = 0.0$ **(b)** $P_{\mu e}$ for different values of δ

Figure 3.5: Electron neutrino appearance probability in the three neutrino oscillation scenario for neutrino energy $E = 0.6$ GeV. The values of the parameters (taken from [34]): $\Delta m^2_{21} = 7.59 \times 10^{-5}$ eV^2, $\Delta m^2_{31} = 2.50 \times 10^{-3}$ eV^2, $\sin^2 2\theta_{12} = 0.86$, $\sin^2 2\theta_{23} = 0.998$, and $\sin^2 2\theta_{13} = 0.05$.

There are two possible strategies of determining the value of δ. One is to measure the difference $\Delta_{CP} = |P_{\mu e} - P_{\bar{\mu}\bar{e}}|$:

$$\Delta_{CP} = 4\sqrt{P_{\text{atm}}}\sqrt{P_{\text{sol}}}\sin\Delta_{32}\sin\delta. \tag{3.36}$$

The other approach is to explore differences between the first and second oscillation maximum (see Fig. 3.5b).

Measuring CP violation requires that all of the three mixing angle are non-zero. This is evident from the fact that the product of $\sqrt{P^{\mu e}_{\text{sol}}}\sqrt{P^{\mu e}_{\text{atm}}}$ multiplying the CP violating term in Eq. 3.32 is

$$\sqrt{P^{\mu e}_{\text{sol}}}\sqrt{P^{\mu e}_{\text{atm}}} \propto \sin\theta_{12}\sin\theta_{23}\sin\theta_{13}, \tag{3.37}$$

which further highlights the importance of determining the value of θ_{13}.

3.2 Neutrino mixing in matter

The probabilities shown in the previous sections were obtained assuming neutrinos propagate in vacuum. The mixing behaviour, however, is modified in matter as neutrinos can coherently scatter (the momentum of the outgoing neutrino is unchanged) from the surrounding particle. This was first demonstrated by Wolfenstein in [42].

Neutrinos of all three flavours can interact with neutrons, protons, and electrons in matter via the exchange of a Z^0 boson (Fig. 3.6a). As was mentioned already, such type of processes are called neutral current (NC) interactions. In the case of electron neutrinos, a charge current (CC) coherent scattering from the matter electrons involving $W^{\pm}$ exchange is also possible (Fig. 3.6b).

Both NC and CC processes introduce additional terms in the Hamiltonian describing the evolution of the neutrino states that affect the neutrino wave function and change oscillation probabilities. Some of the principle features of the matter effect on neutrino oscillations can be illustrated in the two-neutrino framework, which will be considered next. The detailed discussion of the matter effect in the case of the three flavour oscillations is, however, beyond the scope of this work and can be found in the relevant literature (for example, [43] [44]).

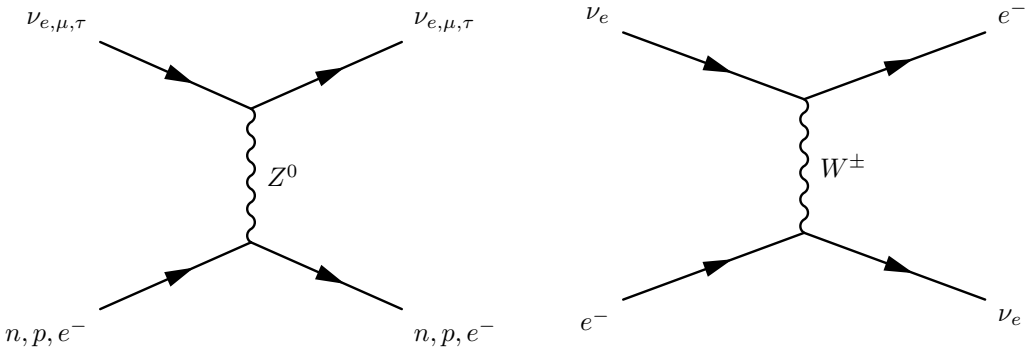

(a) Neutral current (NC) process **(b)** Charged current (CC) process

Figure 3.6: Scattering of neutrinos in matter.

For the case of two-neutrino mixing, the oscillation probabilities are given by (see Appendix B.1)

$$P_{\mu e} = \sin^2 2\theta_M \sin^2 \left(1.27 \frac{L(\text{km})}{E(\text{GeV})} \Delta m^2_M(\text{eV}^2)\right), \tag{3.38}$$

and

$$P_{\mu\mu} = 1 - \sin^2 2\theta_M \sin^2 \left(1.27 \frac{L(\text{km})}{E(\text{GeV})} \Delta m^2_M(\text{eV}^2)\right), \tag{3.39}$$

where θ_M and Δm^2_M are related to the vacuum parameters θ and Δm^2 according to

$$\Delta m^2_M = \Delta m^2 \sqrt{\sin^2 2\theta + (\cos 2\theta - a/\Delta m^2)^2}, \tag{3.40}$$

$$\sin 2\theta_M = \frac{\sin 2\theta}{\sqrt{\sin^2 2\theta + (\cos 2\theta - a/\Delta m^2)^2}}. \tag{3.41}$$

The "matter" parameter a depends on the Fermi constant G_F that sets the coupling

strength of the interactions, the matter electron density n_e, and the neutrino energy

$$a = 2\sqrt{2}G_F n_e E = 7.5 \times 10^{-5} \rho(\mathrm{g/cm^3}) E(\mathrm{GeV})\ (\mathrm{eV})^2, \tag{3.42}$$

where ρ is the density of the medium.

The interesting consequence of the matter interactions for the neutrino oscillations is the possibility, first noted by S. Mikheyev and A. Smirnov [45], of a resonant amplification of the flavour conversion. This effect can be achieved when a neutrino energy is such that

$$\Delta m^2 \cos 2\theta = 2\sqrt{2}G_F n_e E. \tag{3.43}$$

The mixing between the two neutrino states then becomes maximal ($\theta_M = \pi/4$). Thus even a small vacuum mixing angle θ can result in large flavour conversions.

Alternatively, the resonance condition in Eq. 3.43 can be satisfied for a given neutrino energy by having the "right" electron density n_e^{crit}:

$$n_e^{\mathrm{crit}} = \frac{\Delta m^2 \cos 2\theta}{2\sqrt{2}G_F E}. \tag{3.44}$$

This is of particular importance for the neutrinos propagating through the sun's interior. Since the sun has a variable density, it is possible for the neutrinos to go through a layer where the condition in Eq. 3.44 is met. This would give rise to a

large flavour conversion of the electron neutrinos to other flavours. Consequently the MSW effect, as it is now called after Mikheyev, Smirnov, and Wolfenstein, became an attractive explanation of the solar neutrino problem.

3.2.1 Matter effects in accelerator neutrino beamlines

For accelerator-based neutrino beams, the matter density is approximately constant and the relevant oscillation probabilities are $P_{\mu\mu}$ and $P_{\mu e}$.

The survival probability, $P_{\mu\mu}$, is approximately given by the following expression [44]:

$$
\begin{aligned}
P_{\mu\mu} = 1 &- \sin^2 2\theta_{23} \sin^2 \Delta + \alpha c_{12}^2 \sin^2 2\theta_{23} \Delta \sin 2\Delta \\
&- \alpha^2 \sin^2 2\theta_{12} c_{23}^2 \frac{\sin^2 A\Delta}{A^2} - \alpha^2 c_{12}^4 \sin^2 2\theta_{23} \Delta^2 \cos 2\Delta - 4 s_{13}^2 s_{23}^2 \frac{\sin^2 (A-1)\Delta}{(A-1)^2} \\
&+ \frac{1}{2A} \alpha^2 \sin^2 2\theta_{12} \sin^2 2\theta_{23} \left(\sin \Delta \frac{\sin A\Delta}{A} \cos (A-1)\Delta - \frac{\Delta}{2} \sin 2\Delta \right) \\
&- \frac{2}{A-1} s_{13}^2 \sin^2 2\theta_{23} \left(\sin \Delta \cos A\Delta \frac{\sin (A-1)\Delta}{(A-1)} - \frac{A}{2} \Delta \sin 2\Delta \right) \\
&- 2\alpha s_{13} \sin 2\theta_{12} \sin 2\theta_{23} \cos \delta \frac{\sin A\Delta}{A} \frac{\sin (A-1)\Delta}{(A-1)} \\
&+ \frac{2}{A-1} \alpha s_{13} \sin 2\theta_{12} \sin 2\theta_{23} \cos 2\theta_{23} \cos \delta \sin \Delta \left(A \sin \Delta - \frac{\sin A\Delta}{A} \cos (A-1)\Delta \right),
\end{aligned}
\tag{3.45}
$$

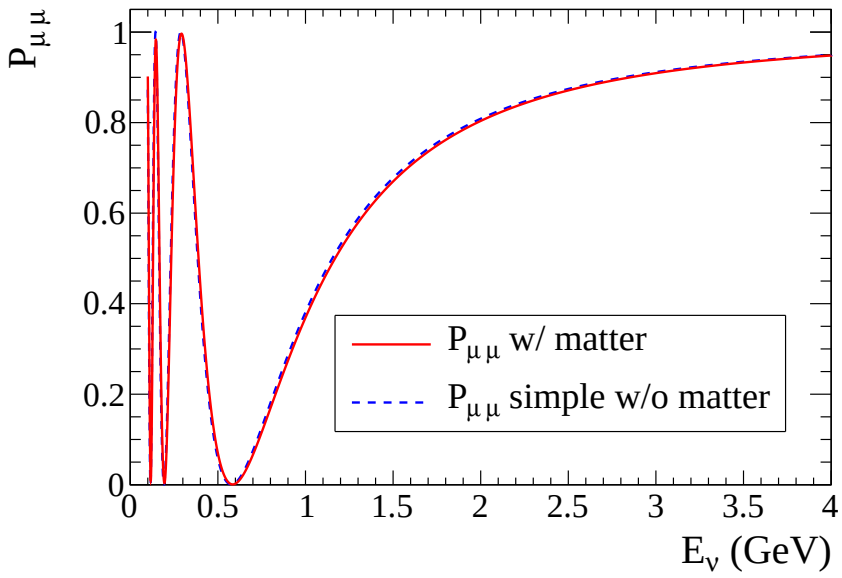

Figure 3.7: Muon neutrino survival probability as a function of the neutrino energy with and without matter effects for a baseline of 295 km. The values of the parameters (taken from [34]): $\Delta m^2_{21} = 7.59 \times 10^{-5}$ eV^2, $\Delta m^2_{31} = 2.50 \times 10^{-3}$ eV^2, $\sin^2 2\theta_{12} = 0.86$, $\sin^2 2\theta_{23} = 0.998$, and $\sin^2 2\theta_{13} = 0.05$. The Earth matter density is taken to be 3.2 g/cm^3 as in [46].

where

$$\Delta = \frac{\Delta m^2_{31} L}{4E}, \quad A = \frac{a}{\Delta m^2_{31}}, \quad \alpha = \frac{\Delta m^2_{21}}{\Delta m^2_{31}}. \tag{3.46}$$

Although Eq. 3.45 is quite complex, Eq. 3.31 is still a good approximation. This is illustrated in Fig. 3.7 where both expressions plotted for a 295 km baseline look very similar.

The appearance probability can be approximately written [47] as

$$
\begin{aligned}
P_{\mu e} = {} & 4c_{13}^2 s_{13}^2 s_{23}^2 \sin^2 \frac{\Delta m_{31}^2 L}{4E} \left(1 + \frac{2a}{\Delta m_{31}^2}(1 - 2s_{13}^2)\right) \\
& + 8c_{13}^2 s_{12} s_{13} s_{23} (c_{12} c_{23} \cos\delta - s_{12} s_{13} s_{23}) \cos \frac{\Delta m_{32}^2 L}{4E} \sin \frac{\Delta m_{31}^2 L}{4E} \sin \frac{\Delta m_{21}^2 L}{4E} \\
& - 8c_{13}^2 s_{13}^2 s_{23}^2 \cos \frac{\Delta m_{32}^2 L}{4E} \sin \frac{\Delta m_{31}^2 L}{4E} \frac{aL}{4E}(1 - 2s_{13}^2) \\
& - 8c_{13}^2 c_{12} c_{23} s_{12} s_{13} s_{23} \sin\delta \sin \frac{\Delta m_{32}^2 L}{4E} \sin \frac{\Delta m_{31}^2 L}{4E} \sin \frac{\Delta m_{21}^2 L}{4E} \\
& + 4s_{12}^2 c_{13}^2 (c_{12}^2 c_{23}^2 + s_{12}^2 s_{13}^2 s_{23}^2 - 2c_{12} c_{23} s_{12} s_{13} s_{23} \cos\delta) \sin^2 \frac{\Delta m_{21}^2 L}{4E}.
\end{aligned}
\tag{3.47}
$$

After setting $a = 0$ and dropping the terms on the order of $O(\sin(2\theta_{13}) \sin\Delta_{21})$, Eq. 3.47 becomes equivalent to Eq. 3.32.

Fig. 3.8 shows the plot of $P_{\mu e}$ with and without the matter effects included for a 295 km baseline and matter density of 3.2 g/cm^3. The fractional difference in the probabilities integrated between 0.3 and 3.3 GeV is $\sim 8\%$.

3.3 Summary of the mixing parameters

3.3.1 Solar parameters: θ_{12} and Δm_{21}^2

The measurements of θ_{12} and Δm_{21}^2 parameters come from the analysis of the solar neutrino data from Super-Kamiokande and SNO experiments. The KamLAND experiment, which looked for the disappearance of the reactor produced $\bar{\nu}_e$ [39],

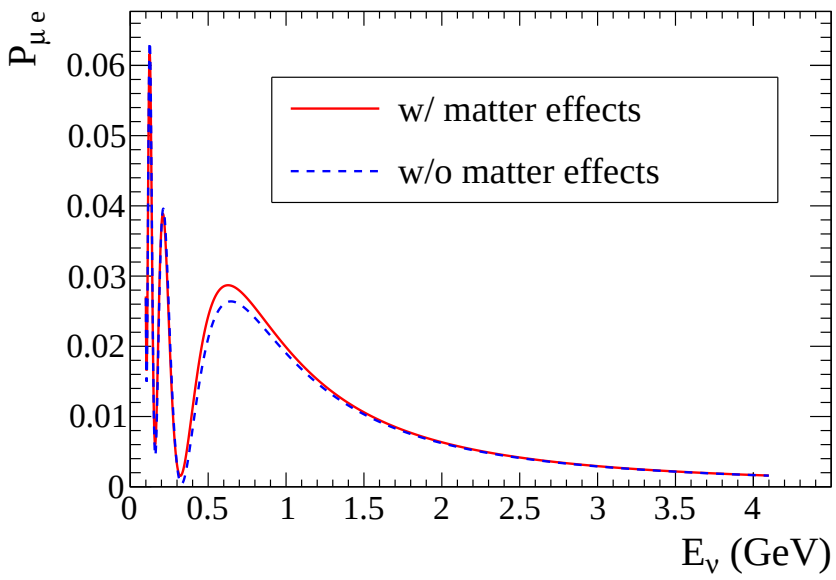

Figure 3.8: Electron neutrino appearance probability as a function of the neutrino energy with and without matter effects for a baseline of 295 km. The values of the parameters (taken from [34]): $\Delta m^2_{21} = 7.59 \times 10^{-5}$ eV^2, $\Delta m^2_{31} = 2.50 \times 10^{-3}$ eV^2, $\sin^2 2\theta_{12} = 0.86$, $\sin^2 2\theta_{23} = 0.998$, and $\sin^2 2\theta_{13} = 0.05$. The Earth matter density is taken to be 3.2 g/cm^3 as in [46].

provides a precise measurement of Δm^2_{21} that places a strong constraint on the solar parameters (θ_{12}, Δm^2_{21}).

Fig. 3.9 shows the results of three flavour analysis [48] of the solar and KamLAND data. The combined fit to these data determines the values of the solar parameter to be:

$$\tan^2 \theta_{12} = 0.468^{+0.042}_{-0.033} \tag{3.48a}$$

$$\Delta m^2_{21} = (7.59 \pm 0.21) \times 10^{-5} \text{ eV}^2 \tag{3.48b}$$

The fact that the solar mixing angle is measured to be $\theta_{12} = \tan^{-1} \sqrt{0.468} \simeq 34^\circ$

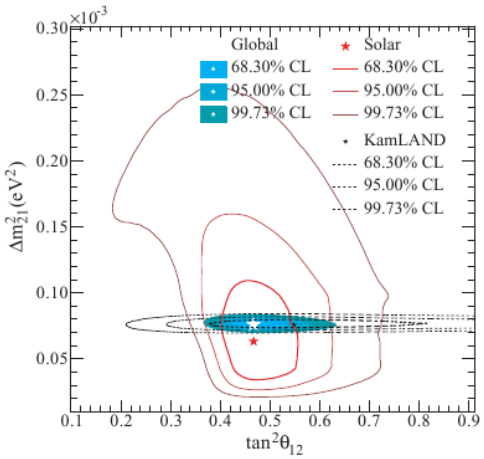

Figure 3.9: Three flavour analysis of solar and KamLAND data from [48]. The results of the analysis of the combined data sets are shown in colour.

implies that $\Delta m^2_{21} > 0$. This is a consequence of the MSW resonance condition Eq. 3.43 requiring $\Delta m^2 > 0$ if $\cos 2\theta > 0$.

3.3.2 Atmospheric parameters: θ_{23} and Δm^2_{32}

The measurements of θ_{23} and $|\Delta m^2_{32}|$ come from the analysis of the Super-Kamiokande atmospheric neutrino data and the data from the accelerator-based experiments K2K and MINOS. The values for the atmospheric parameters obtained from each experiment are listed in Table 3.1. The recent results from T2K, the experiment on which this work is based, are also included.

The results in Table 3.1 indicate that θ_{23} is around $\pi/4$. It is not known, however, in which octant plane this angle lies (if θ_{23} is not exactly $\pi/4$).

	Best fit $\lvert\Delta m^2_{32}\rvert \times 10^{-3}$ eV^2	Allowed $\lvert\Delta m^2_{32}\rvert \times 10^{-3}$ eV^2	Allowed $\sin^2 2\theta_{23}$
SK Atm (L/E) [49]	2.4	1.9 – 3.0	> 0.90
SK Atm (Zenith) [50]	2.1	1.5 – 3.4	> 0.92
K2K [2]	2.8	1.9 – 3.5	> 0.60
MINOS [3]	2.32	2.24 – 2.44	> 0.90
T2K [51]	2.65	2.2 – 3.1	> 0.84

Table 3.1: Measurements of θ_{23} and $|\Delta m^2_{32}|$ from different experiments. All of the allowed intervals are quoted at 90% C.L. except for the MINOS measurement of $|\Delta m^2_{32}|$, which is quoted at 68% C.L.

3.3.3 Limits on the value of θ_{13}

The value of the last mixing angle θ_{13} is not known. Only limits, listed in Table 3.2, have been placed by various experiments. The main goal of the T2K experiment, described next, is to determine the value of θ_{13}.

CHOOZ [35]	$\sin^2 2\theta_{13} < 0.1$ (90% C.L.)
SK Atm [52]	$\sin^2 \theta_{13} < 0.14$ (90% C.L.)
MINOS [53]	$2 \sin^2 \theta_{23} \sin^2 2\theta_{13} < 0.12$ (90% C.L.)
Double CHOOZ [54]	$0.017 < \sin^2 2\theta_{13} < 0.16$ (90% C.L.)
T2K [46]	$0.03 < \sin^2 2\theta_{13} < 0.28$ (90% C.L.)

Table 3.2: Limits on θ_{13} (for $\Delta m^2_{32} > 0$).

4 T2K Experiment

4.1 Introduction

The T2K (Tokai to Kamioka) experiment [33] is a long baseline neutrino oscillation experiment. An intense ν_μ neutrino beam is produced at the Japan Proton Accelerator Research Complex (J-PARC) in Tokai on the east coast of Japan. The beam then travels through the Earth and is detected at the Super-Kamiokande (SK) detector in Kamioka.

The main goal of the experiment is to observe electron neutrino appearance in the muon neutrino beam leading to the measurement of θ_{13}, the last unknown neutrino mixing angle. In addition, T2K aims to determine Δm^2_{32} and θ_{23} oscillation parameters with the precision of $\delta(\Delta m^2_{32}) \sim 10^{-4}$ eV^2 and $\delta(\sin^2 2\theta_{23}) \sim 0.01$ from the disappearance of the beam ν_μ, which will lead to a significant improvement in the current knowledge of the atmospheric parameters (cf. Table 3.1). This is the expected sensitivity of the experiment after 130 days of running with 0.75 MW proton beam power.

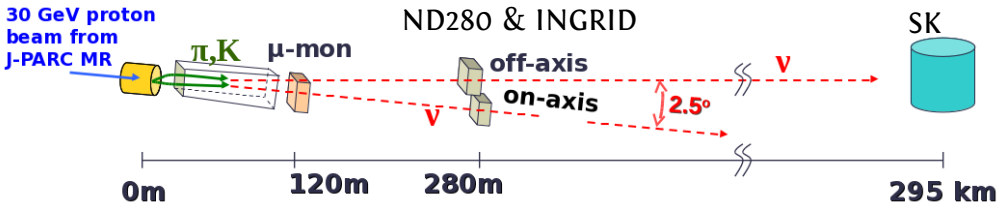

Figure 4.1: A conceptual overview of the T2K neutrino beamline.

The neutrino beam at J-PARC (see Fig. 4.1) is generated by 30 GeV protons striking a graphite target. The hadronic interactions of the beam proton with the nucleons in the target result in the production of many secondary particles, the majority of which are light mesons called pions with some admixture of the heavier K mesons. After being focused by magnetic horns, these short-lived mesons are allowed to decay freely inside a roughly 100 m long helium filled tunnel (decay volume) producing neutrinos. A beam dump placed at the end of the decay volume absorbs the particles that have not decayed and the low energy muons which are generated along with neutrinos in the pion or kaon decays. The high energy muons (with energies above 5 GeV) that pass through the beam dump are detected with a muon monitor (MUMON), allowing an indirect monitoring of the neutrino beam direction and intensity.

The neutrino beam properties are measured by the INGRID and ND280 detectors located approximately 280 m from the target. The INGRID detector, positioned on the axis defined by the proton beam direction ("on-axis"), measures the direction of the neutrino beam and monitors its stability. The ND280 detector

intercepts neutrinos at $\sim 2 - 2.5°$ relative to the proton beam direction ("off-axis" angle) and measures the initial (prior to any significant oscillations having taken place) neutrino beam composition, energy spectrum, and interaction rates (cross-sections). The SK detector is positioned at an off-axis angle of 2.5° and 295 km away from J-PARC and studies changes in the ν beam properties after oscillations.

4.2 Off-axis neutrino beam

T2K is the first experiment to make use of an off-axis neutrino beam, a technique first proposed by Beavis *et al.* [55], to produce a neutrino beam with a small energy spread (narrow band beam).

For a two body decay of a meson (pion or kaon) with a rest mass M, energy E, and momentum p into a neutrino and a muon with rest mass m_μ, the neutrino energy is

$$E_\nu = \frac{M^2 - m_\mu^2}{2(E - p\cos\theta)}, \tag{4.1}$$

where the tiny neutrino mass is neglected and θ is the angle between the direction of the meson and the neutrino daughter, as shown in Fig. 4.2.

Fig. 4.3 shows E_ν for various values of θ as a function of the pion parent momentum p_π. For $\theta = 0$, the energy of the neutrino is proportional to the pion momentum. As pions are produced by energetic protons, they have a wide energy

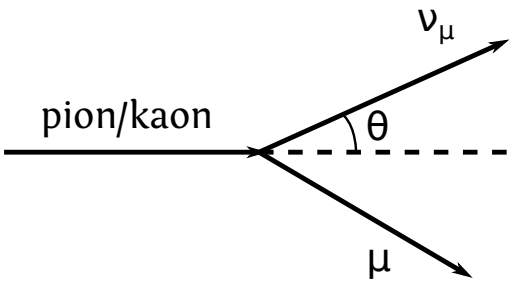

Figure 4.2: Two-body meson decay into a neutrino and a muon. The off-axis angle is the angle θ between the direction of the parent meson and the neutrino daughter.

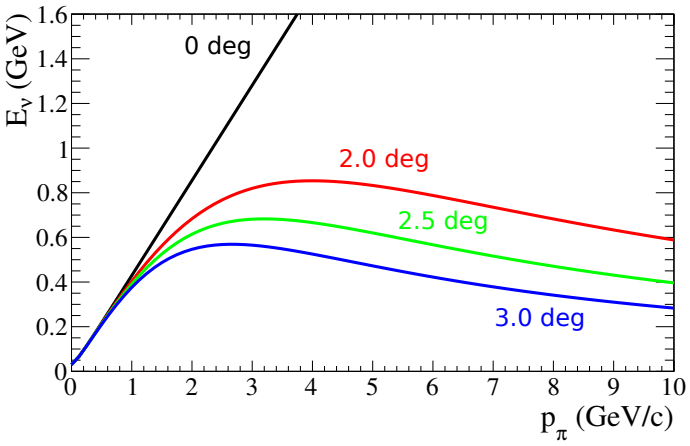

Figure 4.3: Neutrino energy as a function of pion parent momentum for different values of off-axis angle.

distribution. A neutrino detector placed on the axis would therefore observe neutrinos with a broad energy distribution (wide band beam). This is not the case, as Fig. 4.3 illustrates, for detectors placed at some off-axis angle. In this case the neutrino energy is nearly independent of the pion momentum (for $p_\pi > 2$ GeV/c), allowing the production of a narrow-band neutrino beam.

The peak energy of the beam E_ν can be fine-tuned by changing the off-axis

angle to match the maximum of the oscillation probability for a given length of a baseline. This is illustrated in Fig. 4.4 where the top figure shows the ν_μ survival probability (Eq. 3.31) for the T2K baseline of 295 km while the bottom figure shows the un-oscillated expected T2K muon neutrino flux at the SK detector placed at different off-axis angles. With the values of Δm^2_{32} between $(2.2 - 2.8) \times 10^{-3}$ eV^2, the maximum oscillation signal is expected to lie within $0.5 - 0.7$ GeV, giving 2.5° as a suitable value for the off-axis angle.

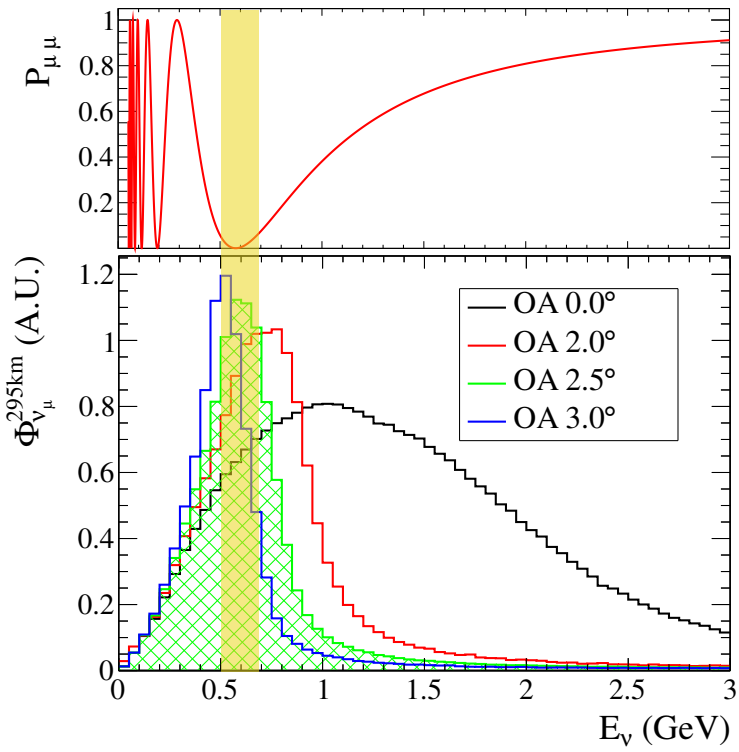

Figure 4.4: The top plots shows the ν_μ survival probability for $L = 295$ km and $\Delta m^2_{32} = 2.5 \times 10^{-3}$ eV^2. The bottom plot shows ν_μ flux (in arbitrary units) for SK placed at different off-axis angles.

The narrow band neutrino beam is particularly important for measuring the electron neutrino appearance. As the signal is expected to be small, it is crucial to maximize the neutrino flux while minimizing the possible sources of backgrounds. In a wide-band beam the majority of neutrinos would not contribute to the oscillation signal, but rather act as a significant source of background.

4.3 Japan Proton Accelerator Complex

J-PARC is a recently built accelerator facility intended to deliver a high intensity proton beam to a variety of experiments. The accelerator complex consists of the linear accelerator (LINAC), the rapid-cycling synchrotron (RCS), and the main ring (MR) 30 GeV synchrotron. Table 4.1 lists some of the design parameters for the three accelerators.

	LINAC	RCS	MR
Beam particles	H^-	p	p
Extraction energy (GeV)	0.4	3	30
LINAC peak current (mA)	50	–	–
Particle per pulse	–	8.3×10^{13}	3.3×10^{14}
Design beam power (MW)	–	1.0	0.75
Harmonic number	–	2	9
Repetition rate (Hz)	50	25	$\sim$0.3
Ring circumference (m)	–	348.333	1567.5
Extraction scheme	–	fast	fast and slow

Table 4.1: Design parameters of J-PARC accelerators.

The proton beam production starts with H^- ions accelerated by the LINAC to

181 MeV. Prior to injection to the RCS, the ion beam is bunched and passed through a charge-stripping foil, converting it to a proton beam. The RCS accelerates two protons bunches per cycle to 3 GeV and the bunches are fast extracted (all bunches are extracted at once) to the MR or the Material and Life Science Experimental Facility (MLF). In case of the MR extraction, 8 out of 9 bunches are populated in four RCS cycles and then accelerated to 30 GeV. The ninth bunch is left empty to accommodate the rise-time of the MR extraction "kicker" magnet. Given the MR circumference of 1567.5 m and the harmonic number of 9 (number of bunches), the time interval between the bunches at the time of extraction (after acceleration to 30 GeV) is

$$\Delta t = \frac{1567.5}{9}\frac{1}{\beta c} \simeq 581 \text{ ns}. \tag{4.2}$$

The protons from the MR are delivered to the neutrino experiment and to a variety of other nuclear and particle physics experiments.

4.4 Neutrino beamline

The proton beam from the MR is fast extracted into the T2K neutrino beamline shown in Fig. 4.5. Each proton pulse (spill) consists of eight bunches separated by 581 nsec, as illustrated in Fig 4.6. The spills occur every 3.02 sec. To increase the delivered beam power, however, the spill frequency will be decreased in the future

to 2.2 sec.

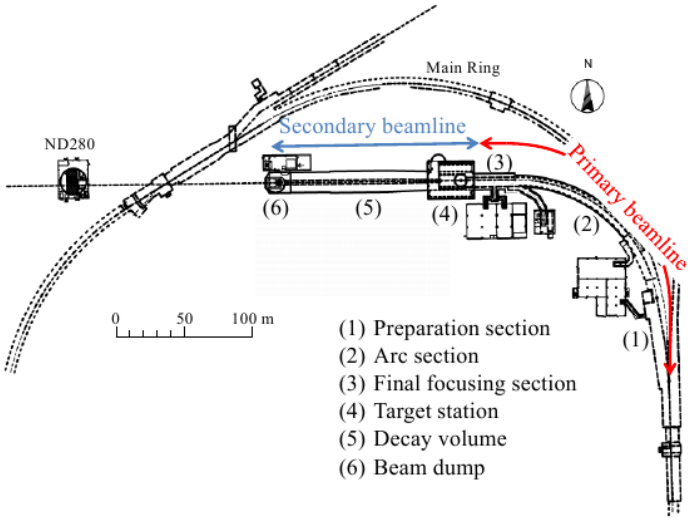

Figure 4.5: Overview of the T2K neutrino beamline (taken from [33]).

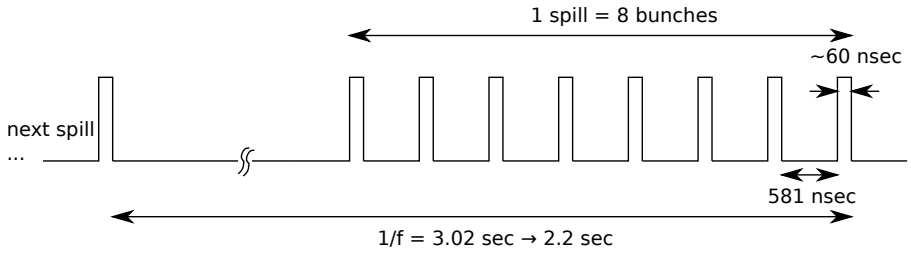

Figure 4.6: Structure of the T2K proton beam.

The neutrino beamline is composed of two sections called the primary and the secondary beamlines. In the primary beamline, the extracted proton beam is bent to point towards the SK detector and guided to the target. The target and all of the components downstream of it are part of the secondary beamline. The design of the neutrino beamline is flexible enough to allow for changing the off-axis angle from 2.5° down to 2.0°.

4.4.1 Primary proton beamline

The primary beamline consists of three sections (Fig. 4.5): the preparation section (54 m long), the arc section (147 m long), and the final focusing section (37 m long). The main function of the preparation section is to tune the extracted beam to match the acceptance requirements of the arc section. The beam is then bent in the arc section by 80.7° to point towards the SK detector using superconducting combined function magnets (perform both focusing and bending of the proton beam). After the arc section, the beam is bent downwards and further focused to fit on the target in the final focusing section.

4.4.1.1 Proton beam angle for off-axis neutrino beam

The downward angle of the proton beam θ_y^{beam} set in the final focusing section determines the off-axis angle. To illustrate this, we begin by introducing a right-handed coordinate system where the horizontal Z axis is defined in such way that the proton beam direction is given by

$$\begin{aligned} n_x^{\text{beam}} &= 0 \\ n_y^{\text{beam}} &= \sin\theta_y^{\text{beam}} \\ n_z^{\text{beam}} &= \cos\theta_y^{\text{beam}}. \end{aligned} \tag{4.3}$$

The SK detector is located relative to the Z axis at an angle $\theta_x^{\mathrm{SK}} = 0.795^\circ$ in XZ and $\theta_y^{\mathrm{SK}} = 1.26^\circ$ in the YZ plane. The directional cosines for the vector pointing towards the detector are

$$\begin{aligned} n_x^{\mathrm{SK}} &= n_z \tan\theta_x^{\mathrm{SK}} \\ n_y^{\mathrm{SK}} &= n_z \tan\theta_y^{\mathrm{SK}} \\ n_z^{\mathrm{SK}} &= (1 + \tan^2\theta_x^{\mathrm{SK}} + \tan^2\theta_y^{\mathrm{SK}})^{-1/2} \end{aligned} \tag{4.4}$$

The off-axis angle is found from

$$\theta_{\mathrm{OA}} = \cos^{-1}\left(\mathbf{n}^{\mathrm{beam}} \cdot \mathbf{n}^{\mathrm{SK}}\right) = \cos^{-1}\left(\frac{\sin\theta_y^{\mathrm{beam}} \tan\theta_y^{\mathrm{SK}} + \cos\theta_y^{\mathrm{beam}}}{\sqrt{1 + \tan^2\theta_x^{\mathrm{SK}} + \tan^2\theta_y^{\mathrm{SK}}}}\right) \tag{4.5}$$

In order to obtain the off-axis angle of 2.5° for the SK location, the proton beam angle is set to $\theta_y^{\mathrm{beam}} = 3.637^\circ$.

4.4.1.2 Proton beam monitors

The quality of the proton beam must be precisely controlled throughout the primary beamline as the stability of the off-axis neutrino beam directly follows from the stability of the proton beam. A well tuned beam is also necessary for high power operation, since beam losses, accumulated or from accidental mis-steering, can lead to activation and damage of the beamline equipment. The intensity, posi-

tion, profile, and beam loss are accurately measured throughout the beamline by 5 current transform monitors (CTs), 21 electrostatic monitors (ESMs), 19 segmented secondary emission monitors (SSEMs), and 50 beam loss monitors (BLMs), respectively. The response of CTs, ESMs, and SSEMs is fast enough to resolve individual bunches.

The CT monitor, shown schematically in Fig. 4.7a, consists of a 50-turn coil wound toroidally around a ferromagnetic core. The passing proton beam induces a current in the coil, resulting in a measurable signal proportional to the beam intensity. The absolute intensity can be measured with 2% uncertainty and the relative intensity with 0.5%. CTs also measure the beam timing to 10 nsec precision.

The beam position is measured with ESMs (Fig. 4.7b) and SSEMs (Fig. 4.7c) with the latter also measuring the profile. The ESMs are non-destructive monitors that determine the beam position from the top-bottom and left-right asymmetry in the currents induced on four electrodes. The measurement precision is better than 0.45 mm where the dominant contributions to the error come from systematic and alignment uncertainties (0.2 mm for systematic uncerainty and 0.1-0.4 mm for alignment precision).

The SSEMs operate destructively (*i.e.*, the beam interacts with the monitor). Two 5 μm thick Ti foils, one with vertical and one with horizontal sets of strips, are inserted in the path of the beam. When hit by the protons, a given strip emits

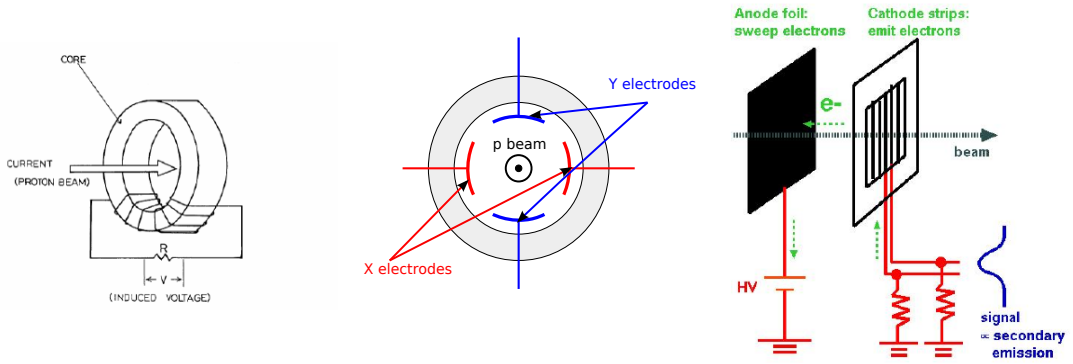

(a) CT monitor **(b)** ESM **(c)** SSEM

Figure 4.7: Schematic views of the T2K beamline monitors.

electrons proportional to the number of protons going through it. The electrons are drifted in the electric field to an anode plane generating a measurable current from each strip. SSEMs measure the beam width with 0.20 mm precision while the systematic uncertainty in the position measurements is 0.45 mm. The interactions of the protons with the SSEM foils cause some beam losses (around 0.005%). The monitors are therefore only used for the beam orbit tuning and are retracted during continuous operation.

The BLMs are proportional counters filled with an Ar-CO_2 gas mixture. The ionization signal is integrated during each spill. If it exceeds a threshold, a beam interlock signal is issued and the extraction to the neutrino beamline is aborted.

4.4.2 Secondary beamline

The primary beamline is connected to the secondary beamline through a beam window, which consists of two Ti-alloy 0.3 mm think shells. The window separates the vacuum of the proton transport pipe from the helium environment of the target station in the secondary beamline.

The secondary beamline, shown in Fig. 4.8, can be described in terms of three sections: the target station, the decay volume, and the beam dump. The target station and decay volume are contained in a single vessel with a volume of $\sim$ 1500 m^3, which is filled with He gas at 1 atm. The helium gas was chosen in order to reduce the pion absorption and minimize NO_X and tritium production.

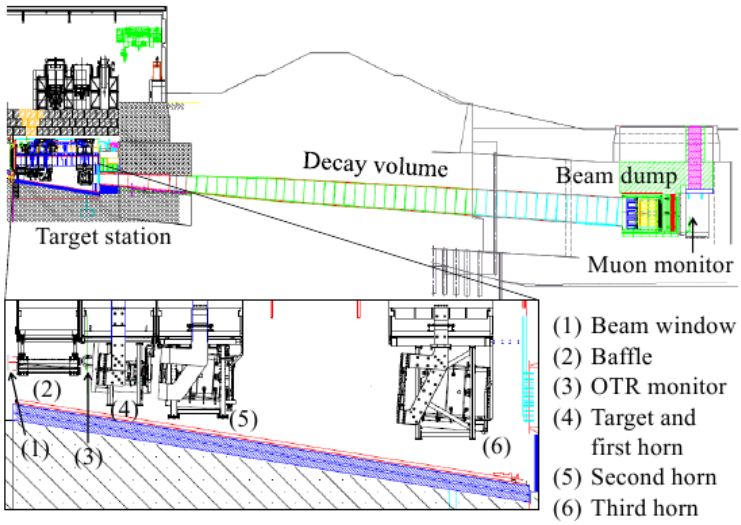

Figure 4.8: Overview of the T2K secondary beamline.

The main components in the target station are the baffle (beam collimator), target, and three horns. The baffle and the horns are suspended from support structures inside the He vessel. The target is positioned inside the first horn, as illustrated in Fig. 4.9. Attached to the front of the first horn is an Optical Transition Radiation (OTR) proton beam monitor, which will be described in detail in the next chapter.

4.4.2.1 Baffle

The proton beam entering the helium vessel via the beam window first passes through the baffle. Its function is to protect the downstream horn from an accidentally de-focused or mis-steered proton beam. It consists of a 1.7 m long, 0.3 m wide, and 0.4 m high graphite block with a 30 mm diameter hole for the beam. The baffle is cooled by water cooling pipes embedded in the graphite.

4.4.2.2 Target and horns

After the baffle, the beam goes through the OTR monitor and then strikes the target. The core of the target is a 26 mm diameter, 91.4 cm long graphite rod. It is surrounded by a 2 mm thick cylindrical shell also made out of graphite. The entire assembly sits inside a Ti case that is 0.3 mm thick. The target is cooled by He gas forced to flow through the gap between the core and the shell and between

the shell and the case.

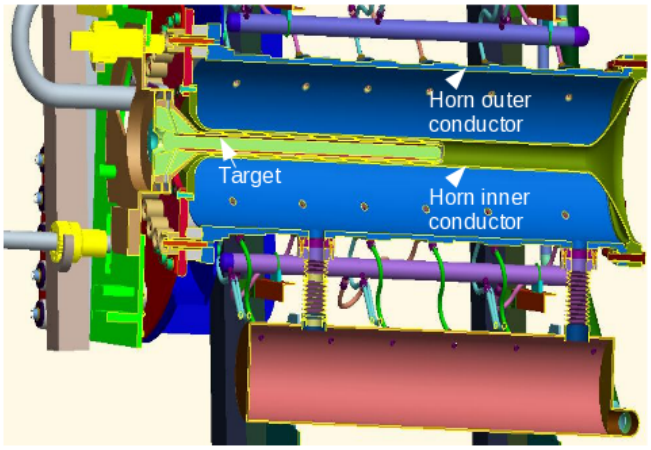

Figure 4.9: Cross-section of the first horn and target.

Each horn consists of an inner and outer conductor, two cylindrically symmetric shells (see Fig. 4.9), made from an aluminum alloy. With each proton beam spill the horns are pulsed with 320 kA (250 kA have been used for the operation up to now), creating a toroidal magnetic field in the volume between the inner and outer conductors whose strength ideally is given by

$$B = \frac{\mu_0 I}{2\pi r} = 0.2 \frac{I\ (\text{kA})}{r\ (\text{mm})}, \tag{4.6}$$

where μ_0 is the magnetic permeability, I is the current, and r is the distance from the horn axis. At $r = 30$ mm (the approximate radial position of the outer surface of the first horn inner conductor), the field applied by the 320 kA current is ~ 2.1 T.

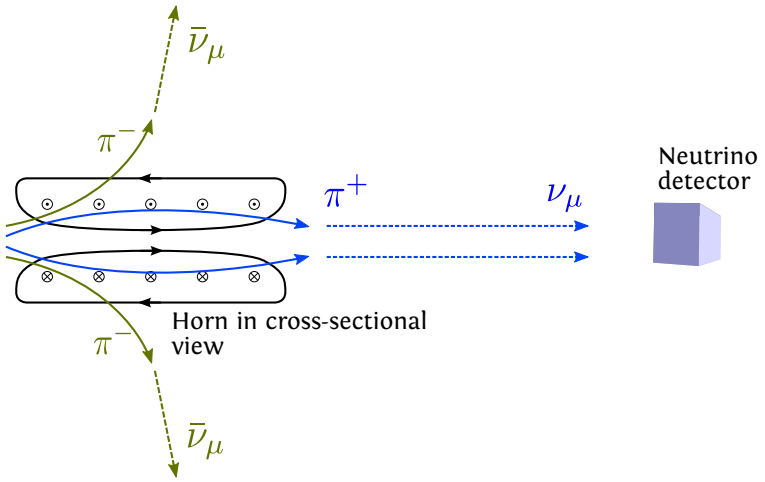

Figure 4.10: Illustration of magnetic horns focusing positive pions and de-focusing negative ones. This configuration results in a beam of neutrinos. To obtain the anti-neutrino beam, the current flow in the horn is reversed and the negative pions are focused instead.

Depending on the direction of the current flow through the inner and outer conductors, either positive or negative particles (pions and kaons) are focused resulting in either a neutrino (the T2K current configuration) or an anti-neutrino beam, respectively. This is illustrated in Fig. 4.10.

	Horn 1	Horn 2	Horn 3
Minimum inside diameter (mm)	54	80	140
Inner conductor thickness (mm)	3	3	3
Outside diameter (mm)	400	1000	1400
Length (m)	1.5	2	2.5

Table 4.2: Design parameters for the T2K horns.

The shape of the inner conductor, its length, and the diameter of the horn determine how long charged particles spend inside the magnetized region and therefore

how much "kick" they get in the transverse direction. For the three T2K horns, these parameters, in addition to the distances between the horns, have been optimized in order to focus secondaries into a nearly parallel beam and maximize the neutrino yield. Table 4.2 lists some of the design parameters for the three horns.

4.4.2.3 Decay volume and beam dump

From the target station the focused beam of secondaries enters the decay volume, which is a ~ 96 m long tunnel filled with He. The unstable pions and kaons decay, producing predominantly muon neutrinos with some admixture of other flavours. Muons, which accompany ν_μ ($\bar{\nu}_\mu$) production, can also decay to a positron (electron) and two neutrinos, $\bar{\nu}_\mu$ (ν_μ) and ν_e ($\bar{\nu}_e$).

At the end of the decay volume, but still inside the helium vessel, is the beam dump (hadron absorber). The dump is 4.69 m high, 3.174 m long, and 1.94 m wide and its 75 ton core is made out of graphite. The cooling is done with two aluminum cooling modules containing water channels which sandwich the core on the sides. Placed downstream are seventeen iron plates (two inside the vessel and fifteen outside) with the total thickness of 2.4 m. Only muons with energies of greater than 5 GeV are able to penetrate the dump.

4.4.2.4 Muon monitor

The energetic muons are detected by MUMON [56, 57]. The detector uses arrays of ionization chambers and Si PIN photo-diodes to register charged particles, which according to simulations are 87% muons and 13% δ-rays (fast electrons). The arrays cover 150×150 cm^2 area and provide a 2D profile of the particle distribution. The mean of this distribution allows to determine the direction of the incoming muon beam. Since muons are produced in unpolarized decays of high energy parents, the muon beam direction follows that of the neutrino beam. Profile measurements at MUMON therefore allow the determination of the neutrino beam direction.

Since the muon yield is sufficiently high, MUMON is also able to monitor the stability of the neutrino beam direction on a spill-by-spill basis. The uncertainty on the neutrino beam direction from the MUMON profile measurement is better than 0.25 mrad while its stability can be monitored with a precision of better than 3%.

4.5 Near detectors

The goal of the near detectors is to measure the direction, energy, neutrino interaction cross-sections, and composition of the neutrino beam prior to oscillation effects.

Short name	Process	Fraction for carbon (oxygen)
CCQE	$\nu_l + n \to p + l$	40.6% (41.7%)
CCπ^+	$\nu_l + N \to N' + \pi^+ + l$	14.7% (14.2%)
CCπ^0	$\nu_l + N \to N' + \pi^0 + l$	3.7% (3.6%)
CC other	$\nu_l + N \to l + X$	13.1% (12.6%)
NC elastic	$\nu_l + N \to \nu_l + N$	16.1% (16.5%)
NC$\pi^\pm$	$\nu_l + N \to N' + \nu_l + \pi^\pm$	3.0% (2.8%)
NCπ^0	$\nu_l + N \to N' + \nu_l + \pi^0$	4.5% (4.4%)
NC other	$\nu_l + N \to \nu_l + X$	4.4% (4.1%)

Table 4.3: Relative contributions of different neutrino interactions channels for the T2K muon neutrinos interacting with carbon and oxygen nuclei. The results are based on the NEUT neutrino interaction generator [58].

The best channel for neutrino energy measurement is the CC quasi-elastic scattering (CCQE) process: $\nu_l + n \to p + l$. In this reaction the energy of the neutrino can be reconstructed from the measurements of the outgoing lepton momentum p_l and angle θ_l according to

$$E_\nu^{\text{rec}} = \frac{1}{2}\frac{(m_p^2 - m_l^2) + 2(m_n - V)E_l - (m_n - V)^2}{(m_n - V) - E_l + p_l \cos\theta_l}, \tag{4.7}$$

where V is the nuclear potential energy required to knock a nucleon out of a nucleus and m_n, m_p, and m_l are the masses of the neutron, proton, and produced leptons, respectively.

The CCQE processes comprise about 41% of possible neutrino interactions at T2K. Table 4.3 gives a summary of various neutrino interaction channels and their relative contributions for the T2K neutrino beam.

4.5.1 INGRID detector

The INGRID (Interactive Neutrino GRID) detector is positioned on-axis and covers an area of 10×10 m^2. Its primary functions are to measure the profile and direction of the neutrino beam and to monitor daily the stability of the neutrino beam intensity.

The detector, shown in Fig. 4.11a, consists of 16 identical modules weighing 7.1 tonnes each. The module, shown in Fig. 4.11b, is a sandwiched structure of 9 iron plates ($124 \times 124 \times 6.5$ cm^3) that provide the target mass for the neutrino interactions and 11 scintillator tracking planes. Surrounding each module are four scintillator planes used to veto particles entering the detector from the outside.

(a) INGRID detector **(b)** INGRID module

Figure 4.11: INGRID detector. On the left is the front view of the detector (neutrino beam is into the page). On the right an expanded view of a single INGRID module is shown.

A neutrino event display typical of a ν_μ CC type reaction that results in a muon

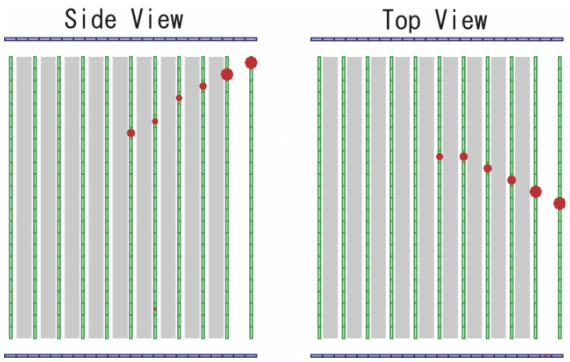

Figure 4.12: Neutrino CC ν_μ event in INGRID.

is shown in Fig. 4.12.

4.5.2 ND280 detector

The ND280 detector is located off-axis and is intended to measure the neutrino flux composition, energy spectrum, and rates for various neutrino interaction channels.

In order to perform charge identification and momentum measurement, the detector is magnetized with the refurbished magnet from the NOMAD experiment [59]. The magnet provides a 0.2 T dipole field in the horizontal direction perpendicular to the beam (along the negative X axis in Fig. 4.13).

ND280 is a collection of a number of different sub-detector systems. At the most upstream end is the Pi-Zero Detector (PØD). Its primary function is to measure the cross-section for the NCπ^0 ($\nu + N \rightarrow \nu + N + \pi^0$) neutrino interactions on a water target. These type of processes constitute a major background for ν_e detection at SK due to the possibility of the mis-identification of two photons from π^0 decay as

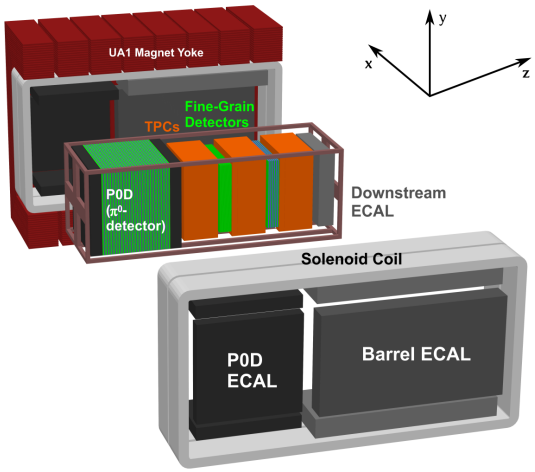

Figure 4.13: An expanded view of the ND280 detector. In this picture the neutrino beam enters the detector from the left along the Z axis.

an electron. The detector consists of scintillator tracking planes interleaved with lead foils and water planes.

There are three Time Projection Chambers (TPCs). They are used to determine a particle momentum from the curvature of the track it leaves in the detectors. In addition, the amount of ionization left by the particle allows to establish its identity (particle identification or PID). The detectors use an argon-based gas mixture, Ar:CF_4:iC_4H_{10} (95:3:2). The ionization electrons drift under the influence of an electric field away from a cathode plane at the centre of the of each TPC to the left or right side of the chamber and are sampled with bulk mircromegas [60]. Arrival time combined with the pattern of the ionization charge deposition on the micromega pads allows to reconstruct a 3D track trajectory.

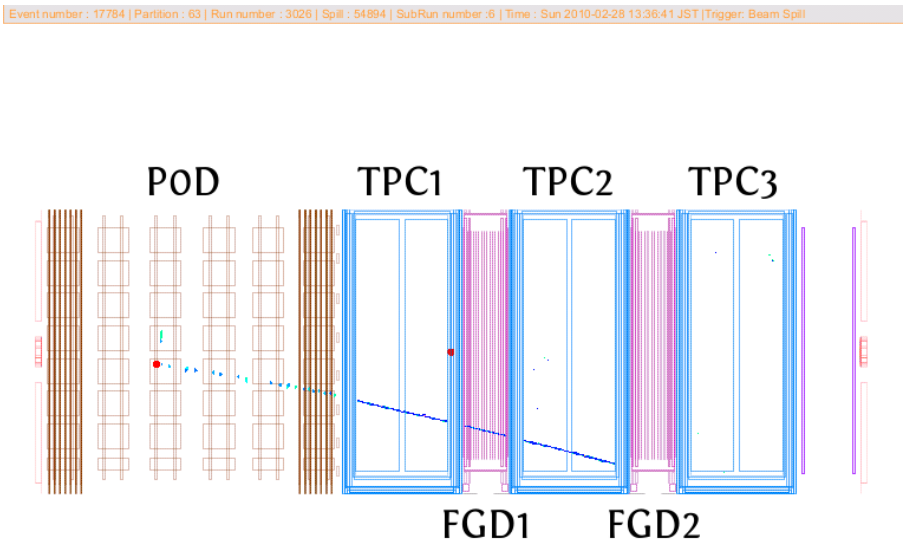

Figure 4.14: Neutrino CC ν_μ event in ND280 originating PØD and producing an energetic muon track that travels through the first TPC, first FGD, and the second TPC.

Two Fine Grained Detectors (FGDs) are placed between the three TPCs. The primary goal of the FGDs is to select a clean sample of CCQE type of events for the measurement of the neutrino energy spectrum. The detectors consist of finely segmented scintillator bars (doped polystyrene), which provide the target mass for the neutrino interactions while also allowing tracking charged particles coming from the interaction vertices. The downstream FGD has water layers in addition to scintillator to allow comparison of the neutrino interaction rates in water with those in carbon.

Surrounding the PØD, TPCs, and FGDs are electro-magnetic calorimeters (ECALs).

They serve to contain γ rays that did not convert to electrons, to reconstruct electromagnetic showers, and to provide identification for electron-muon-pion separation.

Finally, the yoke of the magnet is instrumented with scintillator counters. These are part of the Side Muon Range Detector (SMRD) sub-system. The SMRD is used to detect muons escaping the inner detectors at high angles and to measure their momentum. Additionally it provides triggering for cosmic rays that enter the detector.

An event display of a CC interaction of a beam neutrino is shown in Fig. 4.14. The interaction occurs in the PØD. The resulting energetic muon travels through the first TPC, first FGD, and the second TPC before exiting.

4.6 The far detector

Super-Kamiokande [61] is the far detector in the T2K experiment and, due to its size and scientific output, is one of the more famous neutrino detectors in the world. It sits 295 km west of J-PARC and 1 km underground in the Kamioka mine. The construction of SK began in 1991 and the first data was taken in April, 1996. Since then, there have been four running periods: SK-I, SK-II, SK-III, and SK-IV with the latter still in progress. Over this time the detector has been used to measure the flavour oscillation of the solar, atmospheric, and accelerator neutrinos, resulting in a number of important contributions to the physics of neutrinos.

4.6.1 Overview of Super-Kamiokande

The detector, schematically shown in Fig. 4.15, consists of a large cylindrical cavity filled with 50 ktonnes of pure water and instrumented with more than 13,000 photo multiplier tubes (PMTs). The volume is subdivided by a cylindrical structure into two regions called the inner detector (ID) and the outer detector (OD). The structure also provides support for the PMTs as well as acts as an optical barrier between the two detector volumes.

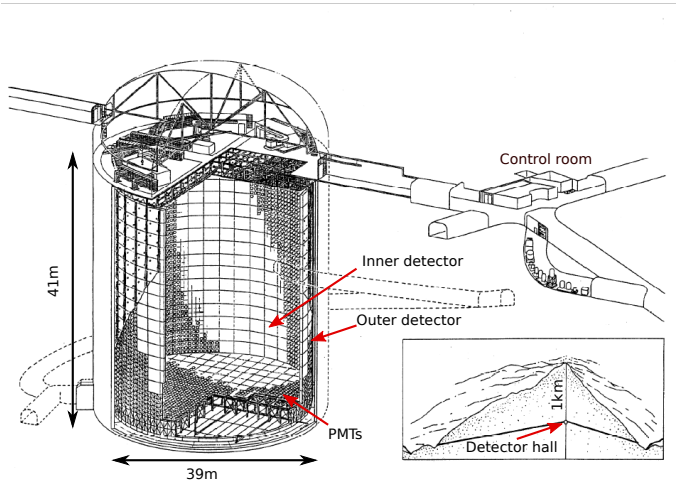

Figure 4.15: Overview of the SK detector. Image taken from [62].

The ID is instrumented with 11,129 inward facing 50 cm diameters PMTs mounted on the inside walls of the support structure. Facing outward and mounted on the other side of the structure are 1,885 20 cm diameter PMTs of the OD. To compensate for the sparse PMT coverage in this region, the walls facing the OD PMTs are covered with a reflective material.

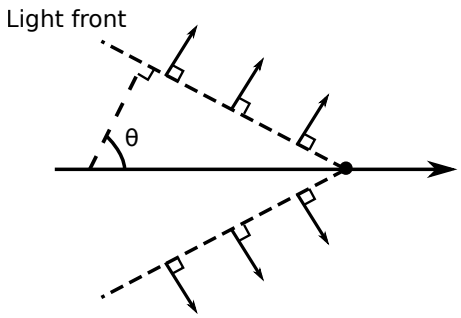

Figure 4.16: Cherenkov radiation.

The detection of neutrinos at SK relies on the Cherenkov effect, a phenomenon where a charged particle emits light when traveling faster than the speed of light in the medium it traverses. The light, as illustrated in Fig. 4.16, is emitted in a cone with half angle θ along the particle track. For the particles that stop inside the detector volume, this results in a ring-like pattern of light on the walls of the detector. The cosine of the emission angle is related to the index of refraction of the medium n and the relativistic $\beta = v/c$ where v is the velocity of the charged particle:

$$\cos\theta = \frac{1}{n\beta}. \tag{4.8}$$

It follows from Eq. 4.8 that there is minimum value of β and consequently a threshold energy below which a particle will not radiate:

$$\beta_{\min} = \frac{1}{n}. \tag{4.9}$$

Neutrinos therefore are only "seen" when they interact with water, producing charged particles with sufficiently high energies in the final state to emit Cherenkov radiation.

The ideal detection channel is the CCQE reaction ($\nu_l + n \rightarrow p + l$) where the charged lepton radiates Cherenkov light. It is also possible to determine the lepton flavour, e or μ, from the shape of the ring pattern. As the heavy muons are less susceptible to scattering than the light electrons, the ring patterns they produce have sharp edges in contrast to the fuzzier electron rings. This is illustrated in Figs. 4.17 and 4.18 which show the T2K ν_μ and ν_e event candidates, respectively.

The energy of the incoming neutrino and its direction are reconstructed from the charge deposition and charge arrival timing collected from the PMTs.

4.6.2 T2K beam events

To select the events coming from the interactions of the T2K beam neutrinos all PMT hits are recorded within a 1 msec time window. The window is synchronized to the expected beam arrival time (ν time-of-flight or TOF) using timing information from GPS satellites. The scheme is illustrated in Fig. 4.19

The acquired data are passed through an offline data reduction software that determines whether the charge deposition is above an energy threshold. The events are then classified according to the hit distribution and recorded for subsequent

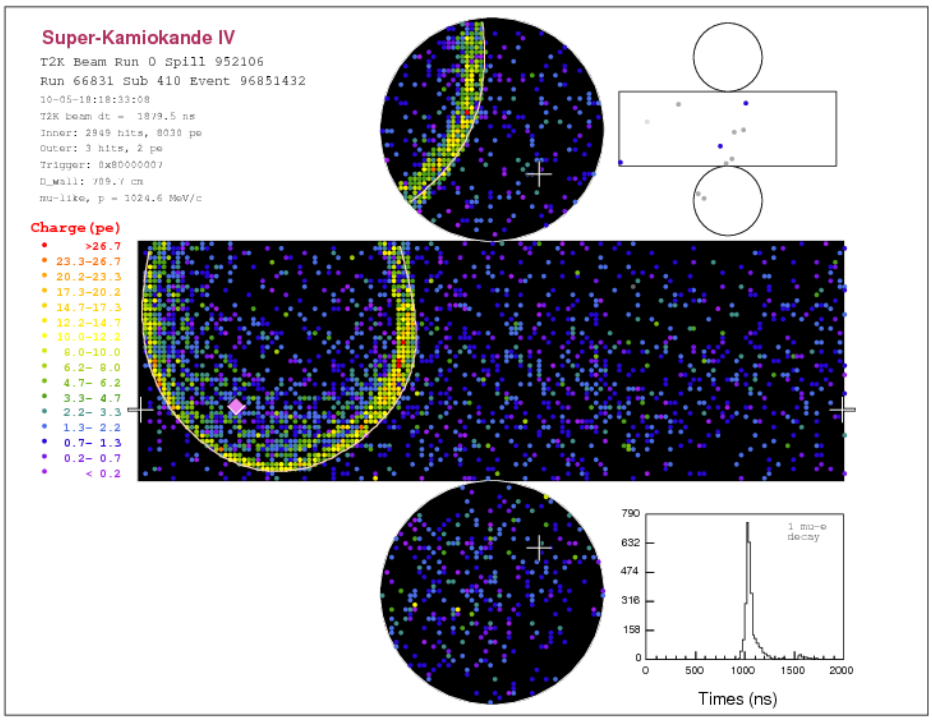

Figure 4.17: A T2K ν_μ event candidate at SK. The large panel shows an unrolled view of the inner detector. The coloured points indicate the position of the hit PMTs and their integrated charge. The circular line shows the fitted Cherenkov ring. The unrolled view of the outer detector is shown in the top-right corner. The distribution of the PMT hit times is shown in the bottom-right corner.

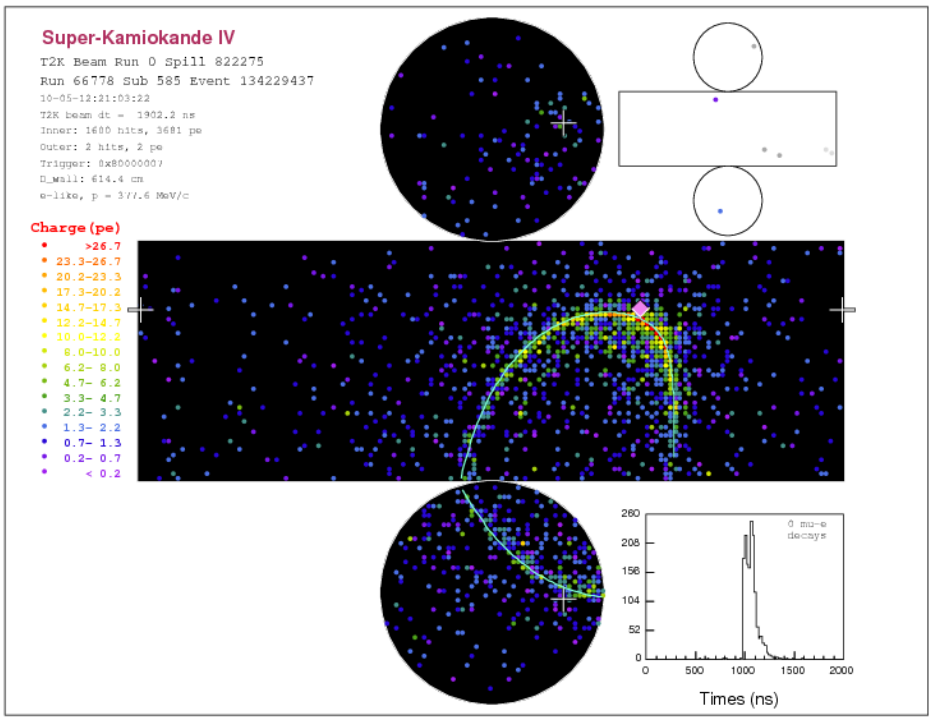

Figure 4.18: A T2K ν_e event candidate at SK. The large panel shows an unrolled view of the inner detector. The coloured points indicate the position of the hit PMTs and their integrated charge. The circular line shows the fitted Cherenkov ring. The unrolled view of the outer detector is shown in the top-right corner. The distribution of the PMT hit times is shown in the bottom-right corner.

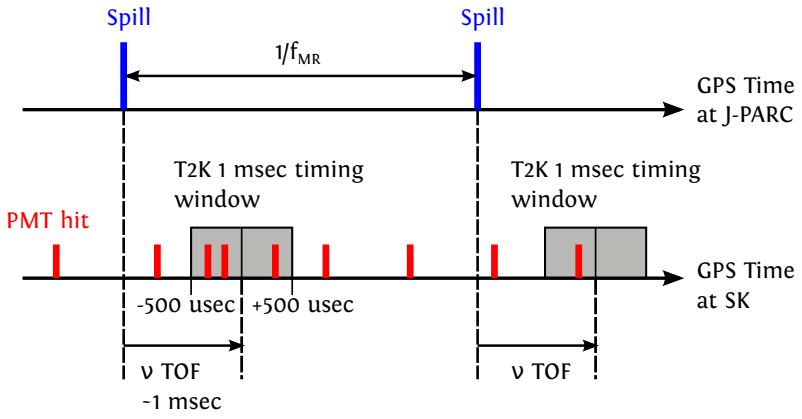

Figure 4.19: Timing of the T2K data acquisition at SK.

analysis.

4.7 First T2K data

The T2K experiment started started collecting data in January 2010. In total, the data equivalent of 1.431×10^{20} protons that hit the target (protons on target or POT) have been accumulated until March 2011. The run periods and the accumulated number of POTs are summarized in Table 4.4. The history of the beam intensity and accumulated POT is shown in Fig. 4.20.

Period	Name	POT
01/2010 – 06/2010	Run I	0.323×10^{20}
11/2010 – 03/2011	Run II	1.108×10^{20}
		1.431×10^{20}

Table 4.4: Run periods and the accumulated number of the protons on target.

The proton beam at any point in the beamline is described by its position,

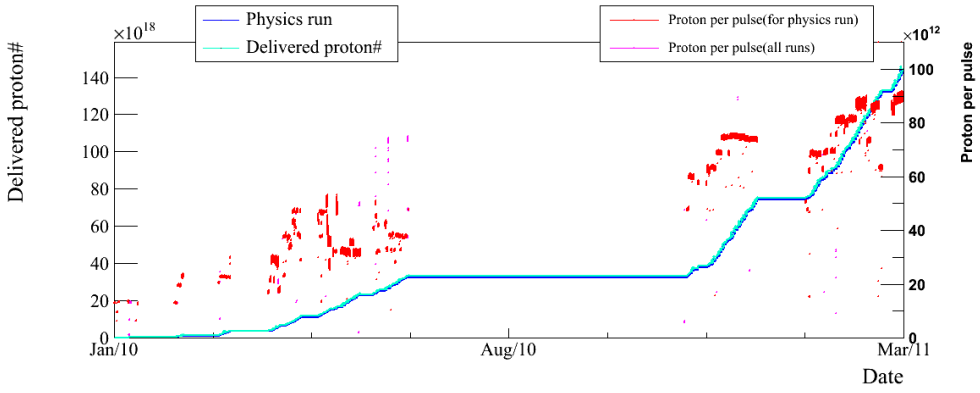

Figure 4.20: History of the instantaneous beam intensity (proton per pulse) and total accumulated number of protons on target.

	Position (cm)	Angle (mrad)	Width (cm)	ϵ (π mm.mrad)	Twiss α
X	-0.037	0.044	0.4273	2.13	0.60
Y	0.084	0.004	0.4167	2.29	-0.09

Table 4.5: Proton beam parameters for Run I.

angle, profile width, emittance ϵ, and Twiss α (see Appendix C). The values of these parameters evaluated at the entrance of the baffle are listed in Table 4.5 and Table 4.6 for the two running periods. These values are obtained from the accumulated measurements from the proton beam monitors in the final section of the primary beamline and the OTR monitor in the secondary beamline (see Appendix C for further details).

	Position (cm)	Angle (mrad)	Width (cm)	ϵ (π mm.mrad)	Twiss α
X	-0.0149	0.080	0.4037	5.27	0.16
Y	-0.0052	-0.007	0.4083	5.17	0.14

Table 4.6: Proton beam parameters for Run II.

A total of 121 T2K neutrino related events have been observed in the SK detector during the two running periods. The INGRID and ND280 detectors collected well over 10^6 and 10^3 events, respectively.

Fig. 4.21 shows the measurement of the neutrino beam centre by the INGRID detector. The dashed lines indicate the expected shifts if the ν beam drifted by ± 1 mrad. The measured values are well within these bounds. The stability of the event rates measured by INGRID is shown in Fig. 4.22. No significant variation in the events rates has been detected.

Fig. 4.23a shows the ND280 measurements of μ^- momentum produced in CC interactions ($\nu_\mu + N \rightarrow \mu^- + X$). The reconstructed neutrino energy distribution assuming CCQE kinematics (Eq. 4.7) is shown in Fig. 4.23b. The ratio of the total measured to the predicted number of events [46] is

$$R_{\text{Data/MC}} = 1.036 \pm 0.028(\text{stat.})^{+0.044}_{-0.037}(\text{det. sys.}) \pm 0.038(\text{phys. sys.}), \qquad (4.10)$$

illustrating a good agreement between the data and predictions.

The analysis of the initial T2K data gave a first indication of the ν_e appearance [46]. In addition, a clear ν_μ disappearance signal was observed [51].

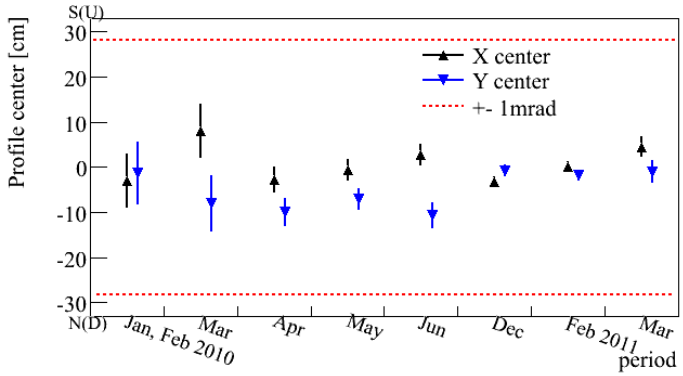

Figure 4.21: Horizontal and vertical profile centre measurements by INGRID.

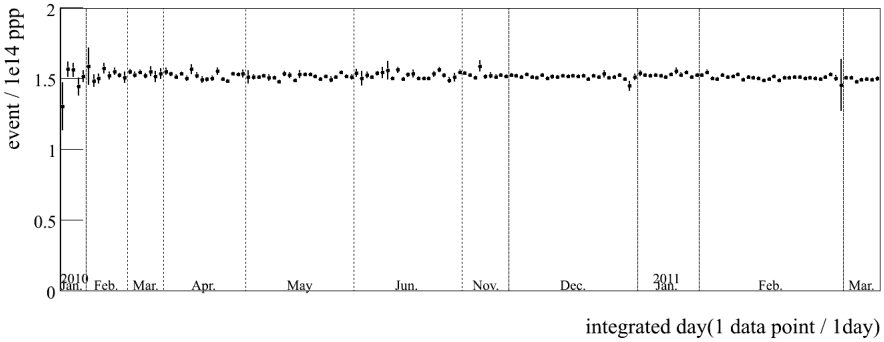

Figure 4.22: Event rate stability in INGRID normalized by 10^{14} protons per spill.

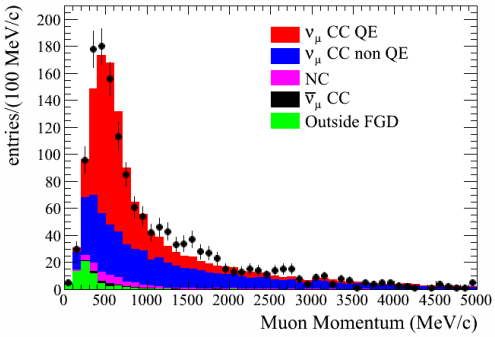

(a) Event distribution as a function of reconstructed muon momentum.

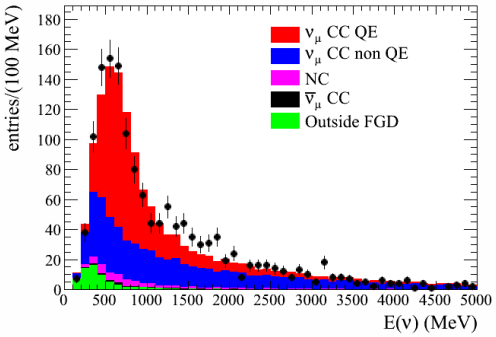

(b) Event distribution as a function of reconstructed neutrino energy assuming CCQE kinematics.

Figure 4.23: Expected and measured distributions of CC ν_μ events in ND280.

5 OTR Monitor

5.1 Introduction

Precise determination of the oscillation parameters depends on accurate measurements of the position and angle of the proton beam at the target. Due to the horn focusing, changes in the proton beam position and angle lead to variations in the direction of the secondary meson beam, effectively changing the off-axis angle and shifting the neutrino energy spectrum at SK. To meet the requirements of the precision for the T2K measurement of the oscillation parameters, the stability of the proton beam position and angle has to be monitored with a precision of 1 mm and 0.5 mrad, respectively. In addition, the profile of the beam has to be measured with a precision of about 10%. This is required for target and horn protection. The intense proton beam can be damaging to the first horn if it is too wide for the target and a significant fraction of the protons in the beam halo pass through the horn. Conversely, if the beam is too narrow, the target can be damaged due to the large energy dissipation over a small area. The task of an Optical Transition Radiation

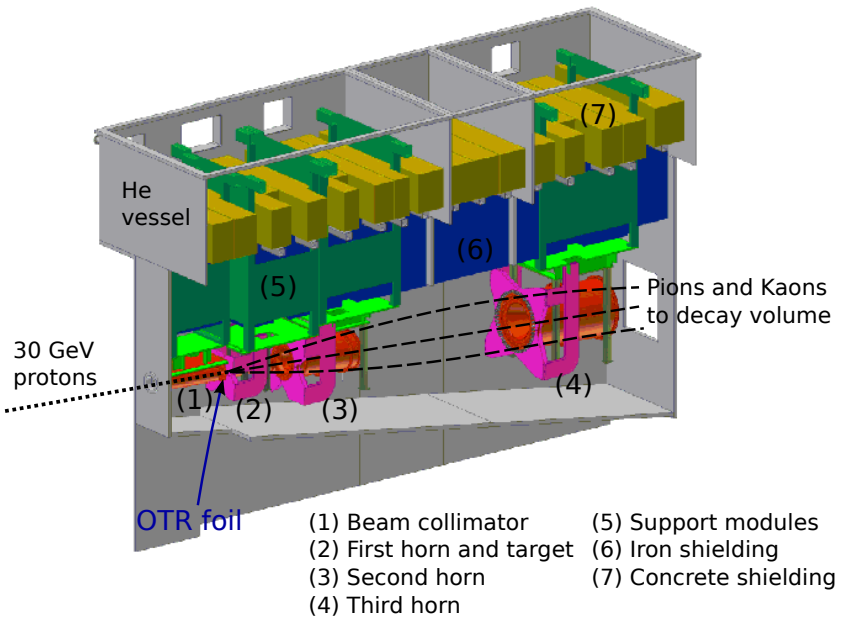

Figure 5.1: This drawing shows the T2K target station area. The OTR foil is placed between the beam collimator and the first horn.

(OTR) monitor [63] is to measure the beam position and profile just upstream of the target.

The monitor utilizes the Optical Transition Radiation (OTR) effect, the phenomenon where electromagnetic radiation is emitted in the visible range when a charged particle traverses a boundary between two media with different dielectric constants.

A theoretical description of transition radiation was first offered by Ginsburg and Franck [64]. The effect was experimentally verified for vacuum-metal boundaries by Goldsmith and Jelley [65]. Since then, OTR has been used at a number of

accelerators to monitor beam characteristics [66–68], where it has been generated by introducing a thin foil in the path of the beam and then recording the emitted light with a camera.

In case of the T2K experiment, the dose expected near the target at 750 kW operation is 5.4×10^8 Sv/hr. This precludes the placement of any electronics nearby. The OTR light is transported by a system of mirrors out of the harsh environment near the target to a safer one where a camera can be operated.

A side view of the T2K target station, discussed in the previous section, is shown in Fig. 5.1. The foil for the OTR production is placed downstream of the baffle approximately 30 cm upstream of the target. A series of mirrors is used to transport the light through channels (to prevent a straight path for ionizing particles to escape) in the iron and concrete shielding. The light emerges through a quartz window in the helium vessel lid where it is collected by a camera.

5.2 Transition Radiation

When a charged particle passes through a boundary from one medium to another its field induces a time-dependent polarization at the surface of the new medium. The radiation emitted by this polarized medium is the transition radiation. The maximum depth in the material at which the coherent emission can be obtained is

called the formation length D. As discussed in [69], it is given by

$$D = \frac{\gamma c}{\omega_p}, \tag{5.1}$$

where ω_p is the plasma frequency of the medium. It is related to the electron number density n_e and vacuum permittivity ε_0:

$$\omega_p^2 = \frac{n_e e^2}{\varepsilon_0 m_e}, \tag{5.2}$$

where m_e is the electron mass.

For example, the plasma frequency for solid titanium is

$$\omega_p^{\mathrm{Ti}} \simeq 1.34 \times 10^{16}\ \mathrm{sec}^{-1}. \tag{5.3}$$

For a 30 GeV proton ($\gamma \simeq 32$) crossing the Ti boundary, D is on the order of 1 μm. Consequently only a thin layer of material is required to produce the transition radiation.

The number of photons N emitted in a frequency range $d\omega$ into a solid angle

$d\Omega$ per particle of unit electric charge e is given by [70]

$$\frac{d^2N}{d\omega d\Omega} = \frac{e^2\beta^2\sqrt{\epsilon_2}\sin^2\theta\cos^2\theta}{\pi^2 c\hbar\omega} \times \left| \frac{(\epsilon_1-\epsilon_2)(1-\beta^2\epsilon_2-\beta\sqrt{\epsilon_1-\epsilon_2\sin^2\theta})}{(1-\beta^2\epsilon_2\cos^2\theta)(1-\beta\sqrt{\epsilon_1-\epsilon_2\sin^2\theta})\left(\epsilon_1\cos\theta+\sqrt{\epsilon_1\epsilon_2-\epsilon_2^2\sin^2\theta}\right)} \right|^2, \tag{5.4}$$

where $\beta = v/c$, v is the velocity of the particle, c is the speed of light, θ is the angle between the photon and particle direction, and ϵ_1 and ϵ_2 are the dielectric constants for the two materials that define the boundary (see Fig. 5.2). While Eq. 5.4 describes the transition radiation produced in the forward direction, emission in the backward direction also occurs. The intensity of the backward radiation can be obtained from Eq. 5.4 by interchanging ϵ_1 and ϵ_2 and setting $\beta \to -\beta$.

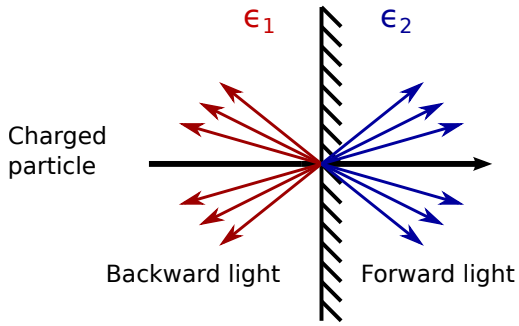

Figure 5.2: OTR emission from a particle crossing a material boundary.

The dielectric constants in Eq. 5.4 have an implicit frequency dependence determined by the dispersive properties of the materials. For metals, a good approx-

imation of this dependence is

$$\epsilon(\omega) = 1 - \frac{\omega_p^2}{\omega^2}. \tag{5.5}$$

We will now consider the transition radiation emitted at optical frequencies (Optical Transition Radiation or OTR) by charged particles crossing a vacuum-metal or metal-vacuum boundary. Propagation of the OTR photons in metal is suppressed, since at optical frequencies $\omega \sim 10^{15}$ and the dielectric constant ϵ is less than zero ($\omega_p \sim 10^{16}$ for metals). Therefore only emission into vacuum, which is backward for a vacuum-metal boundary crossing or forward for a metal-vacuum boundary crossing, needs to be considered.

For a highly relativistic particle that moves from material with $|\epsilon_1| > 1$ into vacuum, Eq. 5.4 can be reduced to [71]

$$\frac{d^2N}{d\omega d\Omega} = \frac{e^2\beta^2}{4\pi^2 c\hbar\omega} \frac{\sin^2\theta}{(1-\beta\cos\theta)^2}. \tag{5.6}$$

This light is emitted in a narrow cone centred around the direction of the moving particle. The maximum emission happens at $\theta \sim 1/\gamma$. Fig. 5.3a shows the angular distribution of the OTR light for 30 GeV protons ($\gamma = 32$) as a function of the polar angle θ. The distribution is symmetric in the azimuthal angle ϕ.

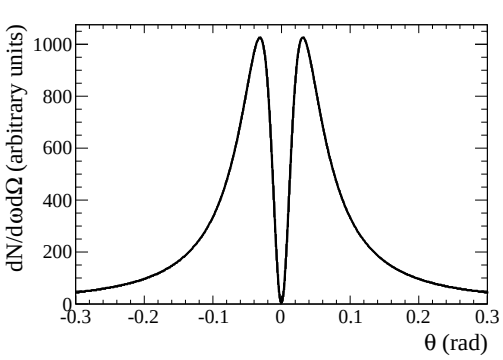

(a) Angular distribution of OTR for 30 GeV protons

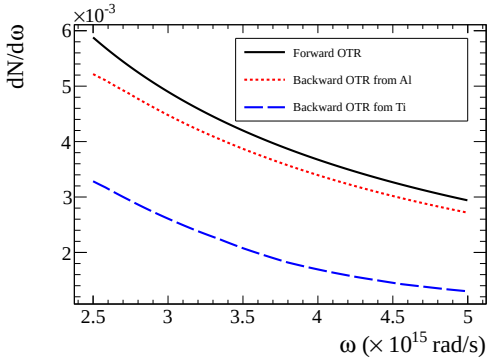

(b) Spectrum of OTR for 30 GeV protons

Figure 5.3: Angular and spectral distributions for OTR. The calculation of the backward OTR spectrum uses the data in [72] for the frequency dependent dielectric constant.

For the backward emitted OTR, $\epsilon_1 = 1$ and $\epsilon_2 = \epsilon$ and Eq. 5.4 reduces to

$$\frac{d^2N}{d\omega d\Omega} = \frac{e^2}{4\pi^2 c\hbar\omega}\left|\frac{\sqrt{\epsilon}-1}{\sqrt{\epsilon}+1}\right|^2 \frac{\sin^2\theta}{(1-\beta\cos\theta)^2}. \tag{5.7}$$

Similar to Eq. 5.6, Eq. 5.7 describes emission of the light into a cone centred around the particle direction. The intensity of this light, however, also depends on the reflective properties of the material through the dielectric constant ϵ.

Fig. 5.3b illustrates the spectrum of the OTR light in the optical frequency range. Spectra of both the forward (Eq. 5.6) and the backward (Eq. 5.7) emissions are shown. For the latter, spectra of OTR from aluminum and titanium are considered.

When particles are not at normal incidence to the material boundary, the for-

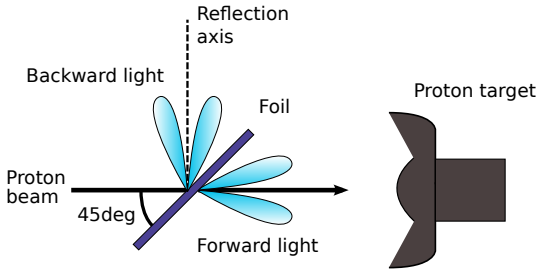

Figure 5.4: OTR light emission from a foil oriented at 45° with respect to the incident beam. The forward light cannot be used as it requires placing optical components in or near the beam path.

ward OTR light is still generated along the direction of the particle motion. The backward emission, however, happens around the axis of the reflection from the material surface. For a thin foil placed at 45° with respect to the direction of charged particle beam, the backward light is emitted at 90° relative to the beam as illustrated in Fig. 5.4. The OTR monitor uses this principle to image the proton beam.

5.3 Optical system

5.3.1 Overview

The layout of the OTR system is shown in Fig. 5.5. The proton beam passes through a foil which is oriented at 45° relative to the beam axis. The light emitted from the upstream surface of the foil (backward light) at 90° with respect to the beam axis is collected and transported through the shielding and out of the target

station vessel by four 90° off-axis parabolic mirrors. The first mirror (mirror 1) collimates the divergent OTR light from the foil. It is then focused by the second mirror to form an intermediary image. This image is used as a virtual object to the mirror 3 which again acts as a collimator. The collimated light emerges from the helium vessel through a 25 cm diameter quartz (BK7-G18) window mounted in the lid of the vessel. It is then focused by the last mirror onto a camera.

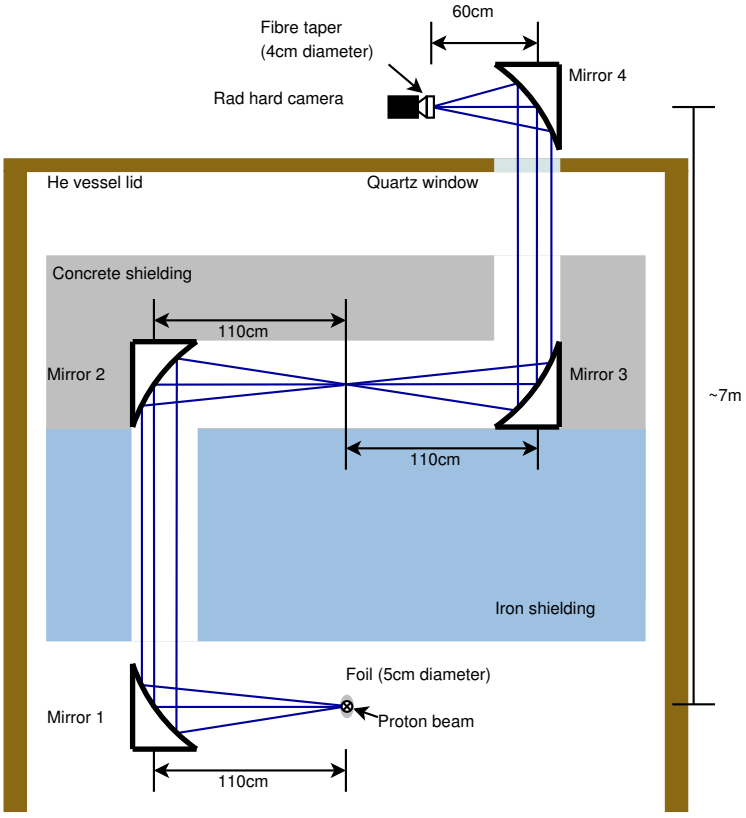

Figure 5.5: This figure shows a slice through the optical path of the OTR system where the proton beam is going into the page and striking the foil. Three light rays illustrate the focusing properties of the optics.

The first three mirrors have the same focal length of $F = 55$ cm, while the last

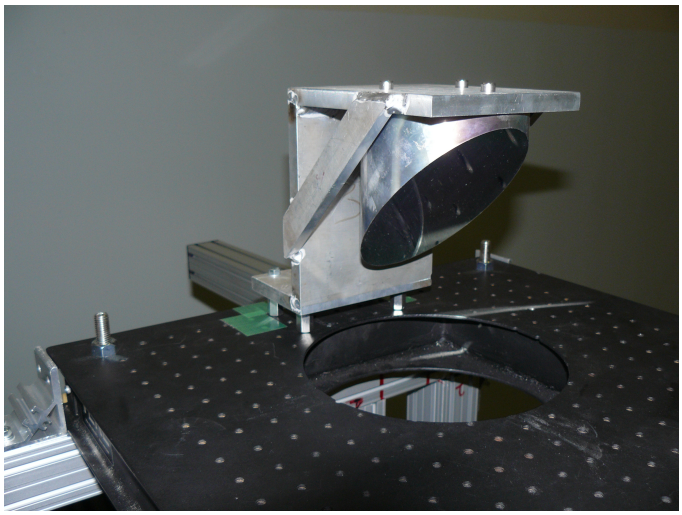

Figure 5.6: View of the mirror 4 mounted on its support.

one has a shorter focal length of $F_4 = 30$ cm. This reduces the image projected on the camera by a factor $F_4/F = 30/55 \simeq 0.55$ relative to the actual object. The camera is equipped with a 40 mm diameter fiber taper optically coupled to an 11 mm camera sensor. Combining the reduction from the optical system and the taper dimensions gives a maximum viewable area of 50 mm on the foil. This is large enough to completely cover the acceptance area defined by a 30 mm diameter hole in the upstream baffle.

5.3.2 Mirrors

Each mirror is machined out of solid aluminum. Fig. 5.6 shows the picture of the mirror 4 mounted on its support structure. The diameter of the mirrors is 12 cm. The reflective surface is coated with a 400 nm thick layer of Al_2O_3, which has a

reflectivity close to 100%. Prior to the fabrication of the mirrors, a small test mirror with this coating was irradiated with a proton beam at TRIUMF. After exposing it to the dose equivalent to 130 years of operation at the location of the mirror 1 no significant deterioration in the reflective properties was observed. This provided confidence in the long term survivability of the mirrors.

5.3.3 Camera

A monochrome video camera (Thermo Fisher Scientific 8710D1M) is used to capture the OTR light. The camera is rated to be radiation tolerant to an accumulated dose of up to 10 kGy, while the expected dose at its location is estimated to be ~ 1 kGy/year with a 750 kW beam operation.

The camera sensor is a radiation-hardened charge injection device (CID). The pixel matrix consists of 755×484 sites with dimensions of $12.0\mu\text{m} \times 13.7\mu\text{m}$. The sensor is controlled remotely by a camera control unit (CCU) located on the ground level of the target station and accessible during beam operation.

The video output is an interlaced analog signal that follows the RS-170 standard. Each frame (full readout of the camera sensor) is composed of the even field followed by the odd field. These correspond to progressive scans of even and odd lines in the pixel array, respectively. The field scan rate is 60 Hz resulting in a frame rate of 30 Hz.

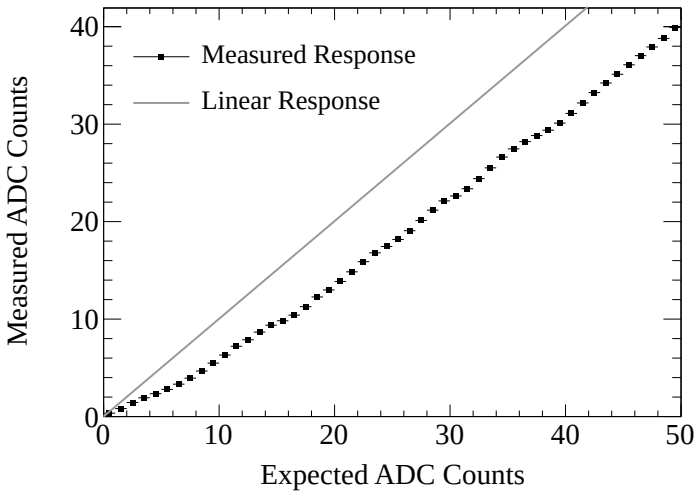

Figure 5.7: The measured camera response in ADC counts is shown as a function of the expected ADC counts assuming linear operation. The response is averaged over the pixels.

The progressive interlaced readout on the camera sensor means that even lines are scanned 1/60 sec ahead of the odd lines. Some fraction of the charge collected at the arrival of the OTR light therefore could be lost through leakage currents before it can be recorded. An exponential decay of the collected charge with a time constant of 77 msec has been observed. This is taken into account when the image data is analyzed.

At low light levels the camera was observed to exhibit a non-linear response. This is illustrated in Fig. 5.7 where the expected response is plotted against the measured values. The cause of this behaviour was understood to be due to impurities in the silicon of the sensor that trap the collected charge. To avoid this problem, a uniform ambient light is used to pre-populate these traps and move the

response of the camera into the linear region.

To increase the dynamic range of the camera, several neutral density filters with different attenuation constants are used. The filters are mounted on a wheel and placed in front of the camera. A given filter can thus be selected remotely by rotating the wheel.

5.3.4 Prototype system

Prior to the construction of the full scale monitor, a prototype system was assembled to demonstrate the detector capability of observing OTR and measuring beam parameters. The system used four parabolic mirrors with the focal lengths 13.8% of the values in the full-scale design. Image capture was done with a charge-coupled device (CCD) photo-sensor. Three different foils made from titanium-alloy, aluminum, and graphite were tested.

The system was deployed at the National Research Council electron linear accelerator in Ottawa. The γ factor of the electron beam was similar to that of the beam at J-PARC, so the angular distribution of the emitted light was expected to be the same. OTR was observed for all of the test foils. Additional tests were made to identify whether the He environment in the T2K target station could potentially affect the light emission or act as a source of background light. No such effects were detected.

The measurement of the beam position and width with the prototype system were estimated to be accurate to 0.2 mm and 15%, respectively. This was sufficiently accurate to proceed with the construction of the full scale system.

5.4 Mechanical design

The OTR mechanical system is illustrated in Fig. 5.8a and Fig. 5.8b. Since the system is located in the high-radiation environment of the target station, direct access is not possible after deployment. The design of the mechanical system therefore had to meet the following criteria:

- the ability to continually calibrate the optics
- stability with temperature
- long-term robustness and survivability
- ease of remote maintenance for part replacement.

5.4.1 The foil disk system

The OTR monitor has several foils that are mounted on a disk as shown in Fig. 5.9a. The disk has eight identical slots that can accommodate 50 mm diameter foils. Seven of the slots are filled while one is left empty. Table 5.1 lists the different foils

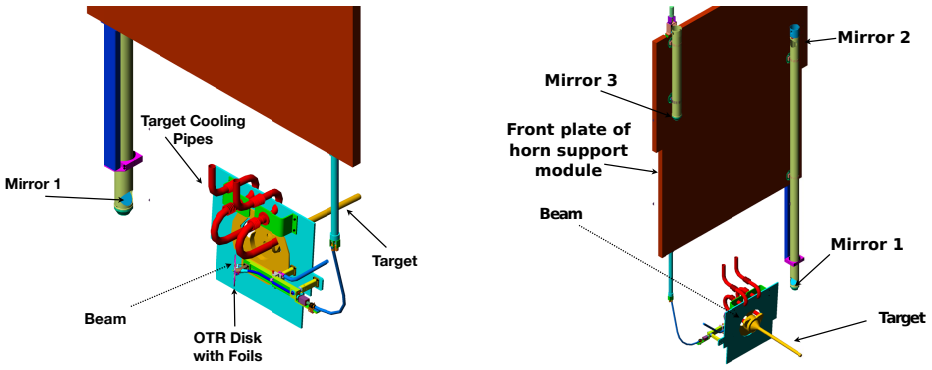

(a) The OTR components near the beam.

(b) A view of the OTR system from the rear, showing components mounted on the front plate of the horn support module.

Figure 5.8: The OTR system components.

used in the system. There are four titanium foils for high-intensity beam operation. In addition there is one aluminum foil and a ceramic wafer to extend the range of operation to lower beam intensities such as used during the beam commissioning. Finally there is a titanium foil with a precisely machined hole pattern. It is used for calibrations of the optical system.

Material (number of foils)	Thickness (μm)	Operation
AF995R (1)	100	$<$ 1 kW beam power
Al 1100 (1)	50	$1 - 40$ kW beam power
Ti 15-3-3-3 (4)		$>$ 8 kW beam power
Ti 15-3-3-3 (1)		calibration with no beam

Table 5.1: Foils used in the OTR system.

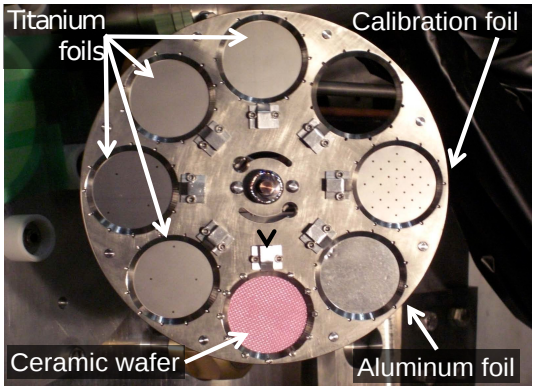

(a) View of the foil disk from the upstream

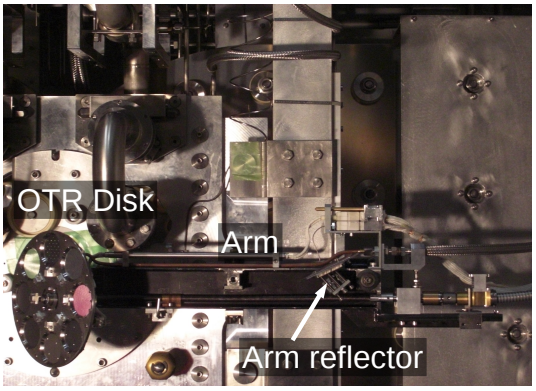

(b) View of the OTR disk on the arm

Figure 5.9: View of the foil disk and the arm from the upstream side.

The disk is mounted at 45 degrees to the beam axis on an arm (Fig. 5.9b) that attaches to the support frame of the first horn. A remotely controlled stepper motor system allows to an operator rotate the disk and place an appropriate foil into the beam path.

There are several systems to ensure the correctness and repeatability of the foil placement in the beam. Each foil position on the disk has a machined titanium button that engages a micro-switch once the foil is in position. In addition, the disk has depressions at each foil site. When the foil is in position, a spring-loaded plunger slides into the depression, securely locking the disk in place.

A combination of the micro-switch and the plunger is the primary method for positioning the foils. In the event of their failure, there is a backup system that relies on a pressurized helium line. The outlet end of the line is placed in close

proximity to the disk surface and the pressure is maintained in the line until the foil moves into the correct position marked by a small hole in the disk. Once the hole and the gas line outlet are aligned, the pressure decreases. This drop is detected with a pressure sensor installed on the line.

After the disk was installed, the centre of the calibration foil was surveyed with respect to the axis through the centre of the first horn (nominal beamline axis). The position of the central calibration hole was measured relative to this axis with 0.3 mm precision.

5.4.2 Mechanical design of the optical system

The first and the second parabolic mirrors along the OTR light path (see Fig. 5.5) are mounted at either end of a long steel tube while a shorter tube houses the third mirror. This is illustrated in Fig. 5.8b.

The tubes are precisely mounted to the back of the front plate of the horn 1 support module. It is possible to lift them out of the helium vessel and install replacements through two ports in the vessel lid directly above the tubes.

The OTR light reflected by the mirror 3 passes through the quartz window in the helium vessel lid. It is collected by the mirror 4 which forms an image on the camera. The camera is mounted on three remotely controlled motorized stages, allowing to make adjustments to its position in three directions. The fourth mirror

and the stages with the camera are mounted on an optical table, which is fixed to the helium vessel lid.

5.4.3 Calibration lighting systems

The optical system is calibrated periodically to monitor any changes in the optical path. This is done by placing the calibration foil in the beam path (the beam is off for this configuration) and lighting the foil from behind. There are three lighting systems in place for this.

Two of them use LED lasers (Sanyo DL3147-060, 650 nm, 7 mW). One of the lasers is mounted just above the quartz window in the vicinity of the mirror 4. The other is located inside the vessel on top of the concrete shielding. The light from each laser is sent down two internally polished steel tubes. The bottom of the tubes have small reflectors that guide the laser light to another reflector on the arm (see Fig. 5.9b), that aims the light to the calibration foil.

The third lighting system consists of three filament lamps. Each lamp is made from a coiled Alchrome wire mounted inside a parabolic reflector. The lamps are operated at a 12 A current. They are located in the same region as the laser tube reflectors and oriented to emit light in the direction of the arm reflector. Fig. 5.10 shows a picture of this region.

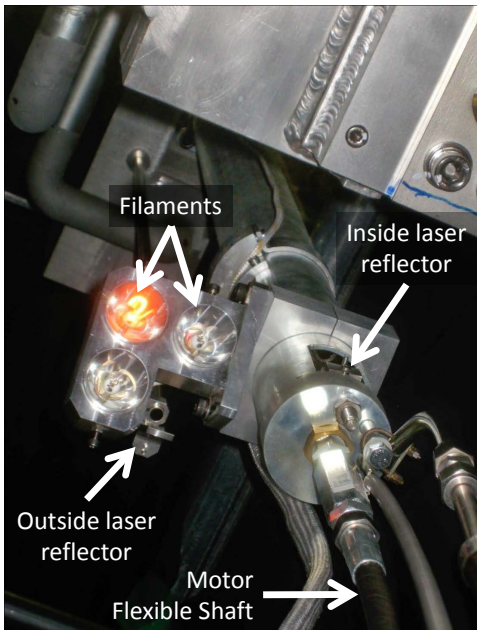

Figure 5.10: Picture of the filament lamps and laser reflectors. The flexible shafts of the disk rotation system is also visible.

5.4.4 Alignment

The optical system was aligned using a small He-Ne laser. The laser was mounted on the disk above one of the foil slots and aligned to point along the beamline through the first horn. A plane mirror was then attached to the same foil slot parallel to the disk. The mirror reflected the laser light at 90° with respect to the beam axis in the direction of the OTR light as illustrated in Fig. 5.11a. Parabolic mirrors were then adjusted one by one, so that the laser light could hit the centre of each mirror traveling along the central path through the optical system to the camera.

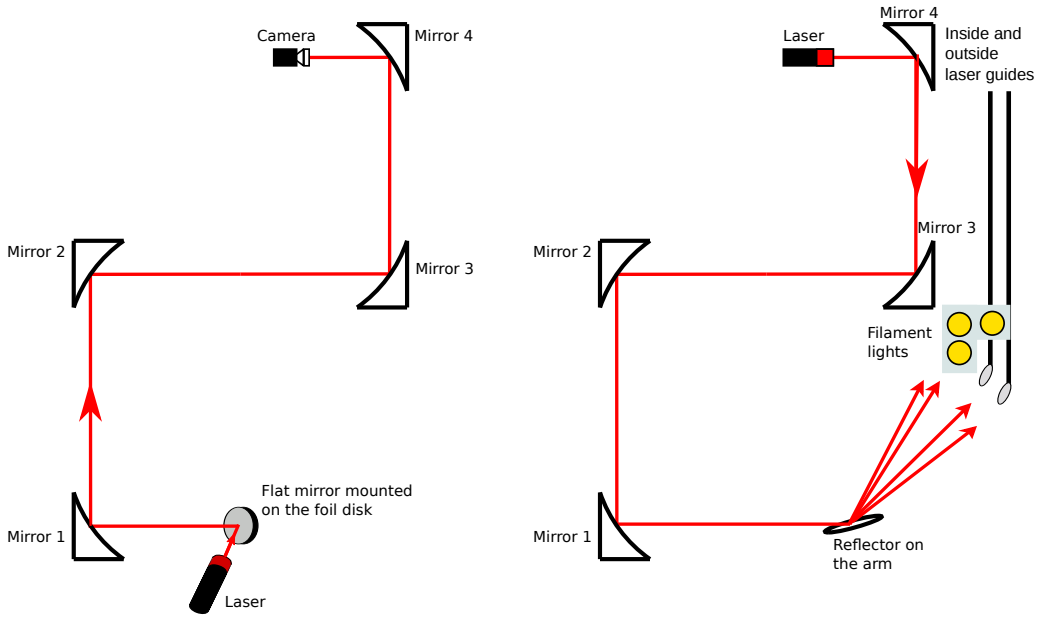

(a) Diagram showing the alignment procedure for the mirrors.

(b) Diagram showing the alignment procedure for the arm reflector.

Figure 5.11: Illustration of the OTR system alignment.

The arm reflector was aligned by shining a laser back from the camera position through the optical system as shown in Fig. 5.11b. The orientation of the reflector was adjusted until the light from the laser could reach the area with the laser reflectors and the filament lamps.

5.5 Data Acquisition and Slow Control

5.5.1 OTR DAQ system

The main functions of the data acquisition system (DAQ) are to trigger, collect and process the image data.

The components of the DAQ system are illustrated in Fig. 5.12. The trigger signals and the image acquisition controls are handled by a Field Programmable Gate Array (FPGA) chip located on a frame-grabber board, which interfaces to a host DAQ computer via a Peripheral Component Interconnect Express (PCI Express) bus. Also located on the board is a TriMedia TM1302 digital signal processor (DSP), which is responsible for the transfer of the digitized image frames to the host computer. Configuration of the FPGA registers is done via TriMedia software.

The analog video signal from the camera is acquired and digitized by the frame-grabber. Fig. 5.13 shows timing signals important for the DAQ operation. The readout cycle is initiated with a pre-trigger, which arrives 100 msec before a possible proton beam extraction to the neutrino beam-line. Following its arrival after a programmable delay (`frame_reset_delay`) a frame reset signal is issued to the camera, which synchronizes it and the readout circuitry to the expected spill arrival time. The trigger signaling the beam extraction to the neutrino beam-line arrives

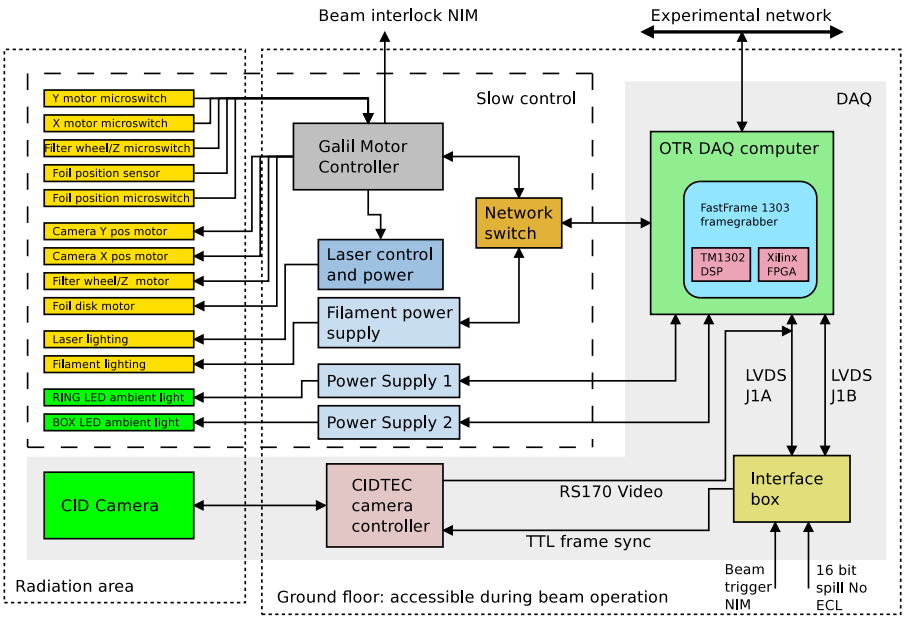

Figure 5.12: OTR monitor slow control and DAQ system.

20 μsec before the spill. After it is received and while the camera data are acquired and digitized by the frame-grabber an interrupt signal (TM interrupt) is sent to the DSP. The timing of the interrupt relative to the frame reset is configurable (`capture_delay`). The interrupt signal informs the DSP that the next available frame will contain the spill data and should be moved from the internal memory buffers to a dedicated memory address on the host computer. After moving the spill image, the DSP also transfers the image data from the two subsequent frames. These images are later used for the pedestal subtraction (see Section 5.6.3).

Once the images are copied to the memory of the host computer, a MIDAS-based [73] front-end application compresses them using the PNG image compression

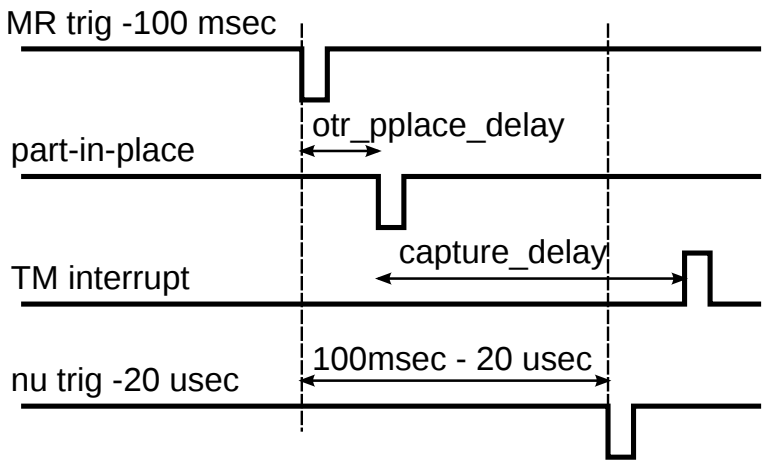

Figure 5.13: Image acquisition signals.

algorithms [74]. The data are then sent to a dedicated event server that handles the distribution of all of the proton monitor data for online analysis and archiving.

The OTR online monitoring program displaying an event from one of the first proton beam extractions to the neutrino beamline at J-PARC is shown in Fig. 5.14. The centre of the T2K target is marked by a yellow cross-hair in the middle panel. The two panels on the right show in the horizontal and vertical projections the results of a 2D fit that extracts the beam position and width. These values along with the measurements from the upstream proton beam monitors are used to determine whether the beam position and width are within tolerance. If they are outside tolerance, an abort signal is sent to prevent further extraction from the main accelerator ring to the neutrino beamline.

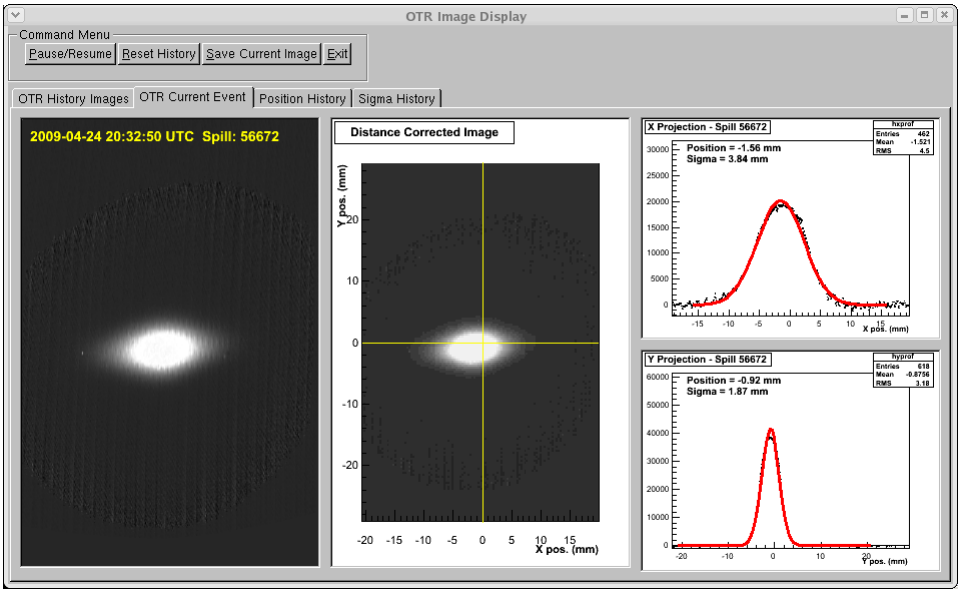

Figure 5.14: OTR online event display showing one of the first proton beam spills on target. The centre of the target is marked by a yellow cross-hair in the middle panel.

5.5.2 Slow Control

The OTR monitor has a number of remotely controlled motors to move different components of the detector. In addition, the lighting system for the periodic calibration of the optics requires a number of power supplies. These elements are part of the slow control system (Fig. 5.12), which is managed using MIDAS.

The hardware control of the disk, filter wheel and camera stage motors is done using a Galil [75] motor control module. The unit also collects the status from the pressure sensor and the micro-switches on the motors. The state of the disk micro-switch is constantly monitored. To avoid possible proton beam extraction

during the foil disk rotation or when the disk is not properly positioned, a beam interlock signal is generated when it is not engaged.

5.6 Image correction and analysis

5.6.1 Efficiency correction

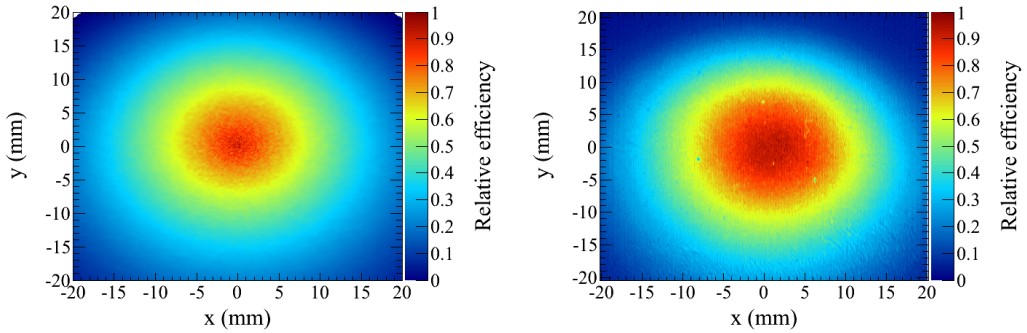

(a) Simulated efficiency of the optical system.

(b) Efficiency measured with the integrating sphere.

Figure 5.15: Simulated and measured light collection efficiencies. Each distribution is normalized by the maximum efficiency, which is at the centre of the image.

Ray tracing simulations of the optical system revealed that within ±15 mm of the foil centre, the relative light collection efficiency varies by more than 50%. This is illustrated in Fig. 5.15a. The significant variation of the light collection efficiency over the size of the beam spot introduces bias into the reconstructed beam position and width.

An integrating sphere was used to provide a uniform light source in order to

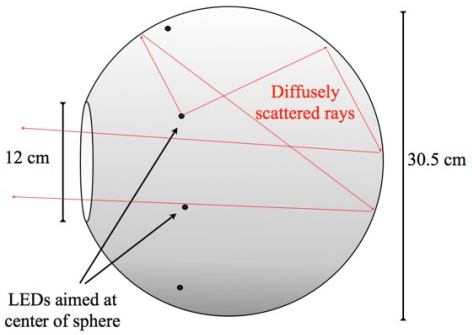

Figure 5.16: A schematic of the integrating sphere used to measure the light collection efficiency.

calibrate the light collection efficiency of the system. This device, schematically shown in Fig. 5.16, is a hollow sphere 30.5 cm in diameter with a 12 cm opening port (output port). The inside surface of the sphere is painted white. Light is injected into the inner volume using eight laser diodes arranged in a circle. There is no direct path between the diodes and the output port requiring any light ray that escapes the sphere to undergo multiple scattering from the rough inner surface of the sphere. This results in a diffuse light distribution at the output. The uniformity of the light over the area of the output port has been measured to be within 5%.

To calibrate the optical system, the integrating sphere was positioned at the foil location with the output port facing the mirror 1. Images of the light through the optical system were then taken with the camera system. These images, shown in Fig. 5.15b, are used to apply the correction for the non-uniform light collection efficiency.

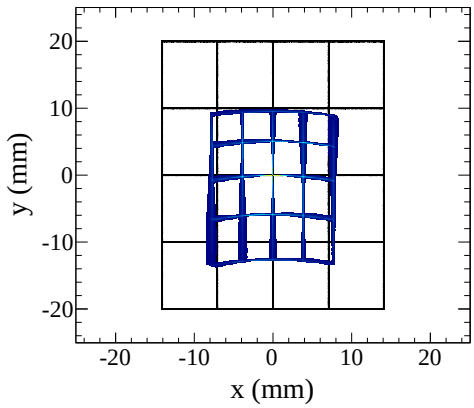

Figure 5.17: The thin black lines show a grid of point sources placed on the foil surface, and the wider lines show the resulting image after simulated rays were traced through the optical system. The size of the image is also reduced by 55% compared to the original due to the smaller focal length of mirror 4 compared to the first 3 mirrors.

5.6.2 Distortion correction

The optical system introduces a certain amount of distortion to the images, which leads to bias in measurements and therefore requires correction. Fig. 5.17 illustrates the effect of the distortion on a uniform grid. It is minimal at the centre of the image, but increases near the edges, and is more pronounced in the vertical direction due to the parabolic nature of the mirrors. The distortion is corrected by imaging the calibration foil.

The calibration foil, shown in Fig. 5.18, has laser-machined holes arranged in a grid 7 mm apart. The two central holes are 0.8 mm in diameter. The rest of the holes have a diameter of 1.2 mm. The dimensions of the holes were optimized

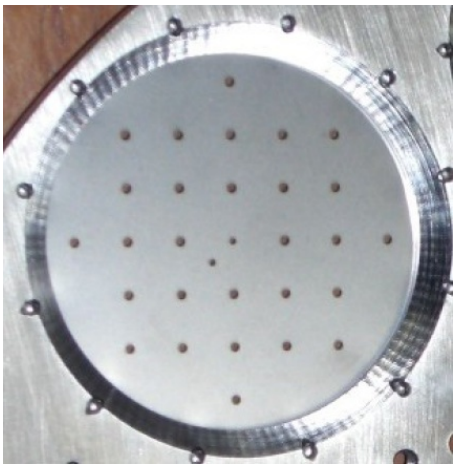

Figure 5.18: The calibration foil with a grid of laser-machined holes.

such that the light output from each hole is high enough to be visible, while its size is kept as small as possible. The relative hole location is known to a precision of better than 0.1 mm. The location of the central hole relative to the proton beam axis is known to the precision of 0.3 mm, as already discussed in Section 5.4. This hole provides an absolute position reference for the images recorded by the camera.

The calibration lighting systems are used to back-light the calibration foil and take images of its hole pattern. This yields not only a reference point relative to the beam axis, but also an image of the grid of holes to correct for distortion in the optical system. The calibration images are taken regularly during periods of no beam operation. This allows monitoring of any movement of the hole pattern with respect to the camera pixels due to changes in the optical path.

The image of the pattern on the back-lit calibration foil is sensitive to the

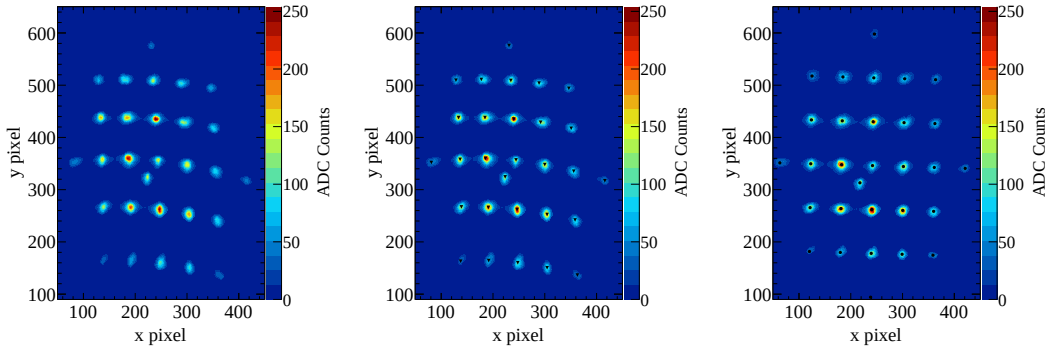

(a) Image of the backlit calibration foil showing the characteristic distortion introduced by the optics.

(b) Image of the distorted calibration foil pattern with centroids of the holes marked by black triangles.

(c) Image of the backlit calibration foil after the distortion correction with the true hole pattern superimposed.

Figure 5.19: Illustration of distortion correction for the calibration foil image.

angles of the incident light (note that the light from the filament lamps and lasers is incident at different angles on the arm reflector). This results in a ~ 0.2 mm shift in the imaged hole positions between different light sources. An unbiased image of the calibration pattern was obtained by placing a light source directly behind the calibration foil on the optical axis (the axis defined by the line of sight between the central hole of the foil and the centre of the mirror 1) and these shifts were corrected.

The distortion of the imaged calibration foil pattern is visible in Fig. 5.19a and follows the expectations from simulations (cf. Fig. 5.17). These calibration images are analyzed to obtain the centroids of the holes marked by black triangles in Fig. 5.19b. This information along with the true hole positions yields a transfor-

mation map that is used to correct image distortions. As an example, Fig. 5.19c shows the image of the calibration foil pattern after the distortion correction with the true positions of the holes superimposed.

The mathematical procedure for constructing the transformation map is to expand the coordinates (u, v) of the undistorted or true image in terms of the coordinates of the distorted or measured image (x, y) as in [76]:

$$u(x, y) = \sum_{i=1}^{6} a_i \phi_i(x, y), \tag{5.8a}$$

$$v(x, y) = \sum_{i=1}^{6} b_i \phi_i(x, y), \tag{5.8b}$$

where ϕ_i, $i = 1 \ldots 6$ is a set of orthogonal functions and the expansion coefficients a_i and b_i are the elements of the transformation map. The functions ϕ_i are constructed from the polynomial basis $H = \{1, x, y, x^2, xy, y^2\}$ using the Gram-Schmidt orthogonalization process [77]. The orthogonality relation for ϕ_i is defined as

$$\sum_{k=1}^{m} W_k \phi_i(x_k, y_k) \phi_j(x_k, y_k) = 0 \qquad\qquad i \neq j, \tag{5.9}$$

where the summation is performed over all m calibration holes of the imaged pat-

tern. The weight coefficients W_k are calculated from the function

$$W_k(x, y) = \exp\left(-\delta\sqrt{(x - x_k)^2 + (y - y_k)^2}\right), \tag{5.10}$$

where δ is a tunable "range" parameter and (x_k, y_k) are the measured coordinates of a k^{th} calibration hole. This function is introduced for the distortion transformation to have a more local character. That is to say, it allows the holes in a given neighborhood of the image to have greater contribution than the ones further away.

Once the orthogonal basis functions are constructed, the transformation map coefficients a_i and b_i can be simply obtained from

$$a_i(x, y) = \frac{\sum_{k=1}^{m} W_k(x, y) u_k \phi_i(x_k, y_k)}{\sum_{k=1}^{m} W_k \phi_i(x_k, y_k) \phi_i(x_k, y_k)}, \tag{5.11a}$$

$$b_i(x, y) = \frac{\sum_{k=1}^{m} W_k(x, y) v_k \phi_i(x_k, y_k)}{\sum_{k=1}^{m} W_k \phi_i(x_k, y_k) \phi_i(x_k, y_k)}, \tag{5.11b}$$

where the pair (u_k, v_k) refers to the true coordinates of a k^{th} calibration hole.

5.6.3 Image analysis

The position and width of the proton beam as well as the total light yield from a given foil is determined on a spill-by-spill basis. The analysis begins by subtracting the pedestal from each spill frame. The pedestal values are obtained from the two

images taken immediately after the spill image. Following the pedestal subtraction, a number of corrections are performed:

1. correction due to the non-uniform light collection efficiency of the optical system using the map obtained with the integrating sphere,

2. correction due to the charge decay in the camera sensor (described in Section 5.3.3),

3. correction of the image distortions with the transformation map obtained from the back-lit image of the calibration foil.

After the image corrections, a two-dimensional fit to the data is performed to extract the proton beam position, profile, and the total light yield.

5.7 Performance and results

5.7.1 Performance summary

The OTR monitor has operated with beam intensities ranging from 1×10^{11} to 1×10^{14} protons per spill. For low beam intensities during the first stages of the T2K beamline commissioning, the ceramic wafer was used. Above 1×10^{12}, the OTR light production was sufficiently high with both aluminum and titanium foils. These foils were used during the periods of the data collection for the physics

analysis. Fig. 5.20 shows an examples of the proton beam profile obtained with titanium (Fig. 5.20a) and aluminum (Fig. 5.20b) foils.

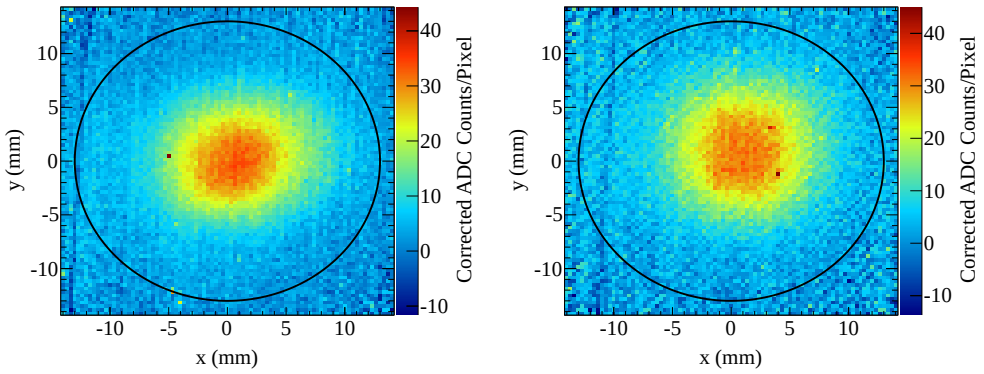

(a) OTR beam image with Ti foil and 9.0×10^{13} protons per spill.

(b) OTR beam image with Al foil and 2.3×10^{13} protons per spill.

Figure 5.20: Example OTR images obtained with the titanium and aluminum alloy target foils. The black circle indicates the location of the edge of the target.

The expected number of the electrons produced in the camera sensor per incident proton on the Ti foil is 2.1×10^{-5}, while the measured value is 4.8×10^{-6} electrons per proton. This discrepancy of 23% may arise from the underestimation of the mirror surface quality in the calculation of the predicted value or loss of the reflective qualities due to possible dust deposits on the mirror surfaces. The OTR light production as a function as the proton beam intensity is shown in Fig. 5.21. A good linearity in the system response is observed for the beam intensities varying over more than one order of magnitude.

The resolution of the OTR monitor is calculated from 50 consecutive spills taken with 7.4×10^{13} protons per spill. Assuming that the beam is stable during

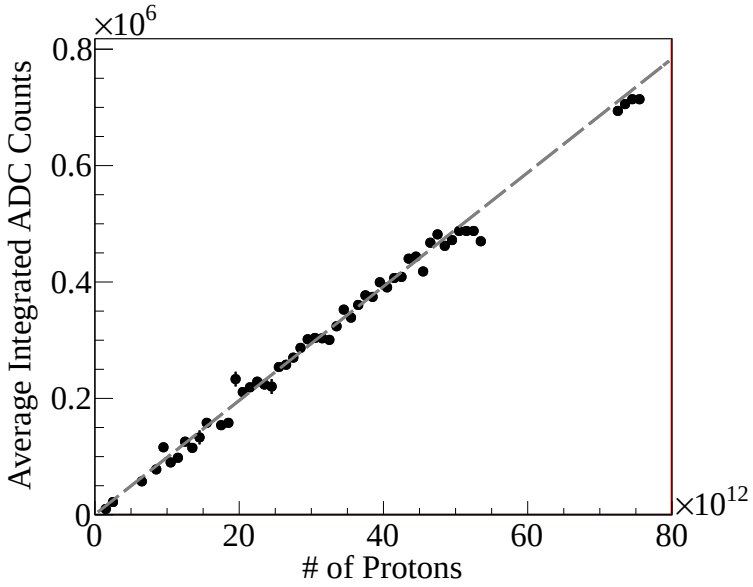

Figure 5.21: Camera response as a function of the number of protons per spill. The dashed line shows the fit to the data.

this period, the RMS of the obtained OTR measurements gives an estimate of the monitor resolution. Table 5.2 lists the values for the measurement resolutions of the beam position and width in the horizontal and vertical directions. All values are below 0.1 mm.

Measurement	Resolution (mm)
Position x	0.069
Position y	0.085
Profile width σ_x	0.068
Profile width σ_y	0.054

Table 5.2: Measurement resolutions of the OTR monitor obtained with the titanium target and 7.4×10^{13} protons per spill.

5.7.2 Systematic uncertainties

The dominant contribution to the uncertainties in the OTR measurements comes from the systematic uncertainties. Table 5.3 list contributions from different sources of the systematic uncertainties.

The largest source of the uncertainty for the position measurements is the 0.3 mm alignment uncertainty from the survey of the calibration foil. Another significant contribution comes from the alignment of the calibration light sources. As discussed earlier, the fact that the calibration lights are not positioned on the optical axis introduces a bias in the images of the calibration pattern. Conservatively this translates into $0.20 - 0.25$ mm uncertainty in the position measurements.

Source	δx(mm)	δy(mm)	$\delta\sigma_x$(mm)	$\delta\sigma_y$(mm)
Calib. foil alignment	0.302	0.300	0.087	0.102
Signal model	0.005	0.003	0.436	0.376
Background model	0.090	0.115	0.010	0.031
Fitter bias	0.004	0.015	0.105	0.140
Calib. light alignment	0.210	0.251	0.046	0.038
Pixel charge decay	0.101	0.084	0.019	0.030
Distortion correction	0.029	0.039	0.083	0.111
Others sources	0.095	0.057	0.079	0.085
Total	0.404	0.432	0.473	0.441

Table 5.3: Sources of systematic uncertainties for absolute proton beam position and width measurements by OTR monitor.

For the width measurements, the dominant source of the systematic uncertainty comes from the choice of the model used to fit the signal. Nominally a 2D Gaussian

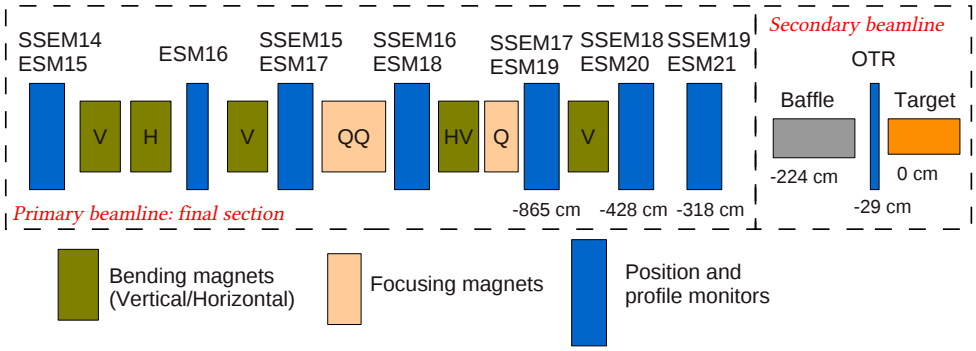

Figure 5.22: Proton monitors and beamline elements upstream of the target.

function is used. Other models are, however, consistent with the data. The uncertainty in the width measurements introduced by the choice of model is 0.38-0.44 mm.

The total uncertainties are less than 0.5 mm, satisfying the precision requirements for the monitor.

5.7.3 Proton monitor results

The OTR monitor in conjunction with the upstream ESMs and SSEMs is used to determine the proton beam position, angle, width, and divergence at the target.

Fig. 5.22 schematically shows the components in the final focusing section of the primary beamline and secondary beamline upstream of the target. The horizontal position and angle are measured using the data from the position monitors downstream of the last focusing magnet. The vertical position and angle are determined from the monitor data downstream of the last vertical bending magnet.

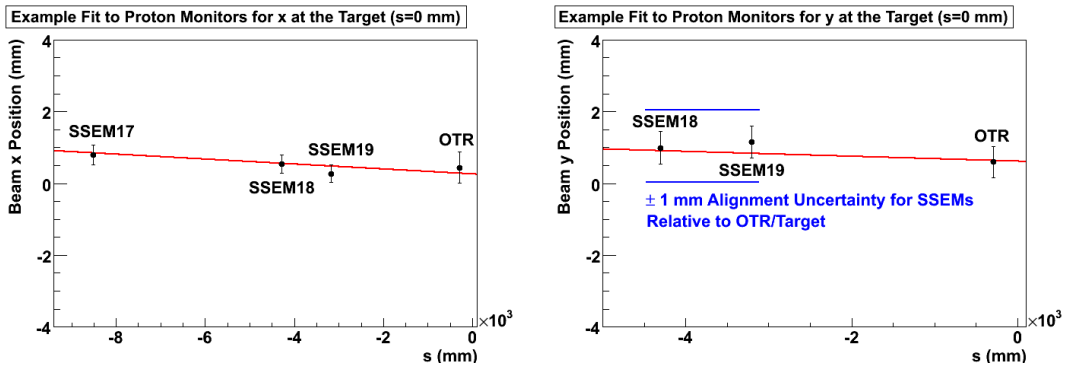

(a) Fit in horizontal direction **(b)** Fit in vertical direction

Figure 5.23: Example fits of the beam position using SSEM and OTR measurements. The target is at $s = 0$.

Examples of the beam orbit fits (the fitting procedure is discussed in more detail in Appendix C) that determine the horizontal and vertical position and angle are shown in Fig. 5.23. The horizontal axis in the plots is the s coordinate defined to be collinear with the nominal beam direction. The errors in the monitor measurements are dominated by the alignment uncertainties.

The beam positions at the target obtained by fitting the proton monitor data can be compared to the position measurements of the muon beam centre made by MUMON. Given there are no significant misalignment in the secondary beamline components, a properly tuned proton beam hitting the target should produce a profile in MUMON which is centred. Fig. 5.24 shows the correlation of the MUMON measurements with the position of the proton beam at the target for runs where the beam was scanned in the x and y directions. At the centre, the MUMON and

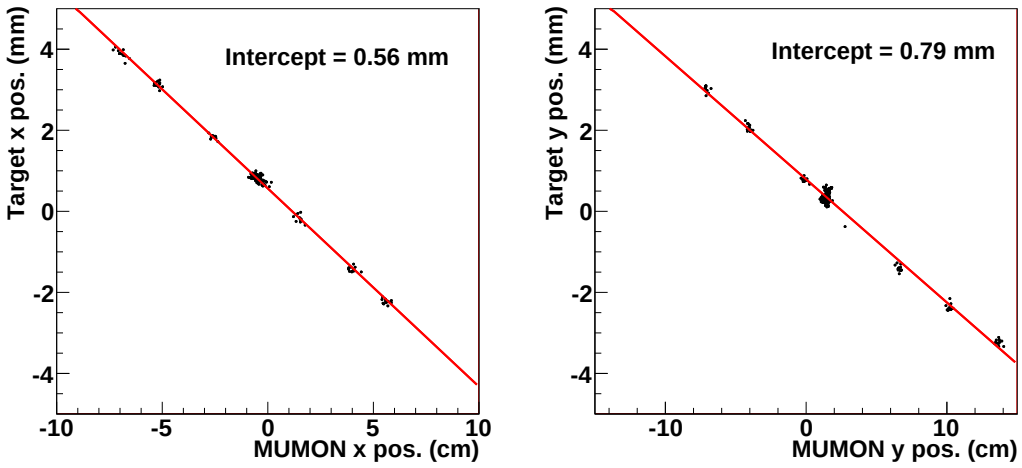

(a) Beam scans in x direction **(b)** Beam scans in y direction

Figure 5.24: Correlation of the MUMON position measurements with the proton beam position at the target. The OTR data was taken with the aluminum foil.

proton beam position measurements agree within alignment uncertainties. The anti-correlation between the beam position and MUMON measurements is due to the horn focusing.

Fig. 5.25 shows the examples of the beam optics fits in x and y. The beam width and divergence at any point in the final focusing section (red curve) are obtained from the OTR and upstream SSEMs measurements. The fit, discussed in more detail in Appendix C, uses Twiss parametrization. Propagation of the beam through the drift space and focusing elements is done with the standard techniques used in the analysis of the accelerator beamline optics. Some inconsistency is observed between OTR measurements (particularly in x) and the fit results. The

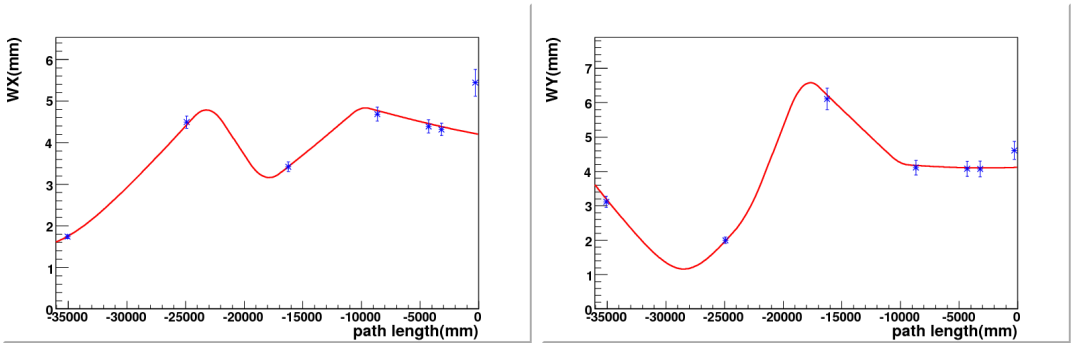

(a) Beam optics fit in x **(b)** Beam optics fit in y

Figure 5.25: Beam optics fit (red curve) to the width measurements by the SSEM and OTR monitors (near $s = 0$ mm).

origin for this discrepancy is currently unexplained. At such beam widths, however, the discrepancy does not lead to any significant effect on the neutrino flux.

The OTR monitor along with the upstream proton monitors not only provide confirmation of the proton beam stability, but also are part of the T2K physics analysis. The proton monitor measurements (Table 4.5 and Table 4.6) form the necessary input for modeling the proton beam distribution in the simulation of the neutrino beamline that provides the predicted neutrino flux.

6 Prediction of the Neutrino Flux

6.1 Introduction

The essential ingredients to measure the oscillation parameters are:

- neutrino flux Φ
- neutrino interaction cross-sections σ
- detector efficiency ϵ.

The number of neutrinos expected to be detected for a given energy (spectrum) is given by these three quantities, and the oscillation probability $P_{\nu_\mu \to \nu_x}$ determined by the set of the oscillation parameters to be measured:

$$N_{\nu_x}^{\mathrm{exp}}(E_{\mathrm{rec}}) = \epsilon(E_{\mathrm{rec}}, E)\sigma(E)P_{\nu_\mu \to \nu_x}(E; \theta, \Delta m^2)\Phi_{\nu_\mu}(E), \tag{6.1}$$

where E and E_{rec} are the true and reconstructed neutrino energy, respectively.

Once a measurement is performed, the observed event distribution $N^{\text{obs}}(E)$ is compared to $N^{\text{exp}}(E)$ to extract the oscillation parameters that best match the observations. Uncertainties associated with the predicted flux and neutrino interaction cross-sections, however, tend to be large. The former is due to the difficulty in precise modeling of the hadronic interactions responsible for generating mesons (hadron production) that produce the neutrino beam. The latter is due to the combination of the scarcity of available cross-section measurements and the large experimental errors associated with them. These factors constrain the precision with which the oscillation parameters can be measured and prevent looking for small signals such as the one expected for $\nu_\mu \to \nu_e$ oscillations.

To achieve better precision and higher sensitivity to the minute oscillation effects, it is necessary to measure the hadron production in a dedicated experiment. In addition, two neutrino detectors are needed: one positioned near the neutrino production site (near detector or ND) and the other located where the oscillation probability is maximal (far detector or FD). The near detector measures the neutrino flux at the source prior to any oscillation effects and establishes the baseline for the far-detector observations. It could also measure the interaction cross-sections with the same neutrino beam to constrain the cross-section uncertainties.

Due to its proximity to the neutrino production source, the neutrino spectrum observed at the near detector is not identical to the one in the far detector. For

the near detector, the neutrinos are produced by a line source (decay vertices are spread out over the decay volume). The far detector, on the other hand, sees a point source of neutrinos. Using the ND measurement to obtain the expectation at the far detector therefore requires extrapolating it to the FD location. The simplest way such an extrapolation from the near to the far (N/F extrapolation) detector can be done is by using the near detector observations $\Phi_{\nu_\mu}^{\mathrm{ND,obs}}(E)$ as a normalization correction to the predicted values for the FD.

The expected number of events at the far detector can then be written as

$$N_{\nu_x}^{\mathrm{FD,exp}}(E_{\mathrm{rec}}) = \epsilon(E_{\mathrm{rec}}, E)\sigma(E)P_{\nu_\mu\to\nu_x}(E;\theta,\Delta m^2)R_{\mathrm{F/N}}(E)\Phi_{\nu_\mu}^{\mathrm{ND,obs}}(E), \qquad (6.2)$$

where $R_{\mathrm{F/N}}(E)$ is the ratio of the predicted flux at the far detector to the one at the near detector:

$$R_{\mathrm{F/N}}(E) = \frac{\Phi_{\nu_\mu}^{\mathrm{FD}}(E)}{\Phi_{\nu_\mu}^{\mathrm{ND}}(E)}. \qquad (6.3)$$

Most of the remaining work will focus on the evaluation of the flux predictions for the T2K experiment and the estimation of the associated systematic uncertainties. The flowchart illustrating the steps involved in obtaining the neutrino flux predictions in T2K is shown in Fig. 6.1.

The Monte Carlo simulation of the neutrino beamline (JNUBEAM) will be described in the next section. After this, an overview of the hadron production

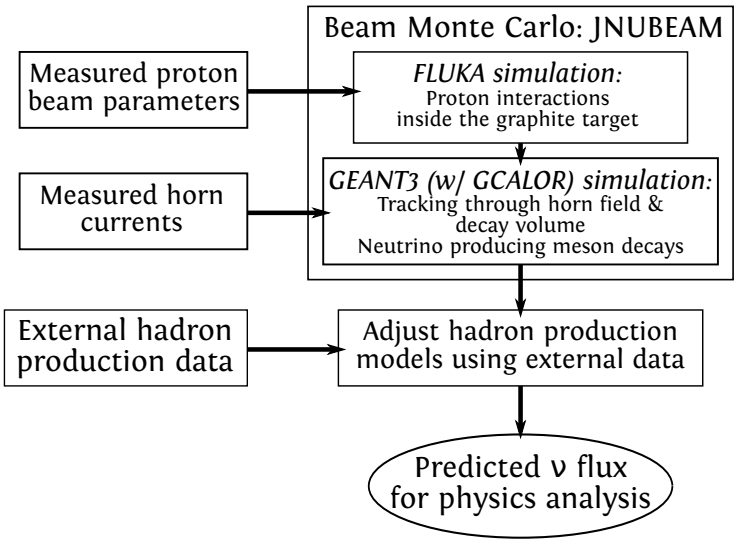

Figure 6.1: Neutrino flux prediction flowchart.

relevant to the T2K experiment will be given and the experimental measurements will be described. In addition, some of the necessary tools needed for the subsequent analysis will be presented. In the following chapter (Chap. 7), the use of available hadron production data to derive neutrino flux predictions will be discussed and the resultant neutrino fluxes for ND280 and SK will be shown. The systematic uncertainties associated with the predictions will be addressed in Chap. 8.

6.2 Neutrino Beam Monte Carlo

The JNUBEAM simulation is based on the FLUKA [78–80] (2008.3b) and GEANT3 [81] particle transport tools. Interactions of the proton beam with the baffle and the graphite core of the target are simulated with FLUKA. The produced particles

are then exported to the GEANT3-based simulation that models the entire T2K secondary beamline and handles the generation of neutrinos.

6.2.1 FLUKA simulation

The geometry layout in the FLUKA simulation is illustrated in Fig. 6.2, where a yz cross-section of the geometry through the $x = 0$ plane is shown. The graphite baffle and the target core are the only beamline components present in the simulation. The baffle is modeled as a rectangular graphite block of dimensions $290 \times 400 \times 1711.45$ mm^3 with a cylindrical hole 30 mm in diameter through the centre. The target core is a simple graphite cylinder 26 mm in diameter and 900 mm long. The distance between the target and the downstream end of the baffle is 526.68 mm. The baffle hole and the volume between the target and the baffle are filled with helium gas.

6.2.2 Treatment of proton beam parameters

The beam protons with 30 GeV kinetic energy are generated upstream of the baffle. The simulation relies on the beam parameters to model the spatial and angular profile distribution of the beam. These parameters are

- position $(\bar{x}, \bar{y})$

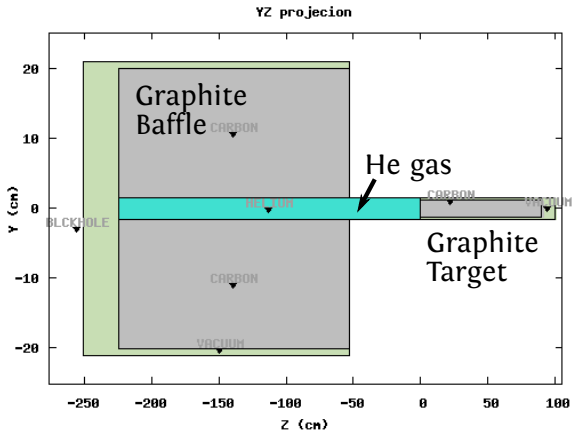

Figure 6.2: The yz cross-sectional view of the geometrical set-up in the FLUKA simulation.

- angle $(\bar{x}', \bar{y}')$
- width (σ_x, σ_y)
- emittance (ϵ_x, ϵ_y)
- divergence parameter (α_x, α_y).

For each coordinate (x or y), the starting position and angle of a given proton is generated randomly according to

$$B(x,x') = \frac{1}{2\pi\sigma_x\sigma_{x'}\sqrt{1-\rho_{xx'}^2}} \times \exp\left(-\frac{1}{2(1-\rho_{xx'}^2)}\left[\frac{(x-\bar{x})^2}{\sigma_x^2} + \frac{(x'-\bar{x}')^2}{\sigma_{x'}^2} - \frac{2\rho_{xx'}(x-\bar{x})(x'-\bar{x}')}{\sigma_x\sigma_{x'}}\right]\right), \tag{6.4}$$

where

- $\sigma_{x'} = \epsilon_x\sqrt{1+\alpha_x^2}/4\sigma_x$
- $\rho_{xx'} = -\alpha_x/\sqrt{1+\alpha_x^2}$.

The technical details of the procedure to sample the distribution in Eq. 6.4 are discussed in Appendix C.3.

6.3 Particle transport and neutrino production

The particles exiting the baffle and the target regions in the FLUKA simulation are transported through the horns, decay volume, and the beam dump by a GEANT3-based simulation. The simulation uses GCALOR [82] to model hadron interactions with the beamline material. The particles are transported until their energy is below the tracking threshold. For hadrons and muons, 0.1 GeV is used for the threshold, while for electrons and photons, it is set to 1.0 GeV.

	π^+	K^+	K^0_L	μ^+/μ^-
ν_μ	$\nu_\mu\mu^+$ (99.9877%)	$\nu_\mu\mu^+$ (63.55%) $\nu_\mu\mu^+\pi^0$ (3.353%)	$\nu_\mu\pi^\pm\mu^\mp$ (27.04%)	$\nu_\mu\nu_e e^-$ ($\simeq 100\%$)
ν_e	$\nu_e e^+$ (1.23×10^{-4})	$\nu_e e^+\pi^0$ (5.07%)	$\nu_e\pi^\pm e^\mp$ (40.55%)	$\bar{\nu}_\mu\nu_e e^+$ ($\simeq 100\%$)

Table 6.1: Particle decay modes with neutrinos as a product implemented in JNUBEAM. The decay branching ratios are shown in brackets. The decay modes for π^- and K^- are the charge conjugates of those for π^+ and K^+.

Table 6.1 lists the neutrino producing decay modes for the various particles that are implemented in JNUBEAM. When one of these decays occurs the energy of the neutrino is calculated according to the appropriate decay kinematics. The contribution of each produced neutrino to the flux is determined by the factor N:

$$N = N_{\mathrm{POT}} \times \Gamma \times P, \tag{6.5}$$

where N_{POT} is an overall normalization given by the number of protons on target, Γ is the appropriate decay branching fraction, and P is the probability of the neutrino to be emitted in a direction of a given detector (INGRID, ND280, or SK). The latter is determined from the distance from the decay vertex to the detector, the direction of the neutrino parent, and the detector solid angle acceptance.

6.3.1 Particle interaction history

During the particle transport, JNUBEAM keeps track of the interactions that lead to the production of any given particle. For every interaction other than elastic scattering, the material, vertex, and momenta and identities of the outgoing particles are recorded. When a neutrino producing decay occurs, the interaction history that led to the production of the neutrino parents is reconstructed from this record and stored along with the neutrino information. The data of the primary proton that initiated the event are stored at the beginning of the interaction history record.

The information available from the interaction history enables a study of the contributions from various hadronic interactions that lead to neutrino production and to tune the MC models based on available hadron production data.

6.4 Hadron production

Using the interaction history it is possible to study which particle productions are important for the neutrino flux predictions at T2K. Table 6.2 lists the fractional contributions of the particles produced in the interactions of the beam proton (secondaries) to the SK neutrino flux without oscillation effects.

Since the T2K target is over 90 cm long, the secondary particles may undergo additional interactions before they escape. Particle interactions are also possible

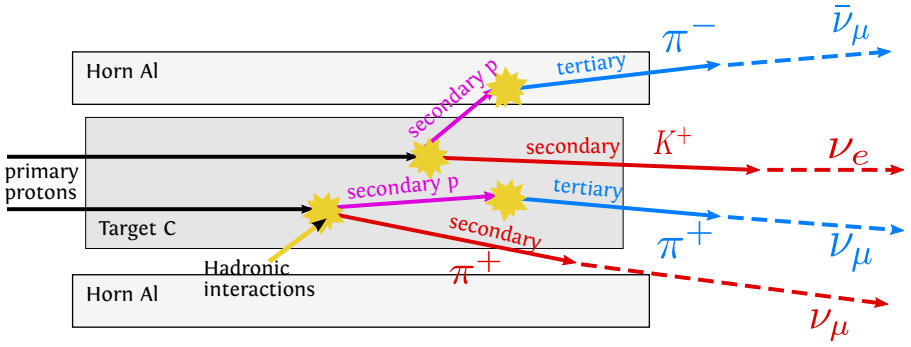

Figure 6.3: Illustration of particle production chains.

Secondary particle	ν_μ	$\bar{\nu}_\mu$	ν_e	$\bar{\nu}_e$
π^+	67.41%	11.72%	38.78%	3.41%
π^-	1.98%	36.55%	1.73%	3.97%
K^+	4.90%	2.19%	26.96%	2.96%
K^-	0.14%	4.99%	0.36%	12.99%
K^0, $\bar{K}^0$	2.83%	4.43%	11.87%	55.86%
Proton	15.80%	21.34%	13.62%	13.00%
Neutron	5.22%	13.54%	5.17%	5.39%
Others (Λ, Σ, $\bar{n}$, *etc.*)	1.73%	5.24%	1.51%	2.42%

Table 6.2: Fractional contributions of secondary particles to the un-oscillated neutrino flux at SK.

with the material (predominantly aluminum) found outside of the target. These concepts are illustrated in Fig. 6.3. Not all of the particles listed in Table 6.2 therefore contribute to the neutrino flux directly (*i.e.*, decay to produce neutrinos). In particular, the sizable contribution of the secondary protons comes from the tertiary particles they produce such as pions, kaons, *etc.* that can decay into neutrinos. The breakdown of the tertiary particle contributions to the SK neutrino flux is listed in Table 6.3.

Tertiary particle	ν_μ	$\bar{\nu}_\mu$	ν_e	$\bar{\nu}_e$
π^+	12.30%	2.06%	6.61%	0.41%
π^-	0.19%	11.50%	0.19%	0.86%
K^+	0.59%	0.26%	3.42%	0.40%
K^-	0.01%	0.66%	0.02%	1.63%
K^0, $\bar{K}^0$	0.29%	0.54%	1.42%	7.46%
Proton	1.69%	3.35%	1.41%	1.39%
Neutron	0.52%	2.09%	0.40%	0.45%
Others (Λ, Σ, $\bar{n}$, etc.)	0.21%	0.89%	0.14%	0.40%
Total	15.80%	21.34%	13.62%	13.00%

Table 6.3: Fractional contributions of tertiary particles produced by secondary protons to the un-oscillated neutrino flux at SK.

As Table 6.2 illustrates the pion contribution is dominant. Understanding pion production is therefore an essential first step for predicting the neutrino flux.

A rather important background in the search of electron neutrino appearance is the intrinsic component of ν_e present in the beam. Since a sizable contribution to the ν_e flux comes from kaons, their production also needs to be studied to properly assess the magnitude of the ν_e contamination.

6.5 NA61/SHINE

One of the main goals of the NA61/SHINE (SPS Heavy Ion and Neutrino Experiment) [83] is to measure the particle yields for the T2K experiment. The experiment uses a 30 GeV secondary proton beam produced by 400 GeV protons slow-extracted (protons are extracted over a few accelerator cycles) from the SPS accelerator at

CERN to measure particle yields from graphite targets. Two types of target are used:

- a 2 cm thin target to study the particle production from the 30 GeV protons without the secondary interaction effects
- a replica of the T2K target (long target) to measure the total particle yields for T2K.

The experiment began collecting data in 2007. The currently available measurements of $\pi^{\pm}$ [83] and K^{+} [84] production from the thin target obtained in the analysis of the 2007 data are used in this work.

6.6 Hadron production data relevant for T2K

Fig. 6.4a shows the angle θ vs momentum p of the secondary pions which contribute neutrinos at SK with the coverage of the NA61 superimposed. Most of the relevant phase-space is covered by the NA61 data.

The $p - \theta$ distribution of the secondary K^{+} mesons that result in a neutrino at SK is shown in Fig. 6.4b. The NA61 K^{+} data covers approximately 60% of the phase-space. Using the K^{+} production data of [85] and [86], the data coverage of the kaon production phase-space can be extended to over 90%.

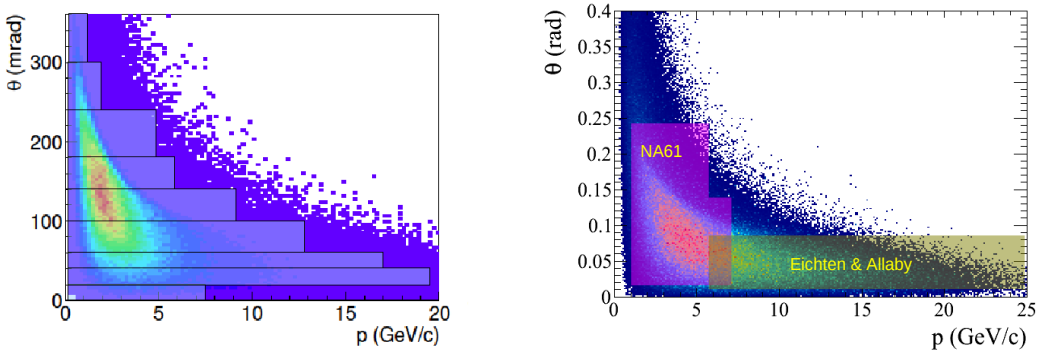

(a) Phase-space of secondary π^+ **(b)** Phase-space of secondary K^+

Figure 6.4: Phase-space of the secondary π^+ and K^+ mesons that produce neutrino at the SK detector. The colour of each point indicates how large the contribution to the neutrino flux is from that part of the phase-space. The coverage of the NA61 measurements and those of Eichten *et al.* [85] and Allaby *et al.* [86] are also shown.

Other available experimental data can also be used to study the systematic uncertainties associated with the hadron production.

The hadron production measurements relevant for T2K are summarized in Table 6.4, where the beam energy, target material, and the particles measured in each experiment are listed.

Experiment	Beam (GeV/c)	Target	Particles
NA61 [83] [84]	31 GeV/c	C	$\pi^{\pm}$, K^+
Eichten *et al.* [85]	24 GeV/c	Be, Al, and others	p, $\pi^{\pm}$, $K^{\pm}$
Allaby *et al.* [86]	19.2 GeV/c	Be, Al, and others	p, $\pi^{\pm}$, $K^{\pm}$
E910 [87]	6.4, 12.3, and 17.5 GeV/c	Be	$\pi^{\pm}$

Table 6.4: Hadron production data relevant for the T2K neutrino flux predictions.

As Table 6.4 illustrates, the beam energy and the target material used by the

different experiments may be different from T2K. Methods to scale the data from one beam energy to another (momentum scaling) and from different materials (material scaling) are therefore needed.

Momentum scaling is also necessary to study the production of tertiary pions. As Tables 6.2 and 6.3 show, these pions have a sizable contribution to the neutrino flux. The tertiary pion production can be evaluated from the NA61 data, but it is necessary to scale these data to lower beam energies.

6.7 Momentum scaling

The idea of momentum scaling was proposed by Feynman while analyzing data from inelastic particle collisions [88]. He noted that in the inclusive reactions of the type

$$a + b \to c + X,$$

where a and b are two colliding particles and c is the produced particle accompanied by unspecified products X, the (Lorentz) invariant cross-section $Ed\sigma_c/d\vec{p}$ is independent of the total available centre of mass energy $\sqrt{s}$ (set by the momentum of the interacting particles) if described using a suitable set of parameters. He suggested that such parameters would be the transverse momentum p_T and a variable

x_F, now referred to as the Feynman scaling variable, defined as

$$x_F = \frac{p_L^*}{p_{\mathrm{Max}}^*}, \tag{6.6}$$

where p_L^* is the longitudinal momentum of a produced particle and p_{Max}^* is the maximum available momentum, both in the centre of mass frame of the $a + b$ system.

A slightly different choice for a scaling variable was suggested by Taylor *et al.* [89]. They proposed analyzing the scaling behaviour of the invariant cross-sections in terms of the ratio of the energy of the particle E^* and the maximum energy kinematically available E_{Max}^*

$$x_R = \frac{E^*}{E_{\mathrm{Max}}^*}. \tag{6.7}$$

The variable x_R is called the radial scaling variable.

The idea of the cross-section scaling can be applied to the hadron production data, since it provides a way of taking the invariant differential cross-section in $p-\theta$ phase-space at one beam momentum p_0 and mapping it to $p' - \theta'$ phase-space at a different beam momentum p_0'.

The first step is to find the x_F (x_R) and p_T for a given particle produced with a momentum p and angle θ relative to the direction of an interacting proton. The

square of the total centre of mass energy available when a proton interacts with a stationary nucleon of the target matter is

$$s = (E_0 + m_p)^2 - p_0^2, \tag{6.8}$$

where m_p is the mass of the proton and E_0 is the energy of the beam. The difference of about 1 MeV between the neutron and proton mass is ignored here. This gives

$$s = 2m_p(E_0 + m_p). \tag{6.9}$$

The relativistic $\beta_{\rm cm}$ and $\gamma_{\rm cm}$ of the centre of mass (CM) frame relative to the laboratory frame of reference are

$$\beta_{\rm cm} = \frac{p_0}{E_0 + m_p}, \tag{6.10}$$

$$\gamma_{\rm cm} = \frac{E_0 + m_p}{\sqrt{s}}. \tag{6.11}$$

Given E, p, and θ of a produced particle in the lab frame, the transverse and longitudinal momentum of this particle in the CM frame are

$$p_T^* = p_T = p\cos\theta, \tag{6.12}$$

$$p_L^* = \gamma_{\rm cm}(p_L - \beta_{\rm cm}E), \tag{6.13}$$

while its energy in the CM frame is

$$E^* = \gamma_{\rm cm}(E - \beta_{\rm cm}p_L). \tag{6.14}$$

To calculate the particle x_F (x_R), it is necessary to find $p^*_{\rm Max}$ ($E^*_{\rm Max}$). It can be shown (see Appendix D) that

$$p^*_{\rm Max} = \sqrt{\frac{(s - m^2 - M^2_{\rm Min})^2 - 4m^2M^2_{\rm Min}}{4s}}, \tag{6.15}$$

where m is the mass of the produced particle and $M_{\rm Min}$ is the minimum possible value of the total mass of the other products. The exclusive reaction that gives $M_{\rm Min}$ can be determined from various conservation laws. The values of $M_{\rm Min}$ with the corresponding exclusive channels are listed in Table 6.5 for various types of inclusive reactions.

Since the interaction of the beam protons with the target can involve either $p+p$ or $p+n$ reactions, the average of the $M_{\rm Min}$ is taken when evaluating Eq. 6.15. Once $p^*_{\rm Max}$ is computed, the $E^*_{\rm Max}$ can be easily evaluated using the relativistic energy momentum relation: $E = \sqrt{m^2 + p^2}$.

It should be noted that in the limit $s \gg m^2$ and $s \gg m^2_{\rm Max}$ Eq. 6.15 simplifies

Inclusive reaction	Exclusive reaction	M_{Min} (GeV)
$p+p \to \pi^+ + X$	$p+p \to \pi^+ + (p+n)$	1.878
$p+p \to \pi^- + X$	$p+p \to \pi^- + (p+p+\pi^+)$	2.017
$p+p \to K^+ + X$	$p+p \to K^+ + (p+\Lambda)$	2.054
$p+p \to K^- + X$	$p+p \to K^- + (2p+K^+)$	2.370
$p+p \to K^0 + X$	$p+p \to K^0 + (p+\Sigma^+)$	2.128
$p+p \to \bar{K}^0 + X$	$p+p \to \bar{K}^0 + (2p+K^0)$	2.374
$p+p \to p + X$	$p+p \to p+p$	0.938
$p+p \to n + X$	$p+p \to n + (p+\pi^+)$	1.078
$p+n \to \pi^+ + X$	$p+n \to \pi^+ + 2n$	1.879
$p+n \to \pi^- + X$	$p+n \to \pi^- + 2p$	1.877
$p+n \to K^+ + X$	$p+n \to K^+ + (n+\Lambda)$	2.055
$p+n \to K^- + X$	$p+n \to K^- + (p+n+K^+)$	2.372
$p+n \to K^0 + X$	$p+n \to K^0 + (n+\Sigma^+)$	2.129
$p+n \to \bar{K}^0 + X$	$p+n \to \bar{K}^0 + (p+n+K^0)$	2.376
$p+n \to p + X$	$p+n \to p+n$	0.939
$p+n \to n + X$	$p+n \to n+p$	0.938

Table 6.5: The values of M_{Min} with the corresponding exclusive channel for a given inclusive reaction.

to

$$p^*_{\mathrm{Max}} \approx \frac{\sqrt{s}}{2} \tag{6.16}$$

and x_F reduces to a more familiar form

$$x_F = \frac{2p^*_L}{\sqrt{s}}. \tag{6.17}$$

After evaluating x_F and p_T, the "scaled" p' and θ' can be computed. From the definition of x_F in Eq. 6.6 and the relativistic transformation of p_L in Eq. 6.13, it

follows that

$$x_F = \frac{1}{p'^{*}_{\mathrm{Max}}}\gamma'_{\mathrm{cm}}(p'_L - \beta'_{\mathrm{cm}}\sqrt{p'^2_L + p^2_T + m^2}), \tag{6.18}$$

where the primes indicate that a given quantity is calculated for the beam momentum p'_0. Introducing the following parameters:

$$A = 1 - \beta'^2_{\mathrm{cm}},$$

$$B = -\frac{x_F p'^{*}_{\mathrm{Max}}}{\gamma'_{\mathrm{cm}}},$$

$$C = \left(\frac{x_F p'^{*}_{\mathrm{Max}}}{\gamma'_{\mathrm{cm}}}\right)^2 - \beta'^2_{\mathrm{cm}}(p^2_T + m^2),$$

the general solutions of Eq. 6.18 for p'_L can be written as

$$p'_L = \frac{-B \pm \sqrt{B^2 - AC}}{A}.$$

Since $0 < A < 1$, the more positive solution (the one giving the larger p'_L) is taken:

$$p'_L = \frac{-B + \sqrt{B^2 - AC}}{A}. \tag{6.19}$$

Once p'_L is found, it is trivial to compute p' and θ':

$$p' = \sqrt{p'^2_L + p^2_T}, \tag{6.20}$$

$$\theta' = \arcsin \frac{p_T}{p'}. \tag{6.21}$$

When the x_R scaling variable is used the calculation is similar, except that p'_L is found by solving the equation

$$x_R = \frac{1}{E'^*_{\rm Max}} \gamma'_{\rm cm} (\sqrt{p'^2_L + p^2_T + m^2} - \beta'_{\rm cm} p'_L). \tag{6.22}$$

Defining

$$A = \beta'^2_{\rm cm} - 1,$$

$$B = \frac{x_R E'^*_{\rm Max}}{\gamma'_{\rm cm}} \beta'_{\rm cm},$$

$$C = \left(\frac{x_R E'^*_{\rm Max}}{\gamma'_{\rm cm}} \right)^2 - (p^2_T + m^2),$$

the positive solution for p'_L $(-1 < A < 0)$ is expressed as

$$p'_L = \frac{-B - \sqrt{B^2 - AC}}{A}. \tag{6.23}$$

Once again p' and θ' are computed from Eq. 6.20 and Eq. 6.21 once p'_L is found.

6.8 Material scaling

To scale data from one material to another the approach described by Bonesini *et al.* in [90] is adopted. The invariant cross-section for particle production in a material with the atomic weight A_1 is related to the invariant cross-section in a different material with the atomic weight A_2 according to

$$E\frac{d^3\sigma^{A_2}}{dp^3} = \left(\frac{A_2}{A_1}\right)^{\alpha(x_F,p_T)} E\frac{d^3\sigma^{A_1}}{dp^3}. \tag{6.24}$$

The exponent α depends on the Feynman scaling variable x_F and the transverse momentum p_T. Based on the works by Barton *et al.* [91] and Skubic *et al.* [92], the form for this dependence suggested by Bonesini *et al.* is

$$\alpha(x_F, p_T) = (a + bx_f + cx_F^2)(d + ep_T^2). \tag{6.25}$$

The values of the parameters a – e given by Bonesini *et al.* are for all the particles. Using these values to test the material scaling on the Allaby *et al.* and Eichten *et al.* kaon data do not, however, give satisfactory results. Since both of the experiments have measurements of pion as well as kaon production from Be, Al, and Cu targets, it is possible to fine-tune the values by analyzing the pion and kaon data sets separately.

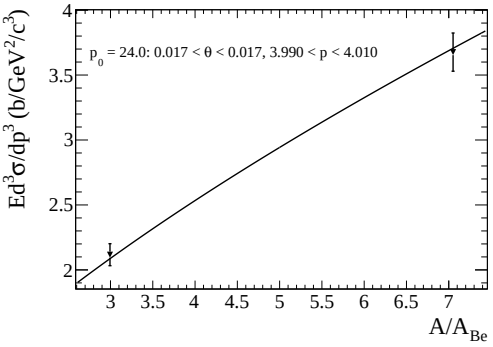

(a) Fit to Eichten π^+ 4 GeV/c and 0.017 rad bin

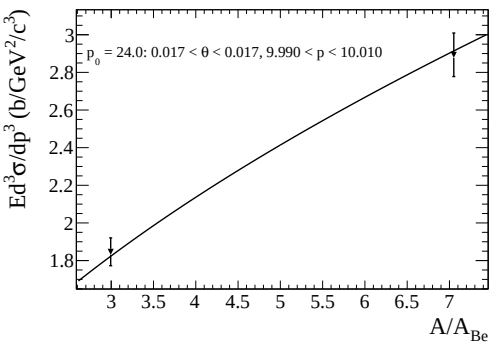

(b) Fit to Eichten π^+ 10 GeV/c and 0.017 rad bin

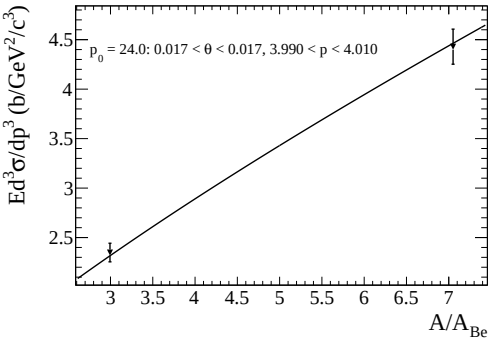

(c) Fit to Eichten K^+ 4 GeV/c and 0.017 rad bin

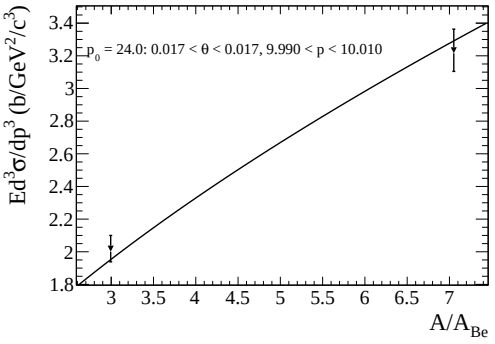

(d) Fit to Eichten K^+ 10 GeV/c and 0.017 rad bin

Figure 6.5: Examples of the material scaling exponent α fit for two (4 and 10 GeV/c) momentum bins at 0.017 rad for the [85] π^+ and K^+ data.

The analysis consists of two steps. First the values of α are determined for each $p-\theta$ bin in the data. Then they are fitted to the polynomial model of Eq. 6.25 to obtain the parameters a – e.

To cancel the correlated error component the Al and Cu measurements are normalized by the Be data. This significantly reduces the overall error and considerably simplifies the treatment of measurement uncertainties. Each $p-\theta$ data bin is fitted

with

$$f(A) = \left(\frac{A}{A_{\mathrm{Be}}}\right)^{\alpha}, \tag{6.26}$$

where $A = A_{\mathrm{Al}}, A_{\mathrm{Cu}}$ and α is the fit parameter. Fig 6.5 shows as an example four such fits to two bins from the [85] π^+ and K^+ data.

	a	b	c	d	e
nominal	0.74	-0.55	0.26	0.98	0.21
fitted π	0.75	-0.52	0.23	1.0 (fixed)	0.21
fitted K	0.77	-0.32	0.0	1.0 (fixed)	0.25

Table 6.6: Parameters for material scaling

After fitting all of the data bins in this manner a table of values of α for each value of $p - \theta$ is obtained. These results are fitted with Eq. 6.25 to extract model parameters. The values of the parameters given by Bonesini *et al.* (nominal) and those obtained from separate analysis of the charged pion and kaon data are listed in Table 6.6. The parameter d has been fixed in the fit to 1.0 to avoid strong correlations with the a term.

The uncertainty associated with the material scaling is estimated by comparing the predicted values from scaling the Eichten and Allaby Be data, $\sigma_{\mathrm{Be}\to\mathrm{Al}}$, to the corresponding measurements from the two experiments taken with the Al target, σ_{Al}. The histograms of the ratios

$$R_{\mathrm{Al/Scaled\ Be}} = \sigma_{\mathrm{Al}}/\sigma_{\mathrm{Be}\to\mathrm{Al}} \tag{6.27}$$

of all of the $p - \theta$ bins are shown in Fig. 6.6 and Fig. 6.7 for pion and kaon data, respectively.

To find the mean and obtain some measure of the spread, the distributions shown in the figures are fitted (χ^2 minimization) with the Gaussian function

$$G = Ae^{-(R_{\text{Al/Scaled Be}}-\mu)^2/2\sigma^2} \tag{6.28}$$

with the normalization A, mean μ, and width σ being the fit parameters. The results of these fits for the mean and width are listed in Table 6.7 and Table 6.8 for pion and kaon data, respectively.

	Allaby π^+	Allaby π^-	Eichten π^+	Eichten π^-
μ	1.00	0.99	0.99	0.99
$\sigma(\%)$	2.7	4.0	2.0	2.5

Table 6.7: Results of the fit to the distribution of $R_{\text{Al/Scaled Be}}$ for the $[85, 86]$ charged pion data.

	Allaby K^+	Allaby K^-	Eichten K^+	Eichten K^-
μ	1.04	0.96	1.02	0.95
$\sigma(\%)$	4.9	5.5	4.6	5.0

Table 6.8: Results of the fit to the distribution of $R_{\text{Al/Scaled Be}}$ for the $[85, 86]$ charged kaon data.

The material scaling works better for pions, while in the case of kaons the distribution of $R_{\text{Al/Scaled Be}}$ is systematically below or above unity by at most 5%. When considering uncertainties due to the material scaling this could be treated

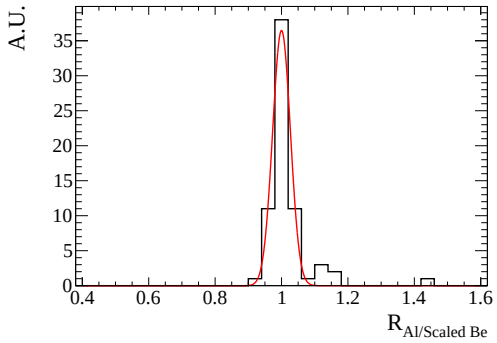

(a) Results for Allaby π^+ data

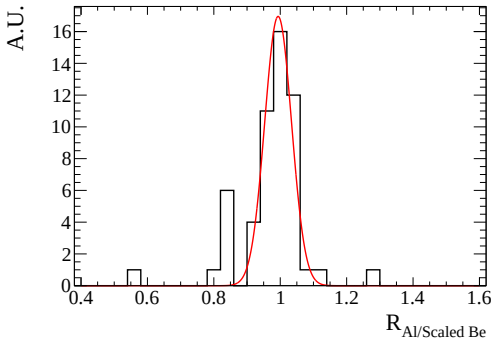

(b) Results for Allaby π^- data

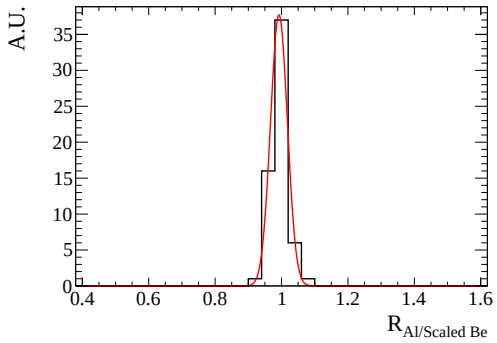

(c) Results for Eichten π^+ data

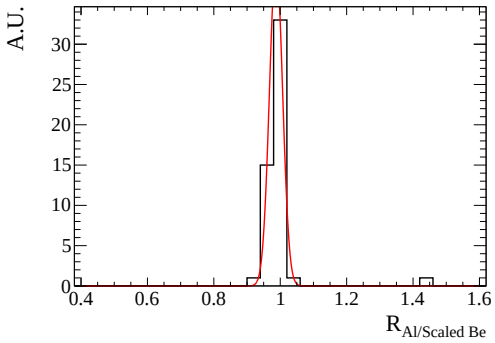

(d) Results for Eichten π^- data

Figure 6.6: Distribution of $R_{\text{Al/Scaled Be}}$ for the $[85, 86]$ charged pion data.

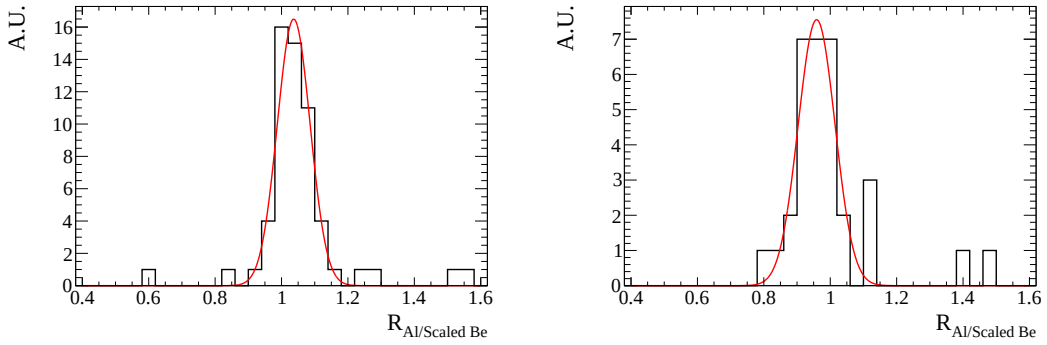

(a) Results for Allaby K^+ data

(b) Results for Allaby K^- data

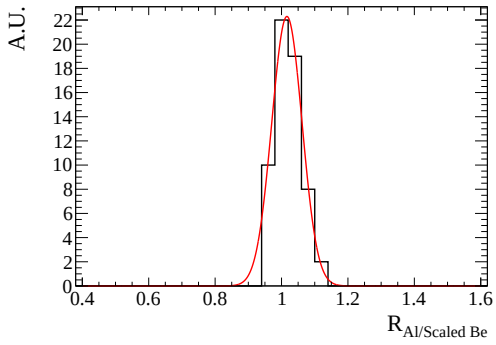

(c) Results for Eichten K^+ data

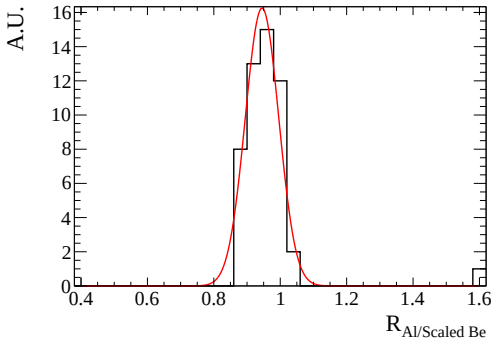

(d) Results for Eichten K^- data

Figure 6.7: Distribution of $R_{\text{Al/Scaled Be}}$ for the $[85, 86]$ charged kaon data.

as a normalization uncertainty, *i.e.*, applied in a correlated way to all the data points. The spread in the distribution of $R_{\text{Al/Scaled Be}}$ values can be applied as an additional uncertainty uncorrelated from data point to data point. Based on the values in Table 6.8 a value of 5% is taken for this type of uncertainty.

7 T2K Neutrino Flux

The T2K neutrino flux predictions rely on the available hadron production data from NA61 and other experiments. These data are incorporated by adjusting or tuning the hadron production models used inside the JNUBEAM simulation. This accounts for the discrepancies between the hadron yields predicted by the models and the ones measured experimentally.

7.1 Hadron production tuning strategy

Hadron production tuning is done be re-weighting the contribution of each neutrino event to the flux based on the comparison of a given model (FLUKA and GCALOR) predictions with the available hadron production data. The term weight here in general refers to a number by which a given simulated process needs to be tuned or adjusted for the output result to match the data. Two types of weights are considered. One is for re-weighting the phase-space distribution of the produced hadrons, which will be called multiplicity tuning and the other for re-weighting the

total interaction rate, which will be referred to as interaction rate tuning.

Before discussing how these weights are obtained, it is necessary to introduce some additional nomenclature. We define production multiplicity as

$$\frac{d^2 n_{\mathrm{h}}}{dpd\Omega} = \frac{1}{\sigma_{\mathrm{prod}}} \frac{d^2 \sigma_{\mathrm{h}}}{dpd\Omega}, \tag{7.1}$$

where σ_{prod} is the total production cross-section and $d^2\sigma_{\mathrm{h}}/dpd\Omega$ is the differential cross-section for the production of hadron h. The production cross-section is obtained from the corresponding inelastic cross-section by subtracting the component for the quasi-elastic scattering, *i.e.*,

$$\sigma_{\mathrm{prod}} = \sigma_{\mathrm{inel}} - \sigma_{\mathrm{qe}}. \tag{7.2}$$

For multiplicity tuning, weights are computed from the ratio of the measured to the predicted differential particle production. Thus for a hadron produced with a momentum p and angle θ (production angle) relative to the direction of the incident particle, as shown in Fig. 7.1a for a charged pion, the weight is determined from

$$w_h(p,\theta) = \frac{d^2 n_{\mathrm{Data}}}{dpd\Omega} \Big/ \frac{d^2 n_{\mathrm{MC}}}{dpd\Omega}. \tag{7.3}$$

For the interaction rate tuning, model (FLUKA, GCALOR) predicted interac-

tion lengths are compared to experimental data. The following definition of the interaction length in terms of the production cross-section is adopted here:

$$\lambda_I = \frac{A}{N_A \rho \sigma_{\text{prod}}}, \tag{7.4}$$

where N_A, A, and ρ are the Avogadro's constant, atomic number, and density of the target material, respectively.

Two different weights are applied depending on whether the particle escapes the material or undergoes interaction. In the case of the escaping particle, the weight is calculated as

$$w_{\text{out}} = e^{-x_{\text{esc}}/(\lambda_I^{\text{Data}} - \lambda_I^{\text{MC}})}, \tag{7.5}$$

where x_{esc} is the distance to the material boundary as shown in Fig. 7.1a. This is just the ratio of the particle survival probabilities in the materials with the interaction lengths λ_I^{Data} and λ_I^{MC}.

For the particle undergoing interaction a weight is calculated according to

$$w_{\text{out}} = \frac{\lambda_I^{\text{MC}}}{\lambda_I^{\text{Data}}} e^{-x_{\text{int}}/(\lambda_I^{\text{Data}} - \lambda_I^{\text{MC}})}, \tag{7.6}$$

where x_{int} refers to the distance a particle has traveled in the material to the interaction vertex, as illustrated in Fig. 7.1a.

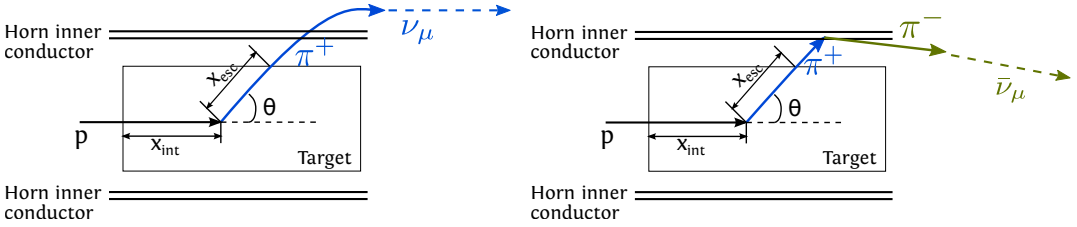

(a) Illustration of an interaction that results in a neutrino

(b) Illustration of out-of-target interaction that results in a neutrino

Figure 7.1: Illustration of interactions.

The total weight for a given neutrino event is calculated as the product of weights for each step in the interaction history. Taking as an example Fig. 7.1a and assuming the pion there decays to a neutrino without any additional scattering, the weight for this neutrino event would in general be the product of Eq. 7.3, Eq. 7.5 and Eq. 7.6.

While the majority of the interactions happen inside the graphite core of the T2K target, a fraction of particles escaping the target can re-interact with surrounding material, which mostly consists of aluminum in the horns. This is illustrated in Fig. 7.1b. For ν_μ and ν_e flux, the estimate of this out-of-target contribution from simulations is about 13%. It is, however, larger for the anti-neutrinos, with approximately 50% of $\bar{\nu}_\mu$ coming from out-of-target interactions. Consequently comparisons of both FLUKA (in-target) and GCALOR (out-of-target) models to the hadron production data are necessary.

7.2 Pion multiplicity tuning

The pion contribution to the neutrino flux is tuned using the NA61 thin target data [83]. To obtain the tuning weights for the pions produced in the proton interaction inside the target, the interactions of the 31 GeV/c protons with a thin carbon target are simulated in FLUKA. The resultant pion yields are binned and normalized in the same manner as the NA61 data to obtain the MC predictions for the pion production multiplicity. A ratio of the simulated and measured multiplicity is then computed to get the weights for different $p-\theta$ bins. Fig. 7.2a and Fig. 7.2b shows the obtained weights for π^+ and π^-, respectively. The NA61 data covers about 92% and 98% of the π^+ and π^- phase-space relevant for the T2K, respectively. For the phase-space not covered by the NA61 data the nominal FLUKA values are used.

For the secondary pions, an appropriate multiplicity weight is determined from the histograms in Fig. 7.2 according to their momentum and angle.

As shown in Table 6.3, there is also a sizable ($\sim$ 12% for ν_μ) contribution to the neutrino flux from the tertiary pions that are produced in the interactions of the secondary protons. To tune the production multiplicity of the tertiary pions, the (p, θ) and the momentum of the secondary proton are used to evaluate the corresponding (p', θ') for 31 GeV/c beam using the x_F scaling variable and following

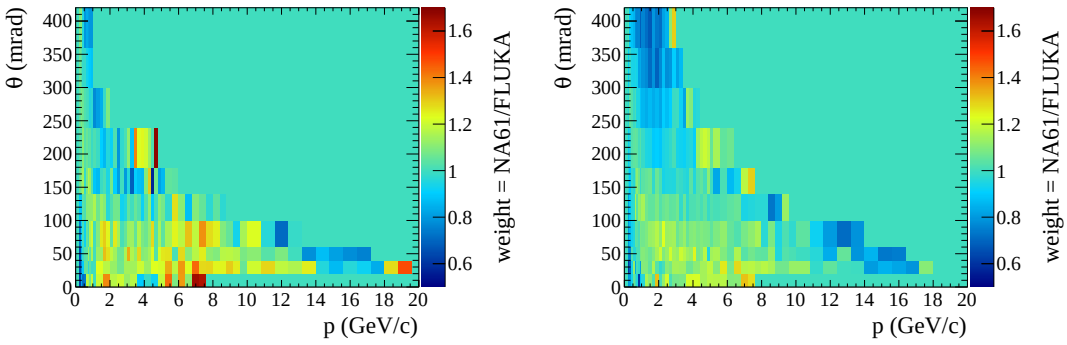

(a) NA61 Data/FLUKA ratio for π^+ **(b)** NA61 Data/FLUKA ratio for π^-

Figure 7.2: NA61 Data/FLUKA ratio for pions.

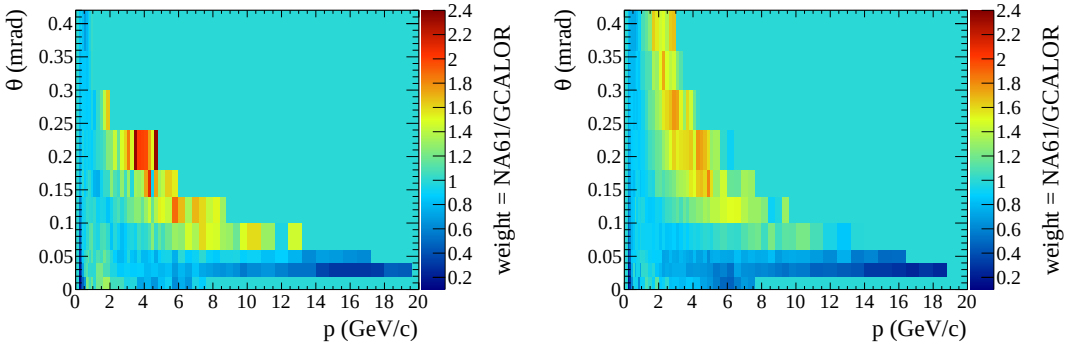

(a) NA61 Data/GCALOR ratio for π^+ **(b)** NA61 Data/GCALOR ratio for π^-

Figure 7.3: Scaled NA61 Data/GCALOR ratio for pions in aluminum.

the procedure described in Section 6.7. An appropriate weight is then determined based on the scaled values of the momentum and angle of the produced pion.

The pion production outside of the target is also tuned. Since a majority of the interactions happen in the aluminum of the horns, the weights are calculated from the ratio of the GCALOR simulated pion multiplicity to the NA61 measurements after they are scaled from C to Al according to the method in Section. 6.8. The

obtained weights are shown in Fig. 7.3a and Fig. 7.3b for π^+ and π^-, respectively.

Finally, the multiplicity of the pions produced in neutron interactions ($\sim 5\%$ contribution) is also tuned. This is done by applying the π^- and π^+ weights to the neutron produced π^+ and π^-, respectively.

7.3 Kaon multiplicity tuning

The kaon production multiplicity in the target is tuned using the data listed in Table 7.1. The tuning is performed for secondary and tertiary kaons produced in the interactions inside the target.

Experiment	Beam (GeV/c)	Target	Particles
Allaby *et al.* [86]	19.2	Be	$K^{\pm}$
Eichten *et al.* [85]	24	Be	$K^{\pm}$
NA61 [84]	31	C	K^+

Table 7.1: Data used in tuning kaon production.

Following the approach of [90], the charged kaon data is also used to estimate the neutral kaon production using a combination of K^+ and K^- data sets:

$$K^0_L = \frac{1}{4}(K^+ + 3K^-). \tag{7.7}$$

The coverage of each data set of the kaon production phase-space relevant for the T2K neutrino flux is summarized in Table 7.2. Figs. 7.4 through 7.6 show the

momentum and the production angle of the secondary kaons contributing to the neutrino flux at SK. The parts of the phase-space covered by the data sets listed in Table 7.1 are shown as well in these figures.

	NA61	Eichten	Allaby	Total
Secondary K^+	60.0%	30.5%	0.9%	91.4%
Secondary K^-	0.0%	40.5%	1.3%	41.8%
Secondary K^0_L	0.0%	35.3%	0.7%	36.0%
All K^+	59.0%	30.8%	1.0%	90.8%
All K^-	0.0%	39.9%	1.2%	41.1%
All K^0_L	0.0%	35.5%	0.7%	36.2%

Table 7.2: Data coverage of the kaons contributing to the neutrino flux at SK

Before comparing the Eichten and Allaby measurements to model predictions, a bi-cubic spline interpolation is performed on these data. Fig. 7.7 illustrates the procedure in the case of the Eichten K^+ data. At first, a set of cubic splines $S_{\theta_i}(p)$ is constructed for each angular bin. One such spline is shown along with the data points in Fig. 7.7b. An interpolated value of the cross-section at any given (p, θ) point (*e.g.*, the one marked by a star in Fig. 7.7a) inside the covered phase-space is then obtained by constructing a cubic spline $S_p(\theta)$ from the values of $S_{\theta_i}(p)$ and evaluating it at an appropriate value of θ.

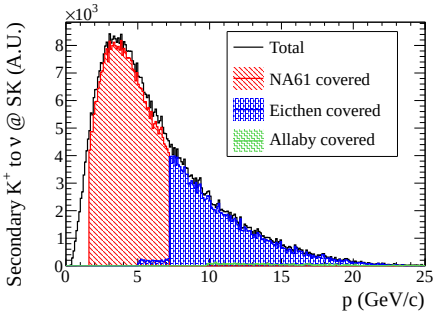

(a) Momenta of secondary K^+

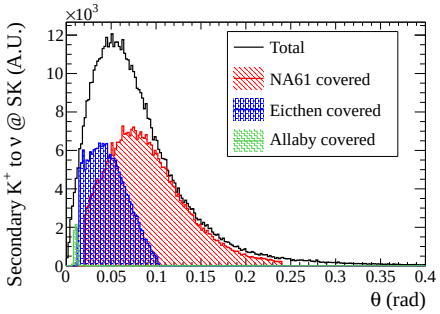

(b) Production angles of secondary K^+

Figure 7.4: Momenta and angles of K^+ contributing to the SK flux.

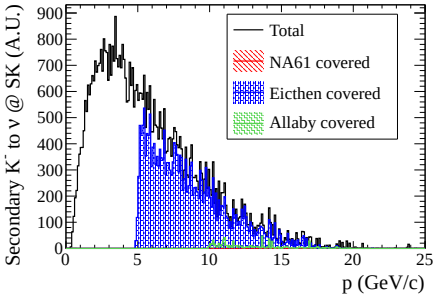

(a) Momenta of secondary K^-

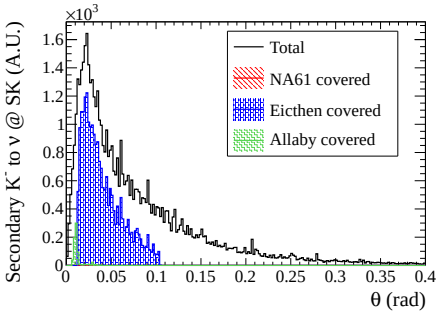

(b) Production angles of secondary K^-

Figure 7.5: Momenta and angles of K^- contributing to SK flux.

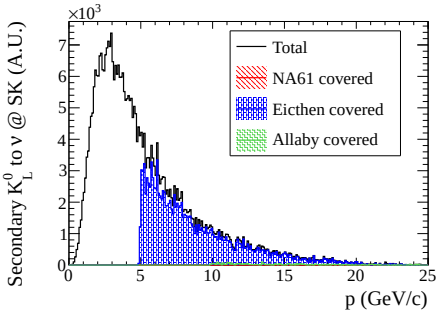

(a) Momenta of secondary K_L^0

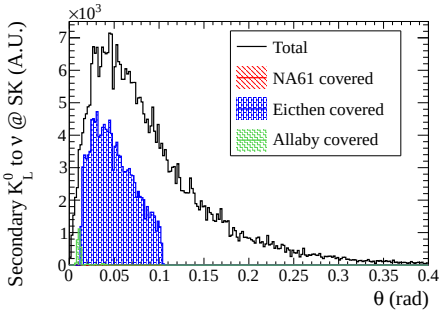

(b) Production angles of secondary K_L^0

Figure 7.6: Momenta and angles of K_L^0 contributing to the SK flux.

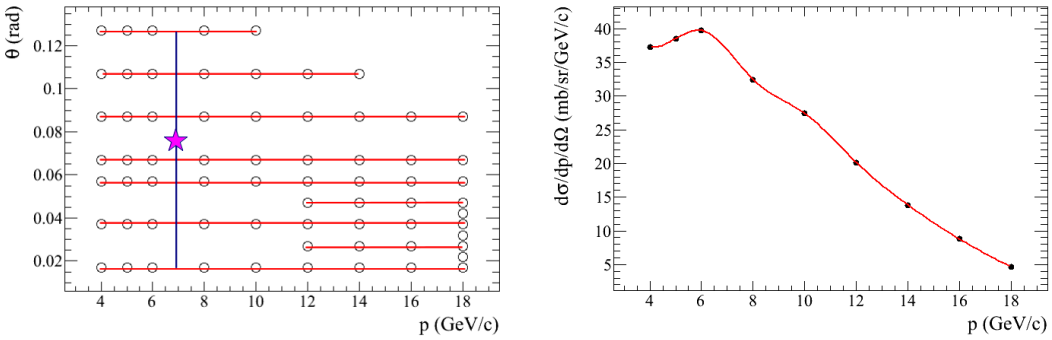

(a) Bi-cubic spline interpolation on a grid of data points

(b) An example of a cubic spline interpolation for the first (0.017 rad) angular bin

Figure 7.7: Illustration of the bi-cubic spline interpolation for a grid of data points.

7.3.1 Kaon tuning procedure

The ratio of the NA61 measurements to the FLUKA predictions (Eq. 7.8)

$$w(p,\theta) = \frac{dn^{\theta}_{\text{NA61}}}{dp} \Big/ \frac{dn^{\theta}_{\text{FLUKA}}}{dp}, \tag{7.8}$$

is used to tune K^+ production multiplicity in the phase-space covered by the NA61 data. Fig. 7.8 shows the obtained ratios for the two angular bins.

The ratio of the measured to predicted double differential cross-sections[2]

$$w(p,\theta) = \frac{d\sigma_{\text{Eichten,Allaby}}}{dpd\Omega} \Big/ \frac{d\sigma_{\text{FLUKA}}}{dpd\Omega} \tag{7.9}$$

[2]The production cross-sections used to normalize the differential cross-section to obtain multiplicities are essentially the same for data and FLUKA for protons on Be and cancel when the ratio is taken.

is used to tune the K^+ production outside of the NA61 phase-space with data sets of Eichten *et al.* and Allaby *et al.* These data are also used to tune the production multiplicity of K^- and K^0_L. The data/FLUKA ratios for the data sets of Eichten *et al.* and Allaby *et al.* are shown in Fig. 7.9 and Fig. 7.10, respectively.

Given the momentum p and angle θ of a secondary kaon, the tuning weight is determined from the prescription shown in Fig. 7.11. To obtain the Eichten (Allaby) data weights, the momentum and angle of the produced kaon has to be scaled from 31 GeV/c to 24 GeV/c (19.2 GeV/c) beam momentum using the x_F scaling procedure described in Section. 6.7. The scaled values of p and θ are denoted by primes in the figure.

The production of the tertiary kaons in the target is also tuned. The weights are linearly interpolated from $w_{\mathrm{NA61}}(p', \theta')$, $w_{\mathrm{Eichten}}(p', \theta')$, and $w_{\mathrm{Allaby}}(p', \theta')$. The primes on p and θ here again indicate that the appropriate beam momentum scaling has been performed. The interpolation is done between a pair of neighboring weights. For example, if the momentum of the secondary proton $p_{\text{sec. prot}}$ is somewhere between $p_{\mathrm{NA61}} = 31$ and $p_{\mathrm{Eichten}} = 24$ GeV/c and both $w_{\mathrm{NA61}}(p', \theta')$ and $w_{\mathrm{Eichten}}(p', \theta')$ weights exist then the interpolated weight is found from

$$w = w_{\mathrm{NA61}} + \frac{w_{\mathrm{Eichten}} - w_{\mathrm{NA61}}}{p_{\mathrm{Eichten}} - p_{\mathrm{NA61}}}(p_{\text{sec prot}} - p_{\mathrm{NA61}}). \tag{7.10}$$

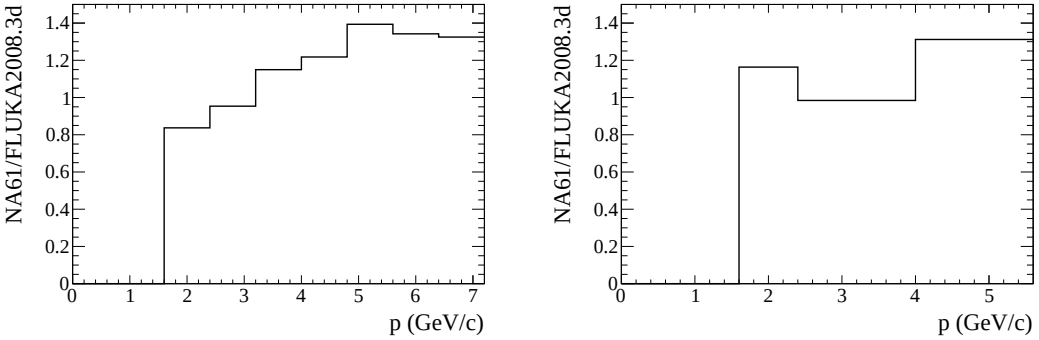

(a) Ratio of the NA61/FLUKA multiplicities for $\theta = 20 - 140$ mrad

(b) Ratio of the NA61/FLUKA multiplicities for $\theta = 140 - 240$ mrad

Figure 7.8: Ratios to the NA61 K^+ multiplicity to the FLUKA predictions.

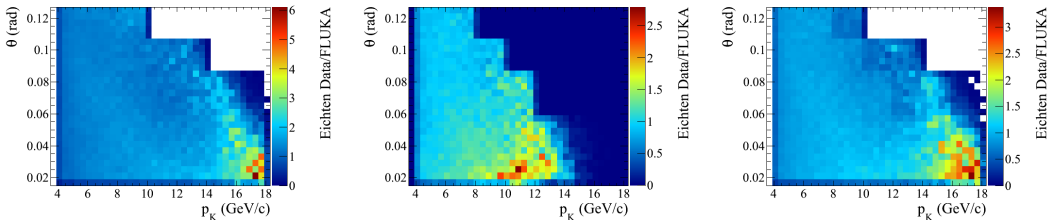

(a) Ratio for K^+ **(b)** Ratio for K^- **(c)** Ratio for K^0_L

Figure 7.9: Ratios of the interpolated kaon production double differential cross-section measurements from Eichten *et al.*, to the FLUKA predictions for 24 GeV/c protons interacting with Be target.

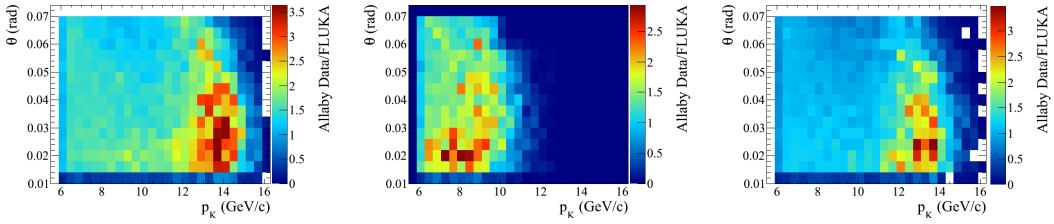

(a) Ratio for K^+ **(b)** Ratio for K^- **(c)** Ratio for K^0_L

Figure 7.10: Ratios of the interpolated kaon production double differential cross-section measurements from Allaby *et al.*, to the FLUKA predictions for 19.2 GeV/c protons interacting with Be target.

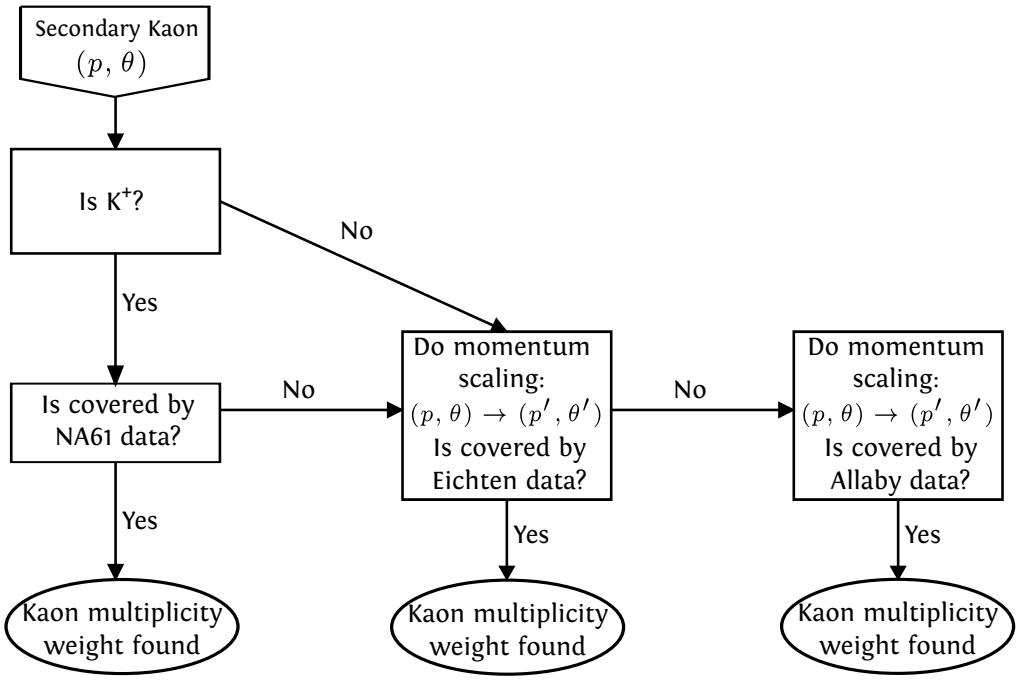

Figure 7.11: Flowchart of secondary kaon multiplicity tuning.

When it is not possible to find two weights to perform such an interpolation, any existing weight is chosen.

The effects of tuning the kaon production inside the target on the neutrino flux are illustrated in Fig. 7.12 and 7.13 for the fluxes predicted at the ND280 and SK detector sites, respectively. Individual contributions from the NA61, Eichten, and Allaby data as well as K_0^L and tertiary production tuning are also shown. As can be seen the contribution of the NA61 kaon data to the ν_μ fluxes is dominant for neutrinos up to about 5 GeV, while tuning of the high energy ν_μ tail is based on the Eichten data. This is consistent with the fact that the Eichten measurements of kaon production are in the momentum range from 6–24 GeV/c when scaled to the

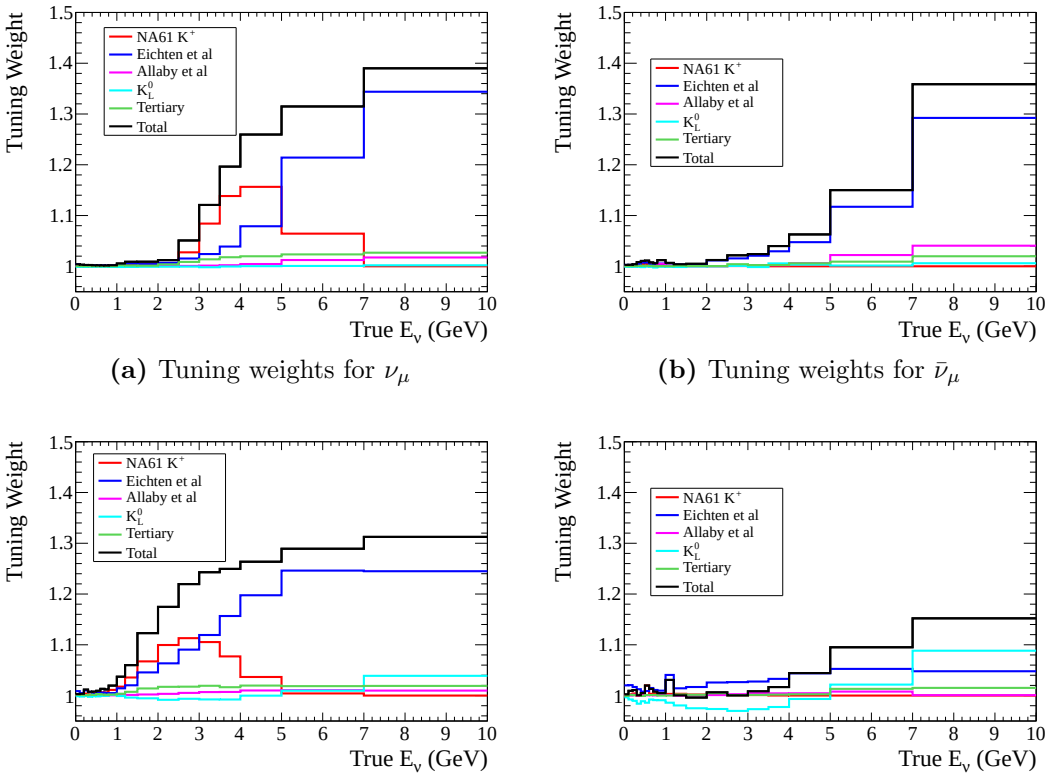

(a) Tuning weights for ν_μ

(b) Tuning weights for $\bar{\nu}_\mu$

(c) Tuning weights for ν_e

(d) Tuning weights for $\bar{\nu}_e$

Figure 7.12: Kaon tuning weights for the ND280 neutrino fluxes.

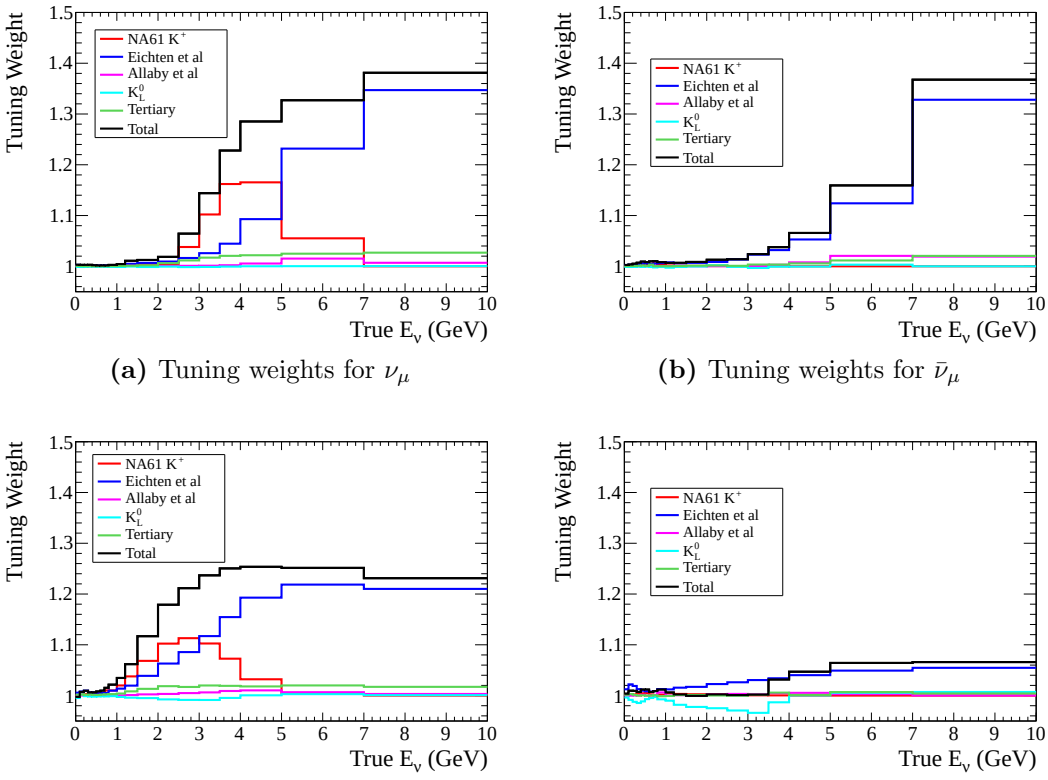

(a) Tuning weights for ν_μ

(b) Tuning weights for $\bar{\nu}_\mu$

(c) Tuning weights for ν_e

(d) Tuning weights for $\bar{\nu}_e$

Figure 7.13: Kaon tuning weights for the SK neutrino fluxes.

T2K beam energy. For ν_e the contribution of the Eichten data is more significant for lower energies. This is due to the fact that these neutrinos come from the three body K^+ decay,

$$K^+ \rightarrow \pi^0 e^+ \nu_e,$$

which leads to a larger probability of a high energy kaon producing a low energy neutrino.

7.4 Interaction rate tuning

To tune the interaction rate, the model predictions are compared to the data listed in Table 7.3. Fig. 7.14 (Fig. 7.15) shows the data and the predicted production cross-sections with the FLUKA, GCALOR, and GFLUKA models for protons, pions, and kaons interacting in carbon (aluminum).

FLUKA reproduces the data reasonably well, meaning that the effect of tuning the interaction rate inside the target (based on FLUKA-data discrepancy) is not significant when compared to the effects of the associated systematic uncertainties. The interaction rate inside the target is consequently not tuned. GCALOR, on the other hand, shows a sizable disagreement with the cross-section data. The out-of-target interaction rates are therefore tuned.

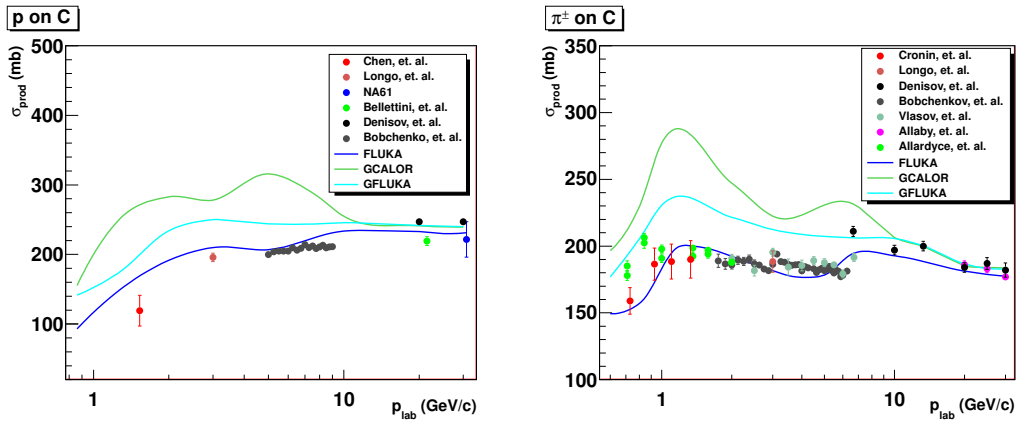

(a) Cross-section for protons on C

(b) Cross-section for charged pions on C

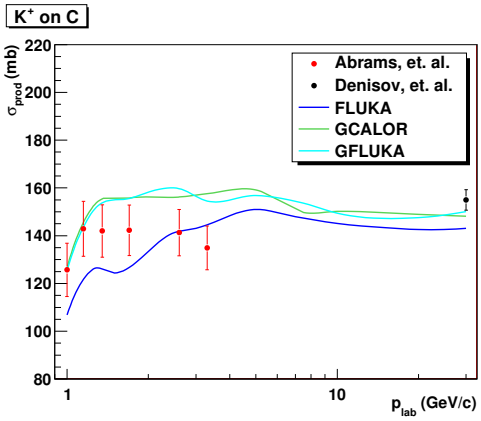

(c) Cross-section for K^+ on C

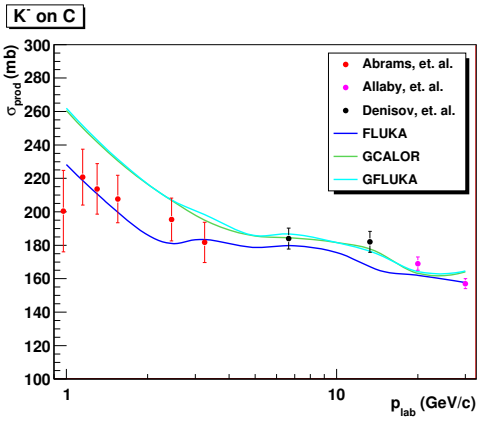

(d) Cross-section for K^- on C

Figure 7.14: Comparison of production cross-section data in carbon with FLUKA, GCALOR, and GFLUKA predictions.

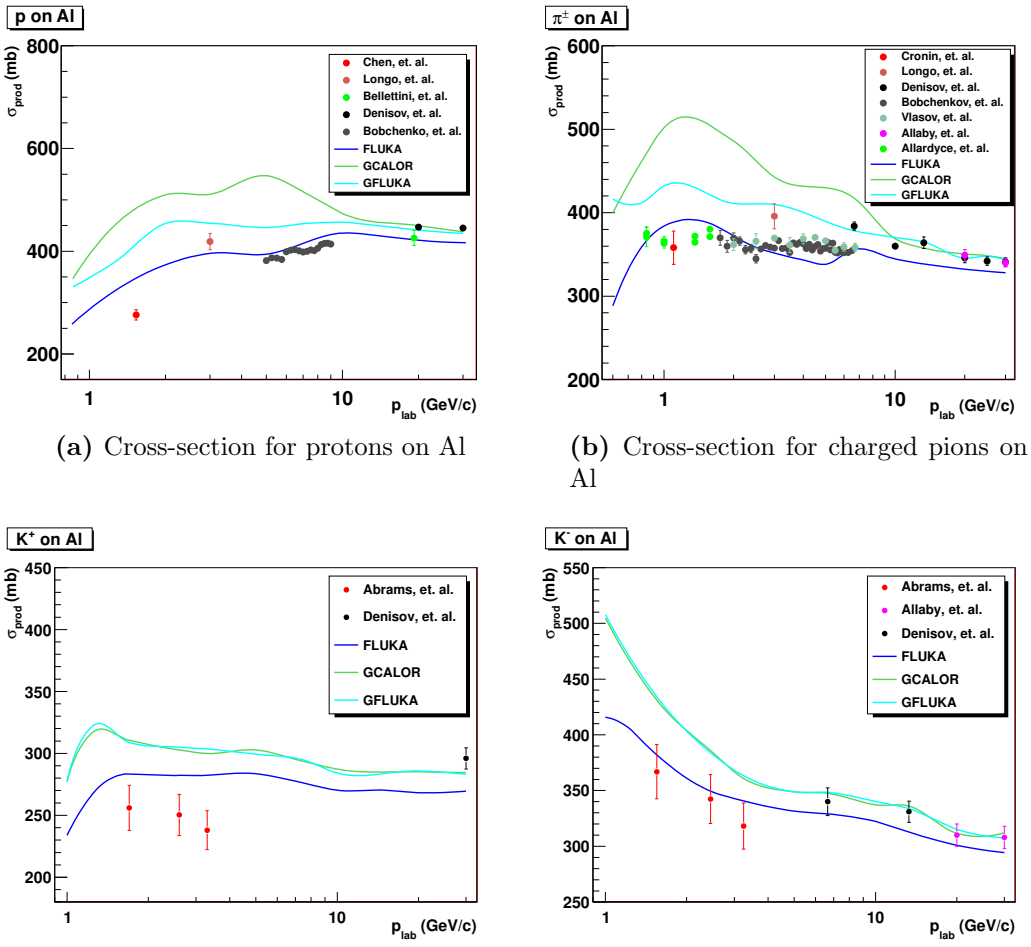

(a) Cross-section for protons on Al

(b) Cross-section for charged pions on Al

(c) Cross-section for K^+ on Al

(d) Cross-section for K^- on Al

Figure 7.15: Comparison of production cross-section data in aluminum with FLUKA, GCALOR, and GFLUKA predictions.

Data	Beam	Material	p_{beam} (GeV/c)	Measurement
Abrams *et al.* [93]	$K^{\pm}$	C, Cu	1-3.3	σ_{inel}
Allaby *et al.* [94]	π^{-}, K^{-}	C, Al, other	20-65	σ_{inel}
Allardyce *et al.* [95]	$\pi^{\pm}$	C, Al, other	0.71-2	σ_{inel}
Bellettini *et al.* [96]	p	C, Al, other	19.3, 21.5	σ_{inel}
Bobchenko *et al.* [97]	π^{-}, p	C, Al, other	1.75-9	σ_{inel}
Carroll *et al.* [98]	$\pi^{\pm}$,$K^{\pm}$, p	C, Al, other	60-280	σ_{prod}
Cronin *et al.* [99]	π^{-}	C, Al	0.73-1.33	σ_{inel}
Chen *et al.* [100]	p	C, Al, other	1.53	σ_{inel}
Denisov *et al.* [101]	$\pi^{\pm}$,$K^{\pm}$, p	C, Al, other	6-60	σ_{inel} or σ_{prod}
Longo *et al.* [102]	π^{+}, p	C, Al	3	σ_{inel}
NA61 [83]	p	C	31	σ_{prod}
Vlasov *et al.* [103]	π^{-}	C, Al	2-6.7	σ_{inel}

Table 7.3: Available inelastic and production cross-section data

7.5 Hadron production tuning results

The tuning performed on the MC flux predictions is summarized in Table 7.4.

FLUKA	GCALOR
$p + C \to \pi^{\pm} + X$	$p + Al \to \pi^{\pm} + X$
$n + C \to \pi^{\pm} + X$	$n + Al \to \pi^{\pm} + X$
$p + C \to K^{\pm} + X$	–
$p + C \to K^{0}_{L} + X$	–
–	Interaction rate

Table 7.4: Summary of the model prediction tuning

Fig. 7.16 and Fig. 7.17 show the results of the hadron production tuning for the neutrino flux predictions for ND280 and SK, respectively. The vertical axis in these plots shows how much the JNUBEAM predicted flux needs to be scaled based on the hadron production data-model discrepancies.

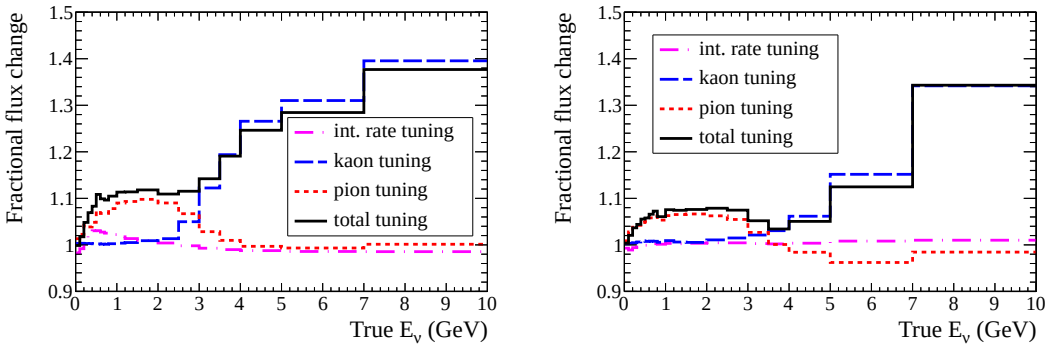

(a) Tuning effects for the ND280 ν_μ flux

(b) Tuning effects for ND280 $\bar{\nu}_\mu$ flux

(c) Tuning effects for ND280 ν_e flux

(d) Tuning effects for ND280 $\bar{\nu}_e$ flux

Figure 7.16: Hadron production tuning results for the neutrino flux predictions for the ND280 detector.

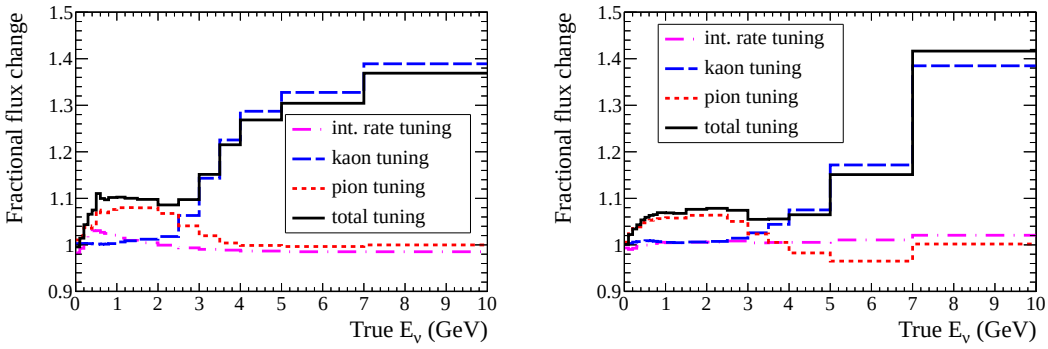

(a) Tuning effects for SK ν_μ flux

(b) Tuning effects for SK $\bar{\nu}_\mu$ flux

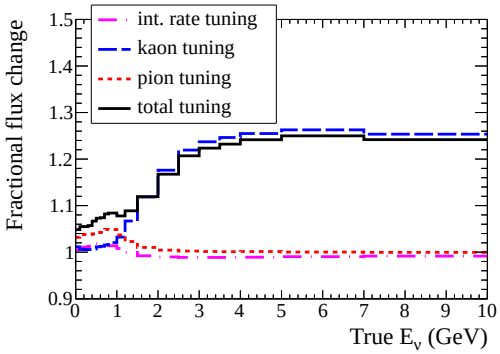

(c) Tuning effects for SK ν_e flux

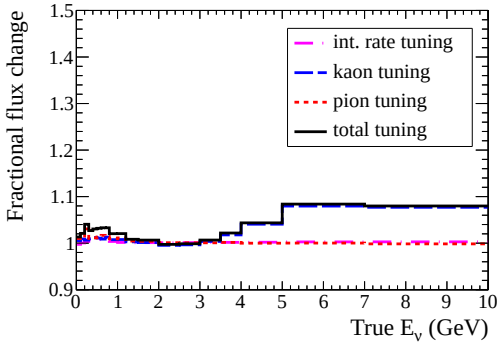

(d) Tuning effects for SK $\bar{\nu}_e$ flux

Figure 7.17: Hadron production tuning results for the neutrino flux predictions for the SK detector.

7.6 Predicted neutrino flux

The neutrino flux predictions for the ND280 and SK detectors are obtained by tuning the JNUBEAM output with the hadron production data. The different proton conditions between the runs (see Table 4.5 and Table 4.6) are accounted by taking a POT weighted sum of the flux predictions for a given detector and neutrino flavour for each run:

$$\bar{\Phi}(E) = \frac{1}{N_{\text{tot}}^{\text{POT}}} \sum_{i}^{\#\text{ of runs}} N_i^{\text{POT}} \Phi_i(E) \tag{7.11}$$

where $\bar{\Phi}(E)$ is the run average of the $\Phi_i(E)$ flux predictions for the i^{th} run with N_i^{POT} being the number of protons on target accumulated in this run and $N_{\text{tot}}^{\text{POT}}$ is the total number of the accumulated POT.

The flux predictions without oscillation effects are shown in Figs. 7.18 and 7.19 for the ND280 and SK detector, respectively. Figs. 7.20 and 7.21 show the same predictions broken down according to the contributions from different neutrino parents. Finally, Fig. 7.22 illustrates the contributions from each neutrino flavour on the same scale for the ND280 (Fig. 7.22a) and SK (Fig. 7.22b) detectors.

The fluxes shown in these figures are normalized to 10^{21} POT, which is the number of the POTs expected per year with 0.75 MW proton beam power. To obtain the predictions for the number of POT accumulated so far (1.431×10^{20}),

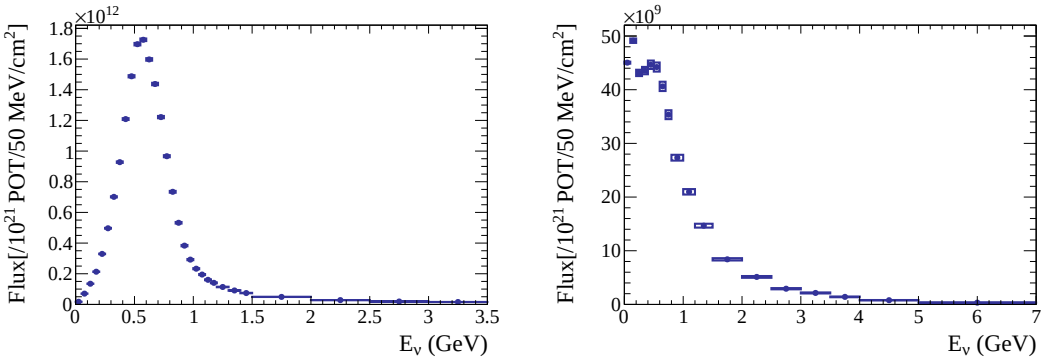

(a) Predicted ND280 ν_μ flux

(b) Predicted ND280 $\bar{\nu}_\mu$ flux

(c) Predicted ND280 ν_e flux

(d) Predicted ND280 $\bar{\nu}_e$ flux

Figure 7.18: The predicted neutrino flux at the ND280 detector. Only the MC statistical errors are shown.

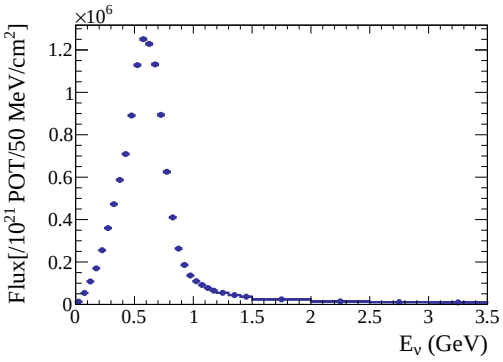

(a) Predicted SK ν_μ flux

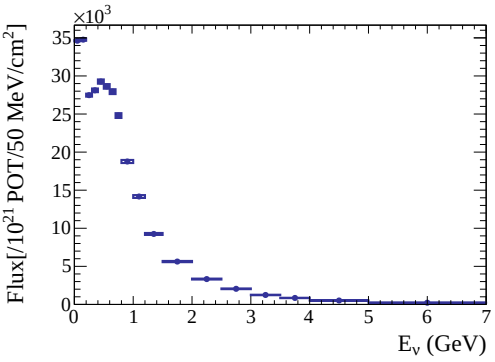

(b) Predicted SK $\bar{\nu}_\mu$ flux

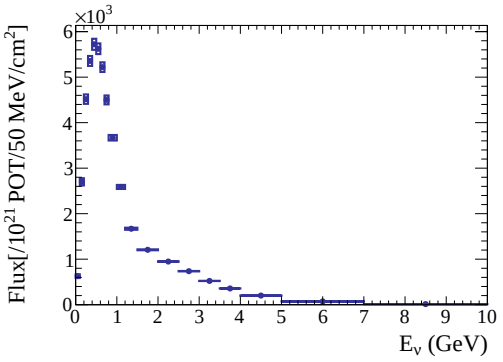

(c) Predicted SK ν_e flux

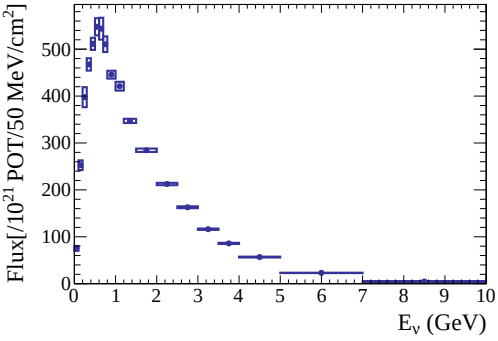

(d) Predicted SK $\bar{\nu}_e$ flux

Figure 7.19: The predicted neutrino flux at the SK detector without oscillation effects. Only the MC statistical errors are shown.

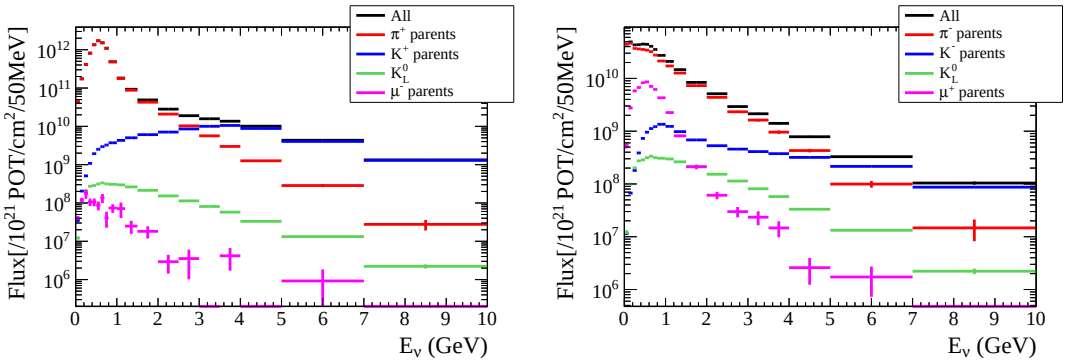

(a) Predicted ND280 ν_μ flux

(b) Predicted ND280 $\bar{\nu}_\mu$ flux

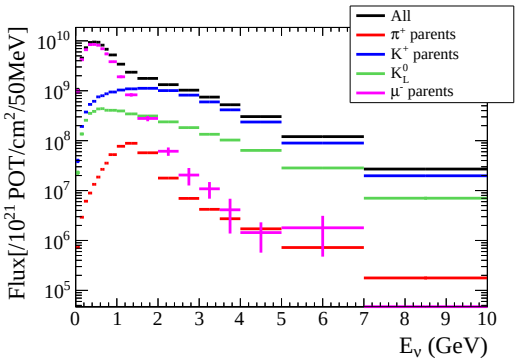

(c) Predicted ND280 ν_e flux

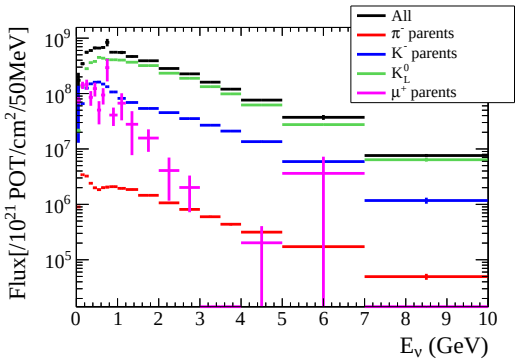

(d) Predicted ND280 $\bar{\nu}_e$ flux

Figure 7.20: The predicted neutrino flux at the ND280 detector separated by parent type. Only the MC statistical errors are shown.

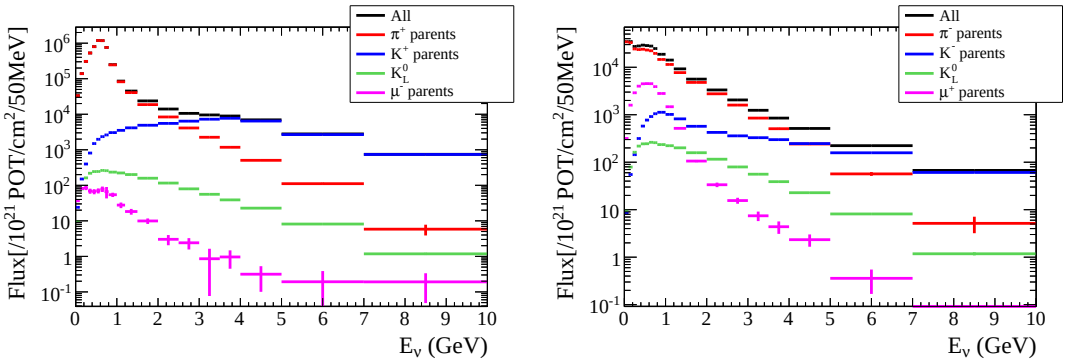

(a) Predicted SK ν_μ flux

(b) Predicted SK $\bar{\nu}_\mu$ flux

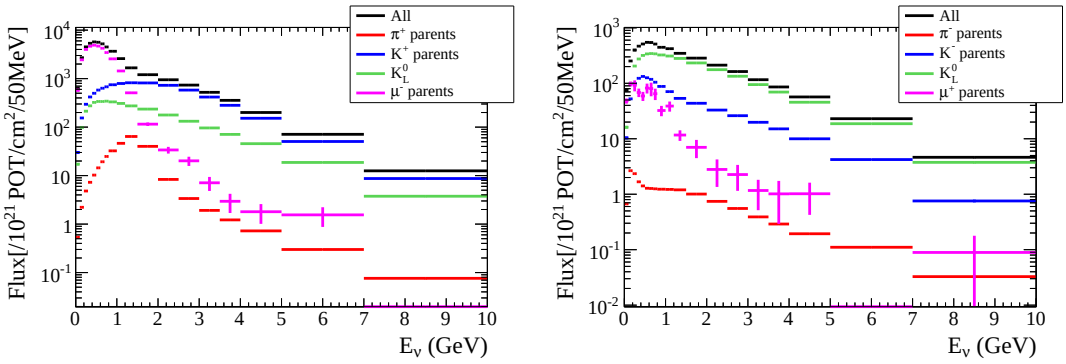

(c) Predicted SK ν_e flux

(d) Predicted SK $\bar{\nu}_e$ flux

Figure 7.21: The predicted neutrino flux at the SK detector separated by parent type without oscillation effects. Only the MC statistical errors are shown.

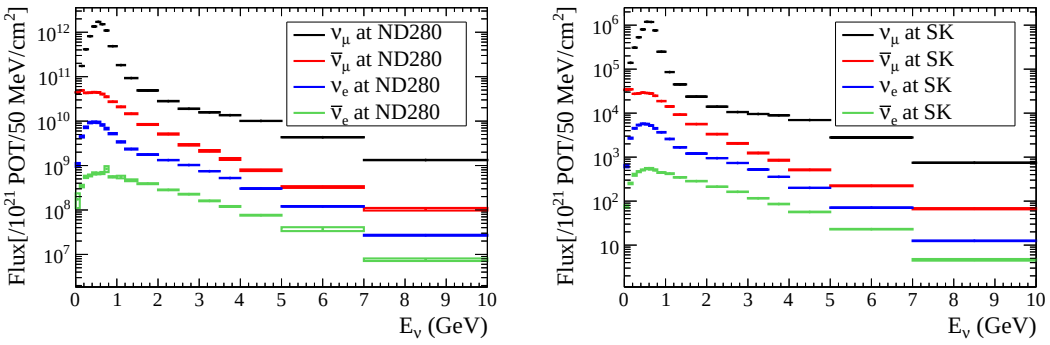

(a) Neutrino flux at the ND280 detector

(b) Neutrino flux at the SK detector

Figure 7.22: Neutrino fluxes at the ND280 and SK detectors. Only the MC statistical errors are shown.

the results in these figures should be re-scaled by a factor of $1.431 \times 10^{20}/10^{21}$.

As can be seen from Figs. 7.20 and 7.21, the majority of muon neutrinos come from pion parents. The high energy tail, however, is dominated by the muon neutrinos originating from kaon parents. The ν_e flux is dominated by contributions from μ decays, which mostly come from the same pion parents that contributed to the ν_μ flux. Similar to ν_μ, the high energy ν_e originate from kaons. However, unlike the case of ν_μ flux, where kaons do not contribute significantly up to $\sim$ 3 GeV, the kaon contribution to the ν_e flux becomes sizable after $\sim$ 1 GeV. As mentioned already, this is the consequence of the fact that in the case of kaons, electron neutrinos come from a three body decay.

The contributions of each neutrino parent and from different neutrino flavours are also summarized in Table 7.5 for the SK neutrino flux without oscillation effects.

		$\pi^{+/-}$	$K^{+/-}$	K^0_L	$\mu^{+/-}$	ν_x/ν_{all}
ν_μ	Total	94.44%	5.46%	0.09%	0.01%	92.67%
	0.5–0.7 GeV	99.79%	0.18%	0.02%	0.006%	97.19%
$\bar{\nu}_\mu$	Total	82.47%	7.00%	1.39%	9.14%	6.05%
	0.5–0.7 GeV	80.13%	2.98%	0.90%	15.97%	2.32%
ν_e	Total	0.97%	34.61%	11.50%	52.92%	1.11%
	0.5–0.7 GeV	0.31%	11.20%	6.23%	82.26%	0.45%
$\bar{\nu}_e$	Total	0.36%	18.49%	73.77%	7.38%	0.17%
	0.5–0.7 GeV	0.23%	22.33%	62.54%	14.89%	0.05%

Table 7.5: Fractional contributions to the flux predictions (without oscillation effects) for SK from different neutrino parents. The last column shows the fractions of each neutrino flavour in the total neutrino flux.

The fractional contributions are computed for both the total flux and the flux in the expected region of the maximum oscillation signal $0.5 - 0.7$ GeV.

Pion decays contribute over 90% to the muon neutrino flux. In addition, pions are responsible (mostly via the muon daughters) for about 52% of the ν_e flux, which is the major background to the ν_e appearance signal. Understanding of these contributions is based on the measurements of the pion production done by the NA61 experiment.

The remaining 48% of the electron neutrinos come from kaon decays. This contribution is constrained using the NA61 K^+ measurements and kaon production data of Eichten *et al.* and Allaby *et al.*

8 Systematic Uncertainties in the Predicted Neutrino Flux

The sources of the systematic uncertainties for the neutrino flux predictions are:

- pion production
- kaon production
- secondary nucleon production
- production cross-section
- proton beam conditions
- neutrino beam direction (off-axis angle)
- component (target and horn) alignment
- horn currents.

A covariance matrix $\mathbf{V}^b$ is used to encapsulate the systematic uncertainties in the predicted neutrino flux. It is a generalization of the standard variances that also includes information on possible correlations between neutrinos of different energies and flavours.

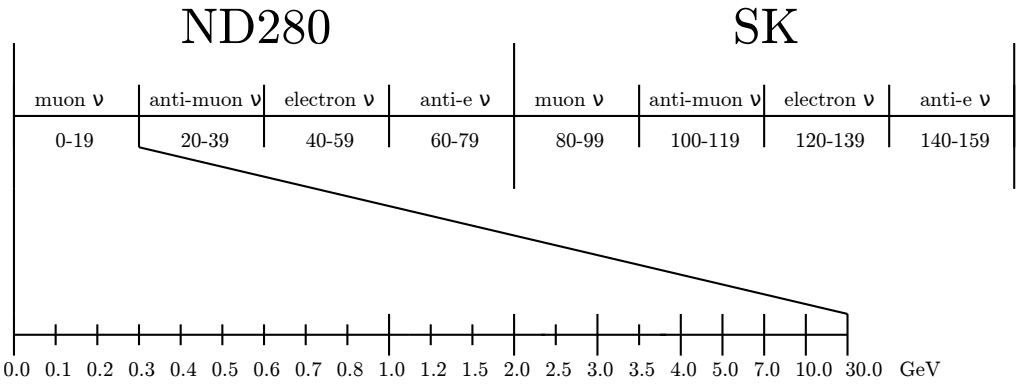

Figure 8.1: Binning and ordering of the flux covariance matrix entries.

For each neutrino flavour and detector 20 energy bins covering the range from 0 to 30 GeV are adopted. The covariance matrix is organized in the following order: ND280 ν_μ (entries 0-19), ND280 $\bar{\nu}_\mu$ (entries 20-39), ND280 ν_e (entries 40-59), ND280 $\bar{\nu}_e$ (entries 60-79), SK ν_μ (entries 80-99), SK $\bar{\nu}_\mu$ (entries 100-119), SK ν_e (entries 120-139), and SK $\bar{\nu}_e$ (entries 140-159). Fig. 8.1 illustrates the binning and the ordering for the covariance matrix entries.

The elements of this covariance matrix are defined as

$$V^b_{EE'} = \rho_{EE'}\sigma_\Phi(E)\sigma_\Phi(E') \tag{8.1}$$

where $\sigma_\Phi(E)$ is the fractional uncertainty for a given energy bin of the neutrino flux and $\rho_{EE'}$ is the correlation coefficient between two energy bins. It follows from Eq. 8.1 that the diagonal elements of $\mathbf{V}^b$ are the squares of the flux uncertainties for a given bin.

Using the flux covariance the systematic uncertainties in the flux predictions can be described with a multi-variate normal distribution:

$$\mathcal{N} \sim \frac{1}{|\mathbf{V}^b|^{1/2}} \exp\left[-\frac{1}{2}(\mathbf{b}-\mathbf{1})^T \mathbf{V}^{b-1}(\mathbf{b}-\mathbf{1})\right]. \tag{8.2}$$

The scale factors $\mathbf{b}$ sampled from this PDF can then be used to vary the nominal flux predictions $\Phi^0(E)$ and study the effects of the systematic uncertainties in the oscillation analysis:

$$\Phi'(E) = b(E)\Phi^0(E). \tag{8.3}$$

The remainder of this chapter will be devoted to the evaluation of $\mathbf{V}^b$.

8.1 Evaluation of systematic uncertainties

The uncertainties are evaluated from variations in the predicted neutrino flux. If a given source of the systematic uncertainty can be described by a small number of uncorrelated parameters, the effects on the neutrino flux can be studied by changing each parameter by one standard deviation. This will be called the "1σ" method.

The uncertainty in the neutrino flux predictions are evaluated according to

$$\sigma_{\Phi}(E) = |R(E)|, \tag{8.4}$$

where $R(E)$ is the ratio of the flux produced from the variation of a given systematic parameter over the nominal flux Φ (predicted flux prior to any changes of the systematic parameters). The covariance between the energies E and E' is computed according to

$$V^{b}_{EE'} = (R(E) - 1)(R(E') - 1). \tag{8.5}$$

If the number of the systematic parameters is large or there are strong correlations between the parameters, the 1σ method becomes difficult to implement. In this case, the uncertainties in the neutrino flux predictions are evaluated from an ensemble of the parameter sets drawn from or thrown according to some normal distribution that represents the systematic uncertainties associated with the parameter values. This approach will be referred to as the "thrown parameter" method.

The uncertainty in the neutrino flux is computed from

$$\sigma_{\Phi}(E) = \sqrt{\frac{1}{N-1}\sum_{j=1}^{N}(\Phi^{j}(E) - \bar{\Phi}(E))^2}, \tag{8.6}$$

where N is the number of the generated parameter throws, $\Phi^j(E)$ is the neutrino flux for the j^{th} throw, and $\bar{\Phi}(E)$ is the mean. The covariance matrix is estimated as a sample covariance according to

$$V^b_{EE'} = \frac{1}{N-1}\sum_{j=1}^{N}\frac{(\Phi^j(E)-\bar{\Phi}(E))(\Phi^j(E')-\bar{\Phi}(E'))}{\bar{\Phi}(E)\bar{\Phi}(E')} \tag{8.7}$$

from the ensemble of $\Phi^j(E)$.

8.2 Pion production uncertainties

The sources of the systematic uncertainties associated with pion production are:

- experimental errors in the NA61 $\pi^{\pm}$ data
- uncertainties associated with the momentum scaling procedure
- uncertainties in the pion production in the regions not covered by data.

8.2.1 Uncertainties in the NA61 pion data

The uncertainties in $\pi^{\pm}$ production are based on the experimental errors in the NA61 data reported in [83]. The statistical uncertainties are uncorrelated between different $p-\theta$ bins. The systematic uncertainties are separated into the contributions from different sources and appropriate bin-to-bin correlations are adopted for

each source.

To propagate the NA61 errors, the pion weights are modified by randomly sampling the statistical and systematic covariances. The systematic uncertainty in the neutrino flux is calculated from the set of the resultant predictions.

8.2.2 Uncertainties in the momentum scaling

The use of momentum scaling when tuning the tertiary pion production introduces an additional source of systematic uncertainty. This has been evaluated by modifying the scaling procedure. The pion production measurements done with protons of 12.3 and 17.5 GeV/c on a Be target by the E910 experiment [87] (see Table 6.4) are scaled to carbon using the material scaling procedure described in Section 6.8. The scaled data sets are then fit separately using the parametrization proposed by Bonesini, Marchionni, Pietropaolo, and Tabarelli de Fatis (BMPT) [90]:

$$E\frac{d^3\sigma}{dp^3} = A(1-x_R)^{\alpha}(1+Bx_R)x_R^{-\beta}(1+a'(x_R)p_T+b'(x_R)p_T^2)e^{-a'(x_R)p_T}, \qquad (8.8)$$

where $a'(x_R) = a/x_R^{\gamma}$, $b'(x_R) = a^2/2x_R^{\delta}$, and $A, B, a, \alpha, \beta, \gamma, \delta$ are seven model parameters determined by the fit to the data. The resultant parametrization is then compared to the FLUKA predictions and a set of tuning weights is obtained.

The tertiary pion production is tuned based on the weights found from a linear

interpolation of 31 GeV/c (NA61), 17.5 GeV/c, and 12.3 GeV/c results. The x_R variable is used instead of x_F (see Section 6.7) to perform the momentum scaling.

When using this procedure, the flux predictions change by a few percent relative to when the nominal scaling method is used. This change is treated as a systematic uncertainty.

8.2.3 Uncertainties in the pion production outside of the data covered regions

To evaluate the uncertainties in the parts of the phase-space not covered by the NA61 $\pi^{\pm}$ data, the BMPT parametrization is used to extrapolate into these regions. The BMPT function is fitted to $\pi^{\pm}$ data and its results are then compared to the FLUKA model predictions to get the tuning weights. The change in the flux predictions observed when the pion production outside of the NA61 covered phase-space is tuned according to the BMPT/FLUKA ratio relative to the nominal case when no tuning is done is taken as a systematic uncertainty. The effect of the uncertainties in the BMPT parameters from the fit to the data is evaluated and included into the systematic uncertainty.

8.3 Kaon production uncertainties

The sources of the systematic uncertainties associated with the kaon production are:

- experimental errors associated with the NA61 K^+ data
- uncertainties associated with the Eichten and Allaby data
- uncertainties associated the momentum scaling procedure
- uncertainties in the kaon production in the regions not covered by the data
- uncertainties in the contribution from kaons produced in the interactions outside of the target graphite.

8.3.1 NA61 kaon uncertainties

The experimental errors in the NA61 measurement of kaon production are shown in Fig. 8.2 in the two angular bins. The dominant uncertainties are statistical and are on the order of $10 - 22\%$ depending on the momentum bin. The systematic uncertainties are mostly on the order of 4% and only become significant (5-10%) for the highest momentum bins. The overall uncertainty for each momentum bin is calculated as a sum in quadrature of statistical and systematic uncertainties. In

addition to the bin errors, the normalization uncertainty of 2.3% in the NA61 data is also applied.

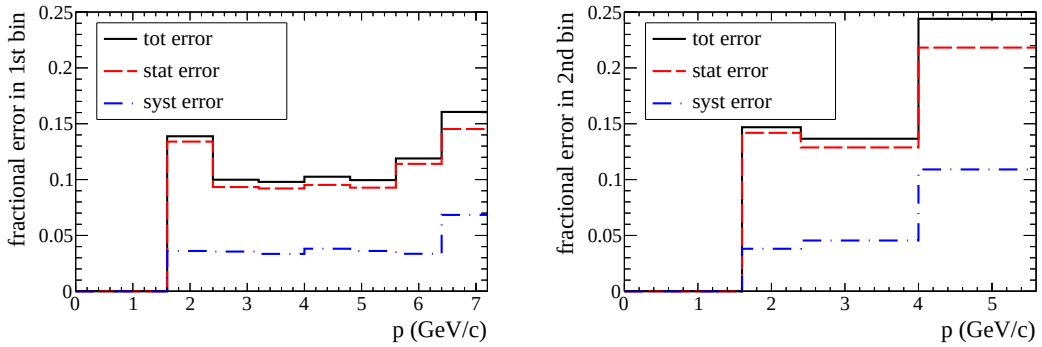

(a) $20 - 140$ mrad bin **(b)** $140 - 240$ mrad bin

Figure 8.2: Uncertainties in the NA61 K^+ multiplicity measurements.

These uncertainties are propagated by adjusting the NA61 based kaon tuning weights by one standard deviation (1σ) one bin at a time for the bin errors, and all the bins simultaneously (fully correlated) for the normalization error. This gives in total eleven different re-weighted Monte Carlo sets (ten different data bins plus overall normalization).

Since the statistical errors are much larger than the systematic uncertainties for most of the bins, the possible correlation between systematic uncertainties for different bins is not treated at this time.

Due to limited statistics the NA61 kaon data had to be coarsely binned. To estimate the effects of such coarse binning on the neutrino flux, the kaon production data in Table 7.1 is fitted with the BMPT model. After the fit is performed, the

integral of the BMPT function in a given NA61 bin is normalized to the NA61 measurement in this bin. To evaluate the binning effect the kaon production is then tuned based on the normalized BMPT function in place of the NA61 measurements. The change in the resultant flux relative to the nominal predictions is included as a systematic uncertainty.

The uncertainties in the neutrino flux predictions from the sources associated with the NA61 kaon production measurements are shown in Fig. 8.3 and Fig. 8.4 for the ND280 and SK detectors, respectively. The labels of "$+1\sigma$ bin 1" etc. refer to the uncertainties due to errors for the seven momentum bins in the first (20–140 mrad) angular bin, while those of "$+1\sigma$ bin 8" etc. correspond to the uncertainties from the three momentum bins in the second (140–240 mrad) angular bin. The covariance for the predicted neutrino fluxes at different energies E and E' is calculated as in Eq. 8.5.

8.3.2 Eichten and Allaby kaon uncertainties

The effects of the uncertainties in the Eichten and Allaby data on the neutrino flux are studied by varying the values of each measurement point within these data sets according to the associated uncertainties.

The considered uncertainties are summarized in Table. 8.1. The normalization uncertainty σ_N is treated as correlated for all the data points and both the K^+ and

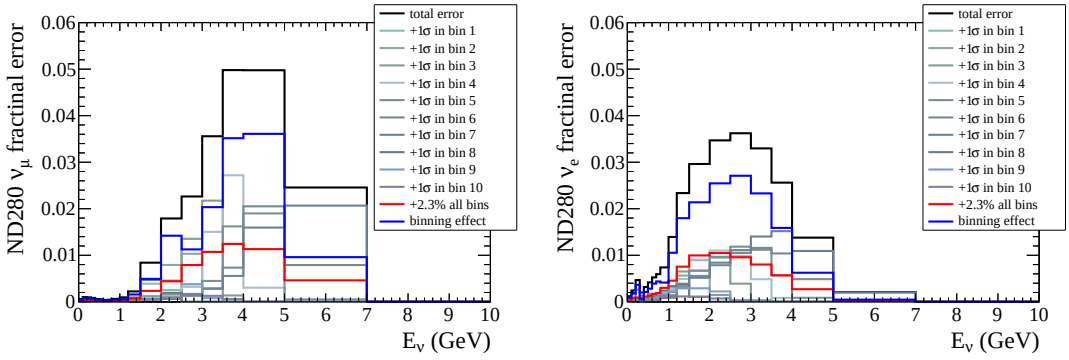

(a) ND280 ν_μ **(b)** ND280 ν_e

Figure 8.3: Systematic errors in the neutrino fluxes at ND280 due to the uncertainties associated with the NA61 K^+ multiplicity measurements.

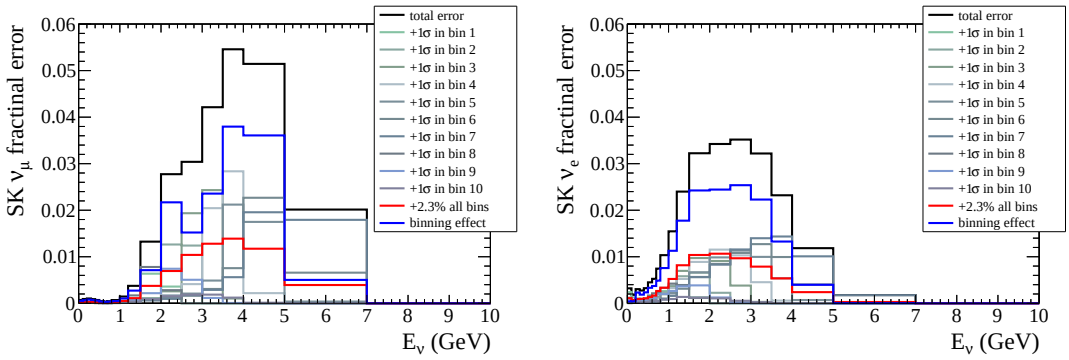

(a) SK ν_μ **(b)** SK ν_e

Figure 8.4: Systematic errors in the neutrino fluxes at SK due to the uncertainties associated with the NA61 K^+ multiplicity measurements.

Experiment	σ_N	σ_θ	$\sigma_{p,\theta}$
Eichten *et al.*	15%	5%	Max 4%
Allaby *et al.*	10%	10%	$2-5\%$

Table 8.1: Summary of the uncertainties in the Eichten and Allaby data. The overall normalization uncertainty is denoted by σ_N. The uncertainty for a given angular bin which is correlated for different momentum bins is labeled as σ_θ. The uncorrelated uncertainty for each $p-\theta$ bin is denoted by $\sigma_{p,\theta}$.

K^- data sets from a given experiment. The uncertainty σ_θ is treated as correlated for the measurements taken at the same angle θ for both K^+ and K^-. Finally, $\sigma_{p,\theta}$ is the error component uncorrelated between different data points.

In addition to the experimental errors, the uncertainties in the scaling from beryllium to carbon (A-scaling) target material are applied. As discussed in Section 6.8, these consist of a normalization type uncertainty $\sigma_N^A = 5\%$ which is correlated for both Eichten and Allaby data and an uncorrelated uncertainty $\sigma_{p,\theta}^A = 5\%$.

To study the effects of these errors, each data point is scaled by a factor f_i. These factors are the products of weights randomly drawn from Gaussian distributions $\mathcal{N}$ with the mean of one and the width defined by the given error source:

$$f_i = \mathcal{N}(1, \sigma_N^A) \times \mathcal{N}(1, \sigma_N) \times \mathcal{N}(1, \sigma_\theta) \times \mathcal{N}(1, \sqrt{(\sigma_{p,\theta})^2 + (\sigma_{p,\theta}^A)^2}). \tag{8.9}$$

The $\mathcal{N}(1, \sqrt{(\sigma_{p,\theta})^2 + (\sigma_{p,\theta}^A)^2})$ term represents the uncorrelated component of the error and is drawn for each point separately. The draws from other distributions

in Eq. 8.9 are made according to the discussed correlations. For example, a factor drawn from $\mathcal{N}(1, \sigma_N)$ is the same for all the points in a given data set.

Each throw of K^+ and K^- data is appropriately (preserving any error correlations) combined according to Eq. 7.7 to obtain sets of predictions for K^0_L and to estimate the uncertainty on the neutrino flux coming from the production of neutral kaons.

After the data points are adjusted based on the thrown scale factors, the bicubic interpolation is performed. The nominal flux tuning weights $w(p, \theta)$ computed according to Eq. 7.9 are then modified according to

$$w^j(p,\theta) = \left(\frac{d\sigma^j_{\text{Eichten,Allaby}}}{dpd\Omega} \Big/ \frac{d\sigma_{\text{Eichten,Allaby}}}{dpd\Omega} \right) \times w(p,\theta), \tag{8.10}$$

where the superscript j indicates an index of a re-scaled data set. Finally, the neutrino flux is tuned using $w^j(p, \theta)$, which results in a modified set of neutrino flux predictions $\Phi^j(E)$. Using Eq. 8.6 and Eq. 8.7, the uncertainty and covariance matrix for flux predictions are computed from an ensemble of 200 $\Phi^j(E)$ distributions.

8.3.3 Uncertainties in momentum scaling

The momentum scaling is required in order to tune the production of secondary kaons with Eichten and Allaby data. It is also involved in the tuning of the tertiary

kaon production.

The momentum scaling is nominally performed using the x_F scaling variable, but a radial scaling variable x_R could also be used. The difference in the tuned flux predictions when x_R is used from those obtained with x_F is treated as a systematic uncertainty associated with the momentum scaling.

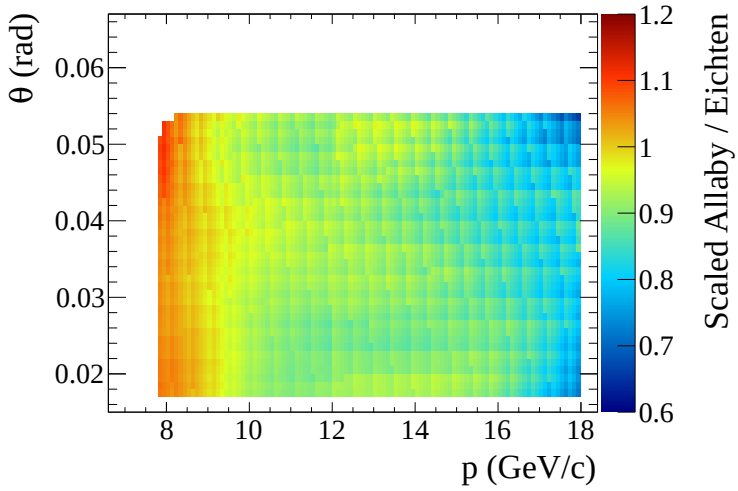

Figure 8.5: Ratio of the scaled K^+ production data from Allaby *et al.* to that of Eichten *et al.*

It is also possible to check the scaling with the data, since kaon production measurements of Allaby *et al.* performed at 19.2 GeV/c could be scaled to 24 GeV/c and compared to those of Eichten *et al.* The comparison of the scaled Allaby data to the Eichten data is shown in Fig. 8.5 for K^+ as an example. The fact that the ratio shown in this figure is not one is dealt with by modifying the Eichten kaon

weights according to

$$w'(p,\theta) = \left(\frac{d\sigma_{\text{Scaled Allaby}}}{dpd\Omega} \Big/ \frac{d\sigma_{\text{Eichten}}}{dpd\Omega} \right) \times w_{\text{Eichten}}(p,\theta). \tag{8.11}$$

The changes in the predicted flux after the tuning with the modified weights is performed are taken to represent the systematic uncertainty.

8.3.4 Uncertainties in kaon production outside of the data covered regions

The BMPT parametrization fitted to the kaon production data is used to extrapolate to the regions of phase-space not covered by the data. The kaon production is tuned in these regions using the ratio of the BMPT to FLUKA predictions Eq. 8.12:

$$w_{\text{BMPT}}(p,\theta) = \frac{dn_{\text{BMPT}}}{dpd\Omega} \Big/ \frac{dn_{\text{FLUKA}}}{dpd\Omega}, \tag{8.12}$$

where n_{BMPT} and n_{FLUKA} are the BMPT and FLUKA predictions for the kaon production multiplicity in the interactions of 31 GeV/c protons with graphite. A systematic uncertainty is assigned based on the discrepancy between the resultant and the nominally tuned flux.

Since the measurements used to construct the BMPT parametrization have experimental uncertainties, these errors also need to be accounted for when assigning

the uncertainties outside of the data coverage. This is done by re-fitting the BMPT parametrization using a hundred throws of the Eichten and Allaby data sets described earlier. The BMPT parameters obtained from each fit are used to calculate the kaon production multiplicity n^j_{BMPT} and the weights in Eq. 8.12 are modified according to

$$w^j(p,\theta) = \left(\frac{dn^j_{\mathrm{BMPT}}}{dpd\Omega} \Big/ \frac{dn_{\mathrm{BMPT}}}{dpd\Omega} \right) \times w_{\mathrm{BMPT}}(p,\theta). \tag{8.13}$$

These weights are used to tune the hadron production in the regions not covered by the data. The errors are then estimated from the resultant variation in the flux predictions relative to the case when only the weights in Eq. 8.12 are used.

8.3.5 Uncertainties in kaon production outside of the target

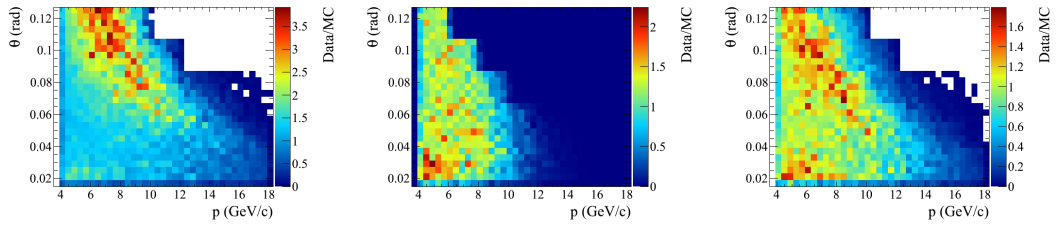

(a) Ratio for K^+ **(b)** Ratio for K^- **(c)** Ratio for K^0_L

Figure 8.6: Ratios to the interpolated kaon production double differential cross-section measurements from Eichten *et al.*, to the GCALOR predictions for 24 GeV/c protons interacting on Al.

To estimate the uncertainties in the kaon production outside of the target, it is necessary to compare the existing data to the GCALOR predictions. The predic-

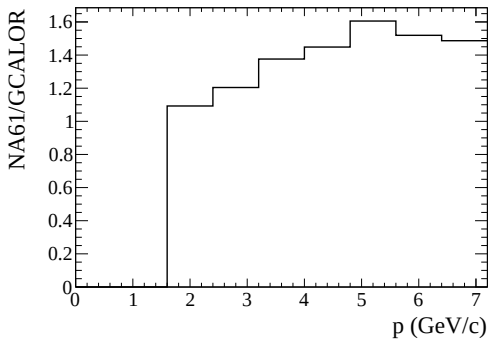

(a) Ratio of the NA61/GCALOR K^+ production for $\theta = 20 - 140$ mrad

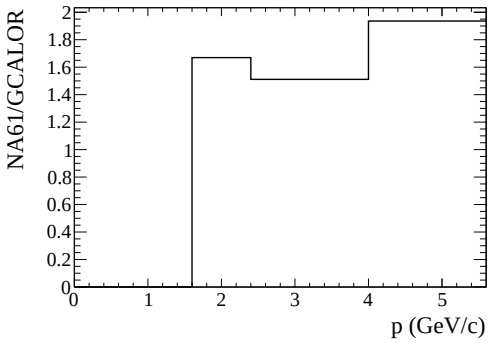

(b) Ratio of the NA61/GCALOR K^+ production for $\theta = 140 - 240$ mrad

Figure 8.7: Ratios to the scaled NA61 K^+ production measurements to the GCALOR predictions.

tions for kaon production are computed by simulating interactions of 24 GeV/c and 31 GeV/c proton beams in aluminum. The GCALOR predicted production with 24 GeV/c is compared to the measurements of Eichten *et al.*, of kaon production from Al target. The ratios of the data to GCALOR predictions for K^+, K^-, and K^0_L production are shown in Fig. 8.6.

To compare the NA61 measurements to the predicted kaon production with a 31 GeV/c proton beam, the data is first scaled from carbon to aluminum by applying the scaling factor $\mathcal{A}$

$$\mathcal{A} = \left(\frac{A_{Al}}{A_C}\right)^{\alpha(x_F, p_T)}, \tag{8.14}$$

where A_C and A_{Al} are the atomic weights of carbon and aluminum, respectively.

As discussed in Section 6.8, the exponent $\alpha(x_F, p_T)$ has the form

$$\alpha(x_F, p_T) = (0.77 - 0.32x_F)(1.0 + 0.25p_T^2). \tag{8.15}$$

For each data bin, α and the scaling factor $\mathcal{A}$ are calculated by taking the p and θ value at the bin centre, determining the corresponding x_F and p_T, and then using Eq. 8.14 and 8.15 to evaluate the required quantities. The ratios of the NA61 scaled K^+ production data to the GCALOR predictions are shown in Fig. 8.7.

The difference of the tuned flux when the weighting of the kaon production in GCALOR is included with the nominal one is assigned as the systematic uncertainty.

8.3.6 Total kaon flux uncertainties

The fractional uncertainties in the neutrino flux predictions associated with the kaon production are shown in Fig. 8.8 for the ND280 and Fig. 8.9 for SK detectors. The contributions from each error source are also shown in these figures.

The largest contribution comes from the uncertainties associated with Eichten and Allaby data ("Other data errors"). These uncertainties are mainly dominated by the overall 15% normalization uncertainty in the Eichten data. The uncertainties associated with the NA61 K^+ production measurements are on the order of 5% and

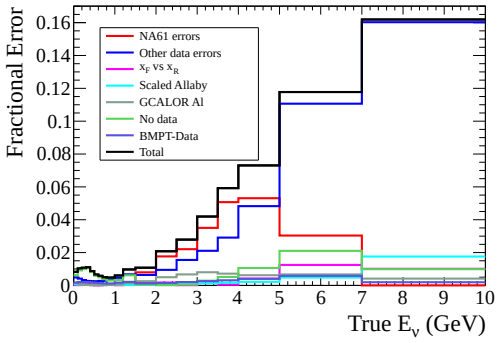

(a) Uncertainty on ν_μ

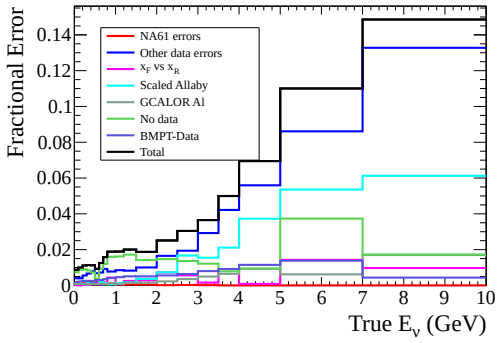

(b) Uncertainty on $\bar{\nu}_\mu$

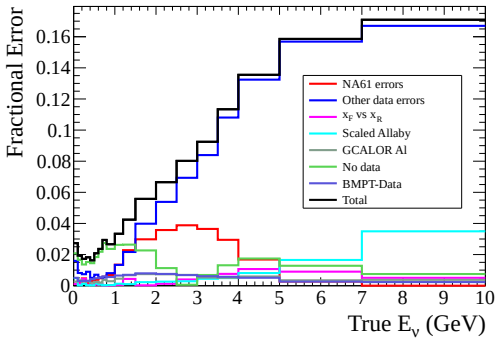

(c) Uncertainty on ν_e

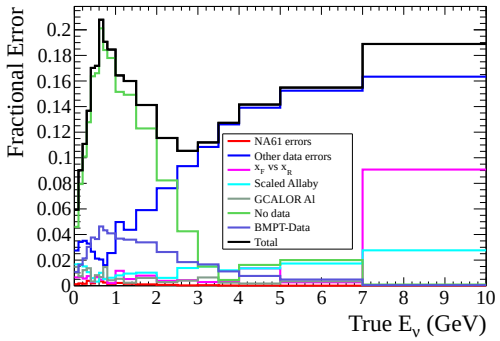

(d) Uncertainty on $\bar{\nu}_e$

Figure 8.8: The uncertainties on the ND280 neutrino flux due to the kaon production.

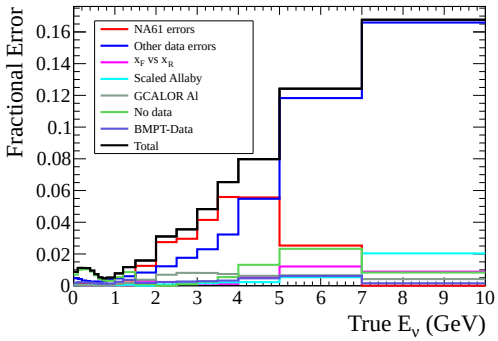

(a) Uncertainty on ν_μ

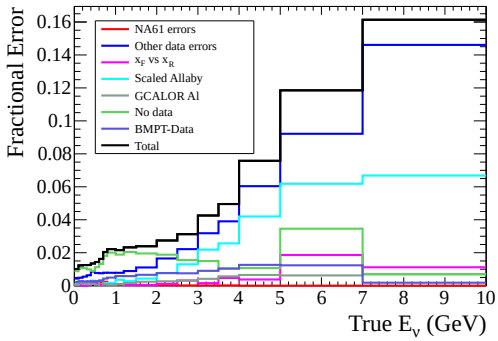

(b) Uncertainty on $\bar{\nu}_\mu$

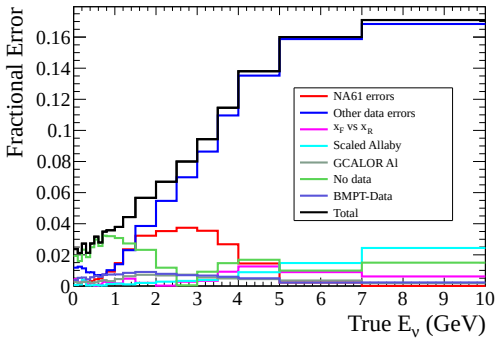

(c) Uncertainty on ν_e

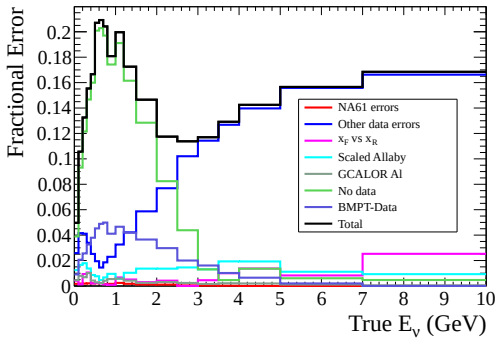

(d) Uncertainty on $\bar{\nu}_e$

Figure 8.9: The uncertainties on the SK neutrino flux due to the kaon production.

4% for ν_μ and ν_e fluxes, respectively.

8.4 Secondary nucleon production uncertainties

Secondary protons and neutrons have a sizable contribution to the neutrino flux. For example, the contribution of protons (neutrons) is around 16% (5%) for the SK ν_μ (see Table 6.2). The $x_F - p_T$ phase-space for the contributing protons and neutrons are shown in Figs. 8.10a and 8.10b, respectively.

There are two components to the proton production: one with $x_F \leq 0.9$ and another for $x_F > 0.9$. This is not the case for neutrons where only those with $x_F \leq 0.9$ contribute significantly. The contribution from high x_F protons is attributed to be coming from quasi-elastic scattering type of events, while the contributions from $x_F \leq 0.9$ is due to hadron production. The evaluation of the uncertainty for the secondary nucleon production is, consequently, separated into two regions.

In the region with $x_F \leq 0.9$ the uncertainty for the secondary nucleon production is evaluated by comparing the FLUKA predictions for proton production in beryllium with the proton production measurements of Eichten *et al.* and Allaby *et al.* Fig 8.11 shows the ratio of the data to the FLUKA predictions of differential proton production multiplicity. The location of the Eichten (circles) and Allaby (squares) measurements is superimposed. The ratio shown in Fig. 8.11 is used to tune the multiplicity of the nucleons produced with $x_F \leq 0.9$. Assuming isospin

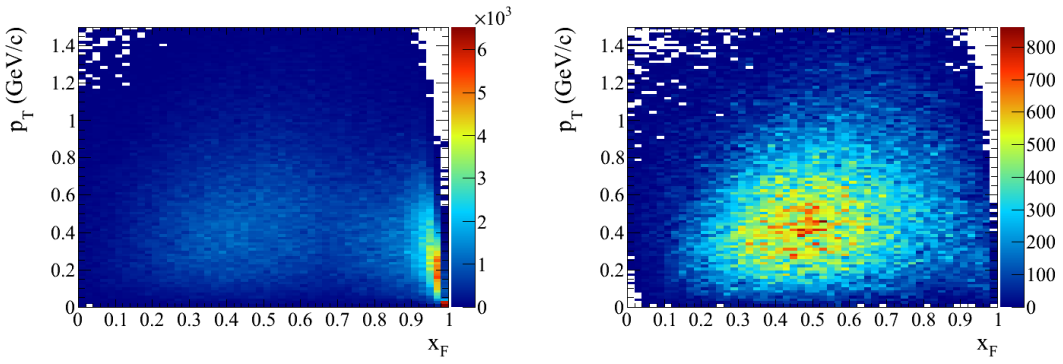

(a) Secondary protons **(b)** Secondary neutrons

Figure 8.10: Distribution of secondary protons and neutrons contributing to the neutrino flux at SK.

invariance the same weights are used for protons as for neutrons.

For the parts of the production phase-space not covered by the data the values of the tuning weights assigned are based on the average weight calculated in the nearby regions. The effects of the normalization uncertainties (dominant sources of the data errors, see σ_N in Table 8.1) are incorporated by scaling the Eichten and Allaby data by 15% and 10%, respectively, independently of each other. Out of the four possible combination (scaling Eichten data by 1.15 and Allaby by 1.10, scaling Eichten data by 0.85 and Allaby by 1.10, etc.), the one giving the largest variation in the flux predictions is chosen to represent the systematic uncertainty due to the data errors.

In the region with $x_F > 0.9$, it is assumed that the incident protons undergo collisions with small momentum transfer and are not destroyed in the interactions.

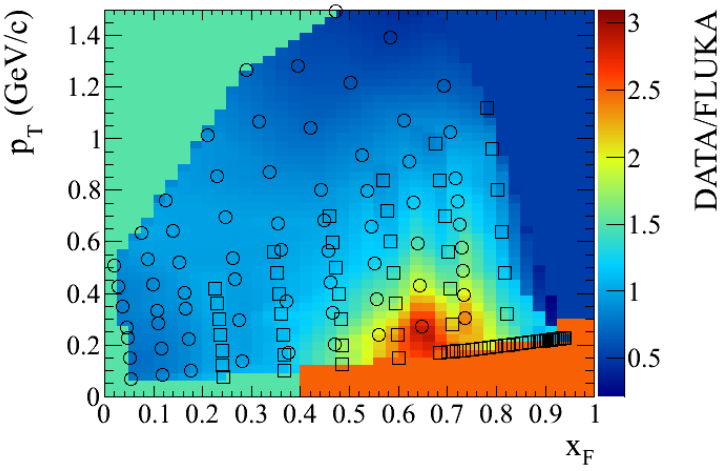

Figure 8.11: Ratio of the secondary proton production measurements to FLUKA predictions. The location of Eichten and Allaby measurements are indicated by circles and squares, respectively. Outside the phase space of the data, factors of 2.5, 1.5 and 0.5 are assigned for the regions coloured by red, green and blue, respectively.

Due to the lack of relevant data, a 100% uncertainty is currently assigned on the multiplicity in this region.

8.5 Production cross-section uncertainties

The systematic uncertainty in the production cross-section is conservatively taken to be represented by the magnitude of the quasi-elastic component σ_{qe}. This is based on the discrepancy observed between the cross-section measurements for protons of Denisov *et al.* [101] and those of Bellettini *et al.* [96], Carroll *et al.* [98], and NA61 [83]. This is illustrated in Fig. 8.12 where these data are plotted. For the measurement of the Bellettini *et al.*, the quasi-elastic contribution of 30.4 mb [83]

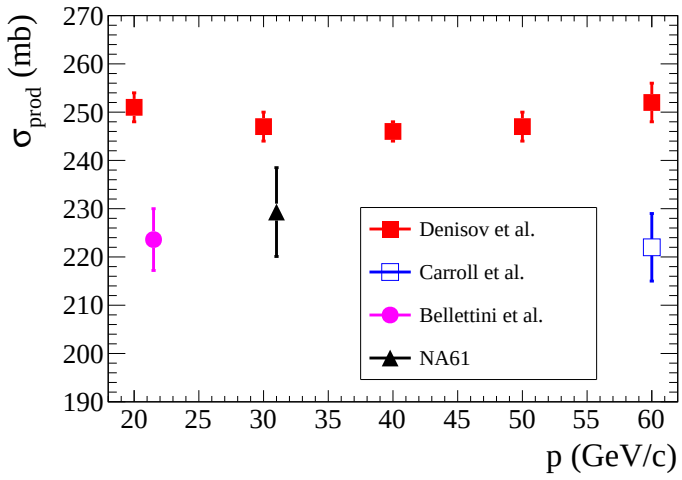

Figure 8.12: Production cross-section measurements for protons on graphite targets for momenta 20–60 GeV/c.

has been subtracted from the reported value of 254 mb. The fact that after the subtraction the measurement agrees well with the NA61 and Carroll results can be interpreted as that the magnitude of the discrepancy is roughly similar to the size of the quasi-elastic cross-section. A conservative approach is therefore taken by using σ_{qe} as the systematic uncertainty.

8.6 Proton beam uncertainties

The uncertainties in the proton beam parameters at the entrance of the baffle are obtained from an orbit and optics fit to the proton monitor data (see Appendix C for the details about the procedure). The values of these uncertainties are summarized in Table 8.2 for the Run I and II periods.

	Run I	Run II
$\bar{x}$ horizontal position (mm)	0.38	0.27
$\bar{y}$ vertical position (mm)	0.58	0.62
$\bar{x}'$ horizontal angle (mrad)	0.056	0.064
$\bar{y}'$ vertical angle (mrad)	0.286	0.320
$\mathrm{cov}(\bar{x}, \bar{x}')$ (mm mrad)	0.011	0.013
$\mathrm{cov}(\bar{y}, \bar{y}')$ (mm mrad)	0.065	0.079
σ_x horizontal profile width (mm)	0.11	0.26
σ_y vertical profile width (mm)	0.97	0.82
Twiss α_x	0.32	0.26
Twiss α_y	1.68	0.49

Table 8.2: Uncertainties in the proton beam parameters.

The dominant sources of the systematic uncertainties in the flux predictions are the beam position and angle in y (vertical direction). These are the two sources that will be considered here. As an example, Figs 8.13a and 8.13b show the ν_μ flux changes for ND280 and SK, respectively, when the $\bar{y}$ and $\bar{y}'$ are changed by one standard deviation. The ratio of the flux predictions obtained with a shifted beam to the nominal ones are plotted.

The uncertainty in the $y - y'$ is described with a bi-variate normal distribution $\mathcal{N}_p$ PDF:

$$\mathcal{N}_p(y, y') = \frac{1}{2\pi\delta_y\delta_{y'}\sqrt{1-\rho^2}} \exp\left(-\frac{1}{2(1-\rho^2)}\left[\frac{\Delta_y^2}{\delta_y^2} + \frac{\Delta_{y'}^2}{\delta_{y'}^2} - \frac{2\rho\Delta_y\Delta_{y'}}{\delta_y\delta_{y'}}\right]\right), \quad (8.16)$$

where:

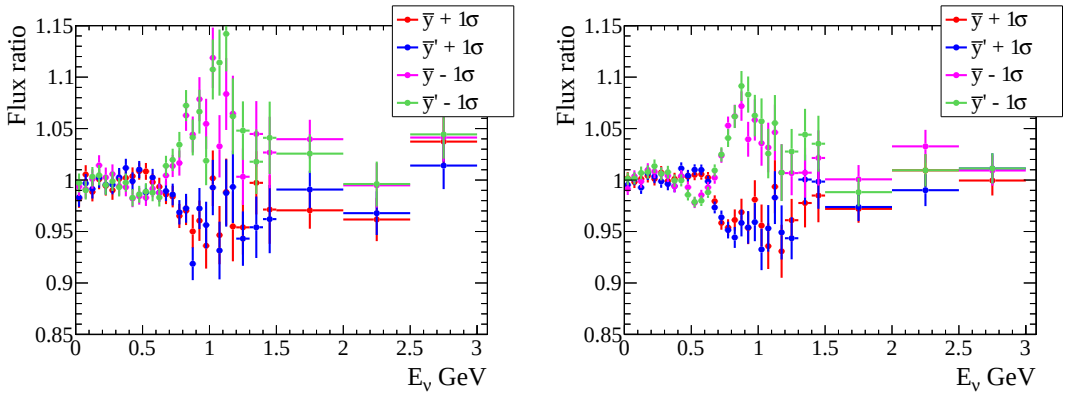

(a) Effects on ν_μ flux at ND280 **(b)** Effects on ν_μ flux at SK

Figure 8.13: Effects of proton beam variations on the ν_μ flux at the ND280 and SK detectors. The error bars represent the MC statistical errors.

- $\Delta_y = y - \bar{y}$
- $\Delta_{y'} = y' - \bar{y}'$
- δ_y and $\delta_{y'}$ are the uncertainties in y and y'
- ρ is the dimensionless correlation coefficient: $\rho = \mathrm{cov}(\bar{y}, \bar{y}')/\delta_y\delta_{y'}$.

The PDF is drawn for the Run I $y - y'$ proton beam conditions in Fig 8.14. The points used to produce the four cases in Fig. 8.13 are marked by stars. They lie on the isocontour curve

$$c = \frac{1}{2\pi\delta_y\delta_{y'}\sqrt{1-\rho^2}} e^{-1/2}, \tag{8.17}$$

which is also shown in Fig. 8.14.

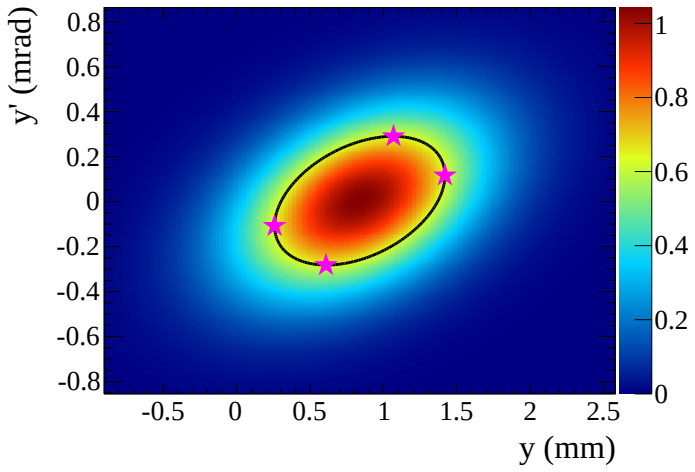

Figure 8.14: PDF for beam position and angle in vertical direction with Run I proton beam parameter values and uncertainties.

8.6.1 Propagating the proton beam uncertainties

In order to evaluate the effects of the proton beam uncertainties on the neutrino flux predictions, the parameter space described by the PDF in Eq. 8.16 needs to be sampled. To do this efficiently, a special MC sample was made with a large emittance in $y - y'$ phase-space. Since the primary proton information (position, direction, and momentum) is stored with each neutrino event, the proton information in the wide beam sample can be re-weighted to obtain a desired proton distribution. In other words, for given values of y and y' drawn randomly from Eq. 8.16 the neutrino flux predictions can be quickly obtained by picking the neutrino events from the wide beam sample that have the desired proton beam parameters.

The beam shape in $y - y'$ (and $x - x'$) is modeled as a bi-variate normal distri-

bution, which is defined in terms of the beam position $\bar{y}$, angle $\bar{y}'$, profile width σ_y, emittance ϵ_y, and Twiss α_y:

$$B(y, y'; \bar{y}, \bar{y}', \sigma_y, \epsilon_y, \alpha_y) = \frac{1}{2\pi\sigma_y\sigma_{y'}\sqrt{1-\rho_{yy'}^2}} \exp\left(-\frac{1}{2(1-\rho_{yy'}^2)}\mathcal{F}\right), \tag{8.18}$$

with

$$\mathcal{F} = \frac{(y-\bar{y})^2}{\sigma_y^2} + \frac{(y'-\bar{y}')^2}{\sigma_{y'}^2} - \frac{2\rho_{yy'}(y-\bar{y})(y'-\bar{y}')}{\sigma_y\sigma_{y'}},$$

where

- $\sigma_{y'} = \epsilon_y\sqrt{1+\alpha_y^2}/4\sigma_y$
- $\rho_{yy'} = -\alpha_y/\sqrt{1+\alpha_y^2}$.

For a given draw of y_i and y_i' from the PDF in Eq. 8.16, each neutrino event generated by protons with (y, y') coordinates in the wide beam sample is re-weighted according to

$$w(y, y') = \frac{B(y, y'; y_i, y_i', \sigma_y^n, \epsilon_y^n, \alpha_y^n)}{B(y, y'; y_w, y_w', \sigma_y^w, \epsilon_y^w, \alpha_y^w)}, \tag{8.19}$$

where superscripts n and w indicate that the parameters correspond to the actual beam conditions for a given run and wide beam conditions, respectively.

Using this approach a set of flux predictions is produced from the wide beam sample and the uncertainties are estimated from this ensemble.

8.7 Off-axis angle uncertainties

The neutrino beam profile is measured by the INGRID detector [104] and the direction of the neutrino beam is inferred from the measured profile centre. The uncertainty on the neutrino beam direction is estimated from the INGRID measurements and the associated experimental uncertainties.

8.8 Alignment uncertainties

After the installation in the helium vessel, the horn alignment was surveyed with respect to the proton beamline. The survey errors are a source of the systematic uncertainties for the flux predictions. In addition, the alignment of the target inside the first horn is also a source of the systematic uncertainties.

8.8.1 Horn alignment

Table 8.3 gives the summary of the horn alignment survey uncertainties. The definition of the coordinate axis is positive x is on the beam left, positive y is up, and positive s is in the direction of the proton beam.

	Uncertainty
x	0.3 mm
y	1.0 mm
s	1.0 mm

Table 8.3: Horn alignment uncertainties.

The alignment uncertainties are the same for all three horns.

The significance of the horn misalignment in different directions is estimated by moving all three horns in a correlated way by 1σ in a given direction. The results are illustrated in Figs. 8.15 and 8.16, where the ratios of the ν_μ flux generated with all the horns misaligned according to the corresponding uncertainties (Table 8.3) to the nominal flux are shown for ND280 and SK, respectively. The horn misalignment in the y direction has the largest effect on the ν_μ neutrino flux predictions. The effects of the misalignment in the other directions as well as other neutrino flavours are small and are dominated by the MC statistical errors. For this analysis only the effects of the horn misalignment in y direction will be considered.

To evaluate the uncertainty due to the horn alignment errors in y, four MC samples were generated:

- horn 2 moved up by 5 mm (=5σ), Φ^{+}_{H2}
- horn 2 moved down by 5 mm, Φ^{-}_{H2}
- horn 3 moved up by 5 mm, Φ^{+}_{H3}
- horn 3 moved down by 5 mm, Φ^{-}_{H3}.

The horn 1 alignment errors are not considered. This is due to the fact that the OTR monitor is aligned relative to the axis of the first horn and therefore the horn 1 alignment error is included in the proton beam parameter errors.

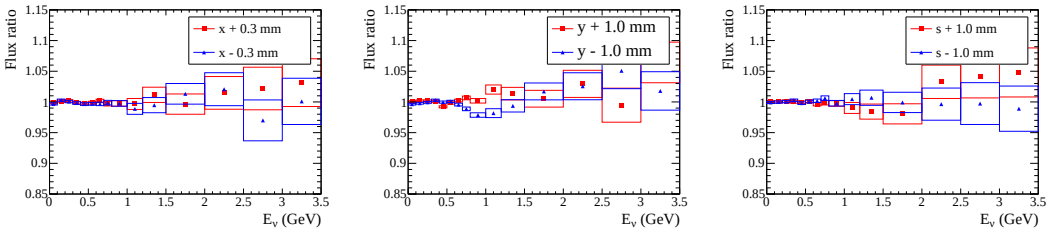

(a) x misalignment by ± 0.3 mm

(b) y misalignment by ± 1.0 mm

(c) s misalignment by ± 1.0 mm

Figure 8.15: Effects of the correlated misalignment in all three horns on the ν_μ flux at ND280.

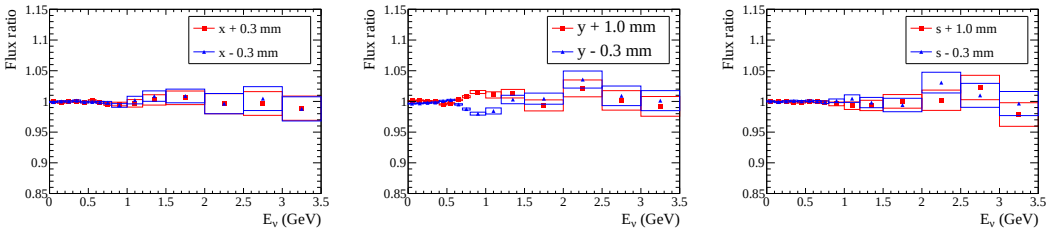

(a) x misalignment by ± 0.3 mm

(b) y misalignment by ± 1.0 mm

(c) s misalignment by ± 1.0 mm

Figure 8.16: Effects of the correlated misalignment in all three horns on the ν_μ flux at SK.

The uncertainties in the neutrino flux predictions due to the horn alignment are estimated from the four MC samples. This is done by taking an average of horn 2 alignment effects linearly combined (full correlation) with that of horn 3 and then scaled by a factor of 5 to estimate the effects at the 1σ level:

$$\delta\Phi_i = \frac{1}{5}\left(\frac{\Phi^+_{H2(i)} - \Phi^-_{H2(i)}}{\Phi^+_{H2(i)} + \Phi^-_{H2(i)}} + \frac{\Phi^+_{H3(i)} - \Phi^-_{H3(i)}}{\Phi^+_{H3(i)} + \Phi^-_{H3(i)}}\right), \tag{8.20}$$

where Φ_i stands for the flux at either ND280 or SK in the i^{th} energy bin.

Figs 8.17 and 8.18 show the fractional flux changes due to the correlated horn 2 and horn 3 alignment errors calculated according to Eq. 8.20.

8.8.2 Target alignment

Table 8.4 summarizes the target alignment from the survey after the target was installed inside the first horn. To evaluate the effects of the target misalignment,

horizontal tilt	1.3 mrad
vertical tilt	0.1 mrad

Table 8.4: Summary of the target alignment.

the target was rotated by 1.3 mrad in the horizontal and 0.1 mrad in the vertical directions. The MC sample produced with the rotated target is then compared to the nominal case and the magnitude of the flux change taken as the systematic uncertainty. The flux ratios of the misaligned target over nominal case for different

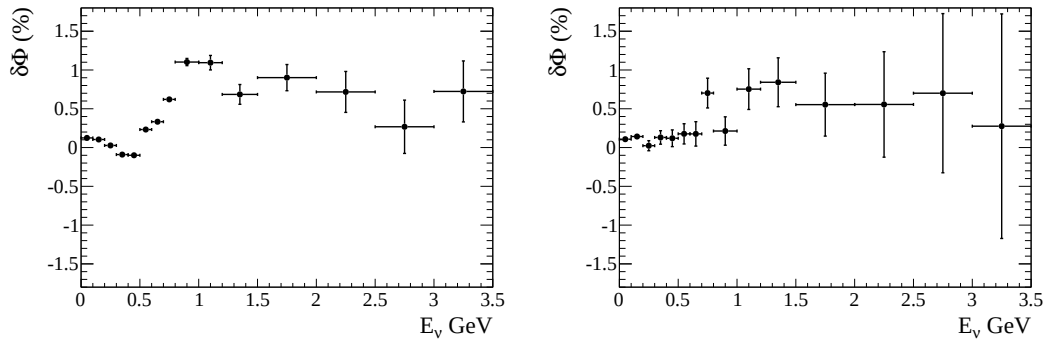

(a) Fractional change for ν_μ flux

(b) Fractional change for $\bar{\nu}_\mu$ flux

(c) Fractional change for ν_e flux

(d) Fractional change for $\bar{\nu}_e$ flux

Figure 8.17: The effects on the ND280 neutrino flux from the horn 2 and horn 3 misalignment by 1 mm.

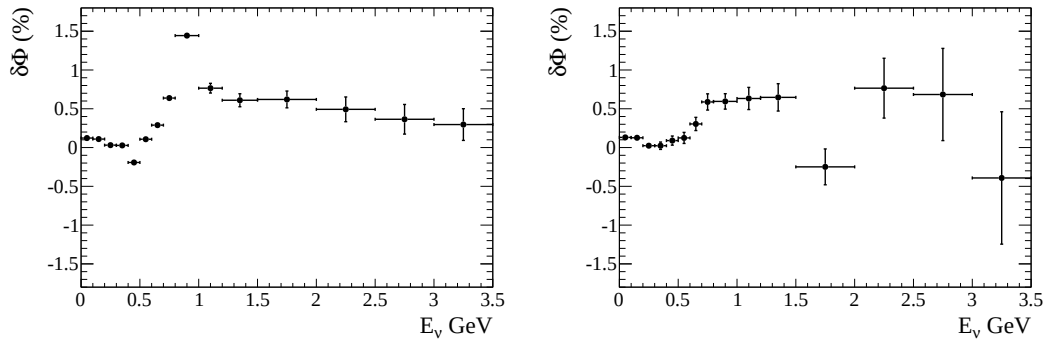

(a) Fractional change for ν_μ flux

(b) Fractional change for $\bar{\nu}_\mu$ flux

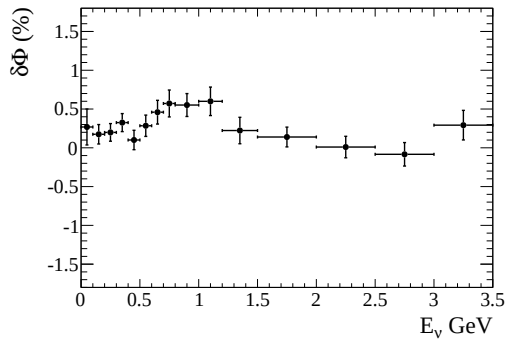

(c) Fractional change for ν_e flux

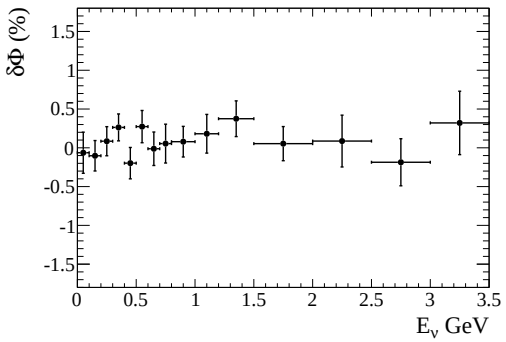

(d) Fractional change for $\bar{\nu}_e$ flux

Figure 8.18: The effects on the SK neutrino flux from the horn 2 and horn 3 misalignment by 1 mm.

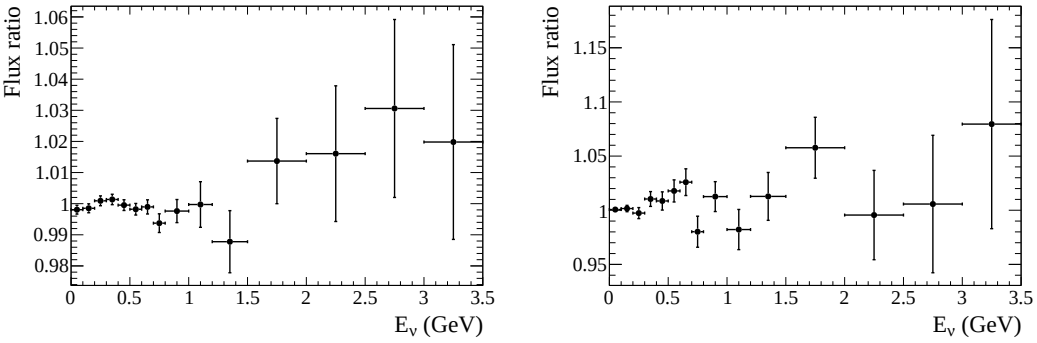

(a) Fractional change for ν_μ flux

(b) Fractional change for $\bar{\nu}_\mu$ flux

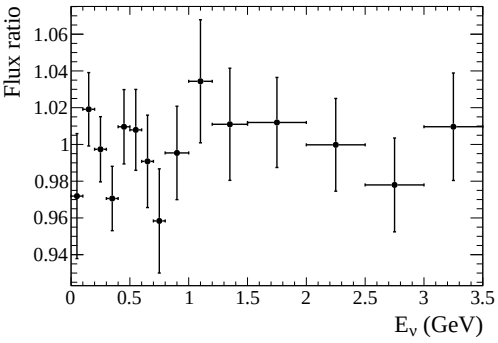

(c) Fractional change for ν_e flux

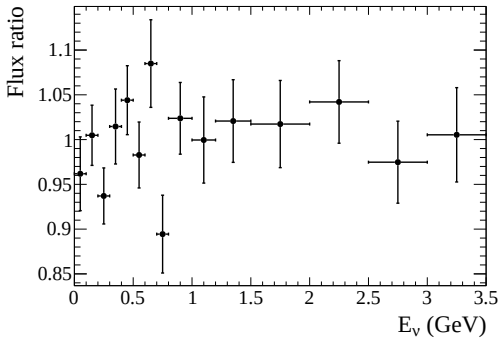

(d) Fractional change for $\bar{\nu}_e$ flux

Figure 8.19: Effects of target alignment for the ND280 neutrino flux predictions. Flux ratios (misaligned target to the nominal target configuration) are shown.

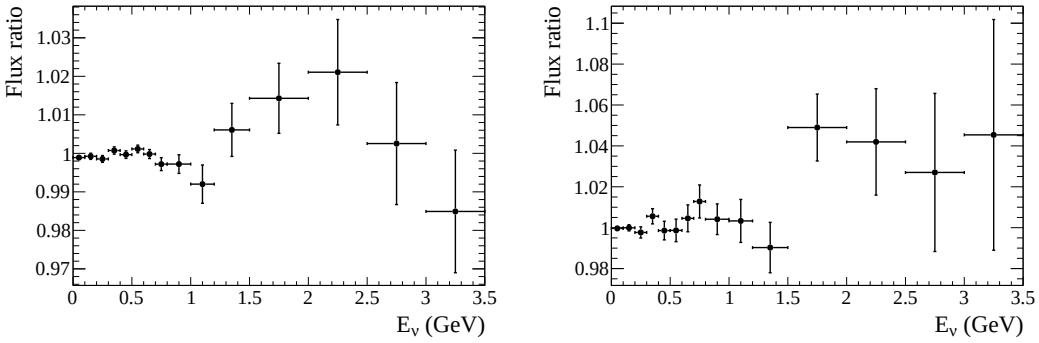

(a) Fractional change for ν_μ flux

(b) Fractional change for $\bar{\nu}_\mu$ flux

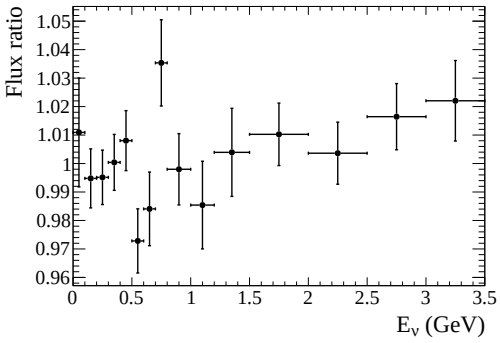

(c) Fractional change for ν_e flux

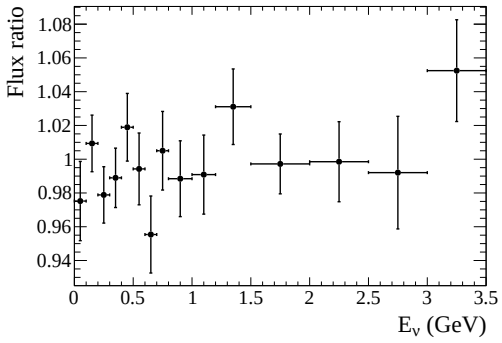

(d) Fractional change for $\bar{\nu}_e$ flux

Figure 8.20: Effects of target alignment for the SK neutrino flux predictions. Flux ratios (misaligned target to the nominal target configuration) are shown.

neutrino flavours are shown in Figs. 8.19 and 8.20 for the ND280 and SK detectors, respectively.

8.9 Horn current uncertainties

The horn current is monitored to a precision of $\sim 2\%$. For a 250 kA operation during Run I and Run II periods, this translates into a 5 kA uncertainty on the absolute current value supplied to the horns. The effect of this error is included as a systematic uncertainty in the neutrino flux predictions.

8.10 Total systematic uncertainty and flux covariance

The total flux covariance is obtained by summing the contributions from each error source. The fractional uncertainties (square root of the diagonal elements of the flux covariance matrix) are shown in Figs. 8.21 and 8.22 for the neutrino flux predictions at the ND280 and SK detector, respectively.

The entire flux covariance matrix is shown in Fig. 8.23. The x and y axes correspond to the bin numbers whose ordering follows the convention shown in Fig. 8.1. As can be seen the matrix is symmetric. The non-zero off-diagonal elements indicate (anti-)correlations between energy bins for different neutrino flavours and the two detectors.

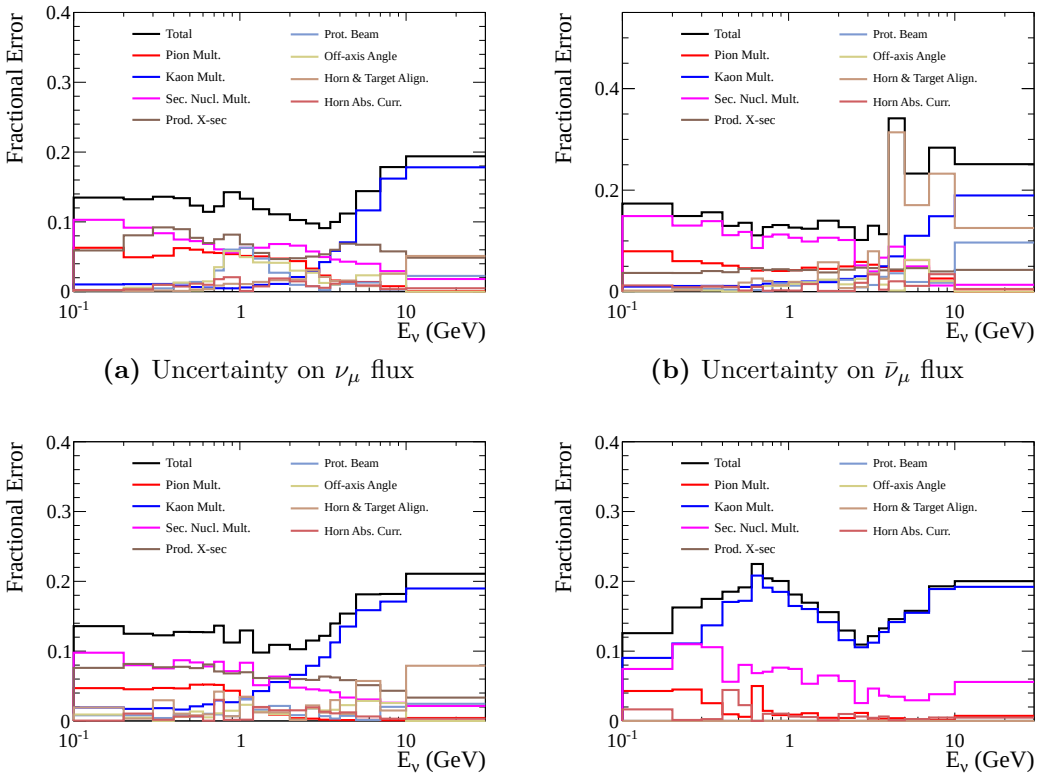

(a) Uncertainty on ν_μ flux

(b) Uncertainty on $\bar{\nu}_\mu$ flux

(c) Uncertainty on ν_e flux

(d) Uncertainty on $\bar{\nu}_e$ flux

Figure 8.21: Fractional uncertainties for ND280 flux predictions.

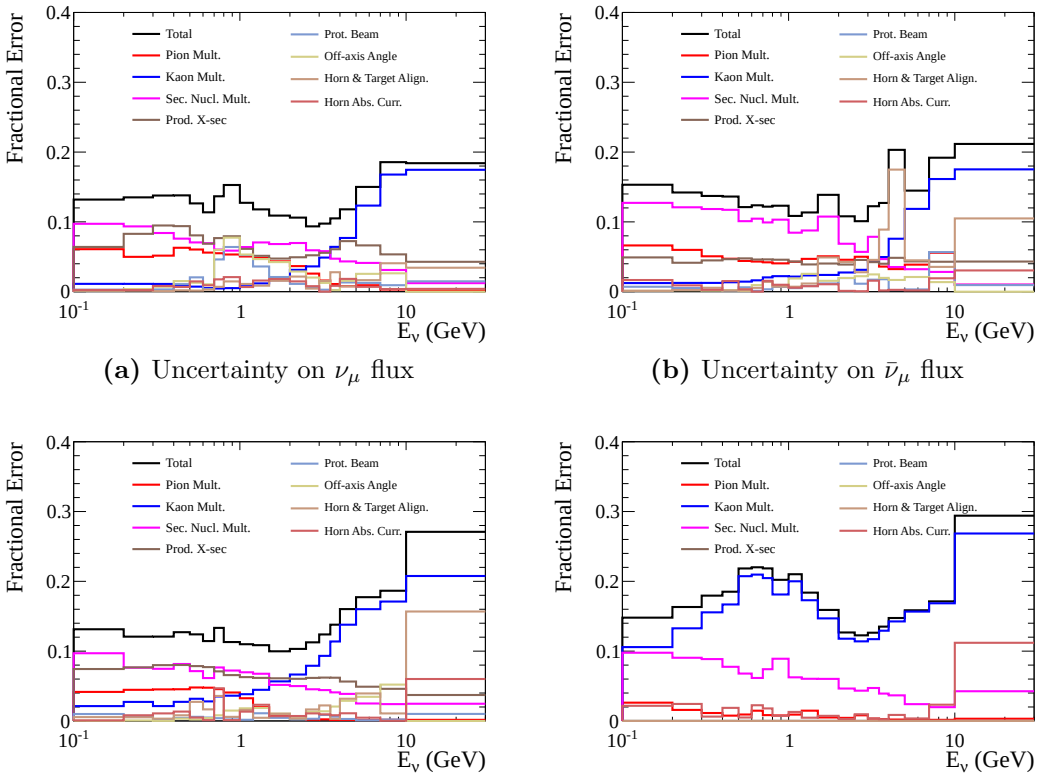

(a) Uncertainty on ν_μ flux

(b) Uncertainty on $\bar{\nu}_\mu$ flux

(c) Uncertainty on ν_e flux

(d) Uncertainty on $\bar{\nu}_e$ flux

Figure 8.22: Fractional uncertainties for SK flux predictions.

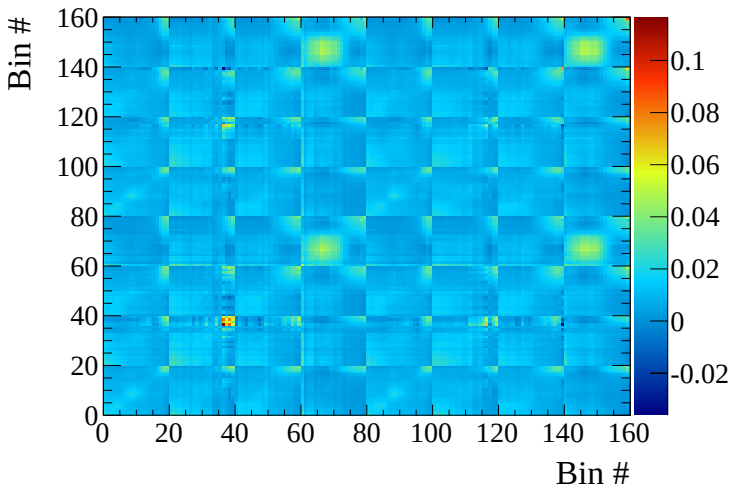

Figure 8.23: Flux covariance matrix. The square root of diagonal elements corresponds to fractional uncertainties for a given energy bin and neutrino flavour.

9 Effects of Flux Systematic Uncertainties on Oscillation Parameters

As discussed in the previous chapter, the systematic uncertainties in the neutrino flux predictions for T2K are encapsulated in the flux covariance matrix $\mathbf{V}^b$. We will now consider the effects of $\mathbf{V}^b$ on the oscillation searches at T2K. We will begin by looking at the ν_μ disappearance and the effects $\mathbf{V}^b$ has on the determination of the θ_{23} and Δm^2_{32} oscillation parameters. We will then consider the ν_e appearance and evaluate the impact of the flux systematic uncertainties on the search for the value of the θ_{13} mixing angle.

9.1 ν_μ disappearance search

In this section we will consider two types of analysis. One is the single detector approach where only the SK measurements are considered. The other uses the information from both near and far detectors. For the single detector approach, the expected flux of the muon neutrinos at SK is evaluated from the JNUBEAM

$\Phi^{\mathrm{SK}}_{\nu_\mu}(E)$ predicted flux as

$$\Phi^{\mathrm{SK,exp}}_{\nu_\mu}(E;\sin^2 2\theta_{23},\Delta m^2_{32}) = P^{\mathrm{SK}}_{\mu\mu}(E;\sin^2 2\theta_{23},\Delta m^2_{32})\Phi^{\mathrm{SK}}_{\nu_\mu}(E), \tag{9.1}$$

where $P^{\mathrm{SK}}_{\mu\mu}(E;\sin^2 2\theta_{23},\Delta m^2_{32})$ is the ν_μ survival probability at the position of SK.

For the two detector approach, the near-to-far extrapolation scheme is adopted. In this case, the expected the expected ν_μ flux at SK is evaluated as

$$\Phi^{\mathrm{SK,exp}}_{\nu_\mu}(E;\sin^2 2\theta_{23},\Delta m^2_{32}) = R^{\nu_\mu}_{\mathrm{F/N}}(E)P^{\mathrm{SK}}_{\mu\mu}(E;\sin^2 2\theta_{23},\Delta m^2_{32})\Phi^{\mathrm{ND280,obs}}_{\nu_\mu}(E), \tag{9.2}$$

where quantity $R^{\nu_\mu}_{\mathrm{F/N}}(E)$, the far/near ratio, is obtained by taking the ratio of the JNUBEAM predicted ν_μ neutrino fluxes for SK and ND280:

$$R^{\nu_\mu}_{\mathrm{F/N}}(E) = \frac{\Phi^{\mathrm{SK}}_{\nu_\mu}(E)}{\Phi^{\mathrm{ND280}}_{\nu_\mu}(E)}. \tag{9.3}$$

Fig 9.1 shows the plot of the $R^{\nu_\mu}_{\mathrm{F/N}}$. The fractional uncertainties on the ratio calculated from the flux covariance $\mathbf{V}^b$ are shown in Fig 9.2. For reference, the fractional errors in the predicted ν_μ flux (Fig. 8.22) are also shown. The uncertainty on the ratio is $< 4\%$ even though the flux uncertainties are $10 - 20\%$.

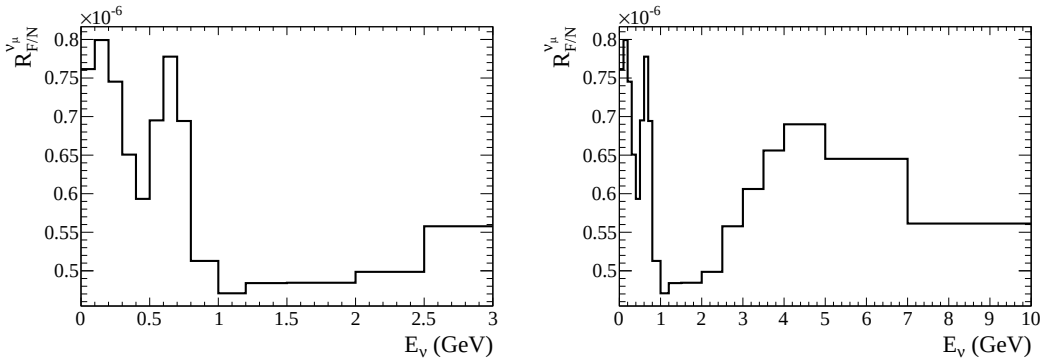

(a) Far/near ratio at low energies **(b)** Far/near ratio up to 10 GeV

Figure 9.1: Far/near ratio for ν_μ flux extrapolation.

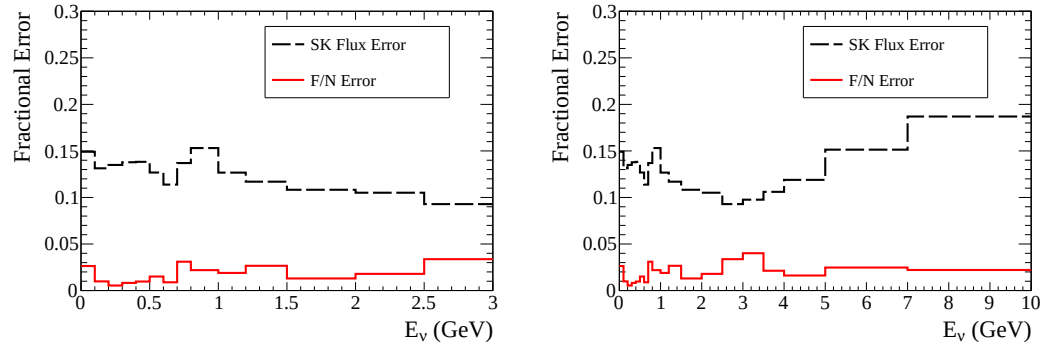

(a) Fractional uncertainty in ν_μ flux and far/near ratio at low energies **(b)** Fractional uncertainty in ν_μ flux and far/near ratio up to 10 GeV

Figure 9.2: Fractional uncertainty in ν_μ flux and far/near ν_μ/ν_μ ratio.

9.1.1 Analysis overview

The muon neutrino disappearance is studied by counting the number of muons detected at SK. These muons are produced in the CC interactions with the water nuclei and identified by the pattern of the Cherenkov light they emit in the detector.

The contributions from non-zero θ_{13} to the ν_μ survival probability in Eq. 3.31

are ignored and the following approximation is used in this analysis:

$$P^{\mathrm{SK}}_{\mu\mu}(E; \sin^2 2\theta_{23}, \Delta m^2_{32}) \simeq 1 - \sin^2 2\theta_{23} \sin^2 \Delta_{32}. \tag{9.4}$$

Also, in the case of the far/near extrapolation, we will take $\Phi^{\mathrm{ND280,obs}}_{\nu_\mu}(E) = \Phi^{\mathrm{ND280}}_{\nu_\mu}(E)$, *i.e.*, replace the observed neutrino energy spectrum with the predicted one. Thus the ND280 detector effects will be ignored.

The SK ν_μ MC events are selected by requiring:

- event is fully contained in the fiducial volume (FCFV)
- the visible energy is greater than 30 MeV ($E_{vis} > 30$ MeV)
- the event is a CC event with a single μ-like ring.

The reconstructed energy spectra of the selected events with $\sin^2 2\theta_{23} = 0$ (no oscillation) and $\sin^2 2\theta_{23} = 1.0$ (maximal mixing) are shown in Figs. 9.3a and 9.3b for $\Delta m^2_{32} = 2.4 \times 10^{-3}$ eV^2.

To study the effects of systematic uncertainties for some set of the oscillation parameters, a large number of pseudo-experiments is performed. For each such experiment the relevant systematic parameters $b^{\mathrm{ND80}}_{\nu_\mu}(E)$ and $b^{\mathrm{SK}}_{\nu_\mu}(E)$ are randomly drawn from the PDF in Eq. 8.2.

In case of the single detector approach, an "observed" reconstructed energy

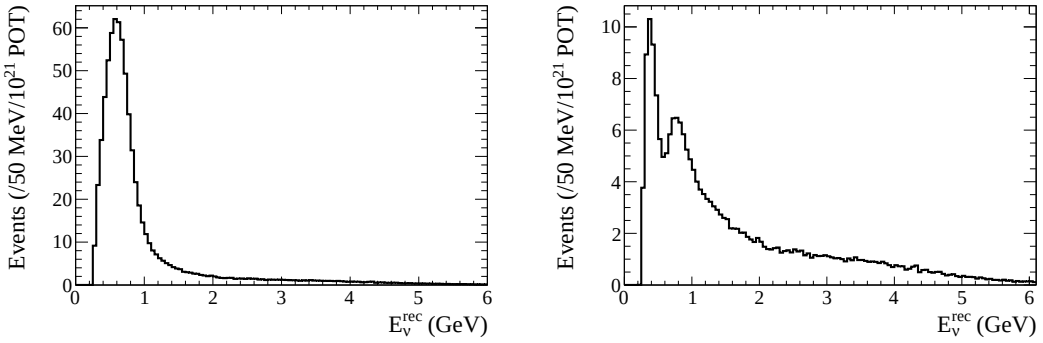

(a) Reconstructed ν_μ spectrum with $\sin^2 2\theta_{23} = 0.0$

(b) Reconstructed ν_μ spectrum with $\sin^2 2\theta_{23} = 1.0$

Figure 9.3: Reconstructed ν_μ spectrum at SK for single ring μ-like FCFV events. The mass difference $\Delta m^2_{32} = 2.4 \times 10^{-3}$ eV^2.

spectrum is produced by re-weighting the MC predicted one by

$$w^n(E) = b^{\mathrm{SK}}_{\nu_\mu}(E). \tag{9.5}$$

In the far/near extrapolation approach, the re-weighting is done as

$$w^n(E) = \frac{R^n_{\mathrm{F/N}}}{R^{\mathrm{true}}_{\mathrm{F/N}}} = \frac{b^{\mathrm{SK}}_{\nu_\mu}(E)}{b^{\mathrm{ND80}}_{\nu_\mu}(E)}. \tag{9.6}$$

These flux weights as well as the oscillation probability are functions of the true neutrino energy. As a first step in the analysis, a 2D distribution of events in the $E_\nu - E^{\mathrm{rec}}_\nu$ plane is constructed. This distribution is obtained from the selected SK MC event sample assuming no oscillations and is shown in Fig. 9.4. The projections of the y bins on the horizontal axis gives the spectrum identical to the one shown

in Fig. 9.3a. For each set of the flux weights and given values of the oscillation parameters, the reconstructed energy spectrum is obtained by re-weighting the $E_\nu - E_\nu^{\rm rec}$ distribution and then summing over all E_ν bins.

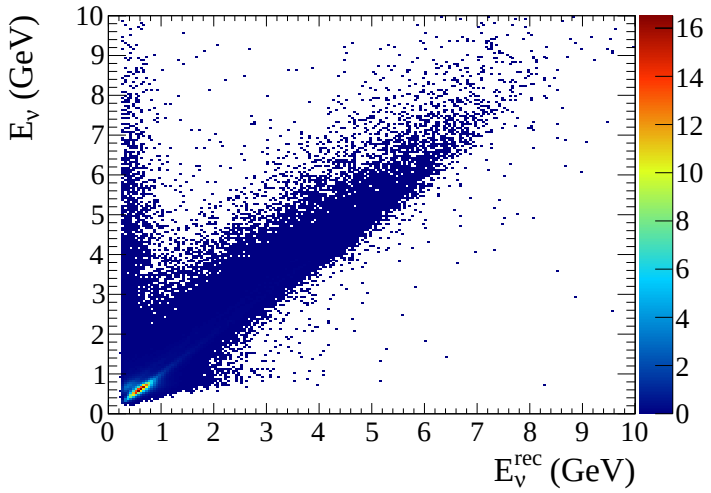

Figure 9.4: Distribution of the selected events in $E_\nu - E_\nu^{\rm rec}$ plane.

The probability that one observes a total number of events $n^{\rm obs}$ given the expectation of $n^{\rm exp}$ is described by the Poisson distribution:

$$P(n^{\rm obs}; n^{\rm exp}) = \frac{(n^{\rm exp})^{n^{\rm obs}} e^{-n^{\rm exp}}}{n^{\rm obs}!}. \tag{9.7}$$

The probability that there are $n_i^{\rm obs}$ events in the i^{th} energy bin is given by the multinomial distribution:

$$P(n_i^{\rm obs}; n_i^{\rm exp}, n^{\rm exp}) = n^{\rm obs} \prod_i \frac{1}{n_i^{\rm obs}} \left(\frac{n_i^{\rm exp}}{n^{\rm exp}}\right)^{n_i^{\rm obs}}. \tag{9.8}$$

The likelihood of observing the spectrum n_i^{obs} is therefore a joint probability of the Poisson and multinomial probability distributions:

$$L = e^{-n^{\text{exp}}} \prod_i \frac{1}{n_i^{\text{obs}}} (n_i^{\text{exp}})^{n_i^{\text{obs}}} = \prod_i e^{-n_i^{\text{exp}}} \frac{1}{n_i^{\text{obs}}} (n_i^{\text{exp}})^{n_i^{\text{obs}}}. \tag{9.9}$$

Taking the natural logarithm of Eq. 9.9 and using the freedom that the shape of the resultant function is unchanged when a constant is added or subtracted, we can write:

$$-2 \ln L = 2 \sum_i \left[n_i^{\text{obs}} \ln \left(\frac{n_i^{\text{obs}}}{n_i^{\text{exp}}} \right) - (n_i^{\text{obs}} - n_i^{\text{exp}}) \right]. \tag{9.10}$$

The quantity $-2 \ln L$ has a χ^2 distribution. To obtain the values of $\sin^2 2\theta_{23}$ and Δm^2_{32} that best describe the pseudo-experiment data, Eq. 9.10 is minimized by varying the oscillation parameters and consequently changing n_i^{exp}.

For each pseudo-experiment χ^2 is computed with true and best fit values of the oscillation parameters and, following the approach of [105], the difference between the two χ^2 values is taken

$$\Delta\chi^2 = \chi^2_{\text{true}} - \chi^2_{\text{best}}. \tag{9.11}$$

As a final step, a value of $\Delta\chi^2_{\text{crit}}$ is chosen such that 68.27% of the pseudo-experiments fall into $\Delta\chi^2 < \Delta\chi^2_{\text{crit}}$ sub-sample. The uncertainties in the oscillation parameters due to the flux systematic uncertainties are then evaluated from the selected sub-

sample by taking the largest deviation of the best fit oscillation parameters from their true values.

9.1.2 Results

A raster scan is performed to probe the oscillation parameter phase-space. This is done by choosing three values of $\sin^2 2\theta_{23}$: 0.90, 0.95, and 1.00 (cf. Table 3.1). At each of these values Δm^2_{32} is scanned in the interval between $2.0 - 3.0 \times 10^{-3}$ eV^2 in steps of 0.2×10^{-3} eV^2. Five thousand pseudo-experiments are used at each point in the oscillation parameters phase-space.

Fig. 9.5 shows the uncertainties in the Δm^2_{32} and $\sin^2 2\theta_{23}$ oscillation parameters obtained from the variations of the flux predictions according to the systematic uncertainties. Results for both one-detector and two-detector approaches are shown. While the uncertainty in the flux predictions is too high to meet the T2K goal of $\delta(\Delta m^2_{32}) \sim 10^{-4}$ and $\delta(\sin^2 2\theta_{23}) \sim 1\%$ precision, the uncertainties in the F/N ratio are rather small. The flux uncertainties are therefore not expected to be a dominant error source limiting the precision of the experiment in the future.

9.2 ν_e appearance search

The electron neutrinos are detected via electrons they produce in the CC interactions with the water nuclei. At SK electrons are distinguished from muons by

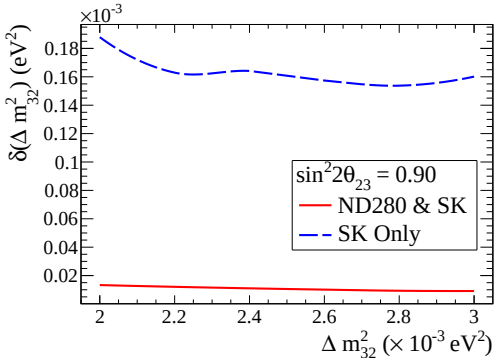

(a) Uncertainty in Δm^2_{32} from flux systematic errors with $\sin^2 2\theta_{23} = 0.90$

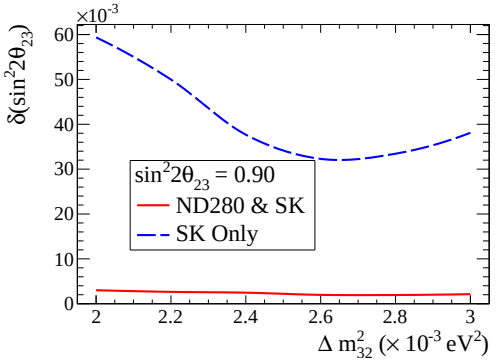

(b) Uncertainty in $\sin^2 2\theta_{23}$ from flux systematic errors with $\sin^2 2\theta_{23} = 0.95$

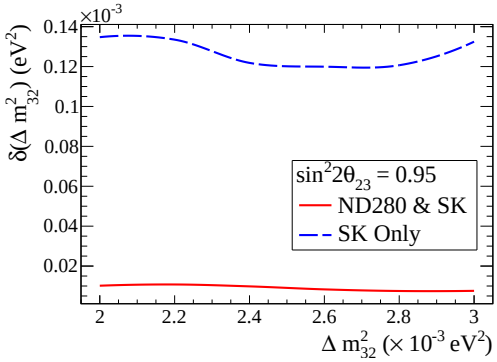

(c) Uncertainty in Δm^2_{32} from flux systematic errors with $\sin^2 2\theta_{23} = 0.90$

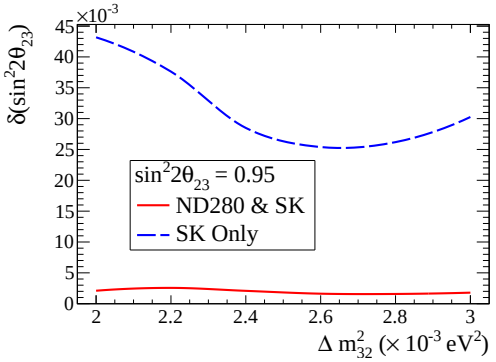

(d) Uncertainty in $\sin^2 2\theta_{23}$ from flux systematic errors with $\sin^2 2\theta_{23} = 0.95$

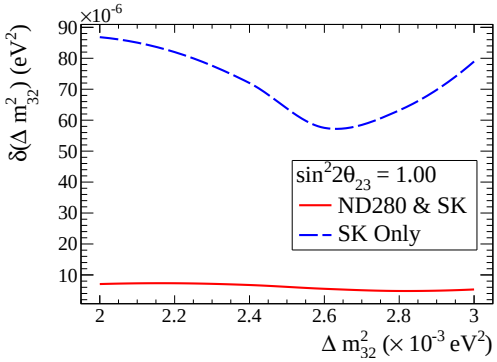

(e) Uncertainty in Δm^2_{32} from flux systematic errors with $\sin^2 2\theta_{23} = 1.00$

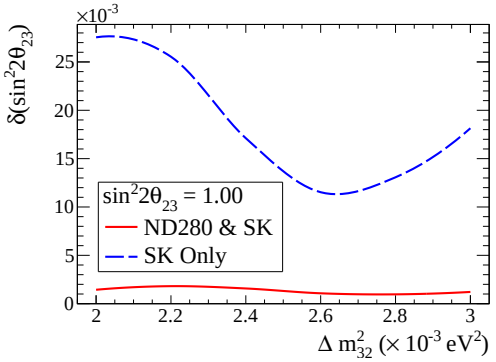

(f) Uncertainty in $\sin^2 2\theta_{23}$ from flux systematic errors with $\sin^2 2\theta_{23} = 1.00$

Figure 9.5: Uncertainties in the Δm^2_{32} and $\sin^2 2\theta_{23}$ oscillation parameters resulting from the systematic uncertainties in the flux predictions.

fuzzier Cherenkov ring patterns in the detector.

The two most important backgrounds in the search for ν_e appearance at T2K are the intrinsic ν_e contamination in the neutrino beam and π^0 mesons produced in NC interactions (NCπ^0) of ν_μ that are incorrectly identified as electrons. In this section we will evaluate the uncertainties in the background predictions arising from the flux systematic uncertainties. Similar to the previous section, these uncertainties will be evaluated with and without ND280 measurement of the ν_μ flux.

The contributions to the number of ν_e detected at SK come from:

- $\nu_\mu \to \nu_e$ oscillations
- ν_μ induced background
- $\bar{\nu}_\mu$ induced background
- ν_e beam contamination.

For the ν_μ-induced background, the flux predictions are evaluated according to Eqs. 9.1 and 9.2 for one-detector and two-detector scenario, respectively. For $\bar{\nu}_\mu$, no near detector information is used and the expected flux is obtained from

$$\Phi^{\mathrm{SK,exp}}_{\bar{\nu}_\mu}(E;\sin^2 2\theta_{23},\Delta m^2_{32}) = P^{\mathrm{SK}}_{\mu\mu}(E;\sin^2 2\theta_{23},\Delta m^2_{32})\Phi^{\mathrm{SK}}_{\bar{\nu}_\mu}(E). \tag{9.12}$$

In the case of the ν_e background prediction, the expected ν_e flux at SK with no

ND280 information is given by

$$\Phi_{\nu_e}^{\mathrm{SK,exp}}(E;\sin^2 2\theta_{23},\Delta m^2_{32},\sin^2 2\theta_{13}) = P_{\mu e}^{\mathrm{SK}}(E;\sin^2 2\theta_{23},\Delta m^2_{32},\sin^2 2\theta_{13})\Phi_{\nu_e}^{\mathrm{SK}}(E). \tag{9.13}$$

For the two detector case, the near-to-far extrapolation is adopted again:

$$\Phi_{\nu_e}^{\mathrm{SK,exp}}(E;\sin^2 2\theta_{23},\Delta m^2_{32},\sin^2 2\theta_{13}) = R_{\mathrm{F/N}}^{\nu_e}(E)P_{\mu e}^{\mathrm{SK}}(E;\sin^2 2\theta_{23},\Delta m^2_{32},\sin^2 2\theta_{13}) \times \Phi_{\nu_\mu}^{\mathrm{ND280,obs}}(E). \tag{9.14}$$

The far/near ratio in this case has the form

$$R_{\mathrm{F/N}}^{\nu_e}(E) = \frac{\Phi_{\nu_e}^{\mathrm{SK}}(E)}{\Phi_{\nu_\mu}^{\mathrm{ND280}}(E)}. \tag{9.15}$$

The ratio is shown in Fig. 9.6.

The fractional uncertainties in the expected neutrino flux from the systematic uncertainties in the flux predictions are shown in Fig. 9.7. As this figure illustrates, there is still an advantage in doing the near-to-far extrapolation, as the flux uncertainties are reduced. The reduction, however, is not as significant as with the case of the ND280 ν_μ to the SK ν_μ extrapolation discussed in the previous section.

To study the effects of the flux uncertainties, we will use the same selection

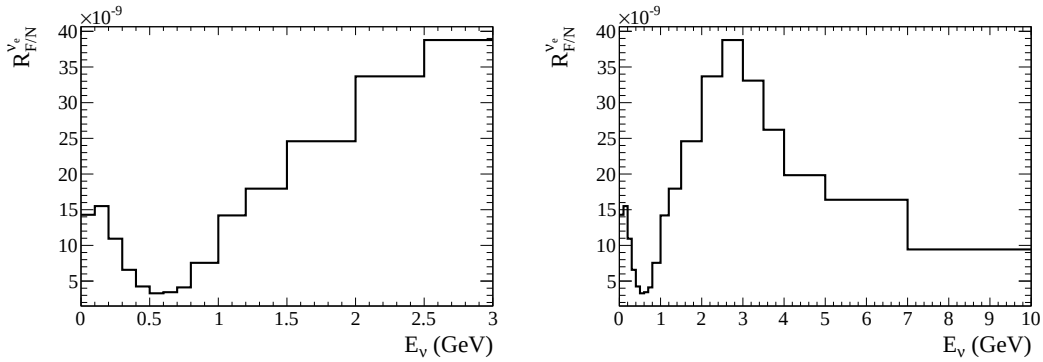

(a) Far/near ratio at low energies

(b) Far/near ratio up to 10 GeV

Figure 9.6: Far/near ratio for ν_e flux extrapolation.

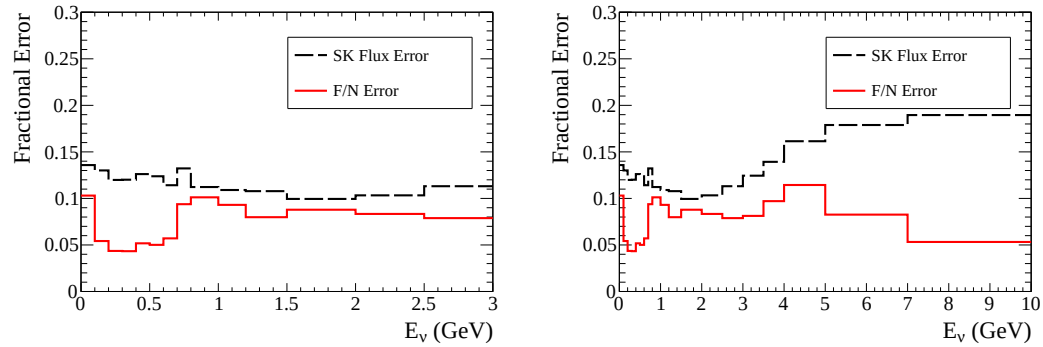

(a) Fractional uncertainty in ν_e flux and far/near ratio at low energies

(b) Fractional uncertainty in ν_e flux and far/near ratio up to 10 GeV

Figure 9.7: Fractional uncertainty in ν_e flux and far/near ν_e/ν_μ ratio.

criteria for the SK events as the ones in the T2K ν_e analysis [46]:

- events are FCFV events
- the visible energy is greater than 100 MeV
- events are associated with a single e-like ring
- no delayed electrons are observed

- the reconstructed invariant mass is less than 105 MeV (suppresses π^0 background)

- the reconstructed energy is less than 1250 MeV.

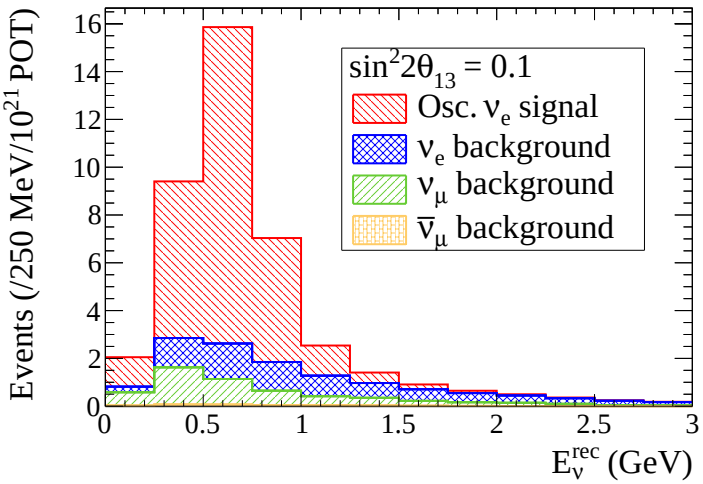

Figure 9.8: Distribution of the selected ν_e events for $\sin^2 2\theta_{13} = 0.1$.

Fig. 9.8 shows the MC predicted reconstructed energy spectrum for ν_e events at SK for $\sin^2 2\theta_{13} = 0.1$. All but the reconstructed energy cut have been applied in this figure. For the ν_e appearance signal, the oscillation probability in Eq. 3.47 is used with the following parameter values:

- $\Delta m^2_{32} = 2.4 \times 10^{-3}$ eV^2

- $\Delta m^2_{21} = 7.6 \times 10^{-5}$ eV^2

- $\sin^2 2\theta_{12} = 0.8704$

- $\sin^2 2\theta_{23} = 1.0$
- $a = 3.2$ g/cm^3
- $\delta = 0$
- normal hierarchy: $\Delta m^2_{32} > 0$.

The ν_μ (and $\bar{\nu}_\mu$) survival probability is calculated according to Eq. 9.4, while the ν_e appearance probability is obtained from Eq. 3.27.

The fractional contributions from different sources to the total number of the selected ν_e events are summarized in Table 9.1 for the oscillation signal assuming $\sin^2 2\theta_{13} = 0.1$.

ν_e signal	74.5%
ν_e background	13.5%
ν_μ background	11.3%
$\bar{\nu}_\mu$ background	0.7%

Table 9.1: Fractional contributions to the total number of selected ν_e events assuming oscillation signal with $\sin^2 2\theta_{13} = 0.1$.

The fractional uncertainties in each contribution as well as the total fractional error in the ν_e expected background from the flux systematic uncertainties are summarized in Table 9.2. It should be noted that the uncertainties for each background source are not weighted by the size of the respective contribution. The total uncertainty, however, takes the fractional contribution of each background source into account.

	SK only	ND280 & SK
ν_e background	10.9%	5.6%
ν_μ background	10.5%	0.7%
$\bar{\nu}_\mu$ background	10.6%	10.6%
Total	10.3%	3.1%

Table 9.2: Fractional uncertainties in each contribution and the total fractional error in the expected ν_e background computed with $\sin^2 2\theta_{13} = 0$.

As Table 9.2 illustrates, the contribution of the flux systematic errors is on the order of 3% with the near-to-far extrapolation. It should be noted that the current uncertainty from the uncertainties in the neutrino interaction cross-sections is on the order of 14%, while the contribution from the systematic uncertainties in the SK measurement is $\sim 15\%$ [46]. The uncertainty in the flux predictions are not a dominant systematic error and, until cross-section and detector systematic errors are significantly reduced, should not limit the precision of the experiment.

As a reference, Fig. 9.9 shows the T2K sensitivity to $\sin^2 2\theta_{13}$ for the normal mass hierarchy. The sensitivity curves are constructed for 5%, 10%, and 20% fractional uncertainties in the expected background.

Fig. 9.10 shows the first results of the ν_e appearance analysis of the T2K data accumulated with 1.431×10^{20} POT. In this data set, six ν_e events that passed all selection criteria were observed while the expected background if $\theta_{13} = 0$ is 1.5 events. The T2K result therefore was the first indication of non-zero θ_{13} at $> 90\%$ confidence.

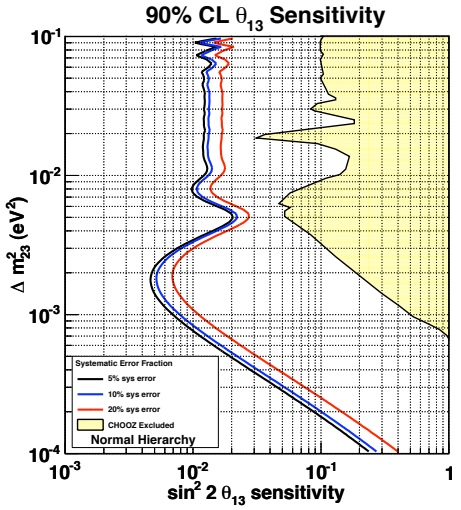

(a) Sensitivity to θ_{13} at the 90% confidence level as a function of Δm^2_{23}. The CHOOZ excluded region is shown in yellow.

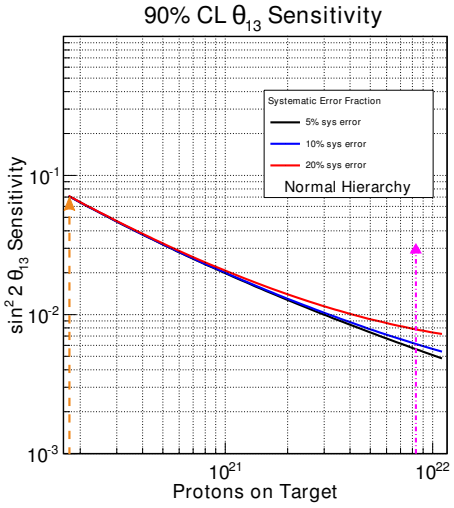

(b) Sensitivity to θ_{13} at the 90% confidence level as a function of protons on target. The orange arrow indicates the current exposure while the magenta one shows the exposure for a 5 year run.

Figure 9.9: The sensitivity of the T2K experiment to θ_{13} for normal hierarchy and fractional uncertainties in the background of 5% (black), 10% (blue), and 20% (red).

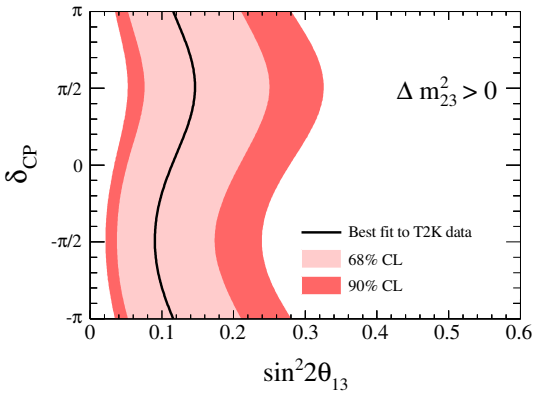

(a) Normal mass hierarchy

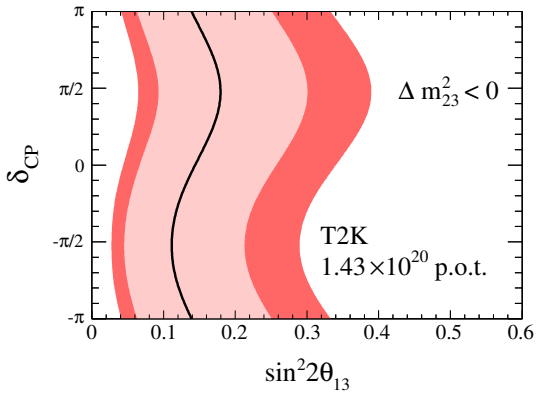

(b) Inverted mass hierarchy

Figure 9.10: T2K best-fit and allowed region of $\sin^2 2\theta_{13}$ and the CP phase δ at 68% and 90% C.L for normal and inverted hierarchy.

10 Conclusions

The T2K experiment is the long baseline oscillation experiment aiming to observe ν_μ to ν_e oscillations and determine the θ_{13} mixing angle. In addition, it also plans to make precise measurements of the Δm^2_{32} and $\sin^2 2\theta_{23}$ parameters.

Successful operation of the T2K experiment relies on the stability of the high intensity proton beam used for the neutrino production. To ensure this is possible an Optical Transition Radiation proton beam monitor has been designed and commissioned. The unique feature of this detector is its ability to operate in the high radiation environment near the T2K target. It has been successfully used to monitor the proton beam stability and determine the beam position and angle with the accuracy necessary to meet the T2K goal of measuring the atmospheric parameters with the precision of $\delta(\Delta m^2_{32}) \sim 10^{-4}$ eV^2 and $\delta(\sin^2 2\theta_{23}) \sim 0.01$.

To achieve high sensitivity to the small θ_{13} mixing angle and significantly improve the precision of the determination of θ_{23} and Δm^2_{32}, T2K uses two neutrino detectors, ND280 and SK, to measure the neutrino flux near the production site

and at the peak of the oscillation probability, respectively. Including the ND280 data into the analysis of the oscillation signals requires a way to relate these observations to the far detector measurements. This connection is derived from the neutrino flux predictions for each detector. This has been the primary focus of this work.

One of the most challenging aspects of determining the neutrino flux is the evaluation of particle yields in the hadronic interactions of the proton beam with the target. The strategy adopted by T2K is to rely on the available hadron production data as much as possible in order to reduce systematic uncertainties.

As the majority of the muon neutrinos are generated in decays of pions, understanding the production of these particles is therefore the first priority. The pion production data from the NA61/SHINE experiment has been instrumental in addressing this issue.

Since the primary goal of the T2K experiment is to detect ν_e appearance in the muon neutrino beam, understanding the intrinsic contamination of the electron neutrinos in the neutrino beam is also critical. A large fraction of these neutrinos come from the decays of muons that are produced along with ν_μ neutrinos in the pion decays. This contribution is therefore well described by the data for pion production from the NA61 experiment. A sizable fraction of the beam electron neutrinos, however, also come from the kaon decays. In this thesis, the analysis

of this contribution has been performed using the NA61 measurement of the K^+ multiplicity in conjunction with the kaon production data from other experiments.

The absolute uncertainty in the ν_μ and ν_e predicted flux for neutrino energies below 3 GeV (where the majority of the T2K neutrino flux is) is under 15%. The relative uncertainty between the neutrino flux predictions (without the contributions from the uncertainties in the ND280 measurements) for ND280 and SK detectors is on the order of 3% for muon neutrinos and between 5-10% for electron neutrinos. The uncertainty on the total number of the beam electron neutrinos expected to be reconstructed in the SK with energies between 100–1250 MeV is on the order of 3%. The systematic uncertainties in the neutrino flux predictions are not expected to be dominant for the oscillation searches at T2K until the errors associated with the neutrino interaction cross-sections and detector measurements are reduced.

To conclude, we would like to emphasize that the parameter θ_{13} holds the key to answering one of the most interesting unknowns: CP violation in the lepton sector, which is one of the pieces in the matter-antimatter asymmetry puzzle. In addition, it can also solve the problem of the neutrino mass hierarchy. Determining the value of this parameter is therefore of great scientific interest and T2K and other experiments will hopefully be able to provide the answers.

Bibliography

[1] Y. Fukuda, Phys. Rev. Lett. 81 (1998) 1562.

[2] M.H. Ahn et al., Phys. Rev. D 74 (2006) 072003.

[3] P. Adamson et al., Phys. Rev. Lett. 106 (2011) 181801.

[4] H. Becquerel, Comptes Rendus 122 (1896) 501.

[5] J. Chadwick, Verh. d. D. Phys. Ges. 16 (1914) 383.

[6] C. Jensen, Controversy and Consensus: Nuclear Beta Decay 1911-1934 (Birkhauser Verlag, 2000).

[7] K. Winter, editor, Neutrino Physics, 2nd ed. (Cambridge University Press, 2000).

[8] J. Chadwick, Proc. Roy. Soc. A 136 (1932) 692.

[9] E. Fermi and F.L. Wilson, AJP 36 (1968) 1150.

[10] H. Bethe and R. Peierls, Nature 133 (1934) 532.

[11] C. Cowen and F. Reines, Nature 178 (1956) 446.

[12] M. Goldhaber, L. Grodzins and A.W. Sunyar, Phys. Rev. 109 (1958) 1015.

[13] J.N. Bahcall, Scientific American 221 (1969) 28.

[14] R. Davis, Phys. Rev. Lett. 12 (1964) 303.

[15] J.N. Bahcall, Phys. Rev. Lett. 12 (1964) 300.

[16] B. Pontecorvo, Chalk River preprint PD-205 (1946).

[17] R. Davis, D.S. Harmer and K.C. Hoffman, Phys. Rev. Lett. 20 (1968) 1205.

[18] B. Pontecorvo, Z. Theor. Exp. Physics 37 (1959) 1751.

[19] M. Schwartz, Phys. Rev. Lett. 4 (1960) 306.

[20] G. Danby et al., Phys. Rev. Lett. 9 (1962) 36.

[21] S. Van der Meer, CERN preprint CERN-61-7 (1961).

[22] M. Perl et al., Phys. Rev. Lett. 35 (1975) 1489.

[23] ALEPH Collaboration, DELPHI Collaboration, L3 Collaboration, OPAL Collaboration, SLD Collaboration, LEP Electroweak Working Group, SLD Electroweak and Heavy Flavour Groups, Phys. Reports 427 (2006) 257.

[24] K. Kodama et al., Phys. Rev. D 78 (2008) 052002.

[25] M. Altmann et al., Phys. Lett. B 616 (2005) 174.

[26] W. Hampel et al., Phys. Lett. B 447 (1999) 127.

[27] J.N. Abdurashitov et al., (2002), astro-ph/0204245.

[28] J. Hosaka et al., Phys. Rev. D 73 (2006) 112001.

[29] B. Pontecorvo, Sov. Phys. JETP 26 (1968) 984.

[30] Z. Maki, M. Nakagawa and S. Sakata, Prog. Theor. Phys. 28 (1962) 870.

[31] H. Chen, Phys. Rev. Lett. 55 (1985) 1534.

[32] B. Aharmim et al., Phys. Rev. C 72 (2005) 055502.

[33] K. Abe et al., Nucl. Instrum. Meth. A 659 (2011) 106.

[34] T. Schwetz, M. Tortola and J.W.F. Valle, (2011), hep-ph/1108.1376.

[35] M. Apollonio et al., Eur. Phys. J. C 27 (2003) 331.

[36] F. Ardellier et al., (2006), hep-ex/0606025.

[37] J.K. Ahn et al., (2010), arXiv:1003.1391.

[38] X. Guo et al., (2006), hep-ex/0701029.

[39] S. Abe et al., Phys. Rev. Lett. 100 (2008) 221803.

[40] K. Eguichi et al., Phys. Rev. Lett. 90 (2003) 021802.

[41] S. Parke, Neutrino Oscillations – Present Status and Future Plans (World Scientific, 2008) .

[42] L. Wolfenstein, Phys. Rev. D 17 (1978) 2369.

[43] V. Barger et al., Phys. Rev. D 22 (1980) 2718.

[44] E.K. Akhmedov et al., JHEP 078 (2004) 1.

[45] S.P. Mikheyev and A.Y. Smirnov, Nuovo Cimento C 9 (1986) 17.

[46] K. Abe et al., Phys. Rev. Lett. 107 (2011) 041801.

[47] B. Richter, (2000), hep-ph/0008222.

[48] B. Aharmim et al., Phys. Rev. C 81 (2010) 055504.

[49] Y. Ashie et al., Phys. Rev. Lett. 93 (2004) 101801.

[50] Y. Ashie et al., Phys. Rev. D 71 (2005) 112005.

[51] K. Abe et al., (2012), arXiv:1201.1386.

[52] J. Hosaka et al., Phys. Rev. D 74 (2006) 032002.

[53] P. Adamson et al., Phys. Rev. Lett. 107 (2011) 181802.

[54] Y. Abe et al., (2012), arXiv:1112.6353.

[55] D. Beavis et al., preprint BNL 52459 (1995).

[56] K. Matsuoka et al., Nucl. Instrum. Meth. A 623 (2010) 385.

[57] K. Matsuoka et al., Nucl. Instrum. Meth. A 624 (2010) 591.

[58] Y. Hayato, Nucl. Phys. (Proc. Suppl.) B 112 (2002) 117.

[59] J. Altegoer et al., Nucl. Instrum. Meth. A 404 (1998) 96.

[60] I. Giomataris et al., Nucl. Instrum. Meth. A 560 (2006) 405.

[61] S. Fukuda et al., Nucl. Instrum. Meth. A 501 (2003) 418.

[62] `http://www-sk.icrr.u-tokyo.ac.jp/sk/index-e.html`.

[63] S. Bhadra et al., (2012), arXiv:1201.1922.

[64] V. Ginsburg and I. Frank, JETP 16 (1946) 15.

[65] P. Goldsmith and J.V. Jelley, Phil. Mag. 4 (1959) 836.

[66] V. Scarpine et al., IEEE Transactions on Nuclear Science 51 (2004) 1529.

[67] J. Bosser et al., Nucl. Instrum. Methods A 238 (1985) 45.

[68] A. Toyoda, Proceedings of DIPAC09, 2009.

[69] J.D. Jackson, Classical Electrodynamics, 3rd ed. (John Wiley and Sons, 1998).

[70] M.L. Ter-Mikaelian, High-energy Electromagnetic Processes in Condensed Media, English language ed. (John Wiley and Sons, 1972).

[71] L. Wartski et al., J. Appl. Phys. (1975) 3644.

[72] D.R. Lide, editor, CRC Handbook of Chemistry and Physics, 81st ed. (CRC Press, 2000).

[73] S. Ritt, P. Amaudruz and K. Olchanski, MIDAS (Maximum Integration Data Acquisition System), `http://midas.psi.ch`, 2001.

[74] G.E. Schalnat et al., `http://www.libpng.org/pub/png/libpng.html`, 2011.

[75] `http://www.galilmc.com`.

[76] G. Wolberg, Digital Image Warping (IEEE Computer Society Press, 1992).

[77] G. Arfken, Mathematical Methods for Physicists, 3rd ed. (Academic Press, 1985) chap. Gram-Schmidt Orthogonalization.

[78] G. Battistoni et al., Proceedings of the Hadronic Shower Simulation Workshop 2006, Fermilab, 2006.

[79] G. Battistoni et al., AIP Conference Proceeding, p. 31, 2007.

[80] A. Ferrari et al., preprint CERN-2005-10 (2005).

[81] Geant – detector description and simulation tool, 1993.

[82] C. Zeitnitz and T.A. Gabriel, Nucl. Instr. Meth. A 349 (1994) 106.

[83] N. Abgrall et al., Phys. Rev. C 84 (2011) 034604.

[84] N. Abgrall et al., (2011), hep-ex/1112.0150.

[85] T. Eichten et al., Nucl. Phys. B 44 (1972) 333.

[86] J.V. Allaby et al., CERN preprint 70-12 (1970).

[87] I. Chemakin et al., Phys. Rev. C 77 (2008) 015209.

[88] R.P. Feynman, Phys. Rev. Lett. 23 (1969) 1415.

[89] F.E. Taylor et al., Phys. Rev. D 14 (1976) 1217.

[90] M. Bonesini et al., Eur. Phys. J. C 20 (2001) 13.

[91] D.S. Barton et al., Phys. Rev. D 27 (1983) 2580.

[92] P. Skubic et al., Phys. Rev. D 18 (1978) 3115.

[93] R.J. Abrams et al., Phys. Rev. D 1 (1970) 1917.

[94] J.V. Allaby et al., Yad. Fiz. 12 (1970) 538.

[95] B.W. Allardyce et al., Nucl. Phys. A 209 (1973) 1.

[96] G. Bellettini et al., Nucl. Phys. 79 (1966) 609.

[97] B.M. Bobchenko et al., Sov. J. Nucl. Phys. 30 (1979) 805.

[98] A.S. Carroll et al., Phys. Lett. B 80 (1979) 319.

[99] J.W. Cronin et al., Phys. Rev. 107 (1957) 1121.

[100] F.F. Chen et al., Phys. Rev. 99 (1955) 857.

[101] S.P. Denisov et al., Nucl. Phys. B 61 (1973) 62.

[102] M.J. Longo and B.J. Moyer, Phys. Rev. 125 (1962) 701.

[103] A.V. Vlasov et al., Sov. J. Nucl. Phys. 27 (1978) 222.

[104] K. Abe et al., (2011), arXiv:1111.3119.

[105] G.J. Feldman and R.D. Cousins, Phys. Rev. D 57 (1998) 3873.

[106] S. Bilenky, Introduction to the physics of massive and mixed neutrinos (Springer-Verlag, 2010).

[107] K. Zuber, Neutrino Physics (CRC Press, 2010).

[108] J. Liouville, Journ. de Math. 3 (1838) 349.

Appendices

A Oscillation Probabilities in Vacuum

To calculate the expression for various neutrino oscillation channels in vacuum, we begin with the general expression for the oscillation probability:

$$\begin{aligned} P_{\alpha\beta} &= |U^*_{\alpha1}U_{\beta1}e^{-i\frac{m_1^2L}{2E}} + U^*_{\alpha2}U_{\beta2}e^{-i\frac{m_2^2L}{2E}} + U^*_{\alpha3}U_{\beta3}e^{-i\frac{m_3^2L}{2E}}|^2 \\ &= |U^*_{\alpha1}U_{\beta1} + U^*_{\alpha2}U_{\beta2}e^{-2i\Delta_{21}} + U^*_{\alpha3}U_{\beta3}e^{-2i\Delta_{31}}|^2, \end{aligned} \tag{A.1}$$

where Δ_{ji} stands for

$$\Delta_{ji} = \frac{\Delta m^2_{ji}L}{4E}. \tag{A.2}$$

For $\alpha = \beta$, Eq A.1 can be written as

$$\begin{aligned} P_{\alpha\alpha} &= ||U_{\alpha1}|^2 + |U_{\alpha2}|^2e^{-2i\Delta_{21}} + |U_{\alpha3}|^2e^{-2i\Delta_{31}}|^2 \\ &= |U_{\alpha1}|^4 + |U_{\alpha2}|^4 + |U_{\alpha3}|^4 \\ &+ 2|U_{\alpha1}|^2|U_{\alpha2}|^2\cos 2\Delta_{21} + 2|U_{\alpha1}|^2|U_{\alpha3}|^2\cos 2\Delta_{31} + 2|U_{\alpha2}|^2|U_{\alpha3}|^2\cos 2\Delta_{32} \\ &= |U_{\alpha1}|^4 + |U_{\alpha2}|^4 + |U_{\alpha3}|^4 + 2|U_{\alpha1}|^2|U_{\alpha2}|^2 + 2|U_{\alpha1}|^2|U_{\alpha3}|^2 + 2|U_{\alpha2}|^2|U_{\alpha3}|^2 \\ &- 4|U_{\alpha1}|^2|U_{\alpha2}|^2\sin^2\Delta_{21} - 4|U_{\alpha1}|^2|U_{\alpha3}|^2\sin^2\Delta_{31} - 4|U_{\alpha2}|^2|U_{\alpha3}|^2\sin^2\Delta_{32} \\ &= (|U_{\alpha1}|^2 + |U_{\alpha2}|^2 + |U_{\alpha3}|^2) \\ &- 4|U_{\alpha1}|^2|U_{\alpha2}|^2\sin^2\Delta_{21} - 4|U_{\alpha1}|^2|U_{\alpha3}|^2\sin^2\Delta_{31} - 4|U_{\alpha2}|^2|U_{\alpha3}|^2\sin^2\Delta_{32} \\ &= 1 - 4|U_{\alpha1}|^2|U_{\alpha2}|^2\sin^2\Delta_{21} - 4|U_{\alpha1}|^2|U_{\alpha3}|^2\sin^2\Delta_{31} - 4|U_{\alpha2}|^2|U_{\alpha3}|^2\sin^2\Delta_{32}. \end{aligned} \tag{A.3}$$

If $\alpha \neq \beta$, it is also possible to simplify Eq. A.1 somewhat. Using the unitarity condition

$$\sum_{i=1}^{3} U^*_{\alpha i}U_{\beta i} = \delta_{\alpha\beta},$$

we can re-write Eq. A.1 as

$$\begin{aligned}
P_{\alpha\beta} &= |U^*_{\alpha2}U_{\beta2}e^{-2i\Delta_{21}} + U^*_{\alpha3}U_{\beta3}e^{-2i\Delta_{31}} - (U^*_{\alpha2}U_{\beta2} + U^*_{\alpha3}U_{\beta3})|^2 \\
&= 4|U^*_{\alpha2}U_{\beta2}e^{-i\Delta_{21}}\sin\Delta_{21} + U^*_{\alpha3}U_{\beta3}e^{-i\Delta_{31}}\sin\Delta_{31}|^2 \\
&= 4(U^*_{\alpha2}U_{\beta2}e^{-i\Delta_{21}}\sin\Delta_{21} + U^*_{\alpha3}U_{\beta3}e^{-i\Delta_{31}}\sin\Delta_{31}) \\
&\times (U_{\alpha2}U^*_{\beta2}e^{i\Delta_{21}}\sin\Delta_{21} + U_{\alpha3}U^*_{\beta3}e^{i\Delta_{31}}\sin\Delta_{31}) \\
&= 4(|U_{\alpha2}U_{\beta2}|^2\sin^2\Delta_{21} + |U_{\alpha3}U_{\beta3}|^2\sin^2\Delta_{31} \\
&+ 2|U_{\alpha2}U_{\beta2}U_{\alpha3}U_{\beta3}|\sin\Delta_{21}\sin\Delta_{31}\cos(\Delta_{32}+\delta)).
\end{aligned} \tag{A.4}$$

For anti-neutrinos, on the other hand, the appearance probability is

$$\begin{aligned}
P_{\bar\alpha\bar\beta} &= 4(|U_{\alpha2}U_{\beta2}|^2\sin^2\Delta_{21} + |U_{\alpha3}U_{\beta3}|^2\sin^2\Delta_{31} \\
&+ 2|U_{\alpha2}U_{\beta2}U_{\alpha3}U_{\beta3}|\sin\Delta_{21}\sin\Delta_{31}\cos(\Delta_{32}-\delta)).
\end{aligned} \tag{A.5}$$

The last term in Eq. A.4 and A.5 gives rise to CP violation if $\delta \neq 0$.

Eqs. A.3 – A.5 are the general expressions for the oscillation probabilities for the case of three neutrino mixing. We will now derive the probabilities for some of the specific appearance and disappearance channels.

We start with the algebraically simplest case of P_{ee}. From Eq. 3.23 it follows that

$$\begin{aligned}
|U_{e1}|^2 &= c^2_{12}c^2_{13}, \\
|U_{e2}|^2 &= s^2_{12}c^2_{13}, \\
|U_{e3}|^2 &= s^2_{13}.
\end{aligned}$$

Substituting these into Eq. A.3 we obtain

$$P_{ee} = 1 - c^4_{13}\sin^2 2\theta_{12}\sin^2\Delta_{21} - \sin^2 2\theta_{13}(c^2_{12}\sin^2\Delta_{31} + s^2_{12}\sin^2\Delta_{32}). \tag{A.6}$$

The next in line is the probability of electron neutrino appearance in a ν_μ beam, $P_{\mu e}$:

$$\begin{aligned}
P_{\mu e} &= |2U^*_{\mu2}U_{e2}e^{-i\Delta_{21}}\sin\Delta_{21} + 2U^*_{\mu3}U_{e3}e^{-i\Delta_{31}}\sin\Delta_{31}|^2 \\
&= |2s_{12}c_{13}(c_{12}c_{23} - s_{12}s_{23}s_{13}e^{-i\delta})e^{-i\Delta_{21}}\sin\Delta_{21} + s_{23}\sin 2\theta_{13}e^{-i\Delta_{31}}e^{-i\delta}\sin\Delta_{31}|^2 \\
&= |2s_{12}c_{13}(c_{12}c_{23} - s_{12}s_{23}s_{13}e^{-i\delta})\sin\Delta_{21} + s_{23}\sin 2\theta_{13}\sin\Delta_{31}e^{-i(\Delta_{32}+\delta)}|^2 \\
&= |c_{13}c_{23}\sin 2\theta_{12}\sin\Delta_{21} - s^2_{12}s_{23}\sin 2\theta_{13}\sin\Delta_{21}e^{-i\delta} + s_{23}\sin 2\theta_{13}\sin\Delta_{31}e^{-i(\Delta_{32}+\delta)}|^2.
\end{aligned} \tag{A.7}$$

Introducing the following quantities

$$\sqrt{P^{\mu e}_{\rm sol}} = c_{13}c_{23}\sin 2\theta_{12}\sin\Delta_{21}, \tag{A.8}$$

$$\sqrt{P^{\mu e}_{\rm atm}} = s_{23}\sin 2\theta_{13}\sin\Delta_{31}, \tag{A.9}$$

$$\sqrt{P^{\mu e}_{\rm tiny}} = s^2_{12}s_{23}\sin 2\theta_{13}\sin\Delta_{21}, \tag{A.10}$$

we can write

$$\begin{aligned} P_{\mu e} &= |\sqrt{P^{\mu e}_{\rm sol}} - \sqrt{P^{\mu e}_{\rm tiny}}e^{-i\delta} + \sqrt{P^{\mu e}_{\rm atm}}e^{-i(\Delta_{32}+\delta)}|^2 \\ &= P^{\mu e}_{\rm sol} + P^{\mu e}_{\rm atm} + P^{\mu e}_{\rm tiny} - 2\sqrt{P^{\mu e}_{\rm tiny}}(\sqrt{P^{\mu e}_{\rm sol}}\cos\delta + \sqrt{P^{\mu e}_{\rm atm}}\cos\Delta_{32}) \\ &+ 2\sqrt{P^{\mu e}_{\rm sol}}\sqrt{P^{\mu e}_{\rm atm}}\cos(\Delta_{32}+\delta), \end{aligned} \tag{A.11}$$

while for anti-neutrinos Eq. A.11 becomes

$$\begin{aligned} P_{\bar{\mu}\bar{e}} &= P^{\mu e}_{\rm sol} + P^{\mu e}_{\rm atm} + P^{\mu e}_{\rm tiny} - 2\sqrt{P^{\mu e}_{\rm tiny}}(\sqrt{P^{\mu e}_{\rm sol}}\cos\delta + \sqrt{P^{\mu e}_{\rm atm}}\cos\Delta_{32}) \\ &+ 2\sqrt{P^{\mu e}_{\rm sol}}\sqrt{P^{\mu e}_{\rm atm}}\cos(\Delta_{32}-\delta). \end{aligned} \tag{A.12}$$

Consequently the last term in Eqs. A.11 and A.12 can lead to the CP violation. Moreover, the contribution of $\sqrt{P^{\mu e}_{\rm tiny}}$ is negligible for oscillation studies on the distance scales set by the Δ_{31} and the neutrino energies from the accelerator beams. This is illustrated in Fig. A.1 where Eqs. A.8 – A.10 are plotted for a rather low ν_μ energy of 100 MeV. The contribution of $\sqrt{P^{\mu e}_{\rm tiny}}$ does not become significant until the distances where oscillations are driven by Δ_{21}. Ignoring this contribution, we can simplify the expressions for the ν_e and $\bar{\nu}_e$ appearance probability to

$$P_{\mu e} \simeq P^{\mu e}_{\rm sol} + P^{\mu e}_{\rm atm} + 2\sqrt{P^{\mu e}_{\rm sol}}\sqrt{P^{\mu e}_{\rm atm}}\cos(\Delta_{32}+\delta), \tag{A.13}$$

$$P_{\bar{\mu}\bar{e}} \simeq P^{\mu e}_{\rm sol} + P^{\mu e}_{\rm atm} + 2\sqrt{P^{\mu e}_{\rm sol}}\sqrt{P^{\mu e}_{\rm atm}}\cos(\Delta_{32}-\delta). \tag{A.14}$$

Finally we calculate the probability for the ν_μ disappearance, $P_{\mu\mu}$:

$$\begin{aligned} P_{\mu\mu} &= 1 - 4|U_{\mu 1}|^2|U_{\mu 2}|^2\sin^2\Delta_{21} - 4|U_{\mu 1}|^2|U_{\mu 3}|^2\sin^2\Delta_{31} - 4|U_{\mu 2}|^2|U_{\mu 3}|^2\sin^2\Delta_{32} \\ &= 1 - 4|U_{\mu 3}|^2(|U_{\mu 1}|^2\sin^2\Delta_{31} + |U_{\mu 2}|^2\sin^2\Delta_{32}) - P^{\mu\mu}_{\rm sol}, \end{aligned} \tag{A.15}$$

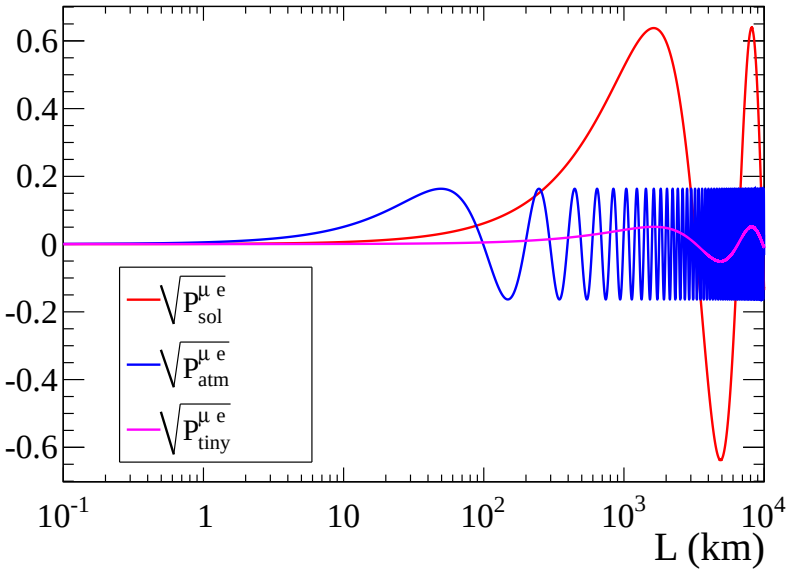

Figure A.1: Contributions to $P_{\mu e}$. The values of the parameters (taken from [34]): $\Delta m^2_{21} = 7.59 \times 10^{-5}$ eV^2, $\Delta m^2_{31} = 2.50 \times 10^{-3}$ eV^2, $\sin^2\theta_{12} = 0.312$, and $\sin^2\theta_{13} = 0.013$.

where

$$P^{\mu\mu}_{\text{sol}} = 4|U_{\mu 1}|^2|U_{\mu 2}|^2 \sin^2\Delta_{21}. \tag{A.16}$$

In the case when the energy of the neutrinos and the distance to the detector are such that we are only sensitive to the $\Delta m^2_{32} \simeq \Delta m^2_{31}$, the $P^{\mu\mu}_{\text{sol}}$ can be neglected and Eq. A.15 can be further simplified to

$$\begin{aligned} P_{\mu\mu} &= 1 - 4|U_{\mu 3}|^2(1-|U_{\mu 3}|^2)\sin^2\Delta_{32} \\ &= 1 - 4c^2_{13}s^2_{23}(1-c^2_{13}s^2_{23})\sin^2\Delta_{32} \\ &= 1 - c^4_{13}\sin^2 2\theta_{23}\sin^2\Delta_{32} - s^2_{23}\sin^2 2\theta_{13}\sin^2\Delta_{32}. \end{aligned} \tag{A.17}$$

This can be shown more rigorously by expanding $\sin\Delta_{31}$ to the first order in Δ_{21}:

$$\sin^2\Delta_{31} = \sin^2\Delta_{32} + \Delta_{21}\sin 2\Delta_{32}. \tag{A.18}$$

Then

$$|U_{\mu 1}|^2\sin^2\Delta_{31} \simeq |U_{\mu 1}|^2\sin^2\Delta_{32} + s^2_{12}c^2_{23}\Delta_{21}\sin 2\Delta_{32}, \tag{A.19}$$

where we have neglected terms on the order of $s_{13}\Delta_{21}$ and higher. Consequently

$$\begin{aligned} P_{\mu\mu} &\simeq 1 - 4|U_{\mu 3}|^2(1 - |U_{\mu 3}|^2)\sin^2\Delta_{32} - 4|U_{\mu 3}|^2 s_{12}^2 c_{23}^2 \Delta_{21}\sin 2\Delta_{32} \\ &= 1 - c_{13}^4\sin^2 2\theta_{23}\sin^2\Delta_{32} - s_{23}^2\sin^2 2\theta_{13}\sin^2\Delta_{32} - c_{13}^2 s_{12}^2\sin^2 2\theta_{23}\Delta_{21}\sin 2\Delta_{32} \end{aligned} \tag{A.20}$$

Near the oscillation maximum $\Delta_{32} \simeq \pi/2$, so that $\sin\Delta_{32} \simeq 1$ while $\sin 2\Delta_{32} \simeq 0$, so the last term does not contribute.

B Oscillation Probabilities in Matter

B.1 General formalism

The effects of the neutrino interactions in matter on the oscillation probabilities can be obtained by solving the Schrödinger equation, Eq. B.1, for the evolved neutrino state $\Psi(x,t)$ in the presence of the appropriate matter potentials. For simplicity, we drop any spatial dependence, *i.e.*, work in the rest frame of ν_i:

$$i\frac{\partial}{\partial t}\Psi(t) = \hat{H}\Psi(t), \tag{B.1}$$

where $\hat{H}$ is the Hamiltonian operator. Expanding $\Psi(t)$ in the flavor eigenstate basis, we obtain

$$\Psi(t) = \sum_{\alpha} f_{\alpha}(t)|\nu_{\alpha}\rangle, \tag{B.2}$$

where $f_{\alpha}^2(t) = |\langle\nu_{\alpha}|\Psi(t)\rangle|^2$ is the probability to find ν_{α} in the state $\Psi(x,t)$. From Eqs. B.1 and B.2 it follows that

$$i\frac{\partial}{\partial t}f_{\beta}(t) = \sum_{\alpha}\langle\nu_{\beta}|H|\nu_{\alpha}\rangle f_{\alpha}(t). \tag{B.3}$$

Arranging $f_{\beta}(t)$ into a vector $(\nu_e, \nu_{\mu}, \nu_{\tau})^T$ and the terms $\langle\nu_{\beta}|H|\nu_{\alpha}\rangle$ into a 3×3 matrix which we will call H and Eq. B.3 can be re-written in a matrix form as

$$i\frac{\partial}{\partial t}f(t) = Hf(t). \tag{B.4}$$

Solving Eq. B.4 for $f(t)$, we get

$$f(t) = e^{-iHt}f(t_0). \tag{B.5}$$

In the case of vacuum oscillations $H = H_0$ where

$$H_0 = \mathbf{U} \begin{pmatrix} m_1 & 0 & 0 \\ 0 & m_2 & 0 \\ 0 & 0 & m_3 \end{pmatrix} \mathbf{U}^\dagger \tag{B.6}$$

and

$$e^{-iHt} = \mathbf{U} \begin{pmatrix} e^{-im_1 t} & 0 & 0 \\ 0 & e^{-im_2 t} & 0 \\ 0 & 0 & e^{-im_3 t} \end{pmatrix} \mathbf{U}^\dagger. \tag{B.7}$$

Imposing the condition that neutrino was born in state α, *i.e.*, $f(t_0) = \delta_{\alpha\beta}$, we obtain

$$f_\beta(t) = \sum_i U_{\beta i} e^{-im_i t} U^*_{\alpha i}$$

or, after using the Lorentz invariance $m_i t = Et' - pL$,

$$f_\beta(L,t) = \sum_i U_{\beta i} e^{-i(Et - pL)} U^*_{\alpha i}$$

which is completely equivalent to Eq. 3.3.

It should be noted, that in the majority of literature H_0 is defined as

$$H_0 = \frac{1}{2E} \mathbf{U} \begin{pmatrix} m_1^2 & 0 & 0 \\ 0 & m_2^2 & 0 \\ 0 & 0 & m_3^2 \end{pmatrix} \mathbf{U}^\dagger \tag{B.8}$$

which follows from the approximation of E_i by $E + m_i^2/2E$. Since the first term results in an overall phase factor multiplying the oscillation amplitude, it disappears when the oscillation probability is computed. Thus only m_i^2 term is considered in H_0. Both Eq. B.6 and Eq. B.8 yield the same results for oscillation probabilities, but Eq. B.8 makes subsequent algebra somewhat easier, so we will use it instead of Eq. B.6.

Returning to the propagation of neutrinos in matter, we construct an effective Hamiltonian as

$$H_M = H_0 + H_Z + H_W. \tag{B.9}$$

The neutral current (NC) interactions (Fig. 3.6a) affect all flavors. Therefore the

Hamiltonian for these type of interactions has the form

$$H_Z = V_Z \begin{pmatrix} 1 & 0 & 0 \\ 0 & 1 & 0 \\ 0 & 0 & 1 \end{pmatrix}, \tag{B.10}$$

where V_Z is determined by the strength of interactions and the density of matter.

The neutral current contribution would generate only an additional overall phase in Eq. B.5 that would disappear when calculating the oscillation probability. Thus these processes have no effect on the flavor oscillations. This is true in general for any H which is proportional to the identity matrix.

In case of the charged current ν_e scattering. the Hamiltonian has the form

$$H_W = V_W \begin{pmatrix} 1 & 0 & 0 \\ 0 & 0 & 0 \\ 0 & 0 & 0 \end{pmatrix}. \tag{B.11}$$

The constant V_W is given by

$$V_W = \sqrt{2} G_F n_e, \tag{B.12}$$

where G_F is the Fermi constant that sets the coupling strength of the interactions and n_e is the matter electron density. For anti-neutrinos V_W is

$$V_W = -\sqrt{2} G_F n_e. \tag{B.13}$$

To illustrate the effects of such interaction on the neutrino oscillations, we consider the case of two neutrino mixing. The free Hamitonian in this case becomes

$$\begin{aligned} H_0 &= \frac{1}{2E} \begin{pmatrix} \cos\theta & \sin\theta \\ -\sin\theta & \cos\theta \end{pmatrix} \begin{pmatrix} m_1^2 & 0 \\ 0 & m_2^2 \end{pmatrix} \begin{pmatrix} \cos\theta & -\sin\theta \\ \sin\theta & \cos\theta \end{pmatrix} \\ &= \frac{1}{2E} \begin{pmatrix} m_1^2 \cos^2\theta + m_2^2 \sin^2\theta & (m_2^2 - m_1^2) \sin\theta\cos\theta \\ (m_2^2 - m_1^2) \sin\theta\cos\theta & m_1^2 \sin^2\theta + m_2^2 \cos^2\theta \end{pmatrix} \\ &= \frac{m_1^2 + m_2^2}{4E} \begin{pmatrix} 1 & 0 \\ 0 & 1 \end{pmatrix} + \frac{\Delta m^2}{4E} \begin{pmatrix} -\cos 2\theta & \sin 2\theta \\ \sin 2\theta & \cos 2\theta \end{pmatrix}. \end{aligned} \tag{B.14}$$

As already discussed, the terms proportional to the identity matrix do not contribute to the oscillation probability, so we can simply write

$$H_0 = \frac{\Delta m^2}{4E} \begin{pmatrix} -\cos 2\theta & \sin 2\theta \\ \sin 2\theta & \cos 2\theta \end{pmatrix}. \tag{B.15}$$

For H_W, we obtain

$$H_W = \frac{V_W}{2}\begin{pmatrix}1 & 0\\ 0 & -1\end{pmatrix} + \frac{V_W}{2}\begin{pmatrix}1 & 0\\ 0 & 1\end{pmatrix}. \tag{B.16}$$

Drooping the last term

$$H_W = \frac{\Delta m^2}{4E}\begin{pmatrix}a/\Delta m^2 & 0\\ 0 & -a/\Delta m^2\end{pmatrix}, \tag{B.17}$$

where

$$a = 2\sqrt{2}G_F n_e E. \tag{B.18}$$

Therefore the total Hamiltonian in matter is

$$H_M = \frac{\Delta m^2}{4E}\begin{pmatrix}-(\cos 2\theta - a/\Delta m^2) & \sin 2\theta\\ \sin 2\theta & \cos 2\theta - a/\Delta m^2\end{pmatrix}. \tag{B.19}$$

Defining

$$\Delta m^2_M = \Delta m^2\sqrt{\sin^2 2\theta + (\cos 2\theta - a/\Delta m^2)^2} \tag{B.20}$$

and

$$\sin 2\theta_M = \frac{\sin 2\theta}{\sqrt{\sin^2 2\theta + (\cos 2\theta - a/\Delta m^2)^2}}, \tag{B.21}$$

Eq. B.19 can be re-written as

$$H_M = \frac{\Delta m^2_M}{4E}\begin{pmatrix}-\cos 2\theta_M & \sin 2\theta_M\\ \sin 2\theta_M & \cos 2\theta_M\end{pmatrix}. \tag{B.22}$$

Comparing Eq. B.22 with Eq. B.15, we can conclude that by replacing θ with θ_M and Δm^2 with Δm^2_M in Eqs. 3.18 and 3.20 the two flavor oscillation probabilities in matter can be obtained:

$$P_{\mu e} = \sin^2 2\theta_M \sin^2\left(1.27\frac{L(\text{km})}{E(\text{GeV})}\Delta m^2_M(\text{eV}^2)\right) \tag{B.23}$$

and

$$P_{\mu\mu} = 1 - \sin^2 2\theta_M \sin^2\left(1.27\frac{L(\text{km})}{E(\text{GeV})}\Delta m^2_M(\text{eV}^2)\right). \tag{B.24}$$

B.2 Disappearance of the solar neutrinos

The MSW effect for the solar neutrinos is discussed in the context of the so called adiabatic matter transitions where it is assumed that the matter density decreases very slowly along the neutrino path. In the two flavor oscillation framework, the matter eigenstates $\tilde{\nu}_i$ can be expressed in terms of the flavor states ν_e and ν_μ by inverting the mixing matrix:

$$\begin{aligned} \tilde{\nu}_1 &= \nu_e \cos\theta_M - \nu_\mu \sin\theta_M, \\ \tilde{\nu}_2 &= \nu_e \sin\theta_M + \nu_\mu \cos\theta_M, \end{aligned} \tag{B.25}$$

where θ_M is given by Eq. B.21. For the neutrinos produced in the layers where $n_e \gg n_e^{\rm crit}$, $\sin 2\theta_M \simeq 0$ and $\theta_M \simeq \pi/2$. Consequently, the neutrino mixing is suppressed, as the mass eigenstates are identical to the flavor eigenstates:

$$\begin{aligned} \tilde{\nu}_1 &\simeq -\nu_\mu, \\ \tilde{\nu}_2 &\simeq \nu_e. \end{aligned} \tag{B.26}$$

Since the reactions in the sun produce ν_e, Eq. B.26 implies that the solar neutrinos are produced in $\tilde{\nu}_2$ eigenstate. For the adiabatic transitions neutrinos will remain in the mass eigenstate and emerge from the sun in the vacuum eigenstate ν_2, which will not oscillate. The flavor content of the mass eigenstate, however, is no longer pure ν_e and contains a mixture of ν_μ and ν_e. The average probability for ν_e to emerge as ν_e is given by (see for example [106], [107])

$$P(\nu_e \to \nu_e) = \frac{1}{2}(1 + \cos 2\theta \cos 2\theta_M(x)), \tag{B.27}$$

where $\theta_M(x)$ is the mixing angle at the production point. It is energy dependent because of θ_M. Different vacuum oscillation parameter values (θ, Δm^2) can lead to different suppression of the energy spectrum of emerging ν_e. Since ν_e gradually evolves into ν_2, no oscillation actually happen for solar neutrinos. The MSW effect, however, does rely on the existence of the neutrino mixing.

C Proton Beam

C.1 Beam orbit fit

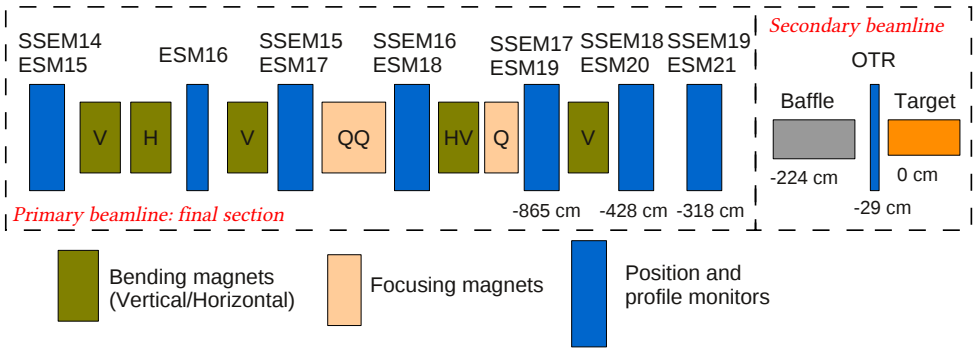

Figure C.1: Proton monitors and beamline elements upstream of the target.

The beamline components in the final focusing section and upstream end of the target vessel are shown in Fig. C.1. The position and angle of the proton beam is obtained by fitting the beam position measurements. In the horizontal x direction, the proton monitors downstream of the last quadrupole magnet are used. In the vertical y direction, the monitors downstream of the last vertical bending magnet are used. In this approach, there is no magnetic field that can change the beam orbit present between different monitors. Consequently the orbit can fit can be done simply by fitting the position data from the beam monitors to a straight line:

$$x(s) = x_0 + x's + x_{\text{offset}}, \tag{C.1}$$

where

- s is the coordinate collinear with the design beam orbit
- $x(s)$ is the fit function in either the x or y coordinate

- x' is the beam angle
- x_0 is the beam center at a given point in the beamline (e.g. target)
- x_{offset} is the offset between the primary and secondary beamline.

The parameters x_0, x', and x_{offset} are determined by fitting the position measurements with Eq. C.1.

C.2 Beam optics fit

C.2.1 Introduction to matrix formalism of beam dynamics

The beam profile in position-angle, $x - x'$, phase-space is represented by ellipse in general given by

$$\gamma x^2 + 2\alpha x x' + \beta x'^2 = \epsilon. \tag{C.2}$$

The parameters α, β, γ are called the Twiss parameters and ϵ is called the emittance. The area of the beam in $x - x'$ is given by $\epsilon\pi$.

The parameters satisfy the following constraint

$$\beta\gamma - \alpha^2 = 1. \tag{C.3}$$

Liouville's theorem [108] requires ϵ to be conserved along a transport line.

The coordinates at any point in the beamline can be obtained from the transformation

$$\begin{pmatrix} x(s) \\ x'(s) \end{pmatrix} = \begin{pmatrix} C(s) & S(s) \\ C'(s) & S'(s) \end{pmatrix} \begin{pmatrix} x_0 \\ x'_0 \end{pmatrix} \tag{C.4}$$

or more compactly in matrix notation

$$\mathbf{x} = \mathbf{M}\mathbf{x}_0. \tag{C.5}$$

The conservation of beam emittance requires that the Twiss parameters transform according to

$$\begin{pmatrix} \beta(s) \\ \alpha(s) \\ \gamma(s) \end{pmatrix} = \begin{pmatrix} C(s)^2 & -2C(s)S(s) & S(s)^2 \\ -C(s)C'(s) & C(s)S'(s) + C'(s)S(s) & -S(s)S'(s) \\ S'(s)^2 & -2C'(s)S'(s) & S'(s)^2 \end{pmatrix} \begin{pmatrix} \beta_0 \\ \alpha_0 \\ \gamma_0 \end{pmatrix}. \tag{C.6}$$

For a simple case of a particle beam traveling through a drift space of length l,

the transformation in Eq. C.4 has the form:

$$\begin{pmatrix} x(l) \\ x'(l) \end{pmatrix} = \begin{pmatrix} 1 & l \\ 0 & 1 \end{pmatrix} \begin{pmatrix} x(0) \\ x'(0) \end{pmatrix}. \tag{C.7}$$

The matrix representing the drift space is therefore

$$\mathbf{M}_{\text{Drift}} = \begin{pmatrix} 1 & l \\ 0 & 1 \end{pmatrix}. \tag{C.8}$$

The transformation of the Twiss parameters in Eq. C.6 in the drift space takes the form

$$\begin{pmatrix} \beta(l) \\ \alpha(l) \\ \gamma(l) \end{pmatrix} \begin{pmatrix} 1 & -2l & l^2 \\ 0 & 1 & -l \\ 0 & 0 & 1 \end{pmatrix} \begin{pmatrix} \beta_0 \\ \alpha_0 \\ \gamma_0 \end{pmatrix}. \tag{C.9}$$

For a quadrupole magnet of length l, the transformation matrix in the focusing plane is

$$\mathbf{M}_{\text{focus}} = \begin{pmatrix} \cos\sqrt{k}l & 1/\sqrt{k}\sin\sqrt{k}l \\ -\sqrt{k}\sin\sqrt{k}l & \cos\sqrt{k}l \end{pmatrix}, \tag{C.10}$$

while the de-focusing plane of a quadrupole is represented by

$$\mathbf{M}_{\text{defocus}} = \begin{pmatrix} \cosh\sqrt{|k|}l & 1/\sqrt{|k|}\sinh\sqrt{|k|}l \\ \sqrt{|k|}\sinh\sqrt{|k|}l & \cosh\sqrt{|k|}l \end{pmatrix}. \tag{C.11}$$

The quadrupole field strength parameter k is determined by the field gradient G and the momentum of a particle beam p:

$$k = \frac{eG}{p}, \tag{C.12}$$

where e is the electric charge.

The propagation of a particle beam through a transport line consisting of some sequence of drift spaces, bending magnets, and quadrupole magnets is represented by a series of transformation matrices $\mathbf{M}_i$ appropriate for each element. The total transformation matrix for some number of elements N is the product of each individual transformation matrix:

$$\mathbf{M} = \mathbf{M}_N\mathbf{M}_{N-1}\ldots\mathbf{M}_3\mathbf{M}_2\mathbf{M}_1. \tag{C.13}$$

C.2.2 Measurement of emittance and Twiss parameters

The beam width σ is related to the emittance and the Twiss parameter β according to

$$2\sigma = \sqrt{\epsilon\beta}. \tag{C.14}$$

According to Eq. C.6, the Twiss parameter β transforms as

$$\beta = M_{11}^2\beta_0 - 2M_{11}M_{12}\alpha_0 + M_{12}^2\gamma_0, \tag{C.15}$$

where the matrix elements M_{ij} are determined by the appropriate sequence of transformations. Multiplying both sides of Eq. C.15 by the emittance ϵ and using Eq. C.14 and Eq. C.3 gives

$$(2\sigma)^2 = M_{11}^2(2\sigma_0)^2 - 2M_{11}M_{12}\alpha_0\epsilon + M_{12}^2\frac{\epsilon(1+\alpha_0^2)}{(2\sigma_0)^2}. \tag{C.16}$$

The parameters ϵ, α_0, and σ_0 are obtained by fitting the width measurements σ_i from the profile monitors in the final focusing section of the primary beamline and the OTR in the secondary beamline.

C.3 Treatment of proton beam parameters in Monte Carlo simulation

The proton distribution in $x - x'$ (x refers to either x or y coordinate) phase-space is modeled by

$$\begin{aligned} B(x,x') =& \frac{1}{2\pi\sigma_x\sigma_{x'}\sqrt{1-\rho_{xx'}^2}}\times \\ & \exp\left(-\frac{1}{2(1-\rho_{xx'}^2)}\left[\frac{(x-\bar{x})^2}{\sigma_x^2} + \frac{(x'-\bar{x}')^2}{\sigma_{x'}^2} - \frac{2\rho_{xx'}(x-\bar{x})(x'-\bar{x}')}{\sigma_x\sigma_{x'}}\right]\right), \end{aligned} \tag{C.17}$$

where

- $\sigma_{x'} = \epsilon\sqrt{1+\alpha^2}/4\sigma_x$
- $\rho_{xx'} = -\alpha/\sqrt{1+\alpha^2}$.

The mean values of position $\bar{x}$ and angle $\bar{x}'$ are obtained from the orbit fit to the position monitor data, which is described at the beginning of this Appendix. The

parameters Twiss α, emittance ϵ, and beam width σ_x are extracted from the orbit fit described in the previous section.

To generate a proton distribution according to Eq. C.17, a pair of independent random numbers r_1 and r_2 is drawn from a Gaussian distribution with a mean of 0 and a width of 1. The x and x' are then calculated from

$$\begin{pmatrix} x \\ x' \end{pmatrix} = \begin{pmatrix} \cos\theta & -\sin\theta \\ \sin\theta & \cos\theta \end{pmatrix} \begin{pmatrix} ar_1 \\ br_2 \end{pmatrix} + \begin{pmatrix} \bar{x} \\ \bar{x}' \end{pmatrix}, \tag{C.18}$$

where the angle θ is

$$\theta = \frac{1}{2} \arctan \frac{2\alpha}{\gamma - \beta}, \tag{C.19}$$

while a and b are given by

$$a = \frac{1}{2} \sqrt{\frac{\epsilon}{\gamma + \alpha \tan\theta}}, \tag{C.20}$$

$$b = \frac{1}{2} \sqrt{\frac{\epsilon}{\beta - \alpha \tan\theta}}. \tag{C.21}$$

D Particle Momentum in the Centre of Mass Frame

In this section we show how the centre of mass (CM) momentum of a particle c produced in the inclusive reaction of the type

$$a + b \to c + X \tag{D.1}$$

is calculated.

The square of the total CM energy available in any frame is

$$s = (E_c + E_X)^2 - (\mathbf{p}_c + \mathbf{p}_X)^2. \tag{D.2}$$

In the CM frame this becomes

$$s = (\sqrt{p^2 + m^2} + \sqrt{p^2 + M^2})^2, \tag{D.3}$$

where m and M are the masses of c and X, respectively, where the latter is

$$M = \sum_i m_i. \tag{D.4}$$

Expanding the right-hand-side of Eq. D.3 gives

$$s = 2p^2 + m^2 + M^2 + 2\sqrt{p^2 + m^2}\sqrt{p^2 + M^2}, \tag{D.5}$$

which leads to

$$((s - m^2 - M^2) - 2p^2)^2 = 4(p^2 + m^2)(p^2 + M^2). \tag{D.6}$$

Expanding the expressions on the left and right gives

$$(s - m^2 - M^2)^2 - 4p^2(s - m^2 - M^2) + 4p^4 = 4p^4 + 4p^2(m^2 + M^2) + 4m^2M^2. \tag{D.7}$$

Eq. D.7 can be easily solved for p^2:

$$p^2 = \frac{(s - m^2 - M^2)^2 - 4m^2M^2}{4s}. \tag{D.8}$$

Thus the momentum of particle c in the CM frame is

$$p = \sqrt{\frac{(s - m^2 - M^2)^2 - 4m^2M^2}{4s}}. \tag{D.9}$$